

https://dspace.org/

Fabrication of a C/C-SiC-TiC-TaC composite by hybrid wet infiltration

Makurunje, Phylis Sarah

2016-04-05
http://hdl.handle.net/10539/20175

Downloaded from a DSpace repository. https://dspace.org/



FABRICATION OF A C/C-SiC-TiC-TaC COMPOSITE BY HYBRID WET INFILTRATION

DISSERTATION

by

PHYLIS SARAH MAKURUNJE

Submitted in fulfilment of the requirements for the degree of
Master of Science in Engineering
Materials and Metallurgical Engineering
University of the Witwatersrand
Johannesburg, South Africa

2015

Supervisor

PROFESSOR IAKOVOS SIGALAS

DECLARATION

I declare that this thesis is my own unaided work except where otherwise acknowledged. It is being submitted for the Master of Science in Engineering at the University of the Witwatersrand, Johannesburg. It has not been submitted before for any degree or examination in any other University.

Signed: _____

Phylis Sarah Makurunje (749539)

Date: _____

ABSTRACT

A novel C_f/C-SiC-TiC-TaC composite was successfully fabricated by performing reactive melt infiltration (RMI) by means of pressureless spark plasma sintering (SPS) at 1700°C to permeate molten 66.7Si-17.9Ti-15.4Ta alloy into a porous C_f/C composite prepared by polymer impregnation and pyrolysis (PIP).

The C_f/C composite preform was of density 1.54g/cm^3 and open porosity 21%, obtained after 3 cycles of PIP with resole phenolic resin. An amorphous carbon matrix was thus obtained and was confirmed by X-Ray Diffraction (XRD) and Raman spectroscopy. The 66.7Si-17.9Ti-15.4Ta alloy prepared by arc melting from $TaSi_2$ and $TiSi_2$ powders formed a solid solution of (Ta,Ti)Si_2 and (Ta,Ti)$_5Si_3$. When the alloy was infiltrated into the C_f/C composite preform cubic face centred carbides of Ta, Ti and Si, and the (Ta,Ti)C solid solution were obtained at 1700°C by SPS for 30 minutes. At 1600°C the UHTC matrix was predominantly unreacted silicides; SiC is the only carbide which was convincingly formed, although (Ta,Ti)C was observed by XRD and SEM to have incipiently precipitated at the C/alloy interface. At 1800°C the carbide formation reactions extended to the reinforcing fibres, thus compromising the fibres' reliability. 1700°C was deemed the excellent trade-off temperature for the formation of the C_f/C-SiC-TiC-TaC composite, wherein an acceptable compromise of the extent of carbide-forming reactions completion and limiting the damage of the melt to the fibres.

Upon exposure to an oxyacetylene flame of at least 3000°C, the C_f/C-SiC-TiC-TaC composite showed thermomechanical degradation first, and thermochemical degradation thereafter. After 7.5s of exposure to the oxyacetylene flame (4 MW/m^2 heat flux) placed 19mm away, the unprotected C_f/C composite showed a mass ablation rate of 0.0402g/s and a linear ablation rate of 0.377 mm/s. The UHTC showed a low mass ablation rate of 0.00388 g/s and a low linear ablation rate of 0.00216 mm/s owing to the scale of the oxides formed adhering to the surface of the composite. The scale, analysed by scanning electron microscopy, X-ray diffraction, electron dispersive spectroscopy and electron probe micro-analysis, showed that the composite constituents had the ability to form glassy self-healing eutectics based on SiO_2 (Ta_5O_2-SiO_2 and $TaTiO_4$-SiO_2). The C_f/C-SiC-TiC-TaC composite is a promising candidate for the sharp nose and leading edges of hypersonic vehicles.

ACKNOWLEDGEMENTS

I have heartfelt gratitude towards the following individuals and institutions that made the completion of this work possible:

My supervisors: Prof. Iakovos Sigalas for believing in me and directing this work in a ground-breaking direction, and Dr. Mathias Herrmann for continually critiquing this work and raising the bar.

Reinmetall-Denel Munition, Somerset for the oxyacetylene flame tests. Thank you Sonja Lotz and Ruben Strydom.

Mintek for the equipment they made available. Special mention goes to Dr. Joseph Moema; Richard Couperthwaite; Edson Muhuma; and Lebohang Mokoena.

SI Group for the phenolic resin donations.

The Microscopy and Micro-analysis Unit (MMU) for training in operating the microscopes.

Patrick Rockebrand for the SPS work and insightful discussions.

Farai Dziike for assisting with XRD and for being a brotherly anchor in my entire work.

Wilson Mogodi for assistance with XRD analysis on TOPAS software.

Ryno Van der Merwe for mercury intrusion porosimetry.

The DST-NRF Centre of Excellence in Strong Materials (CoE-SM) administration staff for always helping timeously whenever I was in need.

My family for the love and support - you are a delight!

All my dear friends for being there! Mcdonald, Sunungurai, Mavoe, Daisy, Tinashe.

My spiritual parents at Word of Life – bravo! Thank you for the support and prayers

---

The support of the DST-NRF Centre of Excellence in Strong Materials (CoE-SM) towards this research is hereby acknowledged. Opinions expressed and conclusions arrived at, are those of the author and are not necessarily to be attributed to the CoE-SM.

That ceiling that we were trying to break through is now the floor of a new dimension, another level – a deeper level.

Israel Houghton

LIST OF SYMBOLS

$\bar{v}_l$	specific molar volume of species *i*
$\emptyset_i$	volume fraction of species *i*
D_i	diffusivity of species *i*
K_{MV}	coefficient of molar volume
L_a	crystallite size parameter
M_i	mole weight of species *i*
W_a	van der Waals adhesive forces
k_r	reaction rate
r_i	pore radius at instance *i*
u_D	front velocity
2θ	diffraction angle
A	area
a,b,c	crystal lattice parameters
θ	contact angle of system
d	mean grain size
h	infiltration height
K_y	Hall-Petch slope
m	mass
$\emptyset_s$	sphericity shape factor
P	perimeter
p	pressure
R	universal gas constant
T	Temperature
t	Time
x	thickness
γ	Shear rate
ΔH_i	heat change of process *i*
ΔT	temperature change
ε	Porosity
η	dynamic viscosity
λ	wavelength of X-rays

ν	dinematic viscosity
ρ_i	density of species *i*
σ_o	materials constant for the starting stress for dislocation movement
σ_y	yield stress,
τ	stress
Φ	porosity
κ	permeability
μ	viscosity
σ	surface tension
τ	tortuosity
E	activation energy
ΔG	Gibbs free energy

LIST OF ABBREVIATIONS

AECL	Atomic Energy of Canada Limited
AMT	Advanced Materials Technology
BET	Brunauer–Emmett–Teller
bcc	body centred cubic
BMIs	bismaleimides
BPR	ball-to-powder ratio
C_f/C	carbon-fibre-reinforced carbon
CVI	chemical vapour infiltration
EB	electron beam
EBSD	electron backscattered diffraction
EDS	energy dispersive spectroscopy
EPMA	electron probe micro-analysis
fcc	face centred cubic
FIB	focused ion beam
HBN	hexagonal boron nitride
hcp	hexagonal close packed
HIP	hot isostatic pressing
HTT	high temperature treatment
LPI	liquid polymer infiltration
LSI	liquid silicon infiltration
MC	Monte-Carlo
MDA	methylene dianiline
MIA	multiple image alignment
MIP	mercury intrusion porosimetry
NASA	National Aeronautics and Space Administration
OOA	out-of-autoclave
PAA	polyarylacetylene

PIP	polymer infiltration and pyrolysis
RMI	reactive melt infiltration
ROI	region of interest
RPR	reaction products region
SAED	selected area electron diffraction
SEM	scanning electron microscope
SI-PIP	slurry infiltration combined and polymer infiltration and pyrolysis
SI-LSI	slurry infiltration and liquid silicon infiltration
SPS	spark plasma sintering
STEM	scanning transmission electron microscope
TEM	transmissions electron microscope
TOPAS	Total Pattern Analysis Solution
UHTC	ultra high temperature ceramic
VPS	vacuum plasma spraying
XRD	X-ray diffraction

TABLE OF CONTENTS

ABSTRACT i

ACKNOWLEDGEMENTS ii

LIST OF SYMBOLS iv

LIST OF ABBREVIATIONS vi

TABLE OF CONTENTS viii

LIST OF FIGURES xi

LIST OF TABLES xviii

CHAPTER 1 – INTRODUCTION 1

1.1 OVERVIEW 1

1.2 BACKGROUND OF STUDY 1

1.3 PROBLEM STATEMENT 4

1.4 AIM AND OBJECTIVES 5

1.5 SCOPE OF WORK 6

1.6 METHODOLOGY OVERVIEW 6

1.7 ORGANISATION OF DISSERTATION 7

CHAPTER 2 – LITERATURE REVIEW 9

2.1 OVERVIEW: COMPOSITE MATERIALS 9

2.2 CARBON MATRIX COMPOSITES 10

2.3 PROCESSING ROUTES 12

2.3.1 Gaseous Precursors Route 12

2.3.2 Liquid Precursors Route 14

2.4 THERMOSET RESINS PROCESSING 15

2.4.1 Thermoset Resins for High Temperature Applications 15

2.4.2 Curing Process 16

2.4.3 Pyrolysis Process 19

2.4.4 Graphitizing Process 20

2.5 ABLATION OF C/C COMPOSITES IN HOSTILE ENVIRONMENTS 24

2.6 CERAMIC MATRIX COMPOSITES - ULTRA HIGH TEMPERATURE CERAMICS (UHTCs) 25
2.6.1 Silicon Carbide (SiC) 27
2.6.2 Boron Carbide (B_4C) 29
2.6.3 Zirconium Carbide (ZrC) 31
2.6.4 Tantalum Carbide (TaC) 34
2.6.5 Titanium Carbide (TiC) 36
2.7 INFILTRATION PHENOMENA 38
2.7.1 Chemical Reaction vs Mass Transfer 39
2.7.2 Capillary Action 40
2.8 SUMMARY 43
CHAPTER 3 – EXPERIMENTAL METHODOLOGY 44
3.1 OVERVIEW 44
3.2 PREPARATION OF MATERIALS 45
3.2.1 CARBON/CARBON COMPOSITE FABRICATION 45
3.2.2 Si-Ti-Ta ALLOY PREPARATION 50
3.2.3 PREPARATION OF C/Si-Ti-Ta REACTION-DIFFUSION COUPLE 54
3.2.4 PREPARATION OF THE C/C-TaC-TiC-SiC COMPOSITE 56
3.2.5 ABLATION RESISTANCE TEST OF THE C_f/C-SiC-TiC-TaC COMPOSITE 57
3.3 MATERIALS CHARACTERISATION 59
CHAPTER 4 – RESULTS 68
4.1 OVERVIEW 68
4.2 THE CARBON-CARBON COMPOSITE 69
4.2.1 Bulk Matrix Microstructure 69
4.2.2 Carbon Fibre-reinforced Carbon Composite Microstructure 71
4.2.3 Interface Microstructure 74
4.2.4 PIP Densification Efficiency 75
4.2.5 Macropores Size Distribution 77
4.2.6 Micropores Size Distribution 81
4.2.7 XRD and Raman Patterns 83

4.3 THE Si-Ti-Ta ALLOY 85
4.3.1 Powder Characterisation 85
4.3.2 Si-Ti-Ta Alloy Characterization 89
4.4 C/Si-Ti-Ta REACTION COUPLES 94
4.4.1 Couple Heat Treated at 1500°C 95
4.4.2 Couples Heat Treated at 1600°C - 1800°C 95
4.5 THE C/C- SiC-TiC-TaC COMPOSITE 104
4.5.1 Phases Present in the Composite 109
4.5.2 Fracture Surface 115
4.6 ABLATED C/C COMPOSITE 122
4.7 ABLATED C_f/C-SiC-TiC-TaC COMPOSITE 127
4.6.1 Microstructure of Ablated UHTCs 128
4.6.2 Phases Present in the Ablated UHTC 135
4.8 SUMMARY 139
CHAPTER 5 – DISCUSSION 140
5.1 OVERVIEW 140
5.2 THE C/C COMPOSITE PREFORM 140
5.3 THE Si-Ti-Ta ALLOY 142
5.4 THE C/C-SiC-TiC-TaC UHTC COMPOSITE 144
5.4.2 Alloy Infiltration 144
5.4.3 Carbides-Formation Mechanism 144
5.5 PERFORMANCE OF THE C/C COMPOSITE 146
5.6 PERFORMANCE OF THE C/C-SiC-TiC-TaC UHTC COMPOSITE 148
CHAPTER 6 – CONCLUSIONS 151
6.1 OVERVIEW 151
6.2 CONCLUSIONS 151
6.3 RECOMMENDATIONS 154
REFERENCES 155

LIST OF FIGURES

Figure 1: (a) Taurus XL rocket meant for launching a US environmental observatory satellite in January 2011 (NASA, n.d.); (b) Exhaust nozzle (Sanjeev, 2013); (c) The SpaceX Falcon 9 v1.1 rocket launching a commercial communications satellite (SES-8) in August 2013 (Foust, 2014); (d) The nine Merlin 1C engines on the SpaceX Falcon 9 v1.1 rocket in (c) (Bergin, 2013) 2

Figure 2: Summarised methodology of experimental work undertaken. 7

Figure 3: The dependence of composite properties on chemical composition, processing conditions and microstructure. 10

Figure 4: The specific strength vs temperature ranges of various materials (Manocha, 2003). 11

Figure 5: A summary of C_f/C composites processing routes (Windhorst & Blount, 1997) 12

Figure 6: A generic process flow for CVI-based C_f/C composites processing routes (Manocha, 2003). 13

Figure 7: The resultant fibre-bundled laminar microstructure of a CVI processed C-matrix (Wang *et al.*, 2012). 13

Figure 8: Generic process flow based on a thermoset precursor and a thermoplastic precursor for making a C_f/C composite (Manocha, 2003). 14

Figure 9: The microstructural changes during a thermoset cure: (A) Monomers before reaction (B) Small molecules develop with inter-branching (C) The gel point is reached (D) Fully cured polymer (Franck, 2004). 18

Figure 10: Structural models for amorphous carbons created by an NVT Monte Carlo (MC) simulation (a) skeletal lattice of a linear carbon polymer (b) tangled sp^2-coordinated carbon structure (c) final carbon structure (Kumar *et al.*, 2005)..... 22

Figure 11: A summary of the main processing routes for ceramic matrix composites.27

Figure 12: The typical microstructure of a C_f/SiC composites (Jiang *et al.*, 2008). 29

Figure 13: The microstructure showing a homogeneous dispersion of the ZrB2–ZrC–SiC ceramic phases in the matrix (Qian *et al.*, 2013)..... 32

Figure 14: A graded matrix obtained in fabricating a C_f/C-SiC-ZrC matrix (Wang *et al.*, 2012); (b) How crack-deflection in a multi-graded ceramic matrix reduces oxygen diffusion (Lamouroux *et al.*, 1999). 33

Figure 15: Ceramic graded-interface obtained by Chen *et al.* (2009)..... 34

Figure 16: Comparison of mass erosion rates for C_f/C-ZrB2; C_f/C-4ZrB2-1SiC; C_f/C-1ZrB2-2SiC; C_f/C-2SiC-1ZrB2-2HfC; C_f/C-2SiC-1ZrB2-2TaC; and C_f/C (Tang *et al.*, 2007). 35

Figure 17: The microstructure and phases in the C_f/C-Si-Ti3SiC2 composite Fan *et al.* (2013). 37

Figure 18: (a) The infiltration height vs time curves for reaction rates k, of (1) no reaction (2) 10^{-9} m/s (3) 10^{-8}m/s (4) 10^{-7} m/s, for pore diameter 0.17μm and initial porosity 50%, (b) decrease in permeability at the pore centreline for the system with reaction rate 10-8 (Nelson and Collela, 2000) 40

Figure 19: Diagrams showing the infiltration height and capillary diameter dynamics. (a) For a single capillary system; (b) For a system incorporating energy dissipation with $dK\ mindK\ max = 2050$; (c) For a system incorporating energy dissipation with with $dK\ mindK\ max = 550$ (Gern and Kochendörfer, 1997) 42

Figure 20: Carbon fibre cloth of twill 2/2 architecture used (left); the arrangement of laminates during the lay-up process (right). 46

Figure 21: Vacuum bagging set-up used for phenolic resin infiltration. (a) schematic representation; (b) and (c) photographed set-up. 47

Figure 22: The C_f/C composite reimpregnation set up 48

Figure 23: The designed curing chamber set up used for curing the impregnated composites. 49

Figure 24: The tube furnace used in carbonising the C_f/phenolic resin composite. 50

Figure 25: The arc melting furnace used to alloy the $TaSi_2$ and $TiSi_2$ powders. 53

Figure 26: The SPS machine used for reactive melt infiltration (left) and the reaction chamber set-up (right). 56

Figure 27: The closed graphite crucible set-up designed pressureless heat treatment in the SPS. 56

Figure 28: (a) The oxyacetylene flame test set-up used; (b) the special sample holder prepared for the C_f/C-SiC-TiC-TaC composite (Courtesy of Rheinmetall-Denel Munition, Somerset West, South Africa) 57

Figure 29: A summary of the mercury intrusion parameters used. 62

Figure 30: Optical micrograph showing the glossy, pseudo-glassy appearance of the carbon matrix. 69

Figure 31: Micrograph of a C_f/C composite in which infiltration of resin was effected without vacuum bagging. The occurrence of conchoidal fracture in the matrix during pyrolysis is evident. 71

Figure 32: An optical micrograph of the C_f/C composite after 3 cycles of PIP. The white phase represents the fibres, the grey phase represents the matrix, and the black phase represents the pores in the composite. 72

Figure 33: Cross-sectional SE-SEM microstructure of the C_f/C composite revealing the profound permeation and lodging of the matrix in-between the inter-fibre gaps within the tows. 73

Figure 34: A micrograph showing the fibre and matrix interface. The presence of pores and cracks in the matrix in-between fibres is evident. 74

Figure 35: The graph of the mass of C_f/C composite and its porosity vs the number of PIP cycles effected. .....**Error! Bookmark not defined.**

Figure 36: Graphs of the mass changes at each cycle stage after infiltration with resin, after heat treatment, and after the overall PIP cycle. ....**Error! Bookmark not defined.**

Figure 37: Differential Curves of volume of mercury intruded with respect to the pore diameter for the C_f/C composites at different PIP cycles. 79

Figure 38: Micrograph showing the diversity of pore sizes in the carbon matrix. 80

Figure 39: The change in the tortuosity factor and permeability in the C_f/C composites against the number of PIP cycles effected on the same. 81

Figure 40: Hysteresis graph of the volume of N_2 adsorbed and desorbed against pressure applied during BET porosimetry. 82

Figure 41: Graph of the differential volume of adsorbed N_2 against the pore diameter from BET porosimetry in the C_f/C composite after 3 cycles of PIP. 83

Figure 42: XRD spectra of C_f/C composites after each cycle of PIP. 84

Figure 43: Raman spectroscopy pattern of the C_f/C which underwent 3 cycles of PIP. 84

Figure 44: SE-SEM micrographs showing the morphology of loose as-received tantalum silicide ($TaSi_2$) powder at x200 magnification (a) and x1000 magnification (b). 86

Figure 45: Diffractogram for tantalum silicide $TaSi_2$ powder. The red lines represent the template pattern for $TaSi_2$ from the EVA database. 87

Figure 46: SE-SEM micrographs showing the morphology of loose as-received titanium silicide ($TiSi_2$) powder at x200 magnification (a) and x1000 magnification (b). 87

Figure 47: Diffractogram for loose titanium silicide ($TiSi_2$) powder. The red lines represent the template pattern for $TiSi_2$ from the EVA database. 88

Figure 48: SEM micrographs for mixed loose titanium silicide ($TiSi_2$) and tantalum silicide ($TaSi_2$) powders. The white phase represents $TaSi_2$ and the black phase represents $TiSi_2$. 88

Figure 49: Backscattered micrograph of the Si-Ti-Ta alloy showing an overview of the microstructure. Regions A,B,C and D represent the variations in the shapes of the alloy grains. 89

Figure 50: Elaborated micrographs of the four regions shown in Figure 55. 90

Figure 51: High magnification SEM image showing the different phases in a polished cross-section of the Si-Ti-Ta alloy. 91

Figure 52: Diffractogram for alloyed $TaSi_2$-$TiSi_2$ powders. 93

Figure 53: BSED-SEM micrographs of cross-sections of the C/Si-Ti-Ta diffusion-reaction couples prepared by contacting carbon powder and Si-Ti-Ta alloy by spark plasma sintering in vacuum at 1500°C (a), 1600°C(b), 1700°C(c) and 1800°C(d) for 30 minutes. 94

Figure 54: BSED-SEM micrograph and associated SEM-EDS maps of the cross-section of the C/Si-Ti-Ta diffusion-reaction couple prepared by spark plasma sintering at 1500°C for 30 minutes. 97

Figure 55: BSED-SEM micrograph and associated SEM-EDS maps of the cross-section of the C/Si-Ti-Ta diffusion-reaction couple prepared by spark plasma sintering at 1600°C for 30 minutes. 98

Figure 56: BSED-SEM micrograph and associated SEM-EDS maps of the cross-section of the C/Si-Ti-Ta diffusion-reaction couple prepared by spark plasma sintering at 1700°C for 30 minutes. 100

Figure 57: EDS maps of the cross-section of the C/Si-Ti-Ta diffusion-reaction couple prepared by spark plasma sintering at 1800°C for 30 minutes. 101

Figure 58: $TaSi_2$-$TiSi_2$ phase diagram (Kudielka, 1956) showing the tie lines at 1600°C - 1800°C. 103

Figure 59: BSED-SEM micrographs of the cross-sections of C_f/C-SiC-TiC-TaC composites comparing the microstructures obtained by increasing the temperature for reactive-melt-infiltration by SPS for 30min. From top to bottom, the RMI temperature was 1600°C, 1700°C and 1800°C. 105

Figure 60: BSED-SEM images showing microstructures of the cross-section of the C_f/C-SiC-TiC-TaC composite prepared by RMI at 1600°C for 30 minutes using SPS. 106

Figure 61: BSED-SEM images showing microstructures of the cross-section of the C_f/C-SiC-TiC-TaC composite prepared by RMI at 1700°C for 30 minutes using SPS. 107

Figure 62: BSED-SEM images showing microstructures of the cross-section of the C_f/C-SiC-TiC-TaC composite prepared by RMI at 1800°C for 30 minutes using SPS. 108

Figure 63: XRD spectra of C_f/C-SiC-TiC-TaC composites whereby reactive melt infiltration was performed by spark plasma sintering at 1600°C, 1700°C and 1800°C for 30minutes. 112

Figure 64: Graph of experimentally determined lattice parameters (after Reitvield refinement) of the (Ti,Ta)C solid solution in the UHTC prepared at 1600°C, 1700°C and 1800°C, against atomic % tantalum exchange. 114

Figure 65: Secondary detector SEM micrographs showing the fracture surfaces of C_f/C-SiC-TiC-TaC composites prepared by SPS at 1600°C, 1700°C and 1800°C for 30min..... 116

Figure 66: BSED-SEM micrograph of a cross-section of the C_f/C-SiC-TiC-TaC composite prepared by SPS at 1700°C for 30min..... 117

Figure 67: BSED-SEM micrograph showing the microstructure of the longitudinal cross-section of the C_f/C-SiC-TiC-TaC composite prepared by SPS at 1700°C for 30min..... 118

Figure 68: BSED-SEM micrograph showing the microstructure of a transverse cross-section of the C_f/C-SiC-TiC-TaC composite prepared by SPS at 1700°C for 30min.119

Figure 69: BSED-SEM micrograph and SEM-EDS elemental maps obtained from the cross-section of the C_f/C-SiC-TiC-TaC composite whereby reactive melt infiltration was performed by spark plasma sintering at 1700°C for 30minutes. 120

Figure 70: BSED-SEM micrograph of a cross-section of the C_f/C-SiC-TiC-TaC composite prepared by SPS at 1700°C for 30min. The figure shows how the matrix cracked, with some matrix blocks even spalling off during ceramographic preparation. 121

Figure 71: Photographs of C_f/C composite discs of 20mm diameter: (a) Unexposed to flame (b) 2.5s flame exposure time (c) 5.0s flame exposure time (d) 7.5s flame exposure time. 123

Figure 72: SE-SEM micrographs of the cross-section of the C_f/C composite exposed to the oxyacetylene flame for 2.5seconds. 124

Figure 73: (a) Schematic of the crater formed by thermomechanical damage; (b) SE-SEM micrographs of the cross-section of the C_f/C composite exposed to the oxyacetylene flame..... 125

Figure 74: XRD diffractogram of the C_f/C composite surface exposed to the oxyacetylene flame for 2.5s, 5.0s and 7.5s 126

Figure 75: UHTC discs of 20mm diameter: (a) Unexposed to flame (b) 2.5s flame exposure time (c) 5.0s flame exposure time (d) 7.5s flame exposure time..... 127

Figure 76: BSED-SEM micrographs of the cross-section of the UHTC exposed to the oxyacetylene flame for 2.5seconds. 129

Figure 77: BSED-SEM micrographs of the cross-section of the UHTC exposed to the oxyacetylene flame for 5.0 seconds 130

Figure 78: SEM micrographs of the cross-section of the UHTC exposed to the oxyacetylene flame for 7.5 seconds. 1-4 are micrographs of the individual layers of the scale which formed on the UHTC. 132

Figure 79: BSED-SEM micrographs of (a) the cross-section (Region 3 in Figure 78), and (b) the upper surface of the UHTC exposed to the oxyacetylene flame for 7.5 seconds 133

Figure 80: XRD diffractograms of the surface of the UHTC exposed to the oxyacetylene flame for 2.5s, 5.0s and 7.5s. 135

Figure 81: EPMA-BSE image of the surface of the ablated UHTC exposed to the oxyacetylene flame. 138

Figure 82: EPMA elemental X-ray count graphs for Ta, Ti, Si and C taken over the 20 points shown in the BSE image (Figure 81). 138

Figure 83: Isothermal ternary phase diagram for the Ta-Ti-C system at 1820°C (English, 1961). 146

LIST OF TABLES

Table 1: A summary of the evolution of postulations on the microstructure of amorphous carbon. 23

Table 2: Properties of the carbide ceramics used to make ultra-high temperature composites (Ultramet, 2013). 26

Table 3: A summary of the main processing routes for ceramic matrix composites by chemical composition (Rosso, 2006). 27

Table 4: Properties of C_f/SiC Composites with 2D reinforcement. (Krenkel & Hausherr, 2011). 29

Table 5: Effects of adding TaC to a C_f/SiC composite for oxidation protection (Yi *et al.*, 2010). 35

Table 6: Comparison of the mass and linear ablation of C_f/C-SiC composite and C_f/C-Si-Ti3SiC2 composite (Fan *et al.*, 2012). 36

Table 7: Summary of materials used. 44

Table 8: The masses used per batch of milling of $TaSi_2$ and $TiSi_2$ powders. 51

Table 9: The milling parameters used in mixing the $TaSi_2$ and $TiSi_2$ powders. 51

Table 10: The SPS parameters and sintering conditions used. 55

Table 11: Conditions of the oxygen and acetylene gases used in the flame for a heat flux of 4MW/cm^2. 58

Table 12: Percent mass changes after each PIP cycle during C_f/C composite densification. 76

Table 13: Resultant pore volume, average pore diameters and density (all determined by MIP) of C_f/C composite after successive PIP cycles. 77

Table 14: EDS results obtained from the positions 1-4 of the SEM image of the Si-Ti-Ta alloy shown in Figure 51. 91

Table 15: Phase weight fractions in the alloy at given RMI temperature as determined by the Lever Rule. 103

Table 16: Lattice parameters of the phases present in the UHTCs prepared at 1600°C, 1700°C and 1800°C by SPS. Lattice parameters were determined by Rietveld refinement using TOPAS software. 113

Table 17: Linear coefficients of thermal expansion for C, SiC, TaC and TiC at specified temperature ranges. 122

Table 18: Mass and linear ablation rates of the C_f/C discs exposed to the oxyacetylene flame for 2.5 seconds, 5.0 seconds, and 7.5 seconds. 124

Table 19: Mass and linear ablation rates of the UHTC discs exposed to the oxyacetylene flame for 2.5 seconds, 5.0 seconds, and 7.5 seconds. 128

Table 21: Comparison of the mass and linear ablation rates of the C_f/C composite fabricated in the present work to similar C_f/C composites in literature. 147

Table 22: Comparison of the mass and linear ablation rates of the C_f/C-SiC-TiC-TaC fabricated in the present work to similar UHTCs in literature. 148

CHAPTER 1 – INTRODUCTION

1.1 OVERVIEW

For more than half a century, ultra-high temperature ceramics (UHTC) have been applied in thermal protection systems (TPS) for hypersonic vehicles and re-entry vehicles (Zaldivar & Rellick, 1991). UHTCs are very suitable materials for sharp leading edges and nosecones in aerospace vehicles, as well as rocket nozzles and exhaust cones.

UHTCs in these applications have to maintain structural and mechanical integrity during service – low weight, high fracture toughness, high stiffness, high creep resistance, high flexural strength – yet in very harsh conditions of temperatures around 3000°C due to aerodynamic heating, and of ablative gases which cause thermochemical and thermomechanical degradation.

In this work, a novel C_f/C-SiC-TiC-TaC composite was fabricated and was aimed at meeting these requirements and be able to withstand such extreme environments encountered by aerospace and aircraft vehicles. C_f/C-SiC-TiC-TaC

1.2 BACKGROUND OF STUDY

Hypersonic technology flight involves speeds which are at least five times the relative speed of sound, that is, above Mach 5 (at least 5600km/h) (Holder & Monaghan, 1960). The idea of hypersonic flight was mooted during the 2nd World War where missile improvements were sought. Research continued especially because of the Cold War (1947 – 1991) which was between the USA and the Soviet Union (Bertin & Cummings, 2003). Both wars precipitated the arms race and the space race which placed huge and urgent, although overambitious, demands on hypersonic technology. It has long been concluded that hypersonic technology was birthed prematurely when there was still a lot of unknown phenomena surrounding it (Bertin & Cummings,

2003; Heppenheimer, 2009). Now, although the discrete hypersonic phenomena are still unknown, hypersonic flight has been progressing.

Hypersonic flight benefits civil aircraft systems, space access systems and military systems. Hypersonic flight is the envy of passenger aircrafts – it will enable flight to any destination in the world in an hour. On the other hand, hypersonic technology's contribution to space transportation is directed towards communications, reconnaissance, civil remote sensing, human space exploration (National Research Council, 1995), and planetary probing applications. A number of these hypersonic vehicles have to undergo atmospheric re-entry where they experience excessive heat fluxes sometimes around 75MW/cm^2 (Anderson, 2006) due to the very high speed of flight. Re-entry challenges are experienced by both orbital vehicles (for space missions) and suborbital vehicles (for military missions) entering within the 100km Earth altitude. As such, hypersonic technology is also useful in military applications for defence and attack – missiles, penetrators and interceptors – as well as intelligence, surveillance, and reconnaissance (ISR) purposes. Figure 1 shows examples of hypersonic flight vehicles and components.

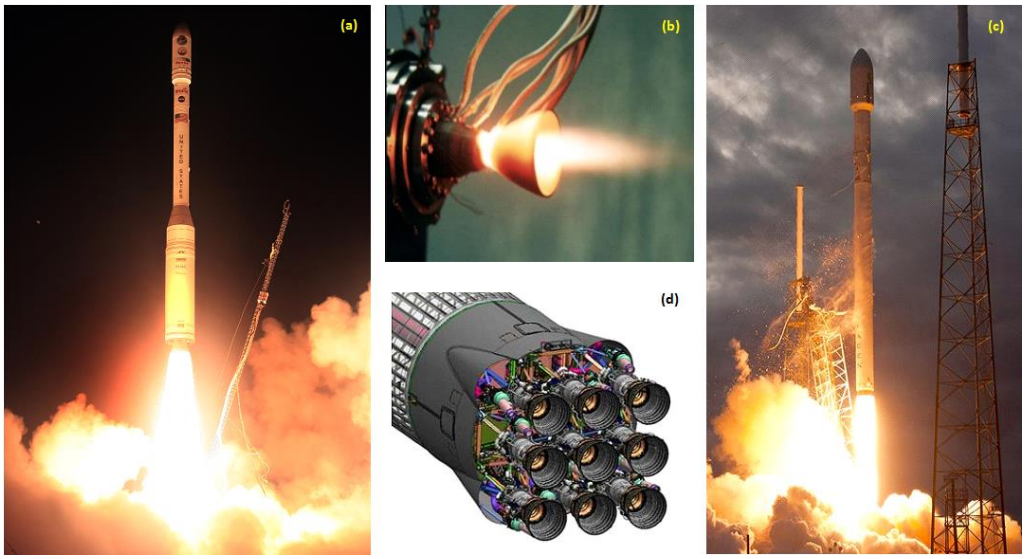

Figure 1: (a) Taurus XL rocket meant for launching a US environmental observatory satellite in January 2011 (NASA, n.d.); (b) Exhaust nozzle (Sanjeev, 2013); (c) The SpaceX Falcon 9 v1.1 rocket launching a commercial communications satellite (SES-8) in August 2013 (Foust, 2014); (d) The nine Merlin 1C engines on the SpaceX Falcon 9 v1.1 rocket in (c) (Bergin, 2013)

When in the hypersonic flight realm, aerodynamic heating governs the multiple phenomena present (Heppenheimer, 2009), resulting in ablative degradation of materials in use. The amount of heat at the leading edges of the vehicles is enormous enough to dissociate and ultimately ionize air molecules around it (Barbante & Magin, 2004; Anderson, 2006; Shi *et al.*, 2012) with increasing Mach number. The ablative degradation of the materials is a combination of thermomechanical and thermochemical processes (Zaman, 2012). The greatest challenge on the thermochemical aspect is the oxidation of the material and the ultimate sublimation of its constituent species. This requirement challenges the materials used in the thermal protection systems of these vehicles.

The current trend has been to combine the structural capabilities of C_f/C composites with the thermal capabilities of ultra-high temperature ceramics (UHTCs) for the extreme environments encountered in hypersonic flight missions. Carbon fibre reinforced carbon composites can maintain structural and mechanical integrity during service. They have low densities of 1,6 – 2,0 g/cm^3 (Manocha, 2003, Devi & Rao, 2013), hardness greater than 20GPa; high fracture toughness of 20–100 Nmm$^{3/2}$ (Manocha, 2003), high stiffness, high creep resistance and high tensile strength (Kerrebrock, 1989; Devi & Rao, 2013) provided the environment is not oxidative. UHTCs possess desirable characteristics of melting points above 3000°C; are relatively light weight materials compared to metals; and show high dimensional, thermal and mechanical stability at elevated temperatures, as presented in Table 2 in Section 2.6. The main challenge that still bedevils the application of UHTCs, however, is their limited ability to endure oxidising environments upwards of 2000°C, let alone 3000°C.

Group IV and V transition elements form borides, nitrides and carbides which serve as UHTCs owing to their high melting points in excess of 3000°C. Opeka *et al.* (2004) emphasize that it is actually the ability of these materials to form oxides with high melting points during service which qualifies them as UHTCs. Here they act as long term anti-oxidation protection systems.

1.3 PROBLEM STATEMENT

Hypersonic flight is seeking to achieve greater and sustainable speed, altitude, range and payload capabilities in these aerospace vehicles – thus the need for improved materials. These materials have to withstand the most extreme conditions: ultra-high temperatures of close to 3000°C, an oxidising environment and ablative exhaust gases. C_f/C composites hybridised with ultra-high temperature ceramics have been the state-of-the-art materials for hypersonic flight applications. So far, no UHTC has been reported to satisfactorily withstand an in-service temperature of 3000°C for more than 360 seconds.

Traditionally, transition metal ceramics were chosen for ultra-high temperature applications on the basis of their melting points primarily. The top performing carbide ceramics known to have melting points above 3000°C are ZrC, HfC, TiC and TaC. Now there is a realisation that the primary criterion ought to be based on the melting points of the oxides they form in-service. It has been established from numerous studies that ZrC, HfC, TiC and TaC form oxides with high melting points, and how SiC and B_4C form crack-sealing glasses.

C_f/C composites with SiC and/or ZrC matrices have been the most researched hybrid composites of all carbide UHTCs. The prominence of ZrC as a component of multi-graded composites is derived from the impressive 2700°C melting point of its oxide (Zhao, 2011). A C_f/ZrC composite would withstand oxidation up to 1940°C; while a C_f/SiC-ZrC composite would go up to 2200°C (Ultramet, 2013).

Hafnium is the second most favoured transition metal used in UHTCs after zirconium, owing to the notable melting point of HfO_2 (2758°C) (Wuchina *et al*., 2007). It has in numerous studies been used in combination with zirconium, especially in boride form. In this case, a stable $(Hf,Zr)O_2$ scale formed, and protects the C_f/C at higher temperatures than most transition metal oxides can.

In an oxidative environment SiC forms glassy SiO_2 which protects the C_f/C composite up to 2000°C (Wuchina *et al*., 2007). Ta_2O_5's melting point (1870°C) is higher than that of SiO_2 (1670°C), although the usefulness of TaC in ablation protection is met by

contradictory findings. Pienti *et al.* (2015) commended the thermomechanical properties of TaC to those of HfC, albeit inferior thermochemical properties. Li *et al.* (2011) recommended the use of combined ceramics to C_f/C composites containing TaC in order to obtain gradients of oxidation protection.

The application of TiC in C_f/C composites for oxidation protection is very limited in literature. The use of Ti in ultra-high temperature environments has been through MAX phases composites and titanium matrix composites (mainly in intermetallic form). TiO_2 is expected to provide oxidation protection to C_f/C composites because of its high melting point of 1850 °C, as well as low diffusion coefficient of oxygen in the same.

This study upholds the contemporary preference towards hybrid (multiphase) ceramic matrices in a given composite. This gives the advantage of complementing the pros and cons of the various ceramics used.

1.4 AIM AND OBJECTIVES

The main aim of this work was to fabricate a C_f/C-SiC-TiC-TaC composite which can serve as a high performance composite able to function in an environment that is oxidative, ablative and above 3000°C.

The aim was to be realised through the following objectives:

- To fabricate a carbon-carbon composite from a carbon fibre woven fabric and a phenolic resin precursor by liquid impregnation and pyrolysis.
- To infiltrate Si-Ti-Ta alloy into the carbon-carbon composite by reactive melt infiltration.
- To determine the matrix layer profile and microstructure formed after the hybrid infiltration methods.
- To characterise the performance of the composite in an ultra-high temperature, oxidative and ablative environment.
- To establish the relationship between the microstructure of the composite to its performance in extreme environments.

1.5 SCOPE OF WORK

This work is limited to the fabrication and characterisation of a novel C_f/C-SiC-TiC-TaC composite. The characterisation work on the resultant composite was limited to its ablative performance in ultra-high temperature environments and did not incorporate mechanical properties characterisation. As such the discussions presented herein overlook the mechanical implications of the reinforcing fibres used.

1.6 METHODOLOGY OVERVIEW

This work sought to combine two wet infiltration methods – Polymer Impregnation and Pyrolysis (PIP) and Reactive Melt Infiltration (RMI) – to make a hybrid ceramic matrix composite. The amorphous carbon deposited during the PIP stage was meant to react with all the constituent elements in the molten $TaSi_2$-$TiSi_2$ alloy infiltrated into the carbon skeletal composite by RMI to give a SiC-TiC-TaC-containing matrix. The resultant carbide ceramics in the matrix were envisaged to be ordered in a sequentially layered pattern owing to the differences in rates of diffusion and reaction with carbon. This gradient was to be considered as multilayers of matrix protecting the carbon fibres from oxidation. The summarised methodology is given in the simplified process flow diagram (Figure 2).

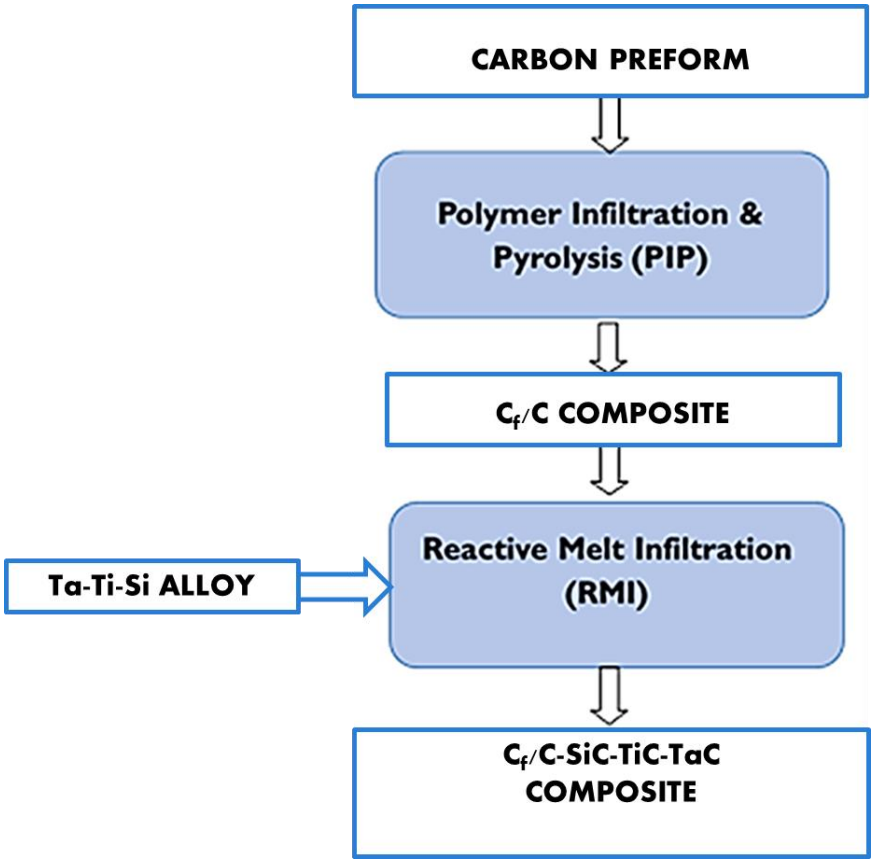

Figure 2: Summarised methodology of experimental work undertaken.

1.7 ORGANISATION OF DISSERTATION

In this chapter the overall aim of this work – to fabricate a C_f/C-SiC-TiC-TaC composite which can serve as a high performance composite able to function in an environment that is oxidative, ablative and above 3000^0C – has been highlighted.

Chapter 2 reviews the available literature on how ultra-high temperature composites are prepared. The discussion highlights the different fabrication routes available for carbon fibre-reinforced carbon composites (C_f/C composites) in general and the liquid polymer infiltration and pyrolysis (PIP) details of phenolic resins in particular. The review is extended to the routes used to produce ceramic matrix composites, with a particular focus on carbide ceramics: ZrC, TaC and TiC as well as the glass-formers SiC and B_4C; and the state-of-the-art reactive melt infiltration (RMI) route. The final part of this review looks into the numerical work associated with the reactive infiltration process.

Chapter 3 details the procedures, techniques and the equipment used in the experimental work which was done in this research. This involved performing two wet infiltration methods – Polymer Impregnation and Pyrolysis (PIP) and Reactive Melt Infiltration (RMI) – to make the C_f/C-SiC-TiC-TaC composite. The composite was then characterized to evaluate and otherwise predict its performance in application in extreme environments.

Chapter 4 presents the results and findings obtained in preparing the C_f/C composite preform and the 66.7Si-17.9Ti-15.4Ta alloy which was to be infiltrated into the same. The chapter points at the challenges and opportunities of infiltrating the alloy at non-eutectic conditions to obtain a C_f/C-SiC-TiC-TaC composite. Results on the ablation resistance capabilities of the UHTC composite, alongside those of the virgin C_f/C composite, are also presented. The changes in the microstructure and phases formed after exposure to the oxyacetylene flame are presented to show the suitability of the fabricated UHTC composite in extreme conditions such as those encountered in hypersonic flight.

Chapter 5 is a discussion of the results presented in Chapter 4. Here a discourse on the structure of amorphous carbons; lattice parameters comparison of the alloy and UHTC phases obtained in this work to those found in literature; and comparison of ablation rates for virgin C_f/C composite and the UHTC to that from previous studies, is presented. Lastly, Chapter 6 presents the conclusions drawn from this study, based on the outcomes presented in Chapter 4. The discussion is extended to recommendations on how to complement the approaches and findings detailed in this dissertation

CHAPTER 2 – LITERATURE REVIEW

2.1 OVERVIEW: COMPOSITE MATERIALS

Composites are materials which consist of two or more discrete and immiscible phases whose properties and functions are complementary. Fibre-reinforced composite materials consist of three main parts: the matrix, the reinforcement and the interface between the two.

The fibre structure is the 'skeleton' of a composite. The fibres impart the mechanical properties required of a composite, especially by increasing the stress and elastic modulus. The matrix is the continuous phase in the composite which holds together the fibre structure and is the conduit for the transfer of forces to the fibres. The matrix also serves to protect fibres from ablative degradation. The interphase has the lowest volume fraction (less than 1 μm thick) (Naslain, 2004; 2006) yet it serves the purpose of transferring loads, deflecting cracks and inhibiting the diffusion of reactive gases to the fibres. Interphases ought to possess comparative and compatible properties with both the fibres and the matrix.

Modern work is focused on producing advanced composites. Advanced composites are those composites which are made of high performance fibres and high performance matrices (Strong, 2008). This makes advanced composites the preferred materials for extreme environments e.g. in aeronautic and aerospace applications.

In this literature review is a discussion on how carbon fibre-reinforced carbon composites (C_f/C composites) are prepared. The different routes available are highlighted with particular focus on the liquid polymer infiltration and pyrolysis (PIP) details of phenolic resins. A detailed discussion on carbon fibres has been deliberately side-lined as it inevitably demands a discourse on mechanical implications of fibre composition, processing, architecture etc. This review intends to address the challenge of ablative degradation in general and oxidative degradation in particular. This is achieved by dwelling on the high performance matrices required to protect the carbon fibre reinforcements from the extreme environments that have been described in Chapter 1.

From C_f/C composites, the discussion is extended to ultra-high temperature ceramic matrix composites. Carbide ceramics are mainly dealt with: ZrC, TaC and TiC as well as SiC and B_4C. The discussion on processing routes is inclined towards the state-of-the-art reactive melt infiltration (RMI) route. The final part of this review looks into the numerical work associated with the reactive infiltration process.

Overall, the aforementioned high performance matrices are discussed at three levels: the chemical composition; the processes applied in manufacturing the matrices; and the resultant microstructure thereof. The resultant properties of the matrices, which are the end of the means, are mentioned as well. The simplified relationship between these aspects is depicted in Figure 3.

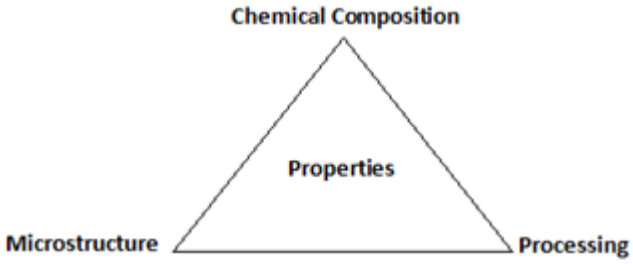

Figure 3: The dependence of composite properties on chemical composition, processing conditions and microstructure.

2.2 CARBON MATRIX COMPOSITES

The impetus for carbon fibre reinforced carbon matrix (C_f/C) composites research began during the 2nd World War with a need for an improved version of graphite material for military materials and aerospace vehicles (Bertin & Cummings, 2003). The first carbon-carbon composite was then made in 1958 at the Chance Vought Aircraft Co., although inadvertently (Dhami & Bahl, 2005). Since then, significant development was realised in the 1960s specifically for re-entry vehicles and rockets (Meetham *et al.*, 2000).

Carbon fibre reinforced carbon composites, simply known as carbon/carbon (C_f/C) composites, They have low densities of 1,6 – 2,0 g/cm^3 (Manocha, 2003, Devi & Rao, 2013), have good mechanical properties at high temperatures (especially in non-oxidising environments) – hardness greater than 20GPa; high fracture toughness of

20–100 $Nmm^{3/2}$ (Manocha, 2003), high stiffness, high creep resistance and high tensile strength (Kerrebrock, 1989; Devi & Rao, 2013) – have low coefficients of thermal expansion and high resistance to thermal shock; and are structurally important in the context of this work due to their significant ablation resistance in extreme environments (high temperature and high pressure) (Manocha, 2003). Figure 4 compares the performance of C_f/C composites to other high performance composites.

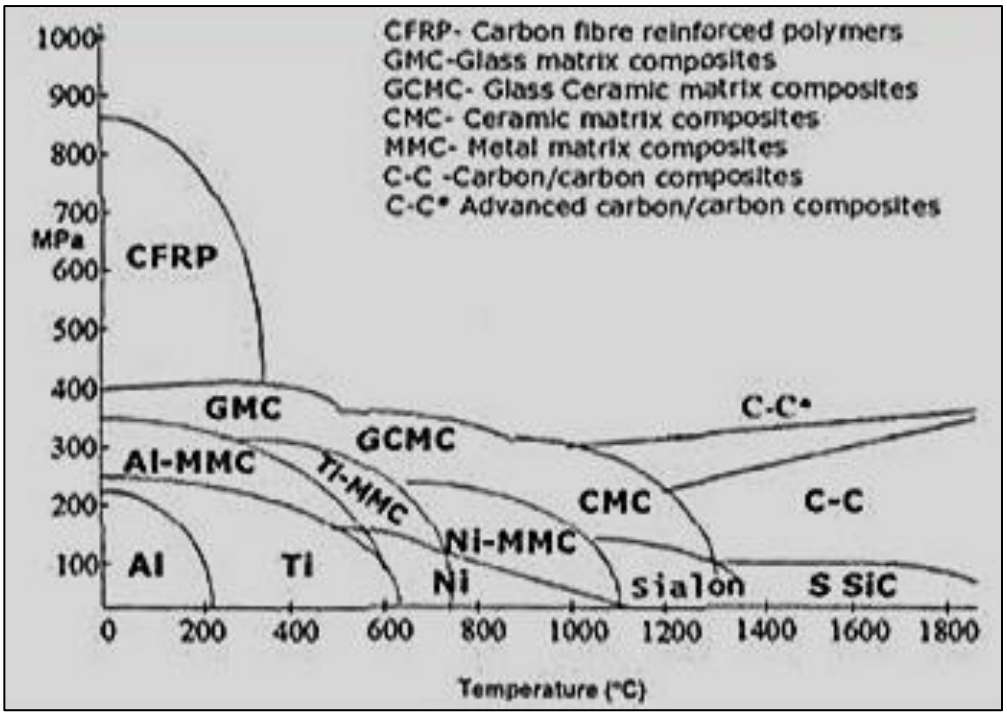

Figure 4: The specific strength vs temperature ranges of various materials (Manocha, 2003).

The precise properties of any C_f/C composite are determined by the specific processing route used, as discussed in Section 2.1.

2.3 PROCESSING ROUTES

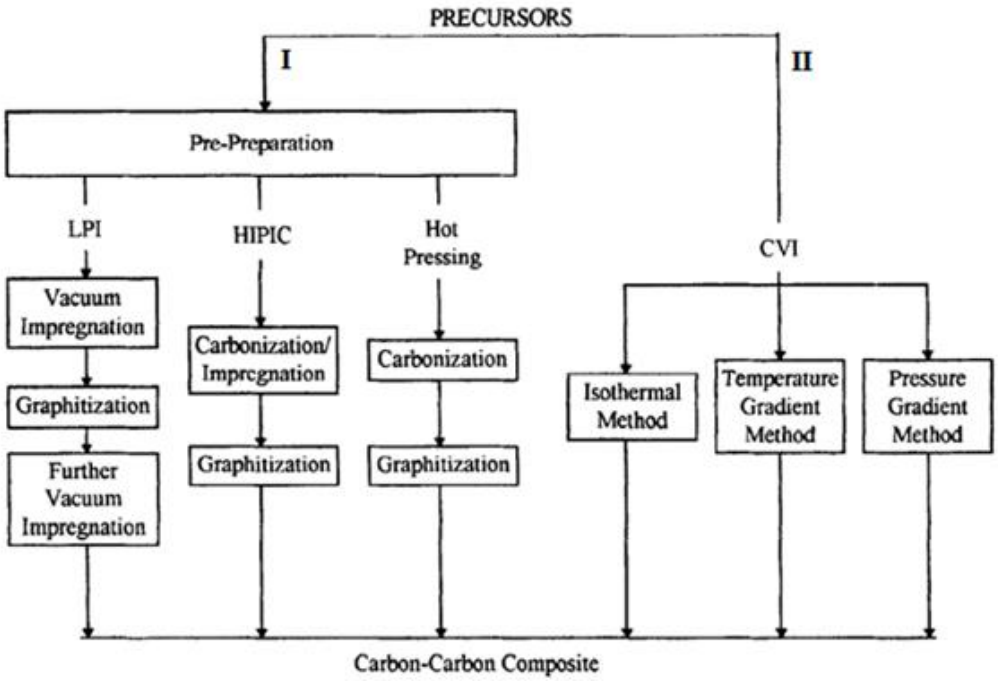

Figure 5: A summary of C_f/C composites processing routes (Windhorst & Blount, 1997)

The processing methods for C_f/C composites are determined by the composition and physical phase of the precursor used as shown in Figure 5.

2.3.1 Gaseous Precursors Route

Chemical Vapour Infiltration (CVI) is a very mature, yet time consuming technology which involves directing a volatile carbon precursor (usually a hydrocarbon) gas in a carrier gas onto a heated substrate at temperatures in the region of 800°C–1200°C. Figure 6 shows the elaborated process diagram for the CVI process. Thermal decomposition of the precursor occurs and carbon is deposited onto the surface as well as in the open pores. The pyrolytic carbon is deposited around fibres in a tiered and bundled manner (Figure 7) whose structure, order and distribution are determined by the processing conditions (Creighton & Ho, 2001). This layered structure parallel to

the fibre orientation gives a favourable interface for crack deflection (Manocha, 2003; Naslain, 2006).

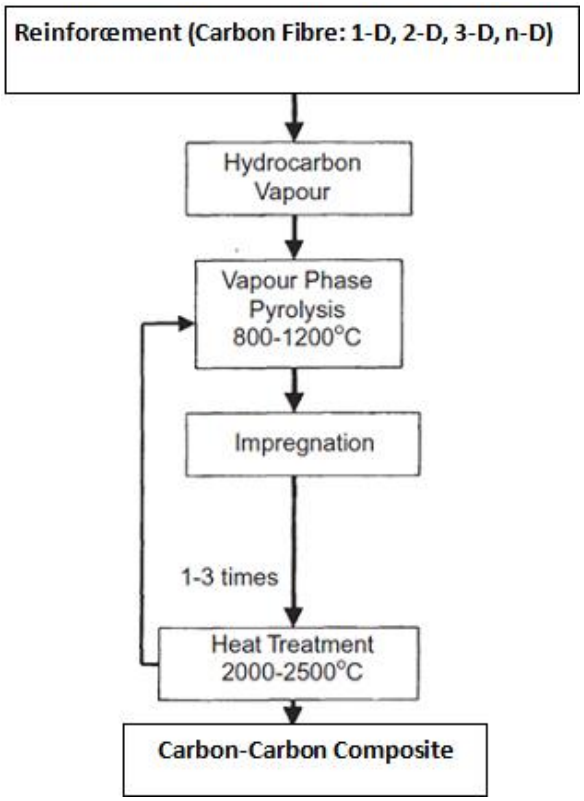

Figure 6: A generic process flow for CVI-based C_f/C composites processing routes (Manocha, 2003).

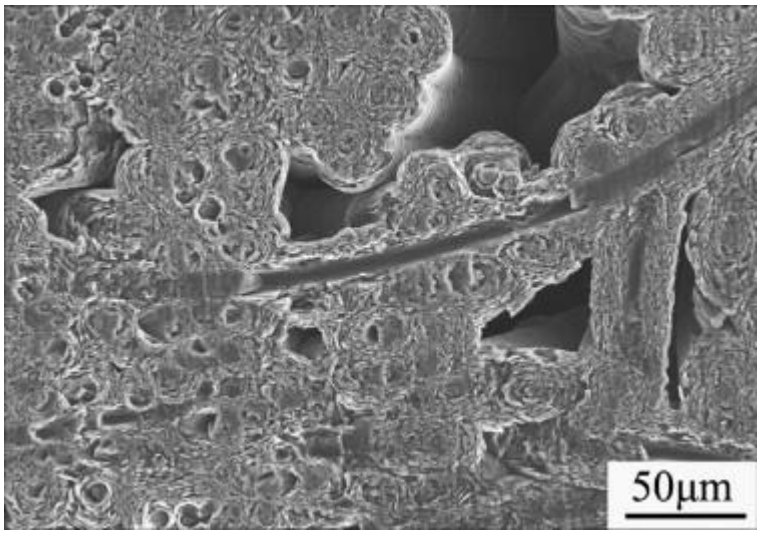

Figure 7: The resultant fibre-bundled laminar microstructure of a CVI processed C-matrix (Wang *et al.*, 2012).

Careful selection and optimisation of temperature, pressure, residence time and the carbon precursor are critical to obtaining the desired morphology (Griffiths & Nilson, 2000). The details of CVI processes, however, are not detailed in this literature review which focues on liquid infiltration processes.

2.3.2 Liquid Precursors Route

Liquid precursors are generally divided into the thermoplastic precursors which give 'soft' carbons, and the thermoset precursors which give 'hard' carbons (Zaldivar & Rellick, 1991). The application of these thermosets as matrices in carbon fibre reinforced composites is considered here.

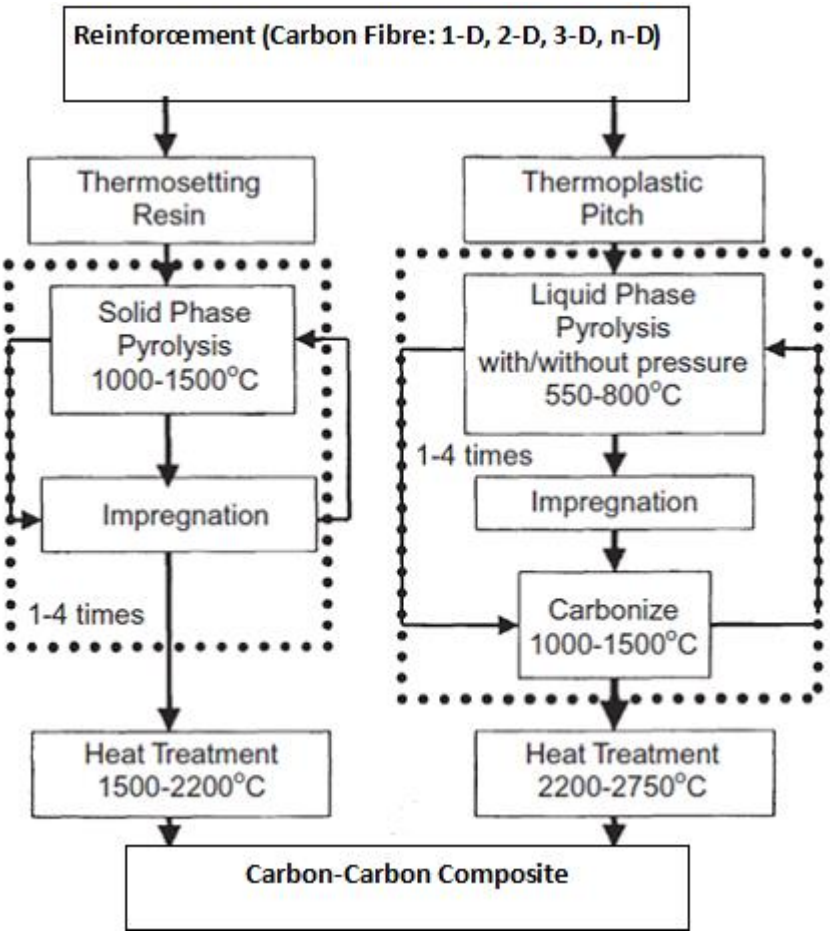

Figure 8: Generic process flow based on a thermoset precursor and a thermoplastic precursor for making a C_f/C composite (Manocha, 2003).

Figure 8 shows the two generic classes of liquid precursors (thermoset and thermoplastic). The diagram elaborates the general processes used in making a carbon-carbon composite depending on the precursor used (Manocha, 2003).

2.4 THERMOSET RESINS PROCESSING

Polymer infiltration and pyrolysis (PIP) technology dominates the wet impregnation methods used for C_f/C composites manufacture. For high temperature applications thermoset polymers are strongly recommended. A resin that is favourable is one that has a low viscosity and good fibre wetting properties; gives a high carbon yield and low shrinkage during heat treatment (Savage, 1993).

2.4.1 Thermoset Resins for High Temperature Applications

Epoxy resin: Epoxy is the most commonly used high performance resin for carbon reinforced polymer matrix composites (Strong, 2008). The most distinct property of epoxy is favourable curing behaviour - low curing temperatures; minimal volatiles; and low shrinkage. It is also easy to control the resultant mechanical properties of the matrix by manipulating the diverse precursors available for epoxy. Its mechanical performance, however, is limited in moist environments.

Polyarylacetylene (PAA) resin: The head application for the PAA resin in the 20th century was in nuclear radiation insulation (Katzman, 1990). The greatest advantage of PAA is in its very high carbon yield of 80% to 90% when pyrolysed owing to its very high degree of crosslinking. Katzman (1990) investigated the potential benefits of the PAA resin in space components and endorsed its suitability. Wang & Zhao (2007) obtained improved thermal and mechanical properties from PAA mixed with propargyl-novolac (PV) resin.

Polyimides: These are known to contain hazardous methylene dianiline (MDA) (Cornell, 2009) and are generally difficult to process. NASA has been conducting numerous researches on improving polyimides for spacecraft applications (Cornell,

2009) because they show favourable mechanical properties. Bismaleimides (BMIs), a class of polyimides, boast of higher thermo-oxidative stability than other resins (Strong, 2008). In addition, BMIs are easier to process although they demand post-curing in the process, unlike the other polyimides.

Phenolic resin: this has a very long history in the application of thermoset resins, and was the first commercial thermoset resin to be made in 1907. Phenolics have excellent thermal behaviour, notwithstanding their significant shrinkage during heat treatment. They are well known for their very low flammability and smoke generation, as well as high char strength (Atta-Obeng, 2011). Carbonised phenolic resins' low cost-to-performance characteristic makes them preferable in C_f/C composites for aerospace and aircraft applications.

The fabrication of C_f/C composites from phenolic resin is of particular interest in the present work. Generally, after impregnation with a phenolic resin, curing follows at temperatures that widely vary in literature, mostly depending on the manufacturer's specifications. The most common range is up to 100-180^{0}C. The curing process sets the phenolic resin and allows crosslinking to occur. Thereafter pyrolysis is performed. Pyrolysis or carbonisation takes place when thermal decomposition occurs in an inert atmosphere and a carbon is left on the preform as volatile material decomposes off. In order to achieve the intended density of a C_f/C composite repeated cycles of impregnation and pyrolysis have to be performed. In some cases the cycles will include graphitization. All these processes are discussed in the following subsections.

2.4.2 Curing Process

Autoclave curing has been a 'de facto' and mature approach for curing thermoset resin composites for many years. It has received extensive attention and shall not be discussed in detail herein. It is important, however, to point out the modern trends that are being developed to replace autoclave curing in the view of its shortcomings which are: the need for energy and capital intensive equipment, imposition of component size limitations and demand for long curing cycles which translate into low production rates.

Out-of-autoclave (OOA) curing technologies for aerospace composites seek to resolve the mentioned concerns of autoclave curing, subject to imparting the same, or better, performance properties. There are very limited academic publications on OOA processes, however. Most of the available information is from commercial manufacturers. The general consensus, nonetheless, is that OOA technology is a very promising approach for high performance composites.

Important to mention is the microwave curing technology. Microwave heating, unlike conventional heating, is achieved through electromagnetic waves. In 2011 Germany's Vötsch Industrietechnik developed the then largest industrial scale microwave oven for curing carbon fibre composites. Curing times were reduced by over 50% and energy consumption by at least 30% (Composites Technology, 2013b). GKN Aerospace of UK, however, recorded an energy consumption reduction of 90% (Composites Technology, 2013a).

Electron beam (EB) is another OOA technology for thermoset curing. Initial development of radiation curing of resins for high performance composites was done about thirty years ago by the Atomic Energy of Canada Limited (AECL) (Lopata *et al.*, 1999). The technology is not yet industrially applied though (Goodman & Palmese, 2002). EB makes use of electron accelerators to produce a high energy beam which is directed at a resin. The resultant mechanism involves the formation of ions and free-radicals, as polymerisation and crosslinking occurs (Singh *et al.* 1996). The process seems to be limited to certain resins which are often referred to as being EB-curable. These EB-curable resins have complications on handling; reaction specificity and compatibility with fibres (Lopata & Sidwell, 2003; Singh, 2001).

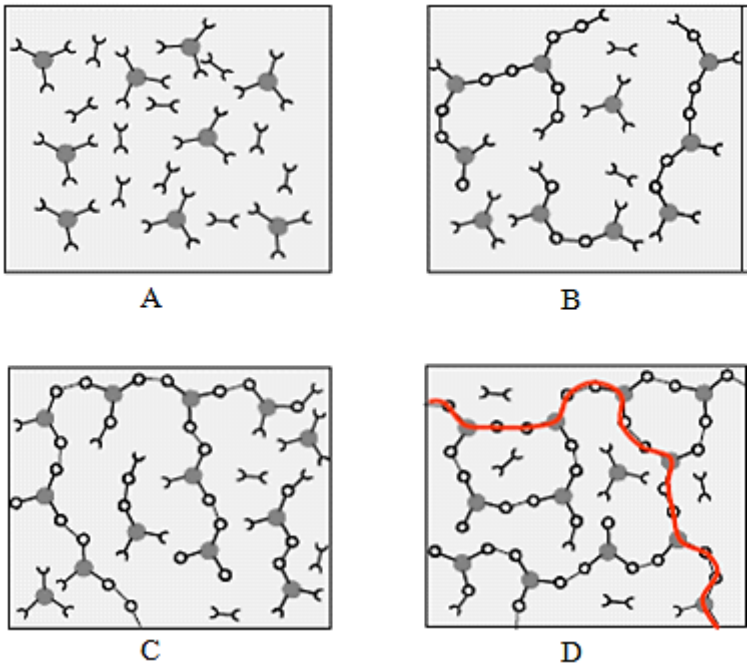

Figure 9: The microstructural changes during a thermoset cure: (A) Monomers before reaction (B) Small molecules develop with inter-branching (C) The gel point is reached (D) Fully cured polymer (Franck, 2004).

Curing is a process which involves polymerization reactions in which multifunctional groups in the reactants participate. Crosslinking occurs by the formation of chains, and this proceeds until a 3D network is formed as depicted in Figure 9. After curing the structure of the matrix consists of phenolic units with methylene based links (Trick & Saliba, 1995).

Thermoset structural development is accompanied by significant rheological changes: the resin changes from a low-melting thermoplastic solid to a low viscosity liquid, to a gel, and then to a stiff solid (Franck, 2004). The influence of the rheological properties of the phenolic resin on the characteristics of the resultant C_f/C composite were studied by Klučáková (2004) who confirmed the same.

Franck (2004) maintains that further heat treatment (post-curing) is required after curing so that first potential crosslinks and that a definitive level of stiffness in the matrix is accomplished. Ko *et al.* (2000) studied the microstructural changes in C_f/C

composites that occur during post cure between 160°C and 300°C for durations of 2h to 50h. They concluded that the post-cure step optimised the composite properties as follows: greater matrix density, limited shrinkage and enhanced cross-linking in the subsequent pyrolysis stage, and improved mechanical properties.

It should be noted how the curing reactions involved in the curing process have not been scrutinized as much in literature as the ones involved in the pyrolysis process.

2.4.3 Pyrolysis Process

The mechanisms of phenolic resin pyrolysis are diverse and still debatable among researchers. The generic agreement is that pyrolysis is a 3-step process. Contention, however, arises on the details of the reactions occurring at each stage. What is well known is that pyrolysis leads to resin matrix shrinkage and cracking, volatiles are released with consequential mass loss, as well as composite expansion. The effects of these changes on the microstructure of the composite were studied by Wang (1996). Wang *et al.* (2009) also showed that the release of volatiles (mainly phenol and methyl derivatives) accounted for over 35% of mass loss and led to degradation of and defects in the matrix. Tzeng and Chr (2002) established 600°C as the transition temperature for the formation of glassy carbon from phenolic resin – formation of voids occurred under 600°C while formation of cracks occurred above 600°C.

Some of the early researchers who proposed mechanisms of phenolic resin pyrolysis were Ouchi and Honda (1959), Conley & Bieron (1963a, 1963b); Jackson & Conley (1964), Ouchi (1966), and Parker (1967).

Research is still on-going on establishing with certainty the mechanisms involved in phenolic resin pyrolysis. Modern researchers include Trick & Saliba (1995, 1997); Ko *et al.* (2000, 2001); Chen *et al.* (2008); Ma *et al.* (2008); Wang *et al.* (2009); Jiang *et al*. (2010, 2012); and Chen *et al.* (2013).

Trick and Saliba (1995)'s work seems to be in alignment with the initial proposals of Ouchi (1966). There is agreement that pyrolysis occurs firstly by further crosslinking from curing, secondly by the decomposition of the crosslinks and lastly by cyclodehydration. Ko *et al.* (2000) observed that 90% of the gases evolved between

400°C and 700°C which they attributed to the occurrence of condensation and crosslinking in the formation of glassy carbon. They also noted that the crystal sizes of the units in the microstructure decreased with increasing temperature. The work of Ma *et al.* (2008) and Jiang *et al*. (2010) was focused on modelling and simulating the pyrolysis process of phenolic resin from experimental results.

Jiang *et al.* (2012) challenged the notion of degradation occurring principally by oxidation reactions which is known to have been initially proposed by Jackson and Conley (1964). These authors proposed that methylene scission was responsible for the degradation of the phenolic resin structure, although the oxidation of methylene still occurs. Jackson and Conley (1964) had attributed degradation to oxidative reactions producing carbon monoxide and dioxide as the major products, and water, paraformaldehyde, methane etc. as minor products. Jiang *et al.* (2012) added that amorphous carbon is formed from both pyrolysis and polycyclic reactions.

Chen *et al.* (2013) on the other hand observed that decomposition (of ether bonds and hydroxymethyl groups) occurs from the initial onset of pyrolysis reactions. Thereafter methylene crosslinks break and finally hydrogen is released from aromatic units.

An even more interesting study on the various microstructures that form at different locations in the carbon-carbon composite after pyrolysis was conducted by Weisshaus (1990). At the bundles they obtained glass-like droplets; on the bulk matrix they observed a glass-like microstructure; inside the pockets formed from the folding nature of the matrix they detected a spherular mesophase microstructure; and close to the fibre bundles they observed grain-like particles.

2.4.4 Graphitizing Process

Graphitization of the carbonised thermoset resin matrix in C_f/C composites is very difficult to achieve. The matrix remains predominantly glassy although graphitic ordered phases restricted to the vicinity of the fibres have been widely reported at temperatures around 2400°C.

Thermoplastic carbon precursors are generally pitch-based. The ‘soft’ carbons that these thermoplastic precursors give are also referred to as ‘microporous’ carbons

(Harris, 2005). ‘Amorphous carbon’ and ‘glassy carbon’ are the two most common microporous carbons discussed in literature. There is sometimes a mix-up on the terminology surrounding these two non-graphitizing carbons, though. Some researchers like Harris (2005) and Inagaki & Kang (2006, 2014) have deliberated on the structures of these two carbons separately, although the distinction on how each is obtained is not very clear. “Glassy” is a term which addresses the carbon’s physical pseudo-glassy appearance and the mechanical property of undergoing conchoidal fracture, more than it reflects its crystallographic structure. In this work, however, amorphous carbon from phenolic resin is dealt with.

The main discrepancies that still need to be resolved are centred on the actual structure of ‘hard’ carbons and explaining the reason for non-graphitizability. The models given by Kumar *et al.* (2005), shown in Figure 10, of the structure of amorphous carbon structure with heat treatment is of interest. Ideas around the structure have evolved from the crystallite-based pioneering work of Franklin (1951) to the ideas of curving sheets by the likes of Ban *et al.* (1975), and now to the modern fullerene-based postulations of Harris & Tsang (1997). Table 1 summarises these postulations from classic to recent.

Kobayashi & Zaldivar (1994) pointed out the advantages of a graphitic matrix over an amorphous matrix in C_f/C composites: a higher strain-to-failure ratio; greater ablation resistance; greater thermal conductivity hence less thermal-mechanical stresses. Amorphous carbon on the other hand, has the advantage of lower processing temperatures and a structure which ensures that cracks are impeded from spreading in the matrix.

Harris & Tsang (1997) suggested that non-graphitizability could emanate from the physical nature rather than the chemical nature of the precursors. They also postulated that the pyrolysis parameters are critical to graphitizing hard carbons. Conversely, they did not precisely qualify the parameters that would be conducive for graphitization.

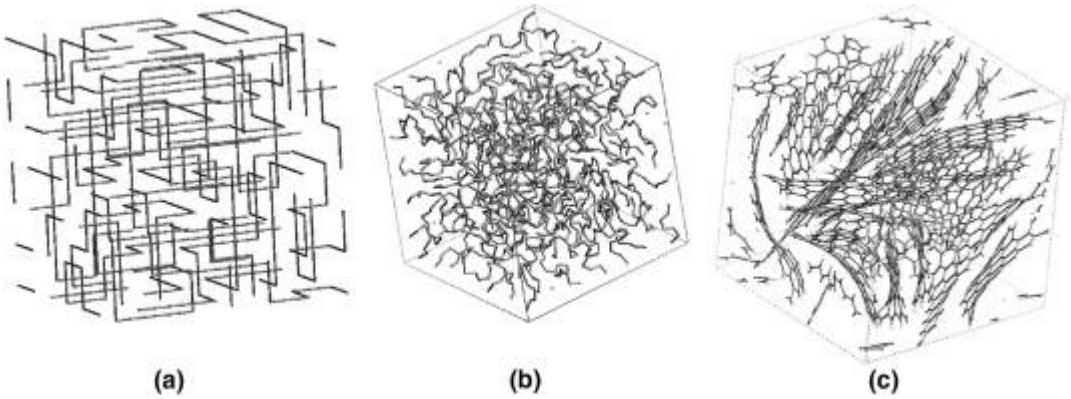

Figure 10: Structural models for amorphous carbons created by an NVT Monte Carlo (MC) simulation (a) skeletal lattice of a linear carbon polymer (b) tangled sp^2-coordinated carbon structure (c) final carbon structure (Kumar *et al.*, 2005)

Table 1: A summary of the evolution of postulations on the microstructure of amorphous carbon.

Contributors	Explanation
Franklin (1951) 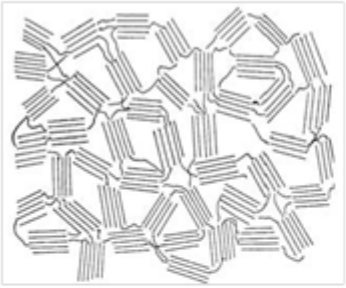	Attributed non-graphitizability to the extremely high activation energy (which is not reached even at temperatures of upto 3000°C) required to orderly realign the crystallites. The model is criticised for showing inadequate information by its 2D nature.
Ban et al. (1975) 	Presented the structure as composed of loosely curled strips or 'ribbons'. Voids are randomly wrapped up in the folds, explaining the high porosity attribute of non-graphitizing carbons.
Harris & Tsang (1997) 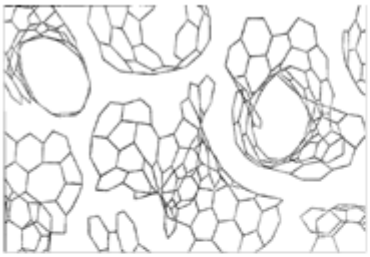	They proposed a model consisting of 'discrete fragments' of hollow 'fullerene-like nano particles'. From HREM, they concluded that the existence of non-haxegonal (pentagon and heptagon) rings in the structure explains the non-graphitizability.
Inagaki (2013) 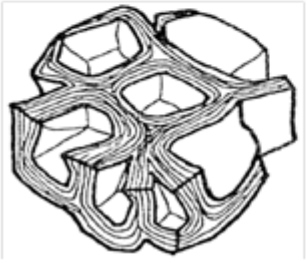	Postulated the model shown revealing a closed pore structure and an irregular honeycomb-like structure of folding pockets.

2.5 ABLATION OF C_f/C COMPOSITES IN HOSTILE ENVIRONMENTS

The high temperature applications that need C_f/C composites most are predominantly ablative. Ablation is a process by which thermochemical and thermomechanical degradation (Zaman, 2012) of a material occurs. C_f/C composites thus maintain the aforementioned mechanical properties provided the environment is not oxidative. C_f/C composites are known to succumb to oxidation at temperatures as low as 500°C in an ablative environment, yet can perform excellently at temperatures as high as 3000°C in an inert environment (Mckee, 1986).

Han (1994) showed how at low temperatures oxidation of C_f/C composites is reaction kinetics dictated and how at ultra-high temperatures oxidation is oxygen-diffusion dictated. This was confirmed by Jacobson (2006) and Guo (2006) who established 800°C and 900°C respectively as the point of transition from reaction-rates to diffusion-rates control.

The mechanism of oxidation is said to be determined by the type of carbon in the C_f/C composite. During the reaction controlled phase of oxidation, deep ablation into the matrix occurs while in the diffusion controlled phase ablation occurs at the edges of the article (Halbig and Cawley, 2004).

A number of researchers (Guo, 2006; Labruquere, 2001) have confirmed that oxidation in C_f/C composites starts at the fibre-matrix interface. Thus the fibre-matrix interface is the weakest link in the C_f/C composite. Thereafter, oxidation occurs in the matrix, and finally in the fibres. The matrix disintegrates at a greater rate than the fibres. Guo (2006) showed that oxidation in the fibres progresses from the sheath, through the layers right to the ultimate core. At this stage the composite would have collapsed completely.

It is therefore necessary to protect the carbon fibres in C_f/C composites. Anti-oxidation protection has been applied at two different levels: externally and internally (Devi & Rao, 2013). External protection systems include oxygen- diffusion-inhibiting coatings and glass-forming sealants Smeacetto *et al.* (2002). External protection systems include oxidation deterrents and matrix substituting ceramics which form oxides with

high melting points (Devi & Rao, 2013). The latter systems are known to provide long term protection at high temperatures.

2.6 CERAMIC MATRIX COMPOSITES - ULTRA HIGH TEMPERATURE CERAMICS (UHTCs)

Group IV and V transition elements form borides, nitrides and carbides which serve as UHTCs owing to their high melting points in excess of 3000°C. Opeka *et al.* (2004) emphasize that it is actually the ability of these materials to form oxides with high melting points during service which qualifies them as UHTCs.

There has been a significant evolution in the ceramic matrices used for high temperature applications. Zr and Hf borides were the first UHTCs to be produced around the mid-20th century for nuclear reactor applications (Wuchina *et al*., 2007; Johnson, 2011). Initial investigations on ZrC and HfC matrices were conducted in the 1960s and their susceptibility to oxidation was deemed unacceptable (Opeka *et al.* 2004) compared to their boride counterparts. The work of Clougherty *et al.* (1968) was one of the early attempts to make a hybrid (multiphase) carbide and boride ceramic matrix. They combined HfB_2, ZrB_2 and SiC. The purpose of the SiC was to refine the grain sizes of the borides formed in order to improve the strength of the matrix. Later on, research on the unaided use of SiC as a ceramic matrix became prominent in the 1970s (Johnson, 2011). Since then, SiC has been considered a 'de facto' component of UHTCs. The 1980s and 1990s saw the dormancy of interest in UHTCs research but this only lasted up to the beginning of the 21st century. Renewed interest in the Zr and Hf carbides has since been revived. The most current trend shows a preference for hybrid ceramics in a given composite. This serves the purpose of complementing the pros and cons of the various ceramics used.

This work is focused on carbide ceramic composites. It is therefore befitting to review the properties of the commonly applied ceramics known to have melting points above 3000°C (ZrC, HfC, TiC and TaC), as well as SiC and B_4C. A summary of the properties of these carbides is presented in Table 2.

Table 2: Properties of the carbide ceramics used to make ultra-high temperature composites (Ultramet, 2013).

Property	C	HfC	TaC	NbC	ZrC	SiC	B_4C	TiC
Melting point, °C	3827*	3890	3880	3500	3540	2987*	2347	3065
Molecular weight, g/mol	12.01	190.54	192.96	104.92	103.23	40.10	55.26	59.89
Density, g/cm^3	2.25	12.70	14.50	7.79	6.59	3.21	2.52	4.94
Thermal expansion, ppm/°C	1.0	6.8	6.6	6.9	7.3	5.3	5.6	7.9
Thermal conductivity, W/m · K	150	22	22	30	20	120	30	50
Specific heat, J/g · K	0.84	0.20	0.19	0.35	0.37	0.67	0.96	0.56
Enthalpy, kJ/g	8.58	1.11	1.11	1.86	1.79	4.1	5.94	2.8
Hardness, kg/mm^2	20	2300	2500	2400	2700	2600	2900	2900
Crystal structure	HEX	FCC	FCC	FCC	FCC	FCC	RDL	FCC
Electrical resistivity, μΩ · cm	—	37–45	25	35	45–55	500×10^6	1×10^6	105
Transverse rupture strength, MPa	—	—	350–400	300–400	—	—	—	—
Young's modulus, GPa	—	350–510	285–560	338–580	350–440	440	460	450
Poisson's ratio	—	0.18	0.24	0.21	0.191	0.21	0.17	0.19
Use temperature in air, °C	500	500	800	800	800	1650	1100	400

* Sublimes.

A summary of the processing routes for ceramic matrix composites is shown in Table 3. The main wet infiltration methods are: slurry infiltration, sol-gel processing and melt infiltration. CVI is the single most applied gaseous route, and hot pressing the most common solid powder technique. A combination or hybrid of these processes, however, is the current focus of ultra-high temperature ceramics techniques. Figure 11 summarises application of processing routes to specific ceramics by chemical composition as presented by Rosso (2006).

Table 3: A summary of the main processing routes for ceramic matrix composites by chemical composition (Rosso, 2006).

Processing route	Matrices
Chemical vapour infiltration	Carbides, nitride carbon, oxides, borides
Viscous phase hot pressing (2D performs)	Glasses, ceramic-glasses
Sol–gel route (2D, 3D performs)	Oxides
Polymer precursor route (3D performs)	SiC, Si_xN_y, $Si_xC_yN_z$
Liquid metal infiltration	Si → SiC
Gas–metal reaction	Oxide (Al, nitrides [Al, Zn, Ti])
Solid-state hot pressing	SiC, Si_3N_4
Prepreg curing and pyrolysis	SiC, Si_3N_4
Hot pressing (2D preforms)	Oxides

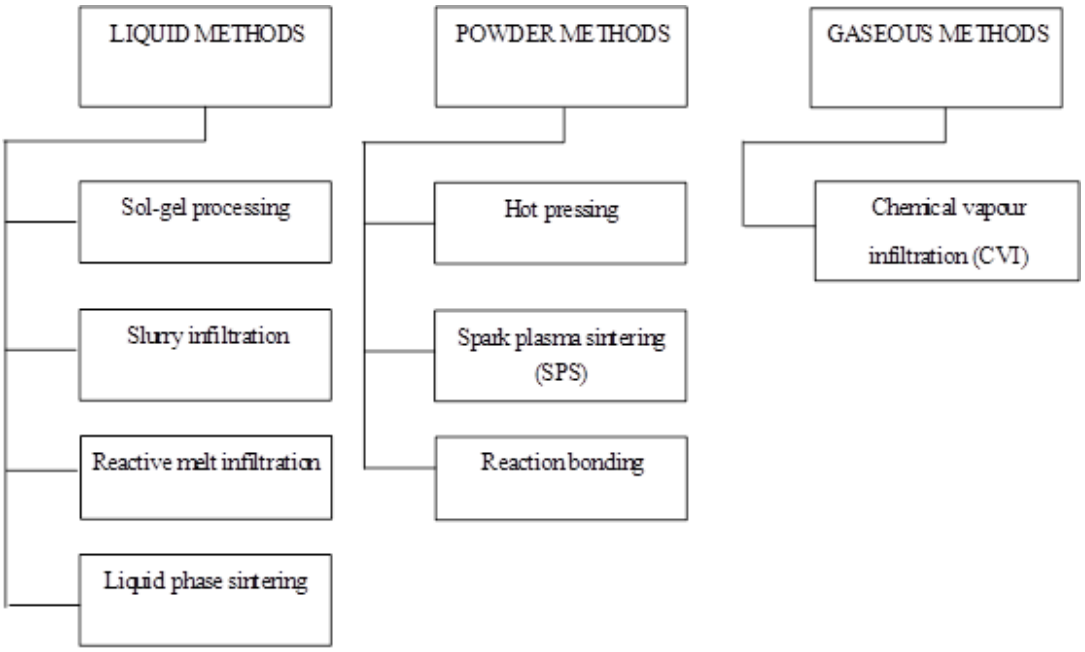

Figure 11: A summary of the main processing routes for ceramic matrix composites.

2.6.1 Silicon Carbide (SiC)

The purpose of SiC in hybrid ceramic composites is to refine the grain sizes of the carbides and borides formed in order to improve the strength of the matrix. It is well known that high temperature processing introduces a coarse grained microstructure

and undesirable porosity. The influence of the grain size on the strength of matrix is related by the archetypal Hall-Petch relation, given in Equation 1:

$$\sigma_y = \sigma_0 + K_y d^{-1/2} \quad (1)$$

Where K_y is the Hall-Petch slope and d is the mean grain size.

SiC in its own right serves as a barrier for C_f/C composites oxidation. In an oxidative environment SiC forms glassy SiO_2 (Equations 2 and 3) which protects the C_f/C composite up to 2000°C (Wuchina *et al*., 2007). On the other hand, a C_f/SiC composite would protect up to 1650°C only (Ultramet, 2013).

$$SiC_{(s)} + 2O_{2(g)} \rightarrow SiO_{2(s)} + CO_{2(g)} \quad (2)$$

$$SiC_{(s)} + 3/2O_{2(g)} \rightarrow SiO_{2(s,l)} + CO_{(g)} \quad (3)$$

Chemical vapour infiltration (CVI), liquid polymer infiltration (LPI), or liquid silicon infiltration (LSI) can be used to introduce SiC into C_f/C composites. The properties of the resultant composites have been compared in Table 4. From the table, CVI produced C_f/SiC composites show preferable mechanical properties; although LSI produced C_f/SiC composites indicate a matrix of minimum porosity and good resistance to thermal expansion.

Much experimental and modelling work has been done on the LSI process. Modelling on the infiltration phenomena involved in LSI (a form of RMI) is discussed in detail in Section 3.2. Figure 12 shows a typical 3-dimensional distribution of the SiC (bright phase) in a carbon reinforced composite.

Table 4: Properties of C_f/SiC Composites with 2D reinforcement. (Krenkel & Hausherr, 2011).

	Gas-phase infiltration	Liquid-phase infiltration	
Property	CVI (C/SiC)	LPI (C/SiC)	LSI (C/C-SiC)
Tensile strength, MPa	350	250	80-100
Strain to failure, %	0.9	0.5	0.15-0.35
Young's modulus, GPa	90-100	65	50-70
Compression strength, MPa	580-700	590	210-320
Flexural strength, MPa	500-700	500	160-300
Porosity, %	10	10	2-5
Fibre content, %	45	46	55-65
Density, gcm^3	2.1	1.8	1.9-2.0
Coefficient of thermal expansion, $10^{-6}\,K^{-1}$	5	4.06	2-7
Specific heat, J/kgK^{-1}	620-1400	900-1600	690-1550



Figure 12: The typical microstructure of a C_f/SiC composites (Jiang *et al*., 2008).

2.6.2 Boron Carbide (B_4C)

Borides, when oxidised, form molten B_2O_3 (Equations 4 and 5) whose protection usefulness is limited to about 1200°C (Wuchina *et al*., 2007) due to the subsequent

volatization (Fahrenholtz *et al*., 2007) of the same. A combination of borides and SiC leads to the formation of borosilicate glass at temperatures exceeding 1300°C (Opeka *et al.*, 2004). Parthasarathy *et al*. (2007a; 2007b; 2009) have done extensive work on the oxidation kinetics of materials composed of borides and SiC.

$$B_4C_{(s)} + 4O_{2(g)} \rightarrow 2B_2O_{3(s,l)} + CO_{2(g)} \quad (4)$$

$$B_4C_{(s)} + 7/2O_{2(g)} \rightarrow 2B_2O_{3(s,l)} + CO_{(g)} \quad (5)$$

Boride UHTCs have been fabricated predominantly by powder methods. Bellosi *et al.* (2006) compared the microstructure of HfB_2–SiC, ZrB_2–$MoSi_2$, and ZrB_2–ZrC–SiC composites processed by SPS and by hot pressing. They found preferred and well densified microstructures in the SPS processed composites over the hot pressed ones.

Most of these borides (MB_2, where M=transition metal) have a C32-type hexagonal structure. The crystallographic properties and the physical properties of transition metals borides has been presented by Castaing and Costa (1977) who have drawn their discussion from traditional researchers. A modern review by Fahrenholtz *et al*. (2007) on the borides of Zr and Hf is very insightful and comprehensive.

Recent work involving the combination of borides and carbides includes the work of Monteverde *et al.* (2008) on ZrB_2–SiC composites; these authors reported satisfactory fine-grained microstructures; Carney *et al.* (2011) investigated the effect of adding tungsten to make HfB_2–SiC, HfB_2–SiC–WC, and HfB_2–SiC–WB composites by field-assisted sintering and showed how it improved both the liquid phase sintering involved and oxidation protection of the final composites; Li *et al.* (2011) prepared a C_f/SiC–ZrB_2–TaC from the slurry (derived from TaC and ZrB_2 powders and liquid polycarbosilane) infiltration and obtained acceptable mechanical properties for aerospace applications, although the distribution and adhesion of slurry derived particles to the initial pyrolytic carbon matrix did not match higher temperature derived microstructures; Hu *et al.* (2010) fabricated C_f/SiC–ZrB_2 prepared by combined slurry and precursor infiltration, followed by pyrolysis cycles and commended the method for producing complex articles with pronounced thicknesses; Levine *et al*. (2002) combined the slurry infiltration approach and hot-pressing to produce SiC–ZrB_2 UHTC matrices which they insightfully tested for oxidation resistance.

2.6.3 Zirconium Carbide (ZrC)

C_f/C composites with SiC and/or ZrC matrices have been the most researched hybrid composites UHTCs. The prominence of ZrC as a component of multi-graded composites is derived from the impressive 2700°C melting point of its oxide (Zhao, 2011) formed according to Reaction 6. It also has a lower density than some of its refractory carbide competitors like HfC and TaC. In addition, the proven superiority of the boride version of Zr in UHT applications might have encouraged a general inclination to Zr compounds for the same applications.

$$ZrC\,(s) + (3/2)\,O_2\,(g) \rightarrow ZrO_2\,(s) + CO\,(g) \qquad (6)$$

A C_f/ZrC composite would withstand oxidation up to 1940°C; while a C_f/SiC-ZrC composite would go up to 2200°C (Ultramet, 2013). When the temperature exceeds 2000°C the oxides (ZrO and SiO_2) are said to bond and seal up cracks in the matrix (Li *et al.*, 2012).

Zou *et al.* (2011) were among the first researchers to report the fabrication of C_f/ZrC composites by reactive melt infiltration (RMI). Since then there has been an extensive proliferation of variations of C_f/C-SiC-ZrC composites from Chinese researchers wherein the carbides were formed by RMI. RMI has shown that it produces heterogeneous microstructures (Zou *et al.*, 2011) in the matrix, thus the term "functionally-graded UHTCs" to its products. RMI is a relatively low cost process (by virtue of short processing times) which produces near finished-shape articles. Its major drawback, however, is the requirement for high temperatures to melt the infiltrant before infusing it into the preform and this often leads to damaged fibres and difficult-to-control reaction dynamics (Rosso, 2006).

The distribution of the constituent ceramics in these composites, however, seems varied. For example, from the work of Qian *et al.* (2013) wherein they fabricated a C_f/C-ZrB_2-ZrC-SiC composite for braking applications, they obtained a homogeneous distribution of the ZrB_2, ZrC, and SiC ceramics in the matrix (Figure 13). They attributed this finding to the simultaneous dissolution of the three ceramic precursor solutions used in preparing the composite at the molecular scale.

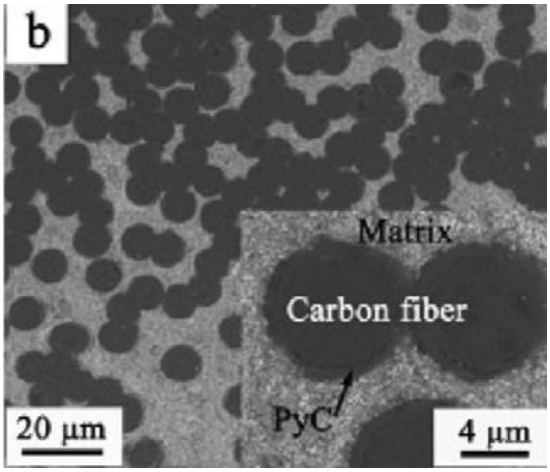

Figure 13: The microstructure showing a homogeneous dispersion of the ZrB2–ZrC–SiC ceramic phases in the matrix (Qian *et al.*, 2013).

Conversely, the matrix in the C_f/C-SiC-ZrC composite (Figure 14(a)) fabricated by Wang *et al*. (2012) showed a graded profile of ceramics – SiC, differential SiC and ZrC, and the residual silicide – respectively from the fibres. Wang *et al*. (2012) attributed this graded microstructure to the reaction kinetics based on the phase diagram of the quaternary system. The diffusion of the pyrolytic carbon through the successive layers of ceramics formed around fibres allowed subsequent reactions to progress accordingly. The products of these reactions similarly formed the subsequent layers. On the other hand, Qian *et al*. (2013) attributed the homogeneity to the process of simultaneously dissolving the ceramic precursors into the C_f/C composites. This explanation, however, seems too simplistic considering the differing kinetics of mass transfer and crystallisation of the constituent ceramics.

Wang *et al.* (2011) derived a model to show the maximum height achieved when ZrC is infiltrated into a carbon preform. Their paper is peculiar as it is one of the few works available on modelling the reactive melt infiltration process outside the SiC system. Furthermore, their model is based on experimental results. They were persuaded that the diffusion of carbon dictated the thickness of the ZrC formed. The explanation is: when a ZrC layer is formed, the unreacted carbon diffuses through this layer and reacts further with incoming Zr melt, thus growing the ZrC layer. The C diffusion was said to increase exponentially with an increase in processing temperature.

$$h_{max} = K\sqrt{\frac{r_0^3}{\eta D_C}} \quad \text{where } K = \sqrt{\frac{c\sigma\ cos\theta}{12B}}\ and\ B = \frac{M_C\rho_{Zr}}{M_{Zr}\rho_C} \tag{7}$$

$h_{max} =$ maximum infiltration height

$M_i =$ mole weight of species i

$\rho_i =$ density of species i

$D_C =$ diffusivity of carbon

$\eta =$ viscosity of the Zr melt

$\sigma =$ the surface tension of the Zr melt

$r_0 =$ the initial radius of the pores

This model could possibly be applied to predict the depth of each layer in a graded hybrid ceramic matrix like shown in Figure 14(b). The multi layers promote deviations and deflection in the crack paths. When oxygen ingresses such a composite, it will experience a tortuous path and this retards the rate of oxidative degradation in the composite.

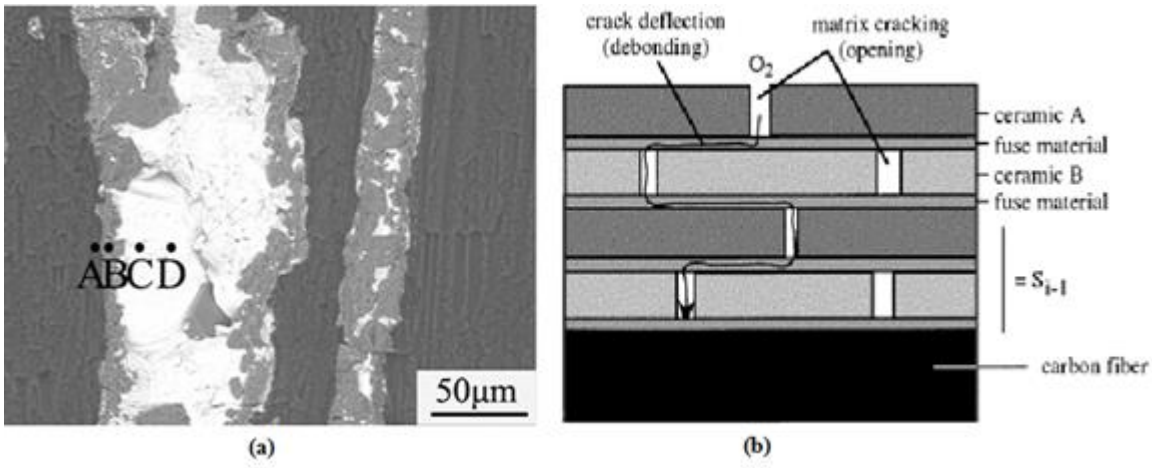

Figure 14: A graded matrix obtained in fabricating a C_f/C-SiC-ZrC matrix (Wang *et al.*, 2012); (b) How crack-deflection in a multi-graded ceramic matrix reduces oxygen diffusion (Lamouroux *et al.*, 1999).

2.6.4 Tantalum Carbide (TaC)

TaC has a density (14.50g/cm^3) which is more than double that of ZrC (7.89 g/cm^3) and more than four times that of SiC (3.21 g/cm^3) as shown in Table 2.

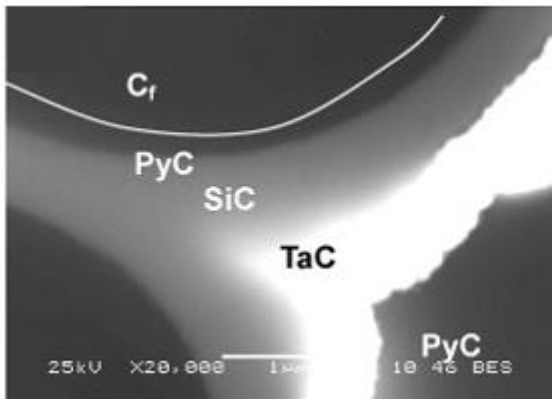

Figure 15: Ceramic graded-interface obtained by Chen *et al.* (2009).

Chen *et al.* (2009) performed CVI using Ar-H_2-CH_3SiCl_3 and Ar-C_3H_6-$TaCl_5$ precursors to deposit SiC and TaC strata around carbon fibres pre-coated with pyrolytic carbon. They successfully obtained the graded interphase as shown in Figure 15. However, they did not necessarily recommend the suitability of TaC for competitive oxidation protection. In the ablation studies they conducted they suggested the formation of $Ta_2O_5 \cdot SiO_2$ system (eutectic temperature of 1556°C) and minute portions of 10CaO $Ta_2O_5 \cdot 6SiO_2$ (melting temperature of 1478°C) when the composite is exposed to an oxyacetylene flame.

$$4TaC\ (s) + 7O_2\ (g) \rightarrow 2Ta_2O_5\ (l) + 4CO\ (g) \qquad (8)$$

The results obtained by Yi *et al*. (2010), which were in agreement with the results of Li (2011), showed improved ablation resistance by adding a TaC coating to a C_f/C-SiC composite as shown in Table 5 . Li (2011) recommended the use of combined ceramics to C_f/C composites in order to obtain gradients of oxidation protection.

Table 5: Effects of adding TaC to a C_f/SiC composite for oxidation protection (Yi *et al.*, 2010).

Sample	Rate of linear ablation (mm/s)	Density (g/cm^3)	Open porosity (%)
C_f/SiC	0.083	2.37	10
C_f/SiC-TaC	0.038	3.03	13

The ablation rate results in Table 5 are in contradiction with the results obtained by Tang *et al.* (2007) shown in Figure 16. Tang *et al.* (2007) attributed the poor ablation resistance of TaC containing composites to the liquid Ta_2O_5 formed during oxidation. Although the composite also contained ZrB2, they did not adequately explain the inadequacy of the liquid Ta_2O_5 in protecting the composite from ablation.

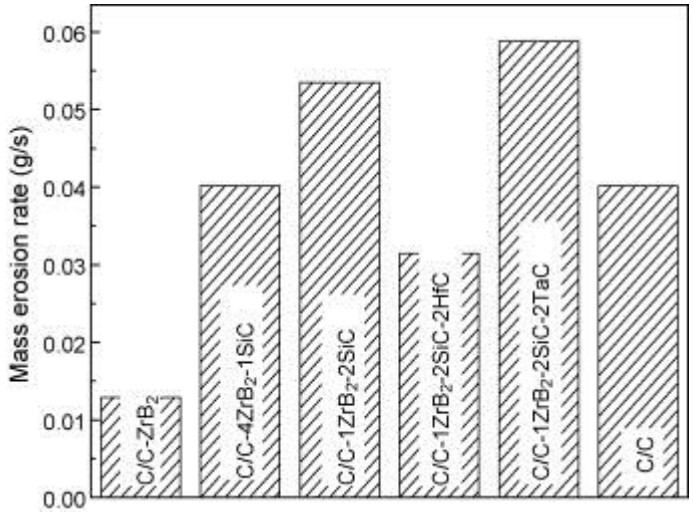

Figure 16: Comparison of mass erosion rates for C_f/C-ZrB2; C_f/C-4ZrB2-1SiC; C_f/C-1ZrB2-2SiC; C_f/C-2SiC-1ZrB2-2HfC; C_f/C-2SiC-1ZrB2-2TaC; and C_f/C (Tang *et al.*, 2007).

There is very limited literature on the synthesis of TaC in C_f/C composites, more so by RMI. Chen *et al.* (2011) infiltrated TaC slurry into a C preform before performing CVI using natural gas which was followed by RMI of Si to react with the C. Their work focused on investigating the thermal diffusivities of the resultant C_f/SiC-TaC composite. The microstructures they presented did not show a necessarily satisfactory

bond between the fibre and the SiC formed. The TaC phase did not show a deliberately function-focused microstructure in the composite also.

The use of refractory silicides in performing RMI in a carbon preform was put forward by Palmisiano *et al.* (2004) through a patent. They asserted the advantage of using refractory silicides for RMI and capitalising on the eutectic point infiltration at much lower temperatures than would be required when using pure metals.

2.6.5 Titanium Carbide (TiC)

Titanium is an early transition metal. The application of TiC in C_f/C composites for oxidation protection is not reported in literature. The use of Ti in high temperature environments has been through MAX phases composites and titanium matrix composites (mainly in intermetallic form)

Titanium Matrix Composites (TMC) development started in the 1980s as materials especially targeted for hypersonic technology. Titanium is well known for its outstanding corrosion resistance and long fatigue life. Its limitations, however, lie in its high reactivity and deterioration of strength in increasing temperature environments, over and above its steep cost. The reactivity of titanium is a concern especially with reinforcement. For example, in SiC_f/Ti composites precipitation reactions occur at the interface (Peters *et al.* 2003).

Fan *et al.* (2012) found out that a MAX-phase containing C_f/C-SiC composite had a better ablation resistance than the C_f/C-SiC composite as shown in Table 6. The lower porosity of C_f/C-Si-Ti_3SiC_2 than the C_f/C-SiC composite also helped in inhibiting oxygen diffusion into the material.

Table 6: Comparison of the mass and linear ablation of C_f/C-SiC composite and C_f/C-Si-Ti3SiC2 composite (Fan *et al.*, 2012).

Materials	Density (g/cm^3)	Open porosity (vol.%)	Mass ablation rate ($mg\ s^{-1}$)	Linear ablation rate ($mm\ s^{-1}$)
C/SiC	2.00	12	10.3 ± 0.8	0.042 ± 0.004
C/SiC–Ti_3SiC_2	2.42	8	6.3 ± 0.3	0.024 ± 0.002

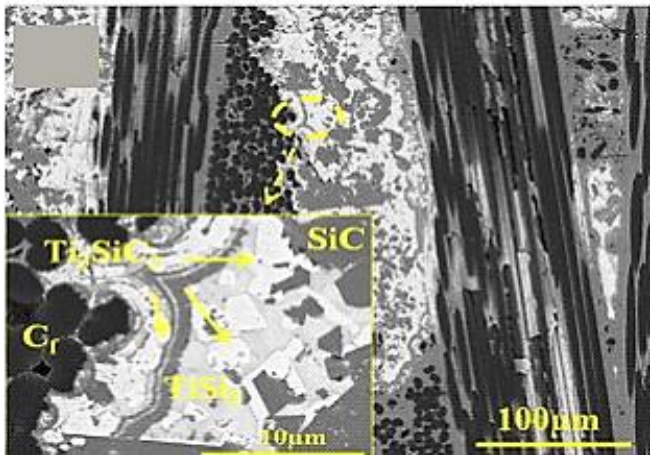

Figure 17: The microstructure and phases in the C_f/C-Si-Ti3SiC2 composite Fan *et al*. (2013).

The initial C_f/Si was slurry infiltrated with TiC–C before performing liquid silicon infiltration. The resultant microstructure and EDS results are shown in Figure 17.

Ablation was said (Fan *et al*., 2012) to proceed by the following reactions:

$$Ti_3SiC_2\,(s) + 5O_2\,(g) \rightarrow 3TiO_2\,(l) + SiO_2\,(l) + 2CO\,(g) \quad (9)$$

$$TiSi_2\,(l) + 3O_2\,(g) \rightarrow TiO_2\,(l) + 2SiO_2\,(l) \quad (10)$$

$$TiC(s) + 3/2O_2\,(g) \rightarrow TiO_2\,(l) + CO\,(g) \quad (11)$$

$$Ti_3SiC_2\,(s) \rightarrow 3TiC_x\,(s) + Si\,(l) \quad (12)$$

The decomposition of the Ti_3SiC_2 led to the formation of TiC_x which proceeded to TiC with the carbon from the oxyacetylene flame. The oxide layers formed by Equations 9-12 were found to be consisting of 32.5 mol% TiO_2 and 67.5 mol% SiO_2. Opeka *et al.*

(2004) commented that the useful oxidation protection of Ti_3SiC_2 is limited to 1000°C. Tribological studies of the same composite were presented elsewhere (Fan *et al.*, 2013).

TiO_2 is expected to provide oxidation protection to C_f/C composites because of its high melting point of 1850 °C, as well as low diffusion coefficient of oxygen in the same.

Having discussed the merits and demerits of various ceramic matrix combinations, it suffices to have a brief deliberation on the aspects involved when infiltrating molten metals, alloys or ceramics into a C_f/C preform with the aim of attaining the aforementioned hybrid matrices.

2.7 INFILTRATION PHENOMENA

Current trends of fabricating ceramic carbides for protecting C_f/C composites are largely focused on liquid infiltration routes, especially reactive melt infiltration (RMI). Liquid infiltration processes have generally been considered more difficult to execute than powder processes in the formation of ceramic composites. The description of the reactive liquid infiltration process has been dominated by modelling work more than actual experimental work. Overall, the modelling work is fragmented and there is no universally accepted model.

The famous and fundamental appendix in the work of Darcy (1856), loosely translated as "The determination of the Law of Flow of Water through Sand", was very critical in describing the flow of a liquid through a permeable medium. Bearing in mind that at elevated temperatures metals have viscosities close to that of water, the application of Darcy Law (Equation 13) to the infiltration of porous carbon preforms by molten metals is appropriate.

$$u_D = \frac{-\kappa}{\mu} \nabla p \qquad (13)$$

Where: u_D = front velocity of infiltrant

κ = permeability of preform

μ = viscosity of infiltrant

$p =$ pressure

2.7.1 Chemical Reaction vs Mass Transfer

Nelson and Collela (2000) arrived at a 2nd order differential model that showed the competition between chemical reaction and mass transfer:

$$\nabla\left(-\frac{\kappa}{\mu}\nabla p\right) = \eta(\bar{v}_{SiC} - \bar{v}_{Si} - \bar{v}_{C}) \quad (14)$$

Where: $p =$ pressure

$\kappa =$ permeability of preform given by $\kappa = \Phi r^2/8$

$\mu =$ absolute viscosity of the infiltrant

$\bar{v}_l =$ specific molar volume of species l given by $\bar{v}_l = MW_l/\rho_l$

$\Phi =$ porosity

$\emptyset_l =$ volume fraction ofspecies l subject to the constraint $0 \leq \emptyset_l \leq 1$

Their study focused on a system that was reaction-dominated and not diffusion-dominated. This meant the left-hand side of Equation 14, derived from Darcy's Law, was dealt with at a zero state. The chemical formation of SiC from Si and C was taken to be a zero-order reaction, with the amount of preform C limiting the reaction.

The justification for assuming reaction-dominated infiltration was explained by Dezellus *et al.* (2003) who showed that the attainment of capillary equilibrium in such systems took 10-10^4s, unlike non-reactive systems which took less than 1s.

The pores were said to close as given by Equation 15 (Nelson and Collela, 2000):

$$r(t) = r_0 - k_r t_r \quad (15)$$

Where: $r_0 =$ initial pore radius

$k_r =$ reaction rate

t_r = reaction time in the local volume of interest

Figure 18 shows the profiles of pore closure for different reaction rates and consequential decrease in permeability in the preform.

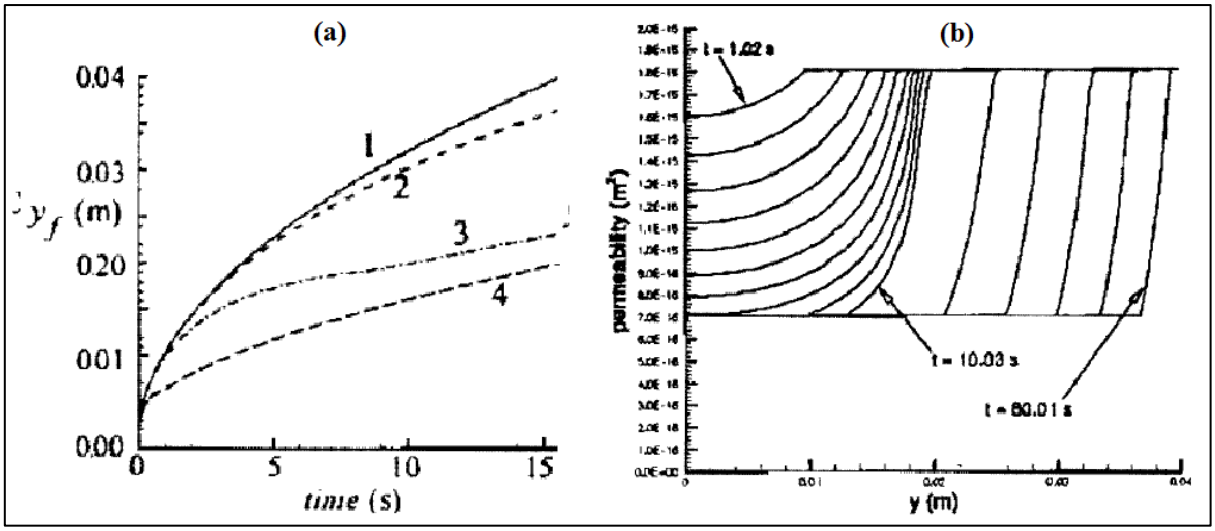

Figure 18: (a) The infiltration height vs time curves for reaction rates k, of (1) no reaction (2) 10^{-9} m/s (3) 10^{-8}m/s (4) 10^{-7} m/s, for pore diameter 0.17μm and initial porosity 50%, (b) decrease in permeability at the pore centreline for the system with reaction rate 10-8 (Nelson and Collela, 2000)

2.7.2 Capillary Action

The capillarity phenomenon is dependent on such parameters as pore size, infiltrant viscosity, temperature, contact angle at the interface triple-line etc.

a. Porosity

Singh and Behrendt (1992) discussed the critical porosity of a preform – the porosity lower than which cessation of infiltration occurs by virtue of choking. The actual porosity of the C_f/C preform has to exceed this critical porosity for the carbide formation reaction to be achieved to completion.

Cessation easily occurs when the diameter of pores in the carbon preform are smaller than is adequate for the created capillary forces to overcome the surface tension on the molten infiltrant (Margiotta, 2009).

The pore diameter at any given time was given by Gern and Kochendörfer (1997) as in Equation 16:

$$d_{K(t)} = d_{K0} - \delta d_{K(t)} = d_{K0} - 2x_{SiC}\left(1 - \frac{1}{K_{MV}}\right) \quad (16)$$

Where: $d_{K(t)}$ = the capillary diameter at time t

x_{SiC} = thickness of the SiC layer formed

d_{K0} = initial capillary diameter (at $t = 0$)

K_{MV} = coefficient of molar volumes

Gern and Kochendörfer (1997)'s model was derived from the macroscopic Navier-Stokes equation which they reduced to the level of one pore and then applied a statistical distribution function to extend the microscopic back to the macroscopic view of infiltration.

They further extended the capillary model to accommodate energy dissipation caused by the varying diameters of capillary pores, from d_{Kmin} to d_{Kmax} . Thus the infiltration behaviour of the melt in arbitrary (non-cylindrical) pores is adequately described. Figure 19 shows the infiltration height achieved for a given pore diameter and infiltration time allowed, from the same model.

a. *Wetting*

The contact angle is a reflection of the infiltrant wetting the preform. The relationship between the adhesive forces due to van der Waals interactions and the contact angle is given by the Young-Dupre´ equation:

$$W_a = \sigma_{lv}(1 + \cos\theta) \quad (17)$$

Where

σ_{lv} is the surface tension of the liquid, and θ the contact angle of the system

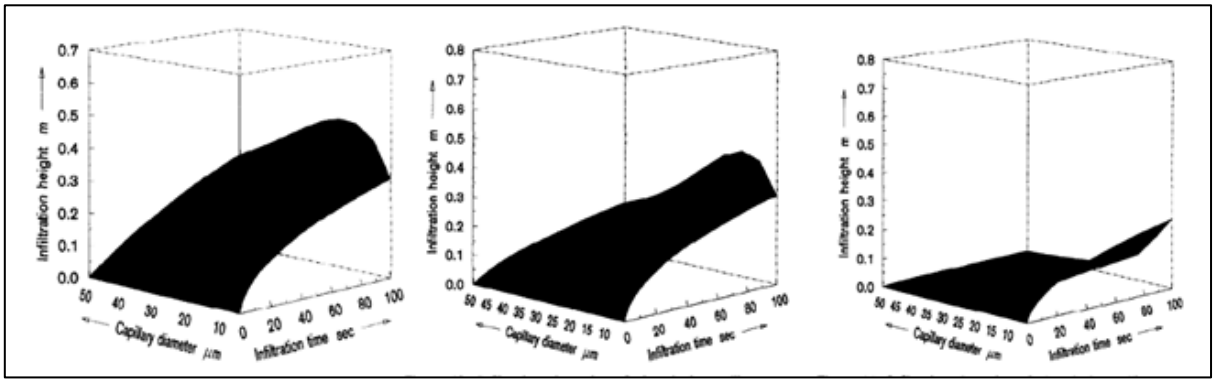

Figure 19: Diagrams showing the infiltration height and capillary diameter dynamics. (a) For a single capillary system; (b) For a system incorporating energy dissipation with $\frac{d_{K\,min}}{d_{K\,max}} = \frac{20}{50}$; (c) For a system incorporating energy dissipation with with $\frac{d_{K\,min}}{d_{K\,max}} = \frac{5}{50}$ (Gern and Kochendörfer, 1997)

The application of the Young-Dupre´ equation is constrained by its assumptions of a non-reactive situation involving a uniform and smooth-surfaced preform, however.

A contact angles less than 90° is considered to indicate the occurrence of wetting. The more the angle approaches 0° the better the wetting involved.

Dezellus et al (2003) postulated an equation (Equation 18) to show how the contact angle changes with respect to time,*t* during the spreading of infiltrant in a reaction-dominated system.

$$Cos\theta_F - Cos\theta = (Cos\theta_F - Cos\theta_0)\exp(-kt) \quad (18)$$

Where:$Cos\theta_0 =$ initial contact angle

$Cos\theta =$ contact angle

$Cos\theta_F =$ final contact angle

$k =$ the rate at which the metal/carbon interface reduces by reaction

From the review by Komolafe and Medraj (2014) on wetting in reactive systems, they showed that there is general consensus among researchers that the wetting process is initially fast and independent of the reaction whose kinetics later control the process.

The literature available on metal-carbon system contact angles largely focuses on Cu- and Al-containing systems. These include the following work: Au and Cu on vitreous carbon and graphite pseudo-monocrystals (Dezellus & Eustathopoulos, 1999); Cu-Sn-Ti on vitreous carbon (Dezellus et. al. 2001); Cu-Cr alloys on carbon (Voitovitch *et al.*, 1999); Al–Si and Al–Ti alloys on pyrolytic carbon, vitreous carbon, and graphite pseudo-monocrystals (Landry *et al.* 1998). Investigations into the contact angles involved in C_f/C and alloyed metals systems are necessary for describing the RMI dynamics.

2.8 SUMMARY

The superb properties of C_f/C composites for UHT applications, and the associated processing methods thereof have been reviewed. The heat treatment of thermoset resin derived carbon matrices and the resultant microstructure have been highlighted. The inability of the C_f/C composites to maintain their properties in oxidising environments, however, has been shown to demand ceramic matrices to serve as intrinsic protection systems. The proclivity of ZrC, HfC, TiC and TaC to form oxides with high melting points, and how SiC and B_4C form crack sealing glasses in service has been presented. The discussion on ceramic matrices has been concluded by brief numerical work associated with the reactive melt infiltration method of producing hybrid ceramic matrix.

CHAPTER 3 – EXPERIMENTAL METHODOLOGY

3.1 OVERVIEW

This chapter presents the experimental work undertaken in fabricating the C_f/C-SiC-TiC-TaC composite. The step by step experimental undertakings consisting of specific discussions of the materials used (summarised in Table 7), the apparatuses set-up, brief descriptions of the equipment and instruments used and the justifications of the choices made herein are presented.

Table 7: Summary of materials used.

Material	Details	Supplier
Carbon Fibre Cloth	200g/m^2, 1000 tex, 2/2 twill	AMT (Johannesburg)
Phenolic Resin	Resole	SI Group (Durban)
$TaSi_2$	99.99% purity, 1-5 microns nominal particle size	Alfar-Aesar (Johannesburg)
$TiSi_2$	99.95% purity, 40 microns nominal particle size	Alfar-Aesar (Johannesburg)

Overall, the experimental work involved performing two wet infiltration steps – Polymer Impregnation and Pyrolysis (PIP) and Reactive Melt Infiltration (RMI) – to make the C_f/C-SiC-TiC-TaC composite. PIP was performed in order to obtain an initial C_f/C composite. RMI was then completed to allow reaction between the initial composite and the constituent elements in the molten $TiSi_2$-$TaSi_2$ alloy infiltrated therein. To test the transport and reaction characteristics of the phases in the alloy with carbon, reaction coupling experiments were performed. The resultant C_f/C-SiC-TiC-TaC composite was then characterised to ascertain its microstructure, chemical composition and its ablation resistance properties.

3.2 PREPARATION OF MATERIALS

3.2.1 CARBON FIBRE/CARBON MATRIX (C_f/C) COMPOSITE FABRICATION

Three cycles of polymer infiltration and pyrolysis (PIP) were performed to impregnate the carbon preform with a carbonaceous matrix. The impregnation of the carbon preform by phenolic resin was performed by the hand lay-up method followed by the vacuum bagging technique.

Resin Infiltration

Phenolic resin (SI Group SS1204) was mixed with 5 wt.% hardener (SI Group SS1028 Catalyst) and stirred thoroughly. The hardener served the purpose of initiating crosslinking in the resin during curing.

Mold Preparation

Before the actual lay-up step the mold on which the composite would be supported was prepared. Five successive coats of high temperature mold release wax (Meguiars Inc.) were applied onto a flat glass block which acted as the mold. Each coat had to be allowed to dry before lightly polishing the glass, to give a smooth finish while keeping the coat intact. The polishing was meant to prevent the composite from sticking onto the mold during processing.

Hand laying-up

The carbon fibre cloth of Twill 2/2 architecture was cut by a pair of shearers into 100mm x 100mm squares. The preform was constructed of 10 laminates arranged in alternating 0° and 90° arrays as shown in Figure 20.

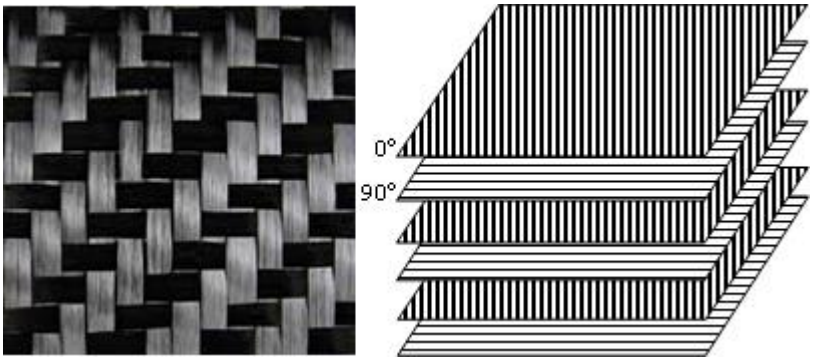

Figure 20: Carbon fibre cloth of twill 2/2 architecture used (left); the arrangement of laminates during the lay-up process (right).

In the hand lay-up step, the composite was built up by sequentially impregnating each laminate with resin and laying it up on top of the subsequent impregnated laminate. Resin was distributed over a laminate and uniformly spread over using a squeegee.

Vacuum Bagging

The impregnated laminates were then sealed in an extruded sheet of plastic bag, and vacuum was pulled in this set up. Between the composite and the vacuum bag, a series of materials – release film, release fabric and breather cloth – were laid up (Figure 21). The breather cloth, a fluffy synthetic 'wool' material, helped in achieving uniform pressure onto the composite as well as taking in excess resin from the preform. The nylon based release fabric ensured a smooth finish on the composite; while the plastic release film (peel ply) was for achieving a non-stick contact between the laminates and the vacuum bagging materials.

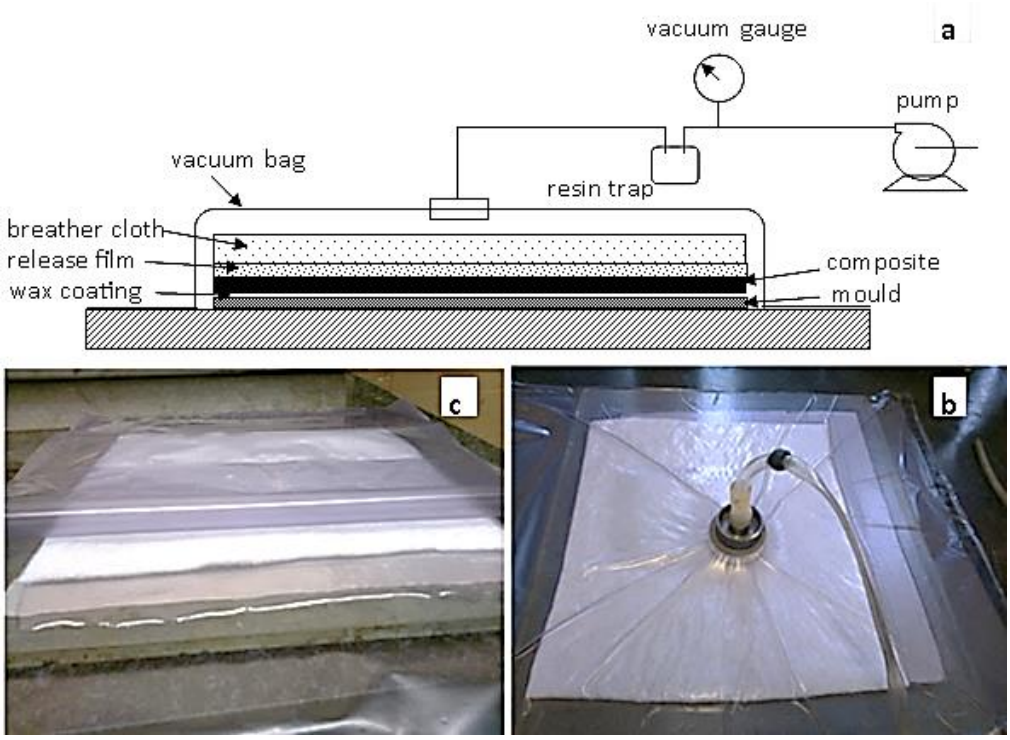

Figure 21: Vacuum bagging set-up used for phenolic resin infiltration. (a) schematic representation; (b) and (c) photographed set-up.

Vacuum bagging was employed to achieve the following:

- the optimum amount of resin impregnates each fibre cloth layer (the optimum amount is achieved through the transfer of excess resin from the laminates to the breather cloth);
- uniformity of the resin throughout the composite which affects the subsequent porosity of the composite after heat treatment;
- to increase the consolidation between respective fibre cloth layers;
- to reduce the amount of air-pockets (from trapped air) which lead to defects in the composites.

As vacuum was pulled the resin infiltrated through the laid-up fibre cloths. When the laminates got saturated with resin, excess resin was collected by the breather cloth and the rest accumulated in the tubing connecting to the vacuum pump.

Infiltration was allowed to complete until the resin was beginning to set. Time was allowed for the resin to initially cure under the same vacuum bagging conditions. The total time for vacuum bagging and initial resin curing was 6 hours.

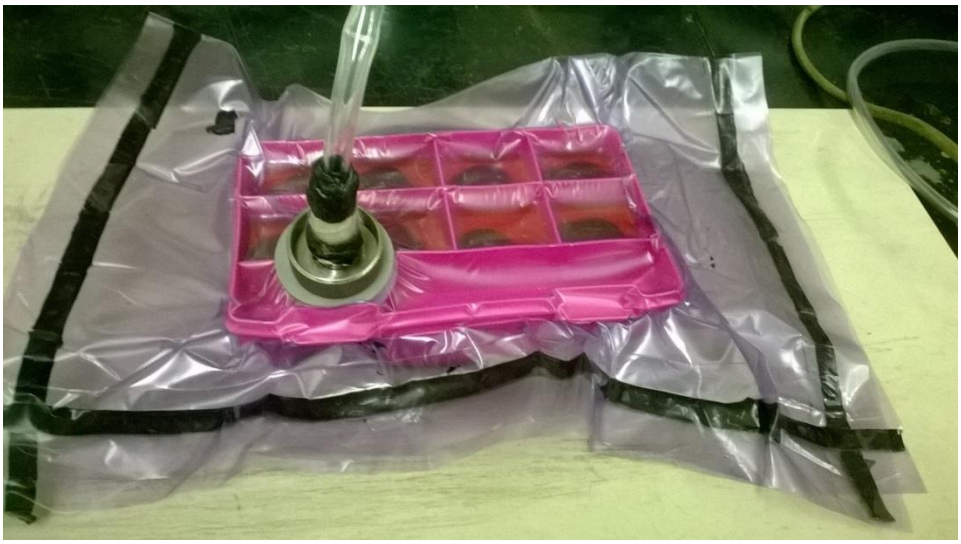

Figure 22: The C_f/C composite reimpregnation set up

Discs of 20mm diameter were then cut out of the resultant composite before undergoing heat treatment. The discs were 3mm thick.

Three successive steps of polymer infiltration, cure and pyrolysis were performed in order to impregnate the C_f/C composite. The heat treated preforms were reimpregnated with phenolic resin using a set up shown in Figure 22. Unlike the hand lay-up method for the first impregnation step, here preform discs were immersed in phenolic resin in a vacuumed bagged container. After allowing capillary infiltration for 2 hours, the discs were then transferred into a vacuum bag set up similar to the one in Figure 20 to allow for equilibration of the phenolic resin absorbed by the discs and to remove excess phenolic resin from them.

Heat Treatment

Curing

The resin-impregnated preforms were cured in an oven set at 100°C for 8 hours in air. Both the heating and cooling rates were at 2°C/min. It was observed that during curing, unsafe fumes of phenol were released from the resin. A setup that would contain the fumes released and direct them to waste was therefore designed (shown in Figure 23).

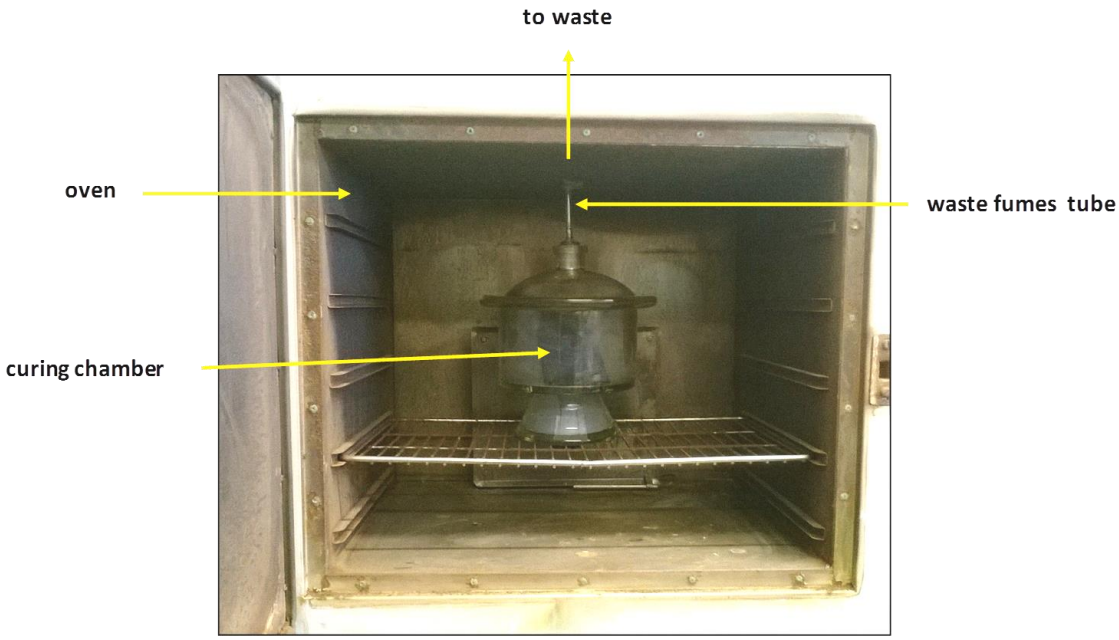

Figure 23: The designed curing chamber set up used for curing the impregnated composites.

Pyrolysis

Pyrolysis was performed in order for carbonization to occur. This involved evaporating all the molecular constituents of the phenolic resin save elemental carbon. Thus pyrolysis was performed at 1000°C for 1 hr in argon atmosphere at 1.5 bar and the argon flowrate was 2mL/s. Heating and cooling rates were set at 5°C/min. The composite discs were pyrolysed in a tube furnace (Figure 24).

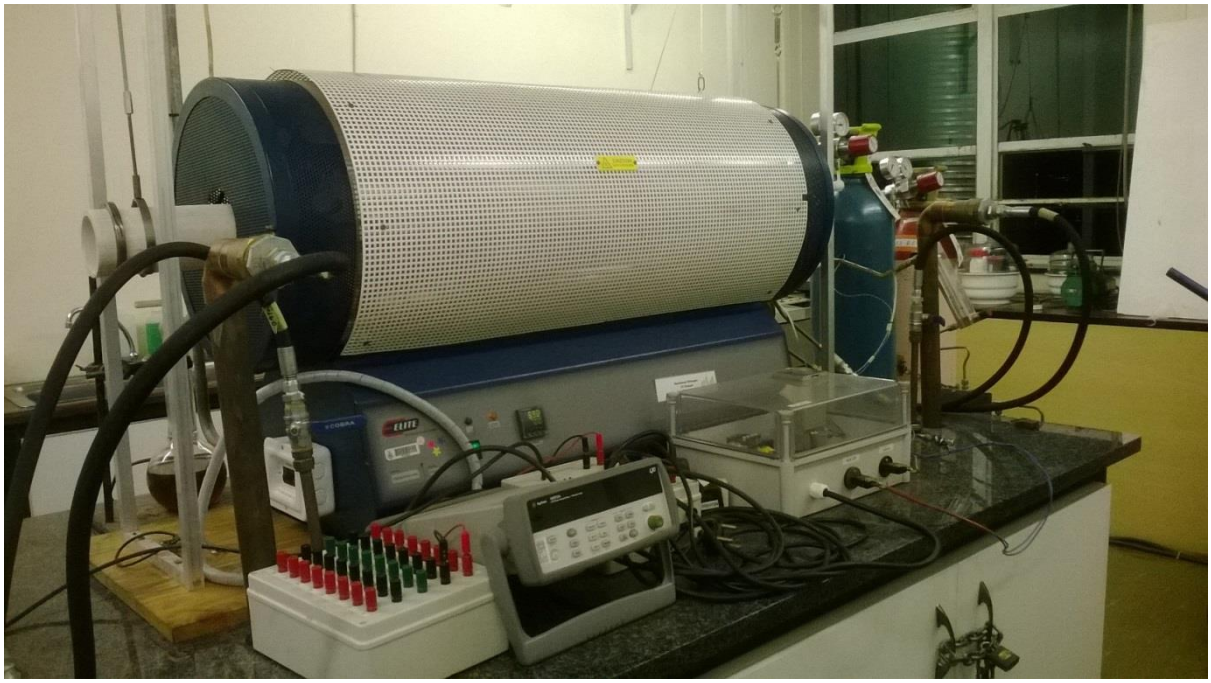

Figure 24: The tube furnace used in carbonising the C_f/phenolic resin composite.

Characterization

The density and porosity characteristics of the C_f/C composites were measured by the Archimedes wet/dry method, quantitative microscopy, mercury intrusion porosimetry and the gas adsorption (Branneur-Emmett-Teller) techniques. The phases in the composite were determined by Raman spectroscopy and XRD, while the microstructure was observed under the scanning electron and optical microscopes.

3.2.2 Si-Ti-Ta ALLOY PREPARATION

Powder Mixing

$TaSi_2$ and $TiSi_2$ powders were weighed before mixing; and the powder masses used per batch of milling are shown in Table 8. The initial mixture contained 17.9 at.% of elemental Ti, 15.4 at.% of elemental Ta and 66.7 at.% of elemental Si.

Table 8: The masses used per batch of milling of $TaSi_2$ and $TiSi_2$ powders.

	Actual Mass (g)	Weight mass (%)	Atomic Mass (%)
$TaSi_2$	100	67	46
$TiSi_2$	50	33	54
Total	150	100	100

The powders were characterised for morphology by SEM and particle size by laser diffraction spectroscopy. The phases in the silicide powders were characterised by XRD.

The initial powders were mixed using the Fritsch Planetary Mono Mill PULVERISETTE in order to allow the two powders to mix to a homogeneous composition. The powders were loaded into a 250ml agate milling pot together with agate milling balls of diameter 10mm. Hexane solvent was added to allow wet grinding to occur. 120ml of hexane was used, considering the capacity of the vial (250ml). The milling parameters used are summarized in Table 9.

Table 9: The milling parameters used in mixing the $TaSi_2$ and $TiSi_2$ powders.

Milling speed	150 rpm
BPR (ball-to-powder weight ratio)	2:1
Milling time	4 h

Wet milling was appropriate as it is known to aid the dissociation of the agglomerated particles. Agate was selected because of the soft milling conditions which were used. The low density of agate meant that the mixing efficiency was greater than otherwise where most of the energy is used for powder particle size reduction. Furthermore, the supplier (Fritsch) recommends the use of the same material for the vial and the milling balls. This stops the possibility of cross-contamination. A ball-to-powder weight ratio (BPR) of 2:1 was adopted, using a total of 30 1cm-diameter agate balls.

Powder Drying

Upon completion of milling, drying was commenced. Drying was achieved by means of the Hiedolph, Laborota 4000Eco rotary evaporator. The hexane solvent was evaporated at 68rpm and 78°C. Dried powder was sieved to separate it from the milling balls.

Powder Compaction

Powder was weighed into 10g batches which were then compacted at normal room temperature by the dry uniaxial pressing method. Owing to the high density nature of the powders, high pressing pressures of up to 70MPa were applied for consolidation of powder particles to occur. Compaction was necessary for the subsequent step of alloying the powders by arc melting wherein arc transfer has a tendency of blowing away the powders during melting. Compaction was therefore aimed at preserving the integrity of the powders during the alloying process.

Avoiding the addition of binding aids was particularly important in this work as most binders, although usually burned away afterward, contain carbon and silicon.

$TaSi_2$-$TiSi_2$ Powder Alloying

Button arc melting was performed on the green compacts using the arc melting furnace shown in Figure 25. The arc was created using a copper electrode with a tungsten carbide tip. The electrode shaft is hollow on the inside to allow is cooling water to circulate during melting. Buttons were contained in a copper hearth which was water-cooled. Ingots were taken out after three melting cycles which involved cold turning.

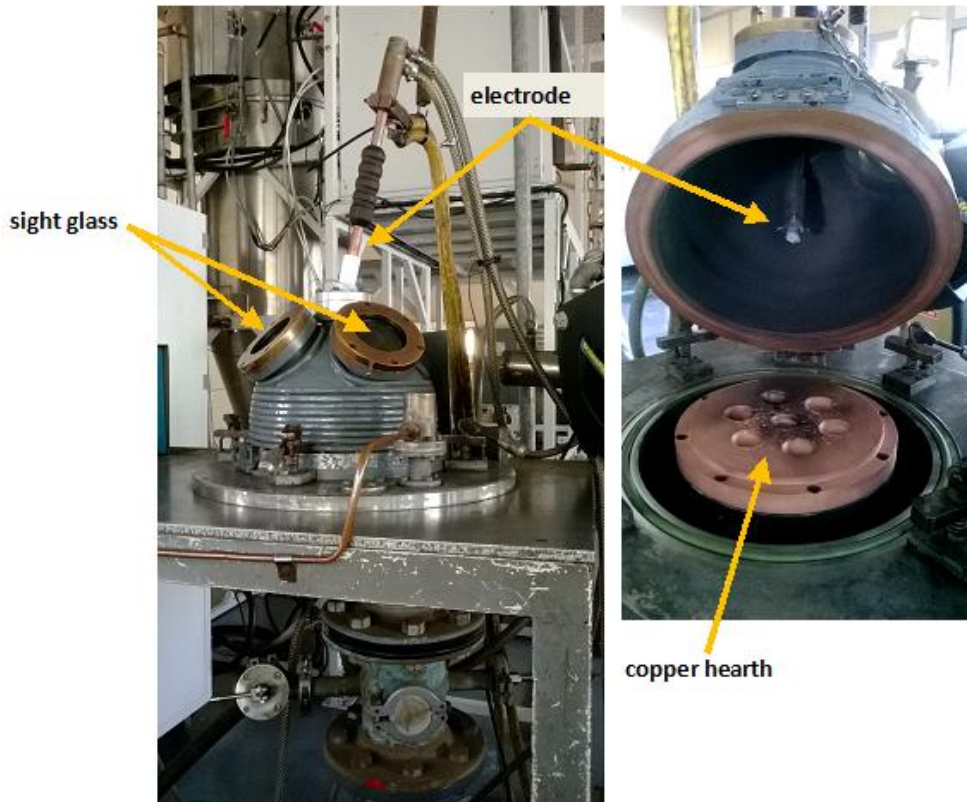

Figure 25: The arc melting furnace used to alloy the $TaSi_2$ and $TiSi_2$ powders.

Each batch consisted of six mixed powder compacts of 10g each; each button was placed into one of the depressions of the copper hearth, as shown in Fig. 26. A titanium getter was also included in the batch and placed in the central button to act as a deoxidizer.

Degassing was effected by first evacuating the chamber using a vacuum pump and maintaining the vacuum at -0.83 bar for 5 minutes. Purified argon was then pumped into the chamber to flush out atmospheric gases; this process was repeated three times. Three cycles of degassing and flushing were necessary in order to expel these possible contaminants, chiefly oxygen, from the chamber.

Arc melting was conducted in an argon atmosphere. The furnace was rated at 100-400A (and a voltage of 44V), the exact amount flowing into the furnace being determined by the transformer setting which is adjusted by a knob. A Hobbart current adjustment transformer was set at 100% so that the maximum supply current would

flow through the system. 3-phase electricity of frequency of 50 cycles was used since arc melting relies on very high currents and low voltages.

The arc was initiated by striking the hearth with the electrode tip. The electrode was immediately directed onto the titanium ingot which underwent localized melting and acted as an oxygen getter. Titanium is known to react with oxygen readily, thus reducing the traces of oxygen which may have been present in the chamber even after degassing. Oxygen is unwanted during arc melting as it has deleterious effects on the reactions that occur.

Melting of the powders occurred when the electrode tip was directed at a particular button. The tip was manoeuvred in small circles until the powder compact had melted satisfactorily and an ingot was formed in the button. Rapid cooling was effected in order to freeze the alloy composition and prevent phase segregation.

Arc melting was particularly useful in this work especially on the issue of inclusion and contaminants. Any inclusions and/or dirt in the Ta-Ti-Si system floated at the top of the ingot as slag. The slag was removed from the ingots by sand blasting.

Powder Crushing and Characterization

The Si-Ti-Ta alloy was pulverised to a powder of average particle size of 10 microns using a zip crusher. The powder was also characterised for morphology by SEM and particle size by laser diffraction spectroscopy. The phases in the alloy were characterised by XRD and EDS.

3.2.3 PREPARATION OF C/Si-Ti-Ta REACTION-DIFFUSION COUPLE

It was necessary to establish the thermodynamic, mass transfer and reactive interaction of permeable carbon with the Si-Ti-Ta alloy – hence diffusion couple studies.

In order to form a couple, the pyrolysed bulk carbon matrix powder was brought into intimate contact with the Si-Ti-Ta alloy powder at a series of temperatures between 1500°C and 1800°C. The idea was to allow the alloy to melt and allow infiltration into the carbon system and react to form carbides of Si, Ti and Ta.

Spark Plasma Sintering (SPS)

The FCT Systeme GmbH HPD5 spark plasma sintering furnace was used. SPS works by the application of a very high current pulsed electric field to the sample placed in a die-punch set as shown in Figure 26. SPS was chosen because of the highly densified near net-shaped products it gives. The fast heating and cooling rates, as well as short sintering hold times, versus the durations in traditional techniques like hot press sintering, are beneficial. This set-up is located in the reaction chamber which is also called the vacuum chamber.

A force of 3 kN was applied to the sample by the two punches. A pulsed electric current (about 4kA) was passed through the sample by means of the graphite dies, which also served as electrodes for conducting electricity to the sample. The die and the sample were heated by the energy of the electric current. A summary of the processing parameters are presented in Table 10.

Table 10: The SPS parameters and sintering conditions used.

Parameter	Quantity
DC Voltage	6V
Heating Rate	200°C/min
Target temperature	1500°C;1600°C; 1700°C; 1800°C
Hold time	30 min
Cooling Rate	200°C/min
Force	3 kN

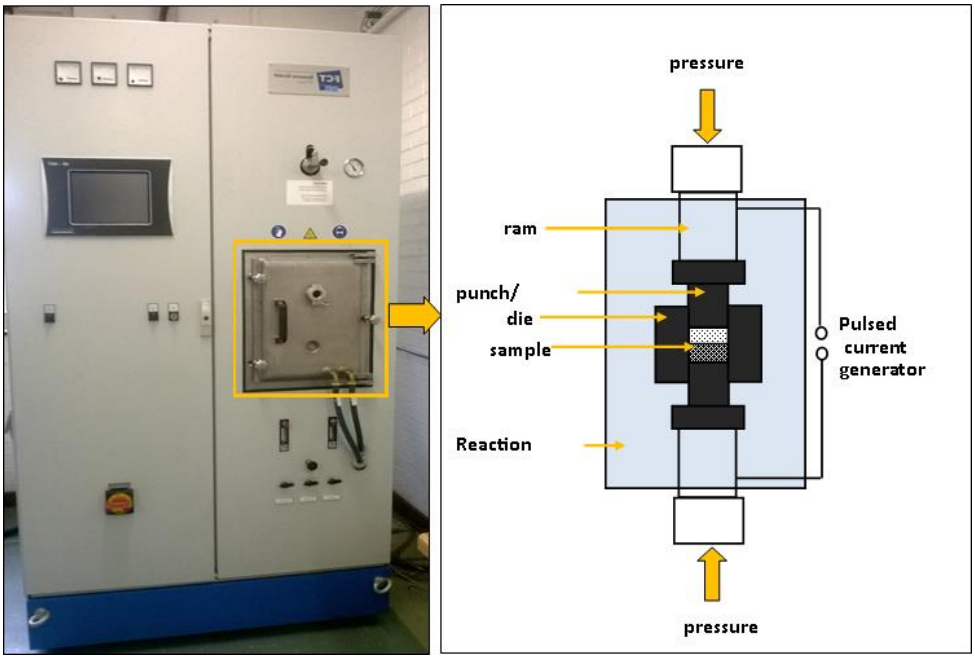

Figure 26: The SPS machine used for reactive melt infiltration (left) and the reaction chamber set-up (right).

3.2.4 PREPARATION OF THE C_f/C-SiC-TiC-TaC COMPOSITE

Having analysed the interaction of the permeable carbon with the Si-Ti-Ta system, the next step was to fabricate the C_f/C-SiC-TiC-TaC composite by spark plasma sintering, which has been discussed in the foregoing section (3.2.3). Pressureless plasma assisted heat treatment was performed using a set up depicted in Figure 27, wherein the closed graphite crucible was coated with hexagonal boron nitride (HBN) on the inside which contained the alloy and composite preform. The coating was used to prevent the alloy powder from reacting with the graphite crucible.

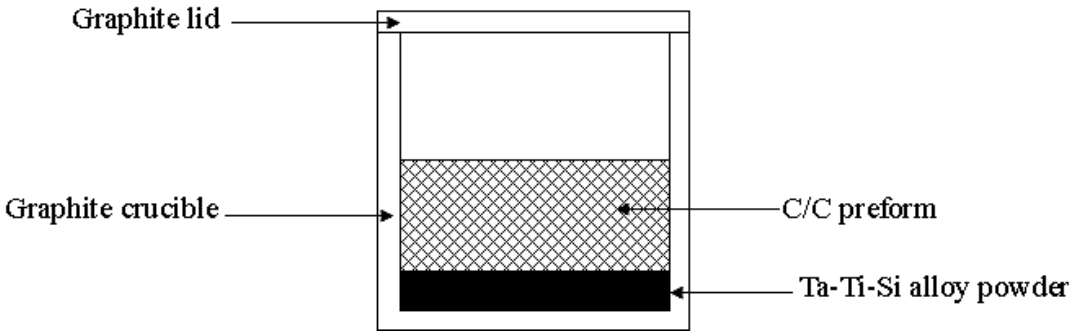

Figure 27: The closed graphite crucible set-up designed pressureless heat treatment in the SPS.

3.2.5 ABLATION RESISTANCE TEST OF THE C_f/C-SiC-TiC-TaC COMPOSITE

The prepared C_f/C-SiC-TiC-TaC composite was tested for its ablation resistance by the oxyacetylene test according to the ASTM E285-80(2002) Standard Test Method for Oxyacetylene Ablation Testing of Thermal Insulation Materials. The set up consisted of a Victor (Model 315) welding torch with a water cooled nozzle, a graphite sample holder, a thermocouple in contact with the back of the sample supported by a spring loaded shaft. The set up was as shown in Figure 28.

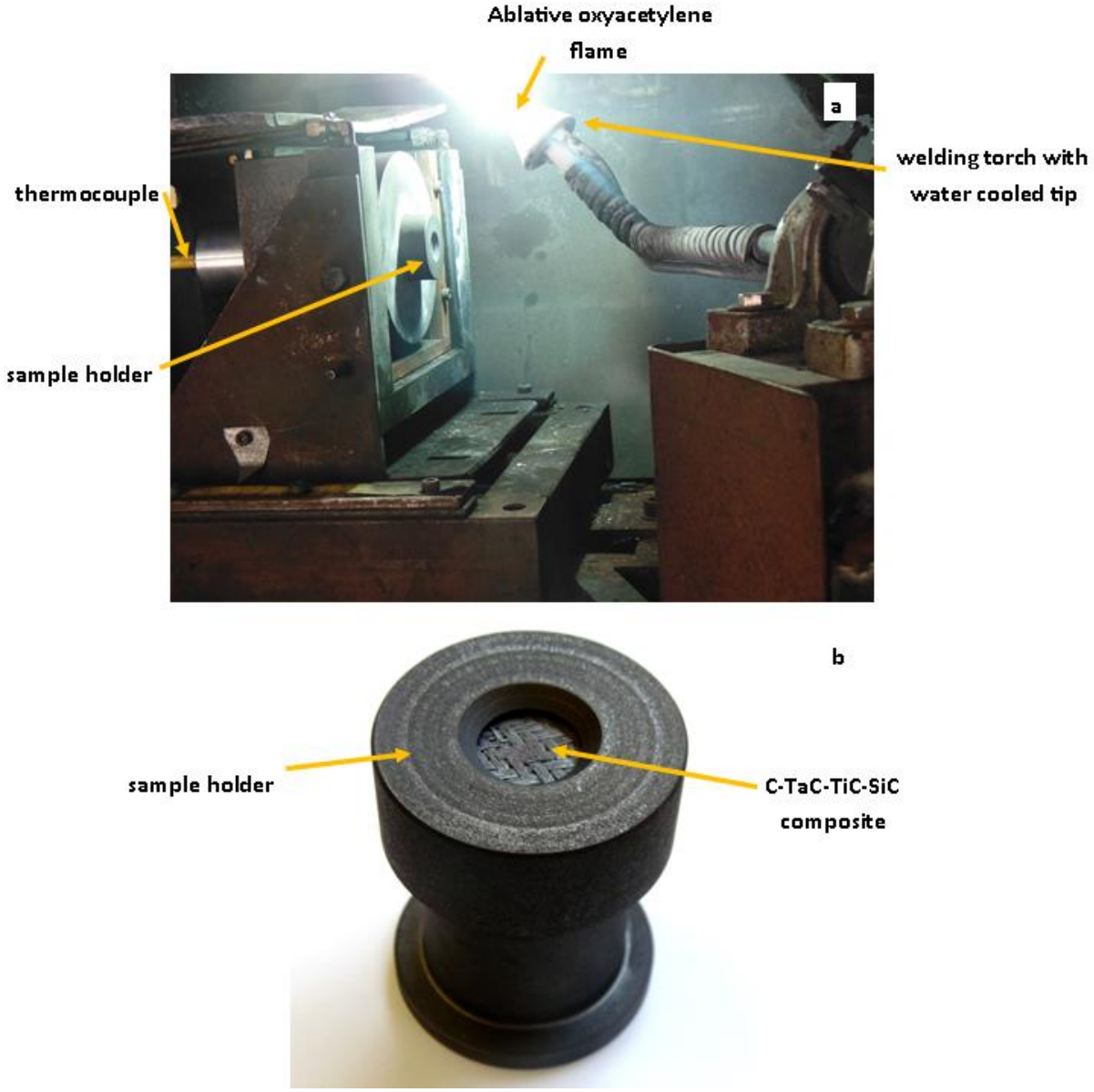

Figure 28: (a) The oxyacetylene flame test set-up used; (b) the special sample holder prepared for the C_f/C-SiC-TiC-TaC composite (Courtesy of Rheinmetall-Denel Munition, Somerset West, South Africa)

The test involved directing an oxyacetylene flame – whose burning gases properties are presented in Table 11 – at the C_f/C-SiC-TiC-TaC composite. The flame at these conditions was known to be at a temperature of at least 3000°C. A timer was set up in such a way that the time at which the sample was exposed to the flame was recorded automatically. The linear ablation and mass ablation rates, and the change in the densities of the samples were measured for a sample exposure time of 2.1 s to 7.9 s and heat flux of 4MW/m^2. The linear ablation (R_l) and mass ablation (R_m) rates were calculated respectively by the following formulae (Equations 18 and 19):

$$R_l = \frac{x_t - x_o}{t} \tag{18}$$

$$R_m = \frac{m_t - m_o}{t} \tag{19}$$

Where:

x_o and x_t are the initial and final composite thicknesses after time t, respectively;

m_o and m_t are the initial and final composite masses after time t, respectively.

Table 11: Conditions of the oxygen and acetylene gases used in the flame for a heat flux of 4MW/cm^2.

	Oxygen gas	Acetylene gas
Temperature, °C	26.5	26.2
Pressure (gauge), kPa	200	253
Flow rate, %	44	56

For comparison purposes, the same oxyacetylene flame test was performed on the C_f/C composite preform discs of 20mm diameter and 3mm thickness. Ablation rates obtained for the 2.5s, 5.0s and 7.5s runs for both the C_f/C composite and the UHTC were used in the comparisons.

Characterization

The compounds formed from the burning of the C_f/C-SiC-TiC-TaC and C_f/C composites were characterised by XRD. Back-scattered electrons detector (BSED) SEM was used to examine the microstructures of the ablated materials; EDS and electron probe micro-analysis (EPMA) were used to quantify the oxides formed. The resultant densities of the ablated C_f/C-SiC-TiC-TaC and C_f/C composites were obtained by the Archimedes wet/dry method.

3.3 MATERIALS CHARACTERISATION

Metallographic Preparation

C_f/C *Composite*

The metallographic preparation of the C_f/C composite specimens presented numerous challenges due to the brittle nature of the pyrolysed carbon and the porosity in the composite.

Attempts to cold mount the samples were not very successful as the resin did not effectively infiltrate the composite, especially the extreme pores (voids and micropores), even under a vacuum. Here the voids did not fully fill up and the micropores did not get infiltrated. Examination of the samples straight after sectioning was resorted to instead.

Si-Ti-Ta Alloy

The alloy ingots were sectioned using a diamond cut-off wheel at the rate of 200rpm and 0.030mm/s feed. The specimens were hot mounted using epoxy resin. Grinding was done with 400, 600; 800; and 1200 grit abrasive silicon carbide paper in order to prepare the samples for polishing. Water was used as the lubricant and coolant. The specimens were subsequently polished using 3μm and 1μm particle sized diamond particles-containing suspensions on polishing cloth. The microstructure was satisfactorily revealed without the need for etching.

Archimedes Wet/Dry Method

Density measurements were performed by the Archimedes Wet/Dry Method. Here the specimens were immersed in ethanol (ρ = 0.707g/cm^3) and the suspended mass (m_s) recorded after the bubbling in the ethanol had ceased. The samples were patted dry and the wet mass (m_w) recorded. The samples were then placed in a drying oven for 1 hour; wherein the absorbed ethanol was evaporated from the samples and the dry mass (m_d) recorded. The apparent densities ρ_a were calculated using the following formula (Equation 20):

$$\rho_a = \frac{m_d}{m_d - m_s} \times \rho_{ethanol} \tag{20}$$

The open porosity (ε) percent was calculated by the formula:

$$\Phi = \frac{m_w - m_d}{m_w - m_s} \times 100\% \tag{21}$$

Although the Archimedes Wet/Dry Method gave an indication of the total porosity (open and closed), it was necessary to determine the effective porosity of the samples. Effective porosity was to give a reflection of the pores that were of practical utility in performing the molten alloy infiltration.

Two porosimetry analysis methods [BET (Brunauer, Emmet, and Teller) and MIP (Mercury Intrusion Porosimetry)] were applied in order to determine the pore volume; pore size distribution; and pore shape properties of the pores contained in the C_f/C composite.

Optical microscopy

Qualitative Technique

The Olympus BX63 optical microscope was used to examine the microstructure of the C_f/C composites. The bright field (BF) mode was useful in viewing the glassy carbon matrix resulting from phenolic resin pyrolysis. The reflectivity of the matrix assisted

in revealing the morphology thereof. Here the depth of field was not even therefore the multiple image alignment (MIA) and z-stacking techniques were applied.

The MIA software calculated the number of image modules to be fitted in the selected region of interest. The images of the modules were acquired sequentially and then colligated together after correcting the image property differences in each module by intelligent pattern recognition.

The confocal laser scanning was utilised in the z-stacking technique. Here the images were acquired in z-plane stacks in order to increase the depth field refinement in the images. This ensured that a uniformly focused image was obtained despite the morphological differences in the specimen.

Quantitative Technique

Optical microscope imaging was conducted and combined with surface analysis (using Olympus Stream Motion v1.3 software) to get quantified characteristics of the pores in the cross-sectional area of the composite specimens. The image was then digitized and the optimal grey-level selected before analysis. The analysis relied on the contrast differences in the binary image created to distinguish between the solid phases and the pore phases. The image consisted of black areas which represented the pores and the white areas which represented the carbon areas (a combination of fibres and the matrix).

The software (Olympus Stream Motion) performed pore detection and analysis of small regions of interest (ROIs) in the image to determine the pore diameters (minimum, maximum and mean), areas, perimeters, shape and sphericity factors at a given colour intensity.

The major challenge encountered in this technique was the limitation of the representativeness of the regions of interest (ROI) analysed. As such, for each sample, three specimens were analysed and the results averaged. Furthermore, noise was inevitably present in optimising the grey level – this led to overlap of phases that were supposed to be different.

Mercury Intrusion Porosimetry (MIP)

MIP was apparently the most practically relevant analysis method in predicting the molten alloy permeation into the C_f/C skeleton. The immediate limitation to the technique was the non-wetting nature of mercury on carbon, forming contact angles greater than 90°. It is well known that the elements used in this work (Ta, Ti, and Si) were able to wet carbon and react with it to form carbides.

The procedure involved the loading of about 3g of specimen discs into a penetrometer of diameter 12mm. The specimen was degassed and evacuated by pulling a vacuum in the penetrometer to a pressure of 13Pa. The penetrometer was pressurized to 6.67Pa and then evacuated again.

Mercury was then pumped into the penetrometer until the specimen was mercury-logged. The pressure of mercury intrusion into the specimens was twofold – at low pressure and then at high pressure. At low pressure intrusion was achieved at 0.51psia mercury pressure. High pressure intrusion was initiated at 0.1 psia and was increased stepwise and allowed to equilibrate in 10s intervals, till it reached $6x10^4$ psia. The volume of mercury intruded was then measured against the pressure of intrusion. A summary of the mercury intrusion parameters are presented in Figure 29.

Summary Report

Penetrometer parameters

Penetrometer:	#s/n - (09) 5 Bulb, 1.131 Stem, Solid		
Pen. Constant:	22.065 µL/pF	Pen. Weight:	60.3763 g
Stem Volume:	1.1310 mL	Max. Head Pressure:	4.4500 psia
Pen. Volume:	6.6486 mL	Assembly Weight:	116.6824 g

Hg Parameters

Adv. Contact Angle:	130.000 degrees	Rec. Contact Angle:	130.000 degrees
Hg Surface Tension:	485.000 dynes/cm	Hg Density:	13.5335 g/mL

User Parameters

Param 1:	0.000	Param 2:	0.000	Param 3:	0.000

Low Pressure:

Evacuation Pressure:	50 µmHg
Evacuation Time:	30 mins
Mercury Filling Pressure:	0.51 psia
Equilibration Time:	10 secs

High Pressure:

Equilibration Time:	10 secs

Blank Correction by Formula

(From Pressure 0.10 to 60000.00 psia)

Figure 29: A summary of the mercury intrusion parameters used.

Brunaeur-Emmett-Teller (BET)

The Micrometrics ASAP 2020 Pore Analyser was used in conducting porosimetry tests on the C_f/C composite specimens. The BET technique was chosen mainly because of the need to confirm the characteristics of the micropores which were identified in the mercury intrusion porosimetry technique as being substantially present – BET is an appropriate technique for very fine pores.

Nitrogen gas was used as the adsorptive in the C_f/C composite with the intent of applying the BET isotherms. The gas would adsorb onto the pore surfaces in the specimen in the form of layers until the total volume of nitrogen gas adsorbed approximated the volume of the pores.

The specimens had to be degassed by pulling a vacuum prior to the main adsorption and desorption process to ensure that the pore surfaces were uncontaminated. Purging was achieved using helium gas at a temperature of 200°C, after which sample evacuation was effected.

Nitrogen was then pumped into the specimen at an analysis bath temperature of -197°C slightly more negative than the boiling point of nitrogen (-195.8°C), and a pressure approximating its saturation vapour pressure. The pumping of nitrogen was achieved through an automated stepwise technique whereby a volume of the absorptive was allowed to reach equilibrium before another was pumped in.

Desorption was then prompted by applying a vacuum of 1Pa. Here the nitrogen evacuation had to be achieved by a similar stepwise approach to the pumping process.

The volumetric conductivity method was then used to determine the amount of nitrogen which was adsorbed. The data was then interpreted by the built-in software which uses the Brunauer, Emmett and Teller (BET) adsorption isotherm equation given by (Equation 23):

$$\frac{1}{\left[V_a\left(\frac{P_o}{P}-1\right)\right]} = \left(\frac{C-1}{V_m C}\right)\left(\frac{P_o}{P}\right) + \frac{1}{V_m C} \tag{23}$$

Where:

P = partial vapour pressure of nitrogen gas at boiling point 77.4°C.

P_o = saturated pressure of nitrogen gas

V_a = volume of nitrogen gas adsorbed at standard temperature and pressure

V_m = volume of gas adsorbed at standard temperature and pressure to produce an apparent monolayer on the sample surface,

C = is a constant related to the enthalpy of adsorption of nitrogen gas onto the sample.

Laser Diffraction

The laser diffraction technique was used to determine the particle size distributions of the $TaSi_2$, $TiSi_2$ powders and their mixes, the pyrolysed bulk carbon matrix powder and the Si-Ti-Ta alloy powder. Here a Malvern Mastersizer 2000 particle size analyser was utilised, wherein a He-Ne beam was directed onto the specimen under examination. The specimen powder to be analysed was mixed with distilled water and a suspension obtained. Dolapix CE64 (Zschimmer-Schwarz, Germany) was used as a dispersant (2 drops in 100ml paste) and ultrasonic water bath treatment (1 minute) was also used to ensure that deflocculation of agglomerated particles. The suspension was then added to a sufficient amount in the particle size analyser's specimen distilled water and the particle size distribution results were read off.

SEM

Scanning electron microscopy examinations were done using the Zeiss Evo 60 EP-SEM and the FEI Quanta 400 SEM.

Powder morphologies and the C_f/C-SiC-TiC-TaC composite fracture surfaces were examined using the secondary electrons (SE) detector. Here the SE mode was engaged because secondary electrons bounce off from minimum sample depth hence revealing the topographical detail of the scanned area.

BSE were utilised to obtain images of sufficient contrast to differentiate the constituents in the specimen by atomic contrast. An accelerating voltage of 20kV was

used for analysis. The BSE mode was used to examine the phases in the Si-Ti-Ta alloy, the C/Si-Ti-Ta couple, and the C_f/C-SiC-TiC-TaC composite (both before and after ablation tests).

The Bruker AXS Quantax 4010 Energy Dispersive X-ray (EDS) spectrometer, coupled to the SEM, was used to obtain both the qualitative and quantitative elemental characteristics of the couples' reaction zones. At least four points were picked across each couple from the points of interest in order to analyse the compositional variations of elements due to reactive and/or transport phenomena. In addition to the qualitative peaks, quantitative analyses were done at each area selected for elemental analysis.

It was essential for us to obtain the spatial elemental distribution images, especially in the reacted zones of the couples, by the use of colour-coded maps. Here it was important to track the diffusion and reaction of each element in the couple system. The known elements were assigned different colours. An area on the reacted zone was selected and comparison of each element map was performed on the same area.

Raman Spectroscopy

The Jobin-Yvon T64000 Raman spectrometer was used to confirm the type of carbon formed in this work. This technique is dependent upon the vibrations in the atoms of a material when excited by electromagnetic radiation. A Raman spectrum is then produced from the interaction of the incident radiation with the vibrational frequencies of the atoms in the material, thus giving information about its molecular structure.

X-Ray Diffraction (XRD)

The Bruker D2 Phaser X-ray diffractometer instrument was employed in performing XRD characterisation. Cobalt (λ = 1.79Å) was used as the target source of X-rays produced at 30kV and 15mA ratings. The diffracted rays were detected by a LynxEye PSD detector with a detector angle range of 5°.The diffractograms obtained were compared to the patterns in the Powder Diffraction File (PDF) accessed through the DIFFRACplus-EVA software.

The alloy ingots were pulverised to a powder of less than 10μm particle size and analysed. A scanning speed of 1.4° 2θ/min and a 0.02° step size were engaged for 50 minutes in scanning across 20-90° of 2θ values. The couples and the C_f/C-SiC-TiC-TaC composite, before and after ablation, were analysed as cross-sectional form without pulverising them to powder.

Quantitative XRD techniques were employed in determining the lattice structures and parameters in the materials – especially the Si-Ti-Ta alloy and the C_f/C-SiC-TiC-TaC composite. Here the materials were indexed in order to establish the Miller indices to each diffraction peak and then determining the lattice parameters.

The alloy consisted of hexagonally shaped crystals; hence the Bruker TOPAS software was used. TOPAS utilised the Pawley algorithm based on non-linear least squares approach and useful in decomposing the peaks in the pattern. The Pawley method was particularly useful in the present work as it is independent of 2θ values in the pattern due to the existence of other 'interfering' phases in the system.

It is known that the lattice spacings in hexagonal crystals are determined by Equation 24:

$$\frac{1}{d^2} = \frac{4}{3}\left(\frac{h^2 + hk + k^2}{a^2}\right) + \frac{l^2}{c^2} \tag{24}$$

Where:
d = lattice spacing
h, k, l = Miller indices of the Bragg plane
a = a lattice constant
c = a lattice constant

The C_f/C-SiC-TiC-TaC composite consisted of cubic shaped crystals and the analytical approach was used to index them. The lattice spacing in cubic crystals is determined by Equation 25:

$$\frac{1}{d^2} = \frac{h^2 + k^2 + l^2}{a^2} \quad (25)$$

Where parameters are defined as in Equation 24.

Furthermore, Rietveld refinement was performed on the obtained patterns for the UHTCs obtained by RMI at 1600°C, 1700°C and 1800°C using the TOPAS software. The refinements were done with the aim of determining the lattice parameters of the observed phases in the UHTCs, and comparing the changes in the parameters with respect to RMI temperature.

Electron Probe Micro-Anaylysis (EPMA)

Since the compositional information regarding the scale formed on the C_f/C-SiC-TiC-TaC composite could not be fully resolved by SEM-EDS, it was necessary to use a more sensitive instrument with higher resolution capabilities in performing the quantitative spot analyses. An ablated UHTC specimen was ground to a thickness of about 0.5mm using 400-grit SiC paper. Extra care was taken not disrupt the fragile scale on the surface of the composite. The specimen was then loaded into the CAMECA SXFive-FE EPMA instrument.

The BSE mode was employed to view the region of interest. A fairly flat region was selected where multiple cracks (at least 3) were located. 20 points were picked in a line with a length of about 10 μm, cutting across the cracks. Quantitative micro-analysis was performed using 3 wavelength dispersive spectrometers (WDS), which were optimally inclined to the specimen to accommodate its surface roughness. Spectrometers used the following crystals:

1. TAP (thallium acid phthalate)
2. PC1 (W/Si Multilayer)
3. LIF (Lithium fluoride)

Beam energy of 15 keV was used in order to avoid the ionization of inner shell electrons. Analysis of results was performed using the PeakSight software. The EPMA technique was also advantageous in that results are shown as those of the oxides of the elements present.

CHAPTER 4 – RESULTS

4.1 OVERVIEW

The results presented in this chapter show how an amorphous carbon preform was obtained with sufficient porosity for RMI to occur. The unanticipated phases (Si and 5-3 silicides of Ta and Ti) obtained in the making the 66.7Si-17.9Ti-15.4Ta alloy, in addition to the anticipated (Ta,Ti)Si_2 phase were identified. EDS studies on the C/Si-Ti-Ta couples helped understand the mechanism of infiltration which involved shifting solid-liquid equilibrium conditions with increasing RMI temperature. XRD results confirmed that the anticipated carbides [(Ta,Ti)C and SiC] did materialize in the UHTC matrices. The performance of these carbides in an oxyacetylene flame test gave indications of the formation of self-healing oxides in the protective scale formed. The UHTC composite's ablative resistance is presented alongside that of the C_f/C composite for comparison sake.

4.2 THE CARBON FIBRE/CARBON MATRIX COMPOSITE

4.2.1 Bulk Matrix Microstructure

After performing 3 cycles of phenolic resin infiltration and pyrolysis, a crumpled and folded leaf microstructure in the matrix of the C_f/C composite was observed, and this microstructure is characteristic of amorphous carbon. Furthermore, the matrix had a peculiar glossiness and a glass-like finish as shown in Figure 30.



Figure 30: Optical micrograph showing the glossy, pseudo-glassy appearance of the carbon matrix.

Figure 31(a) shows the microstructure of the matrix between two fibre cloth layers. The matrix shows complex folds and cups. At the centre of the folding bundle of matrix is a void or cavity. Figure 31 (b) is a micrograph of a zoomed-in cavity from the section in (a). The matrix inside the cavity showed conchoidally fractured shells of matrix which are likely to be formed by the evolving gases during high temperature treatment.

The duration of curing was important in producing the desired microstructure in the final C_f/C composite. Curing phenolic resin for 8 hours produced the most consistent and open porosity. Prolonged durations of curing at 100°C resulted in the oxidation of the phenolic resin, while abridged durations resulted in an insufficiently cross-linked polymer in the matrix.

During the carbonization process, it was observed that at temperatures between 250°C and 350°C there was a continuous popping sound of explosions inside the tube furnace. Thereafter, delaminated C_f/C composite discs whose laminates were scattered all over the inside of the furnace were realised. It was deduced that in the temperature range of 250°C to 350°C, C_f/C composites face potential catastrophic damage. The success rate of non-delaminated C_f/C composite discs after carbonization was 56%. The evolution of gases during carbonisation is a violent process; that is why the matrix in Figure 31(b) shows a 'shattered' appearance. That is why the heat treatment of C_f/C composites demands low ramping rates during both heating and cooling.

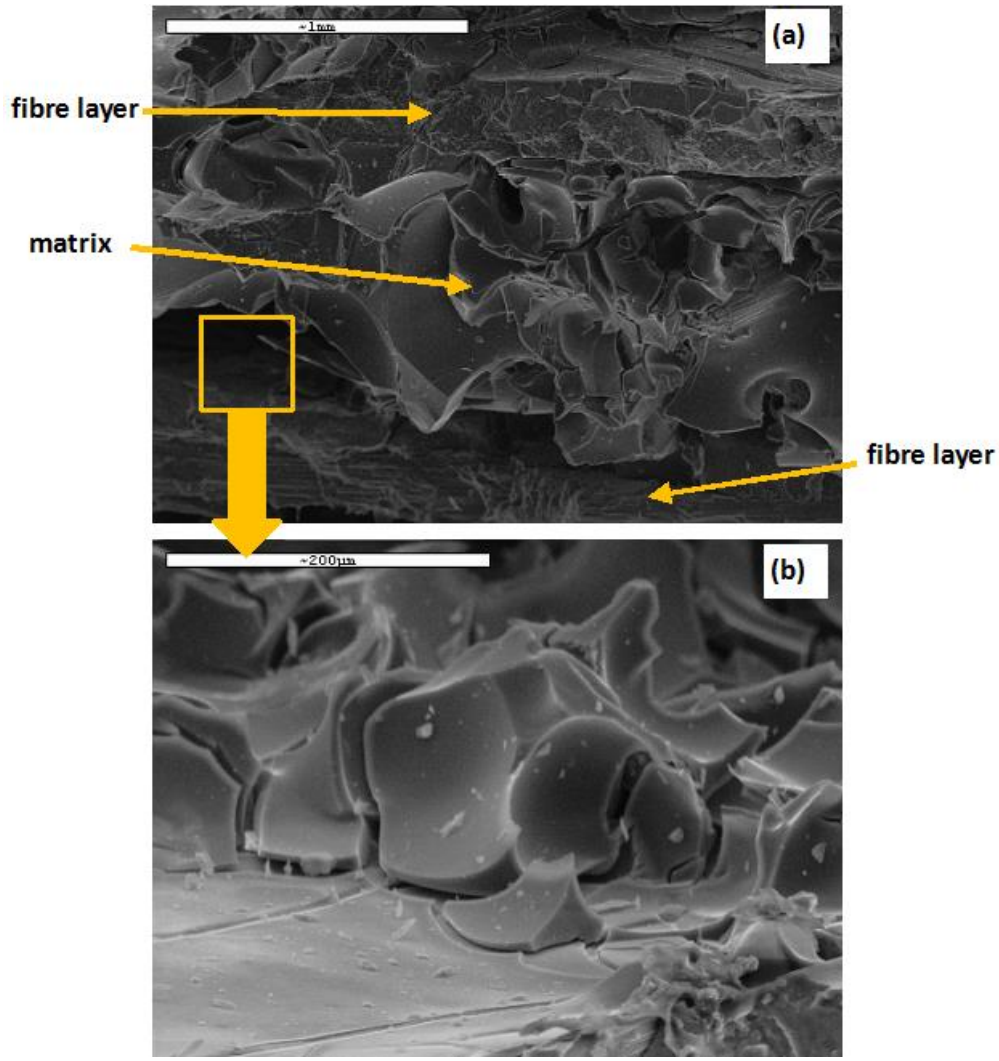

Figure 31: Micrograph of a C_f/C composite in which infiltration of resin was effected without vacuum bagging. The occurrence of conchoidal fracture in the matrix during pyrolysis is evident.

4.2.2 Carbon Fibre-reinforced Carbon Composite Microstructure

The distribution of the matrix within the fibre bundles was studied. The fibres showed that they were thoroughly hemmed in by the carbon matrix and were uniformly distributed in the same (Figure 32). From Figure 32, it was not surprising to find that layers 1 and 3 contained fibres albeit in lower densities than in layers 2 and 4. This was caused by the 2/2 twill type of architecture in which the weft fibre strands ridge over warp fibre strands in the selected region of interest shown in Figure 32.

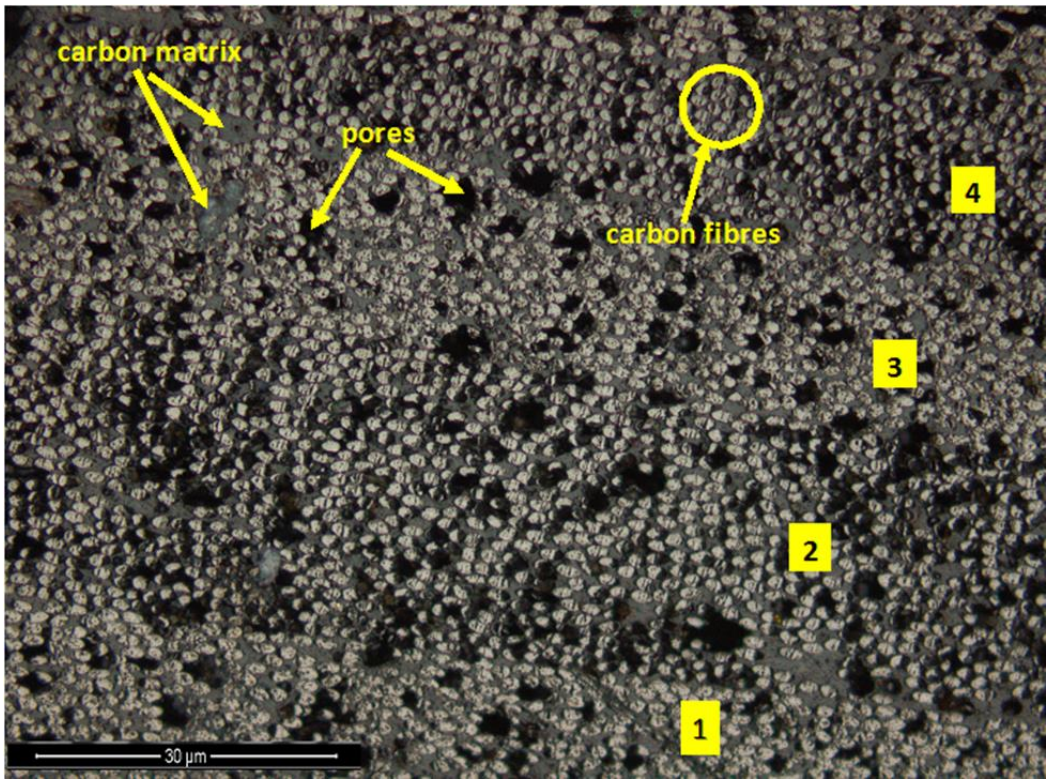

Figure 32: An optical micrograph of the C_f/C composite after 3 cycles of PIP. The white phase represents the fibres, the grey phase represents the matrix, and the black phase represents the pores in the composite.

The microstructure has a fairly uniform network of pores throughout the sample. The microstructure shows two main large pores which can be considered as outliers. These pores might have been formed due to the release of entrapped air during resin and catalyst mixing.

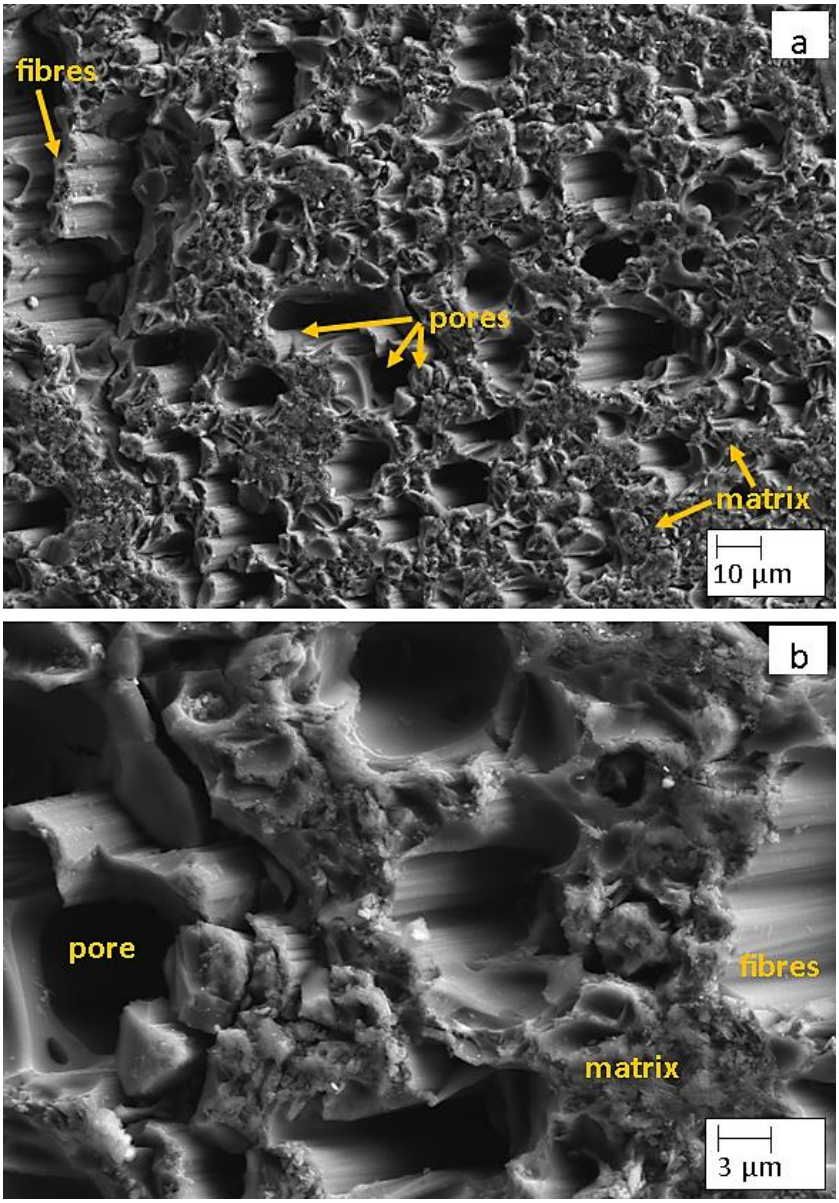

Figure 33: Cross-sectional SE-SEM microstructure of the C_f/C composite revealing the profound permeation and lodging of the matrix in-between the inter-fibre gaps within the tows.

The microstructure shows how the resin infiltrated right into the fibre tows and the individual fibres. Figure 33(a) shows a multiplicity of pores showing how they developed along the length of the fibre tows. The amorphous nature of the matrix is clearly shown in Figure 33(b) which is a magnification of Figure 33(a). The crumpled and folded microstructure of the resin is evident especially at the intertow sites where the resin seemed to have amply lodged more than anywhere else. The figure also shows how the vacuum bagging process facilitated the even and intimate distribution of matrix within the fibre network.

4.2.3 Interface Microstructure

Figure 34 is another exhibit on how the carbon matrix exists in-between the individual fibres.

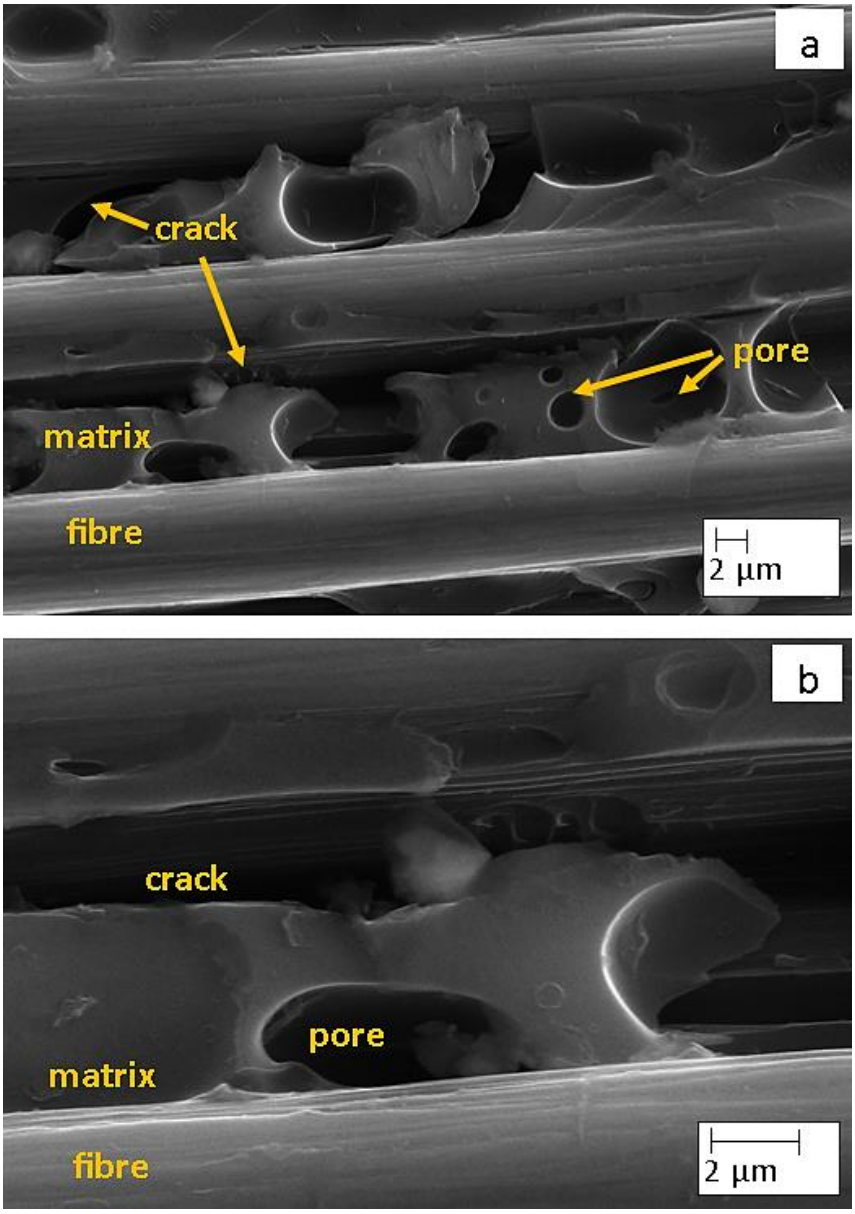

Figure 34: A micrograph showing the fibre and matrix interface. The presence of pores and cracks in the matrix in-between fibres is evident.

The thickness of the matrix trapped within the interfibre spacings is comparable to the individual fibres thickness which, from the micrographs, approximates 6µm. Figure 34 shows how some cracks which developed transversely in the matrix propagated along the fibre-matrix interface. These openings along the interface may also mean that the

alloy to be subsequently infiltrated would lodge itself along the fibre-matrix interface. The longitudinal cracks seemed to be concentrated at the matrix-fibre interface. The approximate width of the gap formed in the longitudinal cracks at the matrix-fibre interface was 1.5µm. These matrix cracks were caused by the contraction of the matrix during carbonization such that the matrix pulled away from the fibres owing to the thermal stresses from the high temperature treatment (HTT).

4.2.4 PIP Cycles Efficiency

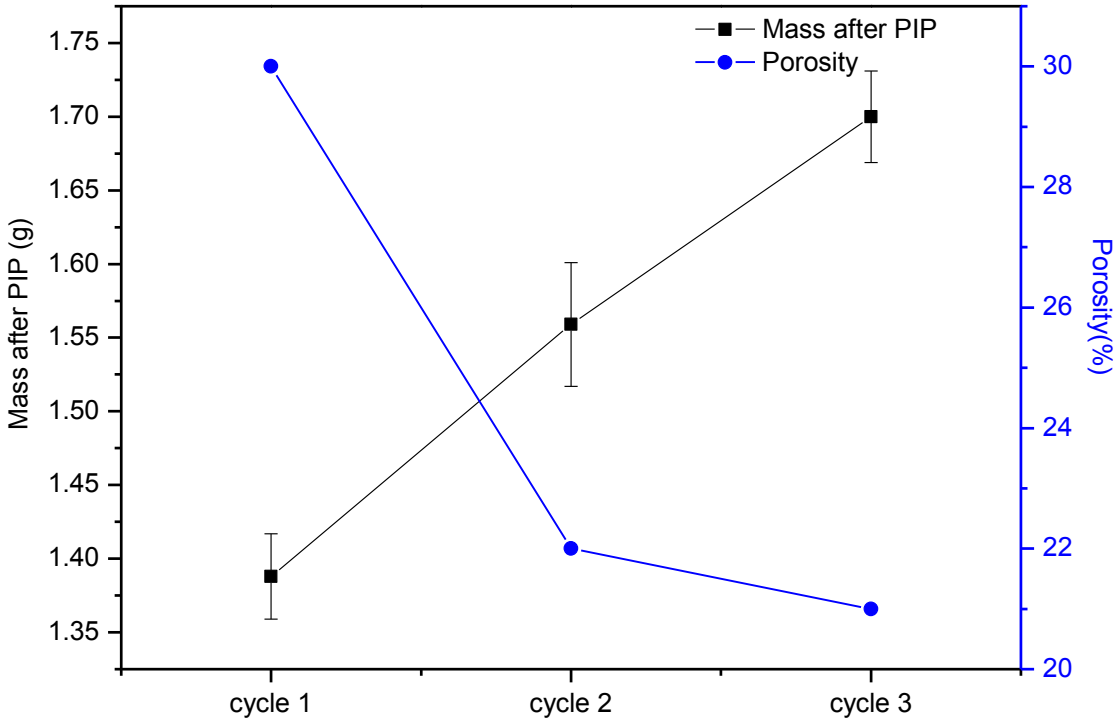

Figure 35: The graph of the mass of C_f/C composite and its porosity vs the number of PIP cycles effected.

The porosity vs number of PIP cycles graph in Figure 35 shows how the porosity started to level off from the second PIP cycle to the third PIP cycle. The mass of the C_f/C composite increased with the number of PIP cycles effected. The rate of mass gain decreased with the PIP cycles. This means the mass versus number of PIP cycles graph would clearly have levelled off if more cycles of PIP had been completed.

The infiltration PIP efficiency results are shown in Table 12.

Table 12: Percent mass changes after each PIP cycle during C_f/C composite densification.

	Cycle 1	Cycle 2	Cycle 3
Mass gain after infiltration, before heat treatment	43%	27%	22%
Mass gain after full PIP cycle	19%	12%	9%
Mass loss during heat treatment	24%	15%	13%

There is a clear decrease in the infiltration efficiency from the first to the third cycles of PIP as illustrated by the mass gain after full PIP cycle. The decrease in the mass of resin lost during heat treatment is indicated by the difference between the mass gain after infiltration and the mass gain after a full PIP cycle. The difference between these two values is represented by the graph of the mass loss during heat treatment vs number of cycle of PIP in Figure 36.

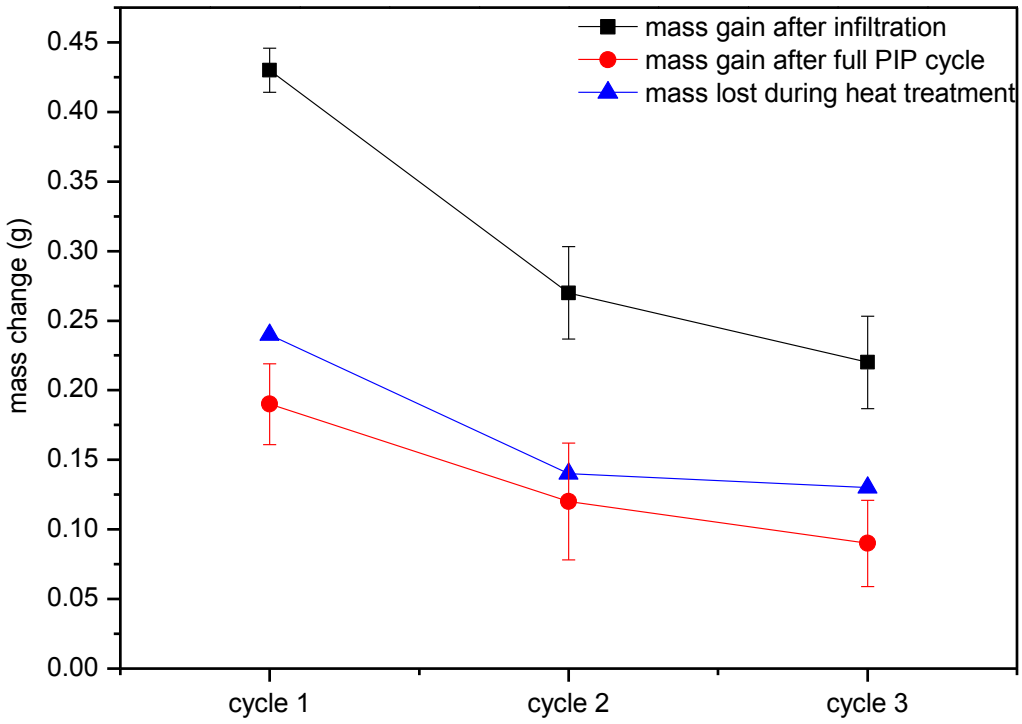

Figure 36: Graphs of the mass changes at each cycle stage after infiltration with resin, after heat treatment, and after the overall PIP cycle.

This difference has a direct correlation with the developed porosity of the composite as with regards to the number of PIP cycles effected. The loss of mass is attributed to

the loss of volatile molecules from the resin during heat treatment. When the volatiles decompose from the resin matrix, they leave pores in the structure.

Table 13 shows how the pore volume in the composite decreased from the first PIP cycle to the second cycle. The change in porosity between the second and the third cycles was marginal and this signified that at the third cycle the maximum serviceable infiltration and pyrolysis efficiency had been attained in the composite.

Table 13: Resultant pore volume, average pore diameters and density (all determined by MIP) of C_f/C composite after successive PIP cycles.

PIP Cycles	1	2	3
Pore Volume (%)	30%	22%	21%
Average pore diameter (μm)	0.076	0.056	0.044
Density (g/cm^3)	1.51	1.53	1.54

4.2.5 Macropores Size Distribution

Information on the macropores in the C_f/C composite was gathered from the MIP results, and information about the micropores was gathered from the BET results. The average pore diameters for the C_f/C composites, obtained from MIP, are presented in Table 13.

The differential plots in Figure 37 are descriptive as regards the pore size distribution in the composites. The differential plots give an indication of the distribution of pores in transitional aspects – from the micropores, to the mesopores and to the macropores. The pore sizes were qualified according to the International Union of Pure and Applied Chemistry (IUPAC) standard (Aligizaki, 2005):

Micropores: <2nm
Mesopores: 2nm – 50nm
Macropores: >50nm

The plots show that there is a significant number of pores falling within the -2.0 – -2.5 logD μm and the 0.5 – 1.5 logD μm size ranges. The pores with a size range of -2.0 – -2.5 logD μm fall under the mesopores category as this translates to 10 – 15nm. On the

other hand, the pores with a size range of 0.5 – 1.5 logD μm fall under the macropores category as their size range translates to 3.2 – 31.6μm.

The distinct peak at about 2.0 logD μm is uncharacteristic of the usually distinctly sharp peak in differential curves which represents the critical pore size (Aligizaki, 2005). In the present case, the said peak actually represents some few anomalous cavities in the C_f/C composite. These cavities were treated as defects in the composite structure.

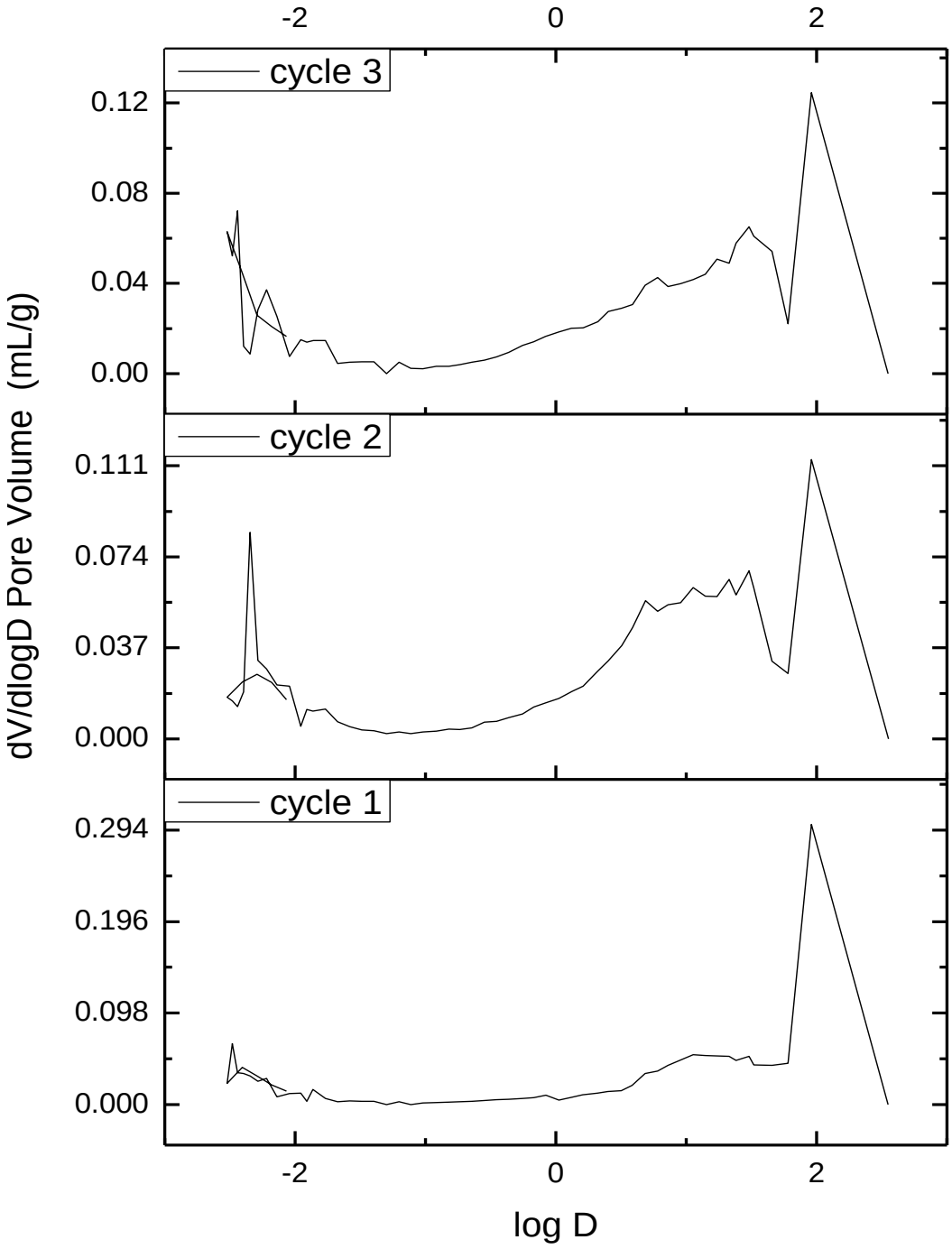

Figure 37: Differential Curves of volume of mercury intruded with respect to the pore diameter for the C_f/C composites at different PIP cycles.

It was observed, from the micrographs, that the micropores occurred as pores within other pores, particularly within the macropores. Here the macropores possessed less depth than the micropores. The debris shown in Figure 38 must have resulted from the conchoidal fracture of the matrix during heat treatment.

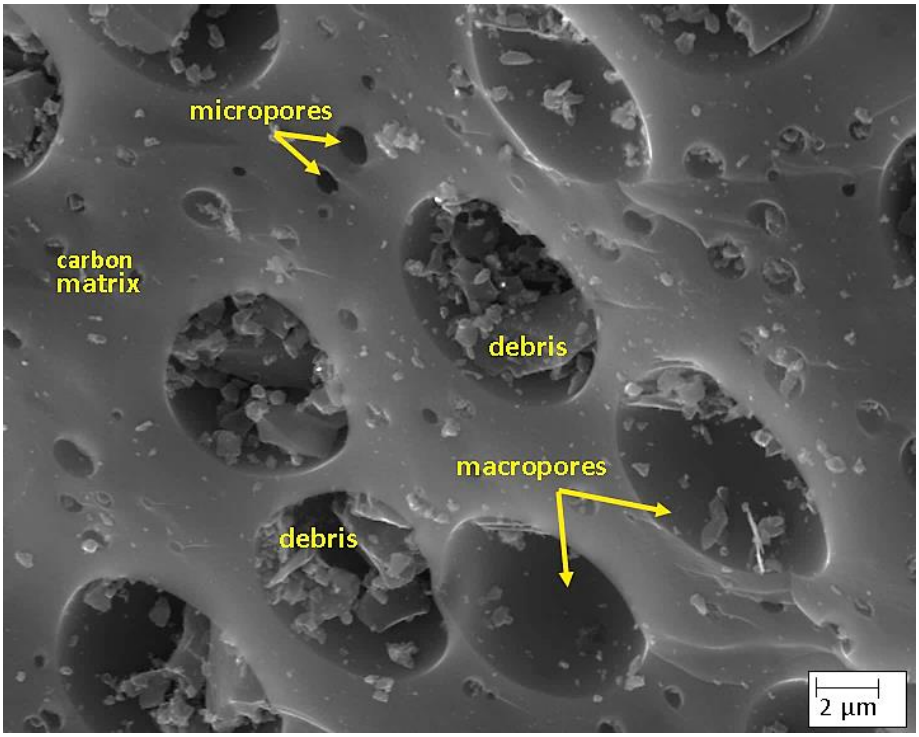

Figure 38: Micrograph showing the diversity of pore sizes in the carbon matrix.

The ease of access of pores and their depth to an infiltrant was reflected by the pore permeability and pore tortuosity parameters (Figure 39). Permeability and pore tortuosity values were secondary data from the MIP results. Tortuosity results gave an idea of the connectivity in the pores – by definition tortuosity is a comparison of the direct path across the depth of a porous body to the actual path a permeating fluid would take. Tortuosity reflected on the availability of the discussed pores to permeation.

Tortuosity is defined as follows (Ahmad *et al.*, 2005):

$$\tau = \left(\frac{L}{L_e}\right)^2 \qquad (26)$$

Where L_e = mean of the actual flow path of fluid, and L = shortest length along the major flow axis.

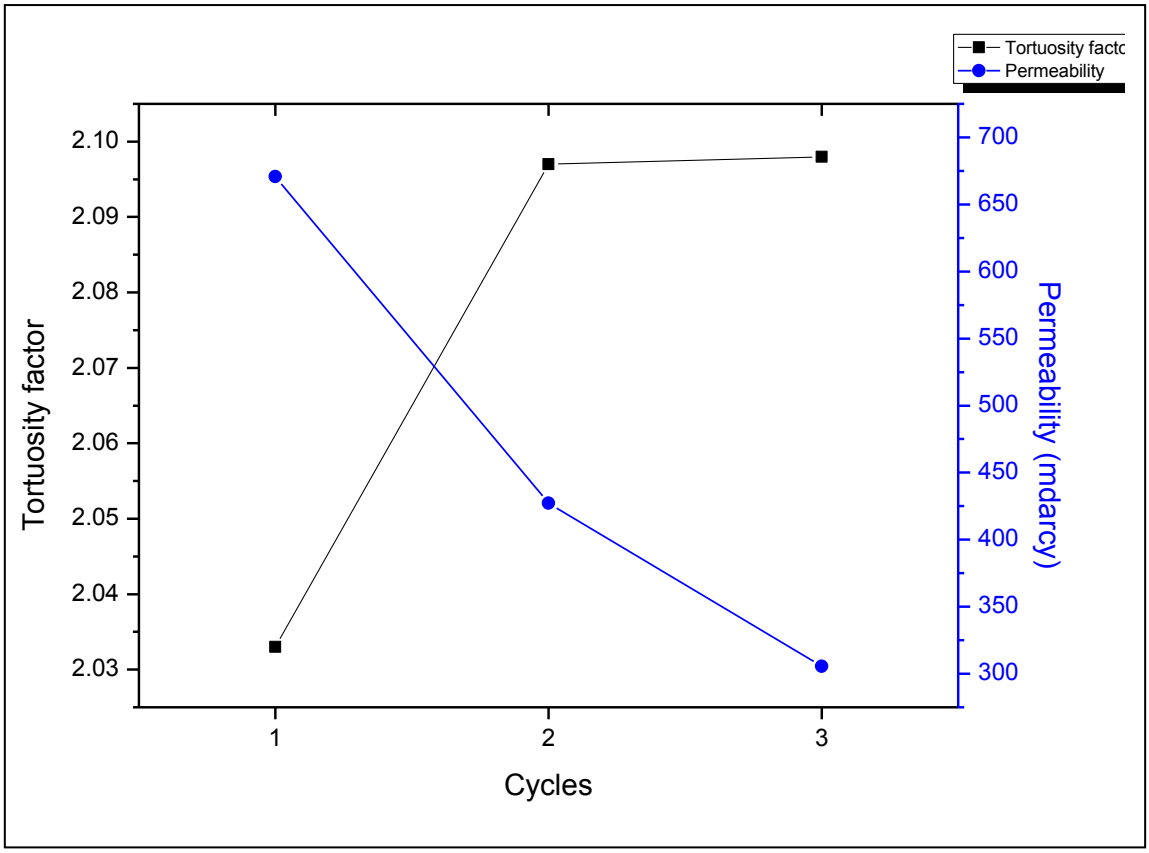

Figure 39: The change in the tortuosity factor and permeability in the C_f/C composites against the number of PIP cycles effected on the same (both graphs determined by MIP).

The permeability in the C_f/C composites decreased, first steeply to the second cycle of PIP, and then the rate of change decreased by the third cycle of PIP. The tortuosity increased significantly from the first PIP cycle to the second cycle, and thereafter it nearly levelled off. A value of tortuosity greater than 2 means that the ratio of L/L_e ratio (from Equation 26) is in the range of approximately 1.42 and 1.5. The tortuosity value was deemed sufficient to point to a composite with an acceptable level of pore network complexity for the subsequent alloy infiltration process. A larger value of tortuosity otherwise compromises the permeability of the composite and the efficiency in the PIP cycles would be less.

4.2.6 Micropores Size Distribution

The most peculiar feature of the plot in Figure 40 is that the BET hysteresis loop remained open after completing the desorption process. This is evidence that the

physisorption process occurred irreversibly. This is a common occurrence especially when dealing with mesoporous materials (Aligizaki, 2005).

The isotherm linear plots of volume of N_2 adsorbed per gram of sample against the relative pressure (P/P_o) for both cycles of PIP show very small and elusive knee bend between 0.1 and 0.2 P/P_o. The lack of a clearly defined knee bend is an attribute of a material which is predominantly macroporous, hence the occurrence of weak adsorption.

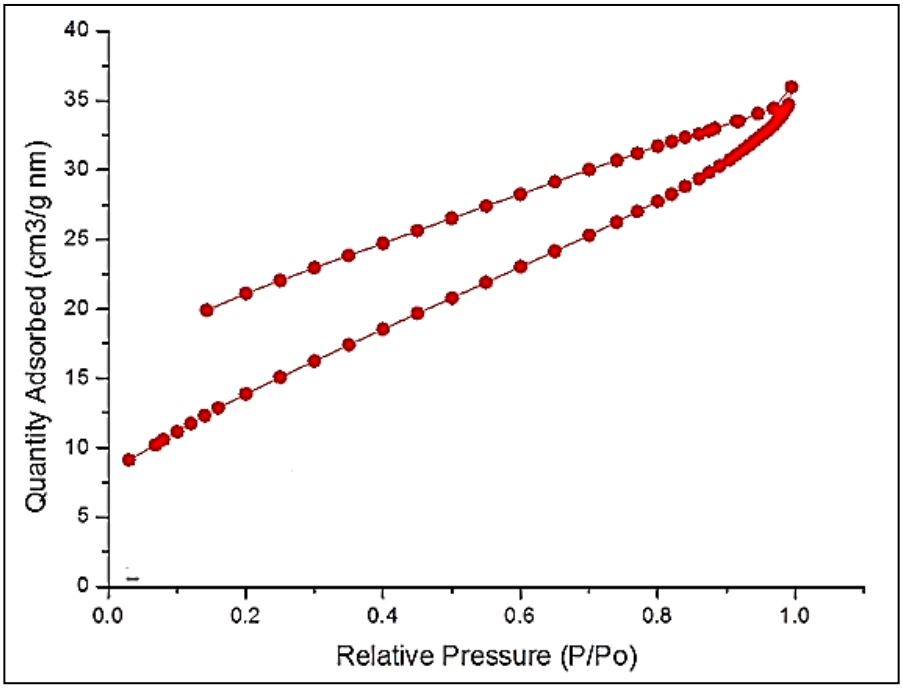

Figure 40: Hysteresis graph of the volume of N_2 adsorbed and desorbed against pressure applied during BET porosimetry.

Figure 41 is a cross-cutting curve which spans across the pore sizes in the C_f/C composite. The nature of the adsorption curve obtained showed the existence of macropores in the specimens.

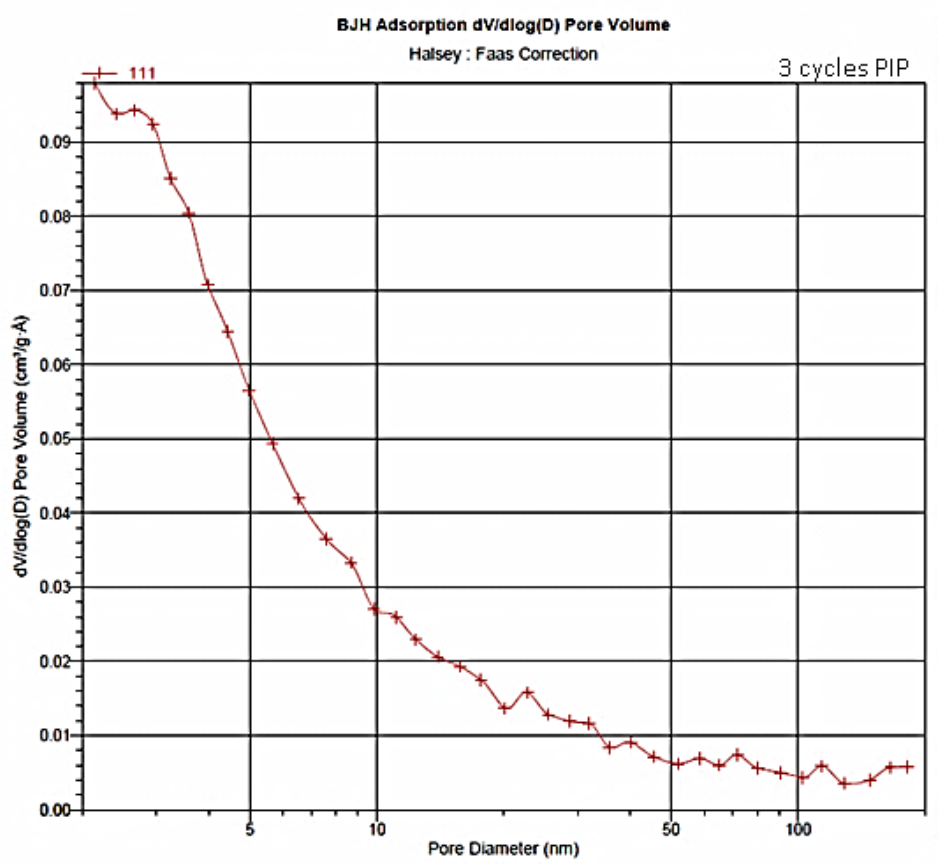

Figure 41: Graph of the differential volume of adsorbed N_2 against the pore diameter from BET porosimetry in the C_f/C composite after 3 cycles of PIP.

4.2.7 XRD and Raman Patterns

All the spectra of the 3 samples show one major peak at about 29° and 30° on the 2θ axis and a very small peak between 51° and 52°. Figure 42 shows how the intensity of the 30° peak increased with an increase in the number of PIP cycles.

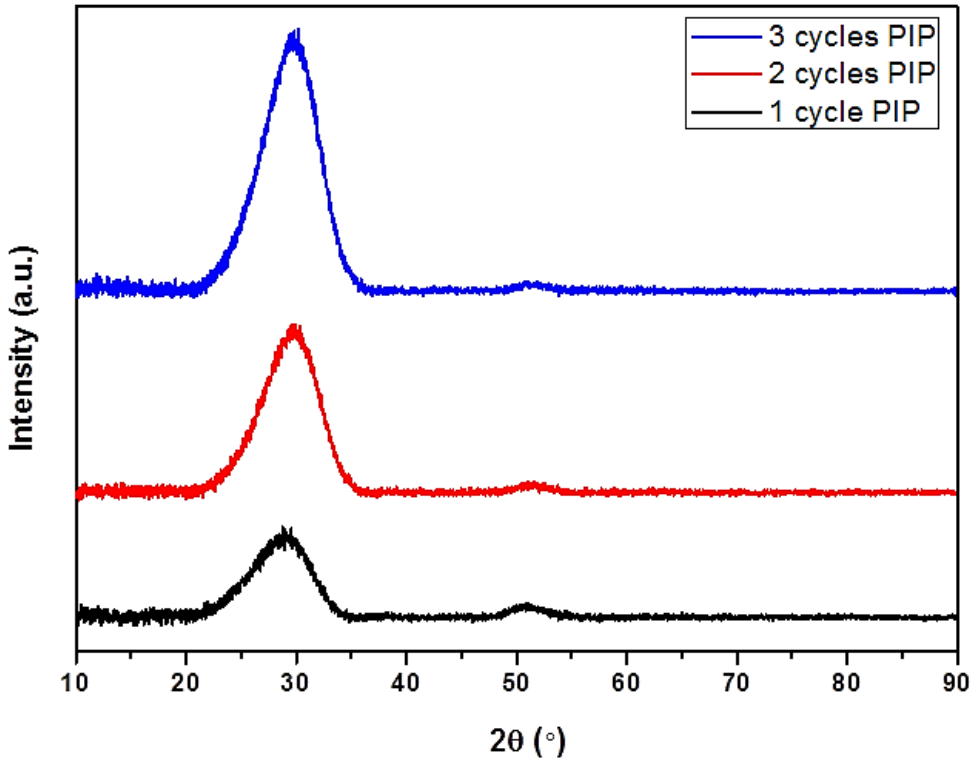

Figure 42: XRD spectra of C_f/C composites after each cycle of PIP.

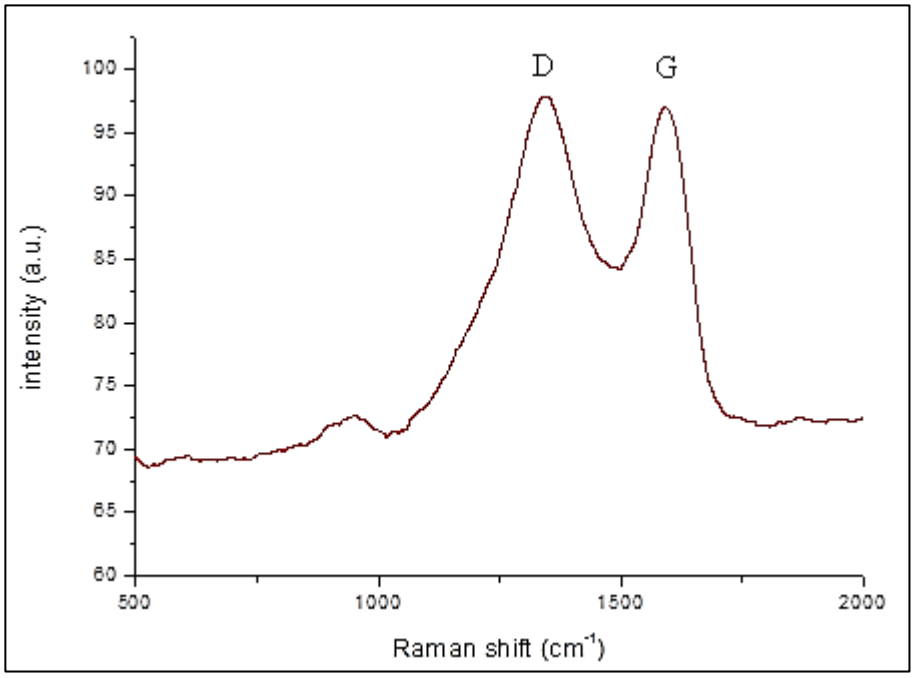

Figure 43: Raman spectroscopy pattern of the C_f/C which underwent 3 cycles of PIP.

Figure 43 shows two peaks with a Raman shift around 1360 and 1600cm^{-1} and these peaks coincide with the well-known Raman G and D bands respectively. The peaks are wide and have approximately the same intensity.

The extent of disorder in the sample can be estimated from the linear relationship between I_D/I_G and the graphite crystallite size parameter (L_a) proposed by Tuinstra & Koenig (1970) given as (Equation 27):

$$\frac{I_D}{I_G} = \frac{C_\lambda}{L_a} \tag{27}$$

Where C_λ is a constant associated with the laser excitation energy.

Evaluation yielded I_D/I_G = 1.01. Here L_a approximates to 45.5, taking C_λ = 44$\dot{A}$ where λ = 514nm.

4.3 THE Si-Ti-Ta ALLOY

4.3.1 Powder Characterisation

The as-received powders of tantalum silicide ($TaSi_2$) and titanium silicide ($TiSi_2$) were analysed by SEM and XRD. The morphology micrographs (Figure 44) of the $TaSi_2$ powder revealed spherically shaped particles with significant agglomeration. A considerable percentage of the agglomerates are greater than 50µm, versus the nominal individual particle size of 1-5 µm. The spherical shape was advantageous in the flowability of the powder during milling. Milling, in the presence of a dispersant, was important in breaking-up these agglomerates, thus increasing the surface area of contact with the $TiSi_2$ powder during compaction. Figure 45 is the XRD spectrum of the $TaSi_2$ showing the perfect match of the phases in the as-received powders with that of pure $TaSi_2$.

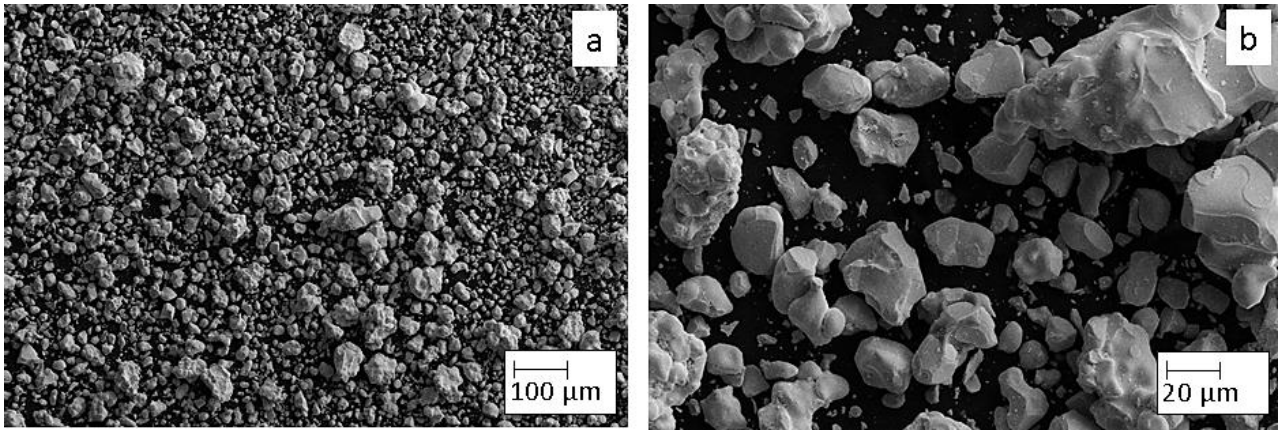

Figure 44: SE-SEM micrographs showing the morphology of loose as-received tantalum silicide ($TaSi_2$) powder at x200 magnification (a) and x1000 magnification (b).

On the other hand, the titanium silicide powder particles showed a high level of angularity. This shape is usually associated with abrasive materials. The micrographs in Figure 46 show a particle size distribution which is wide-ranging. This was due to the market availability of the powder. Furthermore, considering the oxidation proneness of titanium compounds, milling the particles to uniformity was avoided. Similarly to the $TaSi_2$ as-received powder, the X-ray diffractogram in Figure 47 shows an impeccable match of the phases in the as-received powder with that of pure $TiSi_2$. The peak showing at around 27º is isolated and hence cannot wholly constitute a different phase from that of $TiSi_2$.

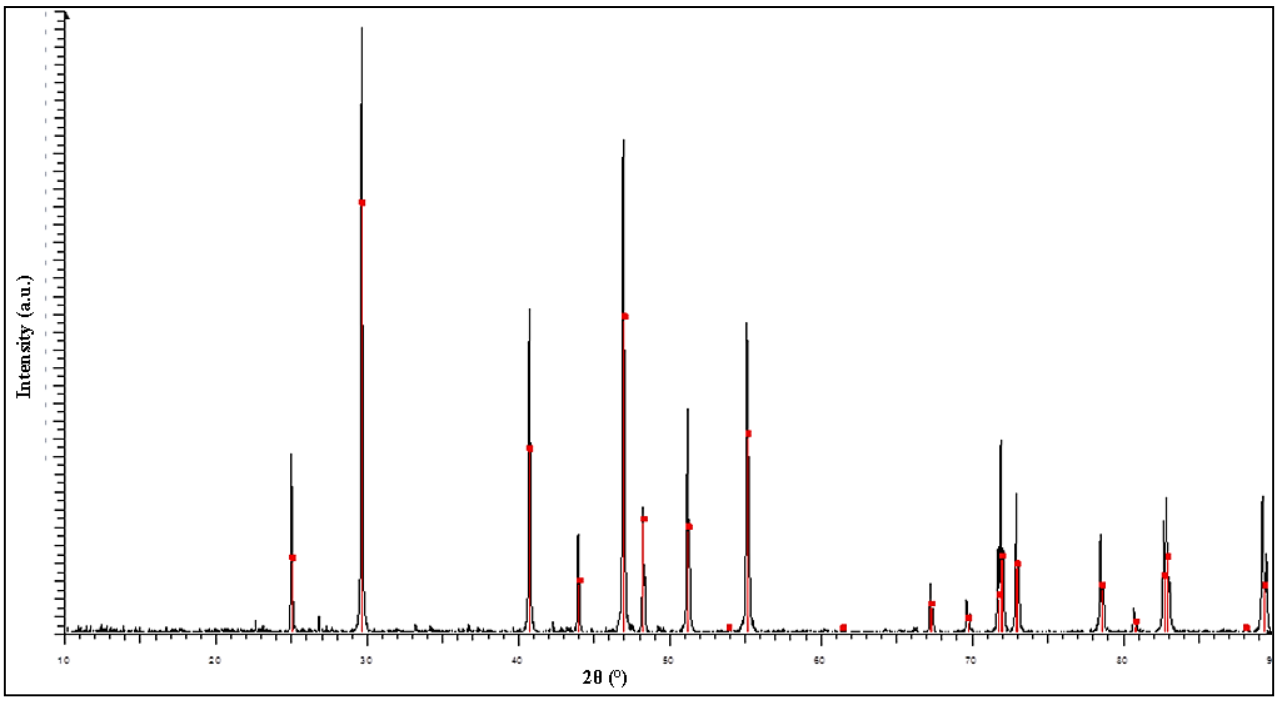

Figure 45: Diffractogram for tantalum silicide $TaSi_2$ powder. The red lines represent the template pattern for $TaSi_2$ from the EVA database.

Figure 48 shows a satisfactorily powder mix of $TaSi_2$ and $TiSi_2$. The micrograph show how most of the $TaSi_2$ particle clusters were broken up and dispersed during milling. The small-sized particles fitted well between the bigger particles interstices.

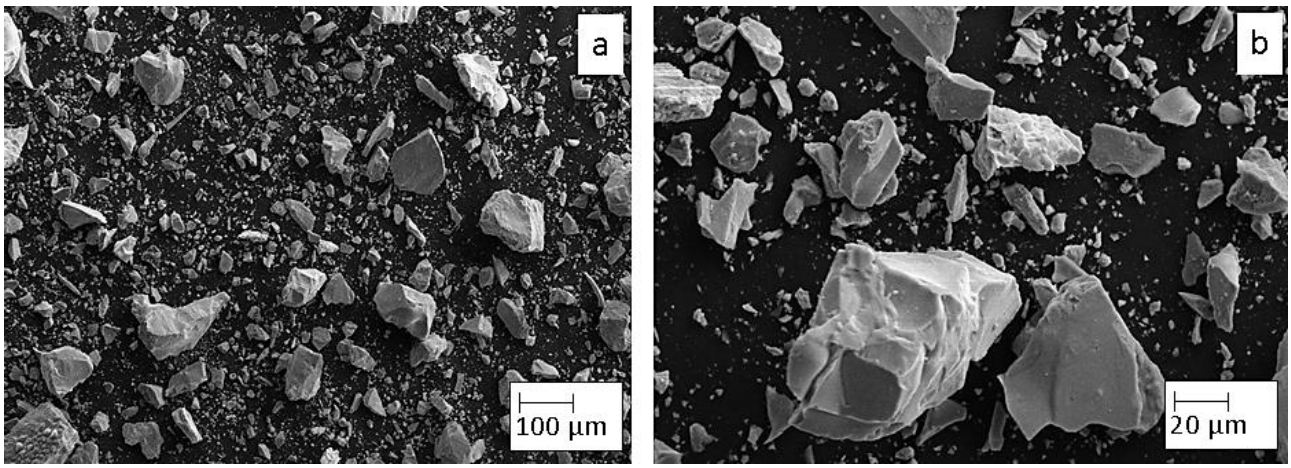

Figure 46: SE-SEM micrographs showing the morphology of loose as-received titanium silicide ($TiSi_2$) powder at x200 magnification (a) and x1000 magnification (b).

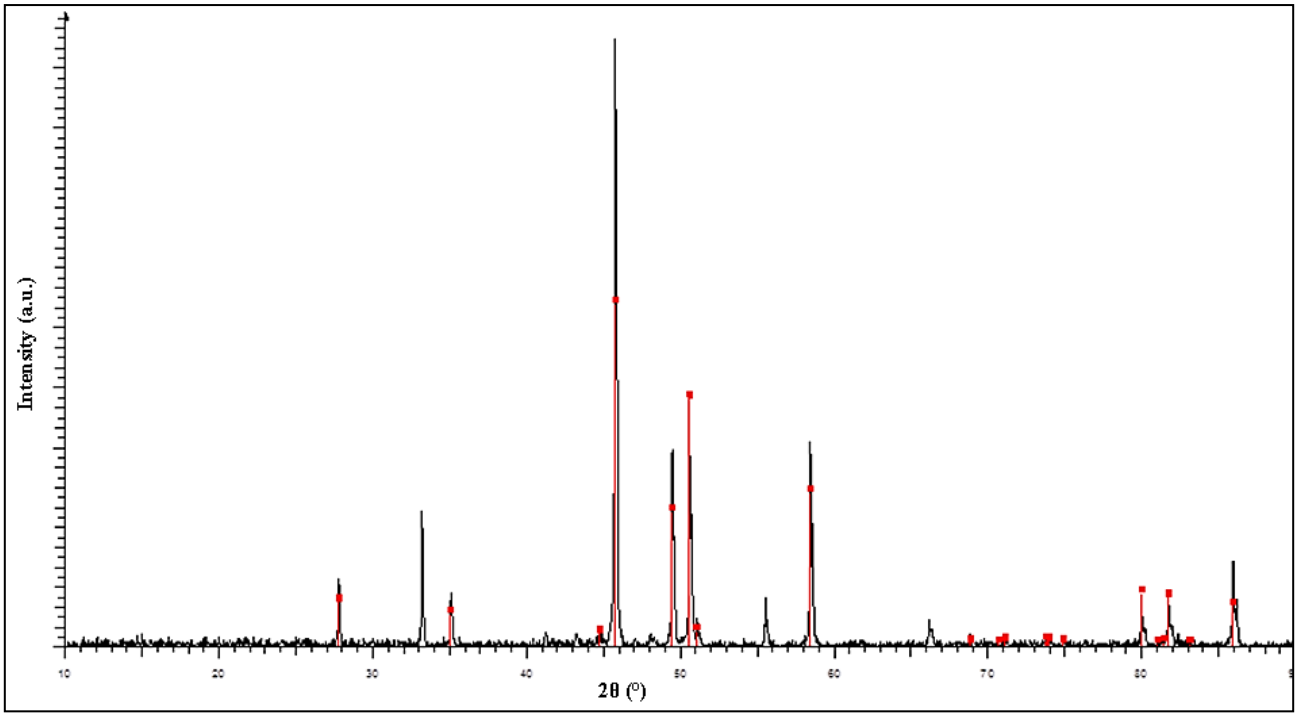

Figure 47: Diffractogram for loose titanium silicide ($TiSi_2$) powder. The red lines represent the template pattern for $TiSi_2$ from the EVA database.

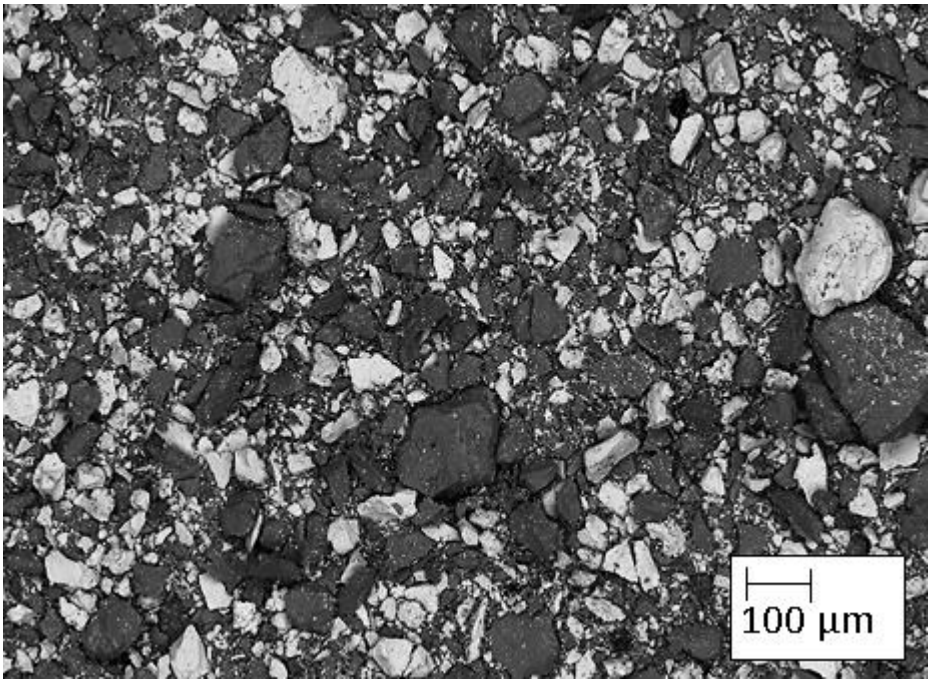

Figure 48: SEM micrographs for mixed loose titanium silicide ($TiSi_2$) and tantalum silicide ($TaSi_2$) powders. The white phase represents $TaSi_2$ and the black phase represents $TiSi_2$.

4.3.2 Si-Ti-Ta Alloy Characterization

An overview of the microstructure of the alloy is given in Figure 49.

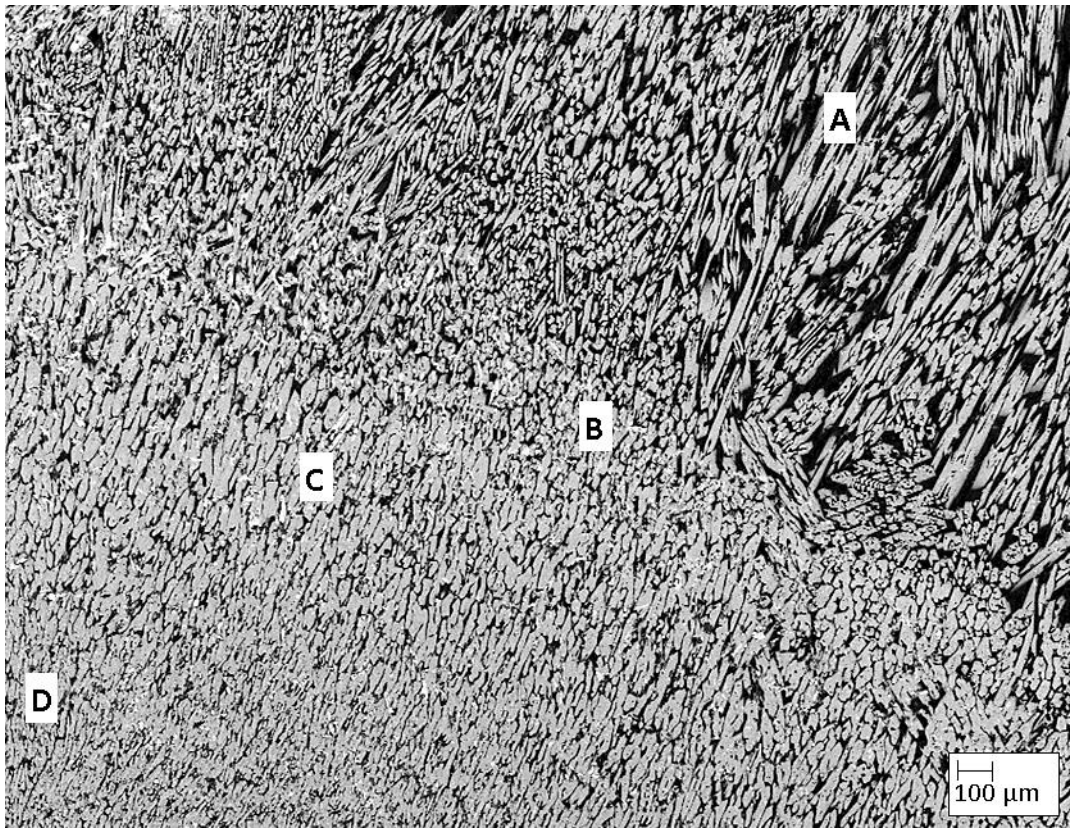

Figure 49: Backscattered micrograph of the Si-Ti-Ta alloy showing an overview of the microstructure. Regions A,B,C and D represent the variations in the shapes of the alloy grains.

A: Represents the central region of the ingot. The microstructure consists of acicular shaped grains with lengths approaching 100µm, arranged in a basket weave-like manner. The grains in the centre have an aspect ratio of >3, as shown in Figure 50 (A) and (C). B is the transition region between the region A and region B microstructure. The grains are almost equiaxed and cusped in shape. The grains in region C have no clear transverse demarcations, although the elongated shape of the grains is obvious. D region is located at the peripheries of the ingot and the grains have an element of arborescence like that of the desert cactus – grains that look like they were growing and branching from one another.

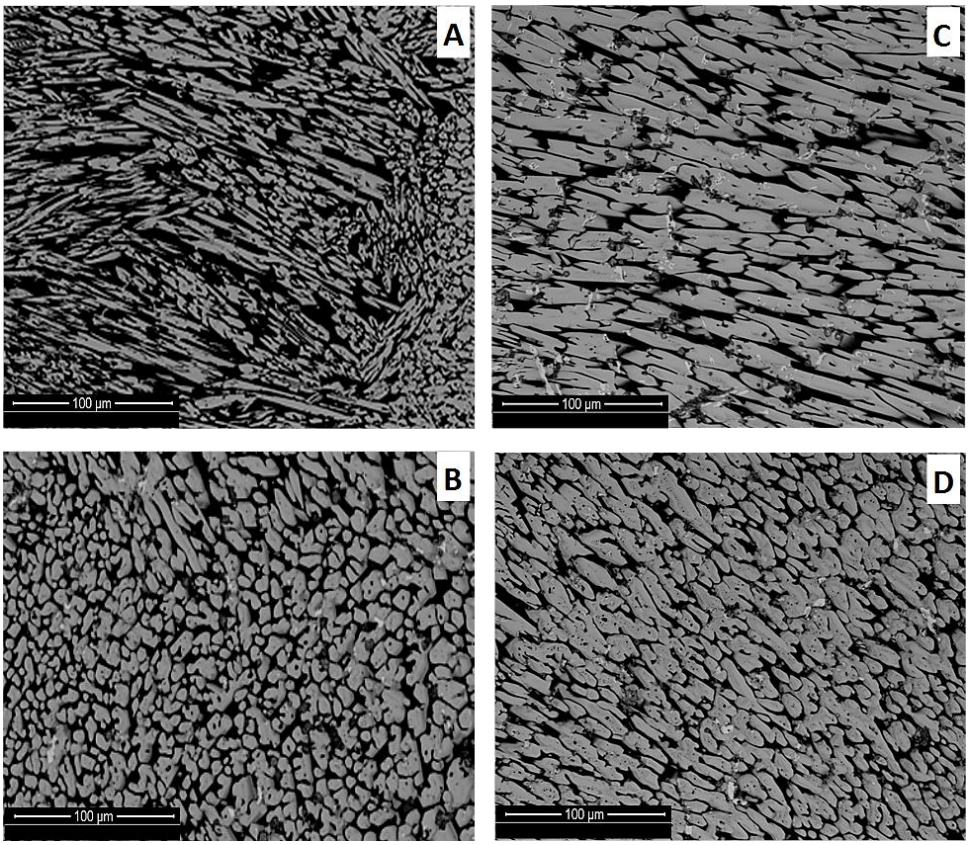

Figure 50: Elaborated micrographs of the four regions shown in Figure 55.

A higher magnification micrograph (Figure 51), together with EDS studies, gave better detail on the distribution of phases in the alloy.

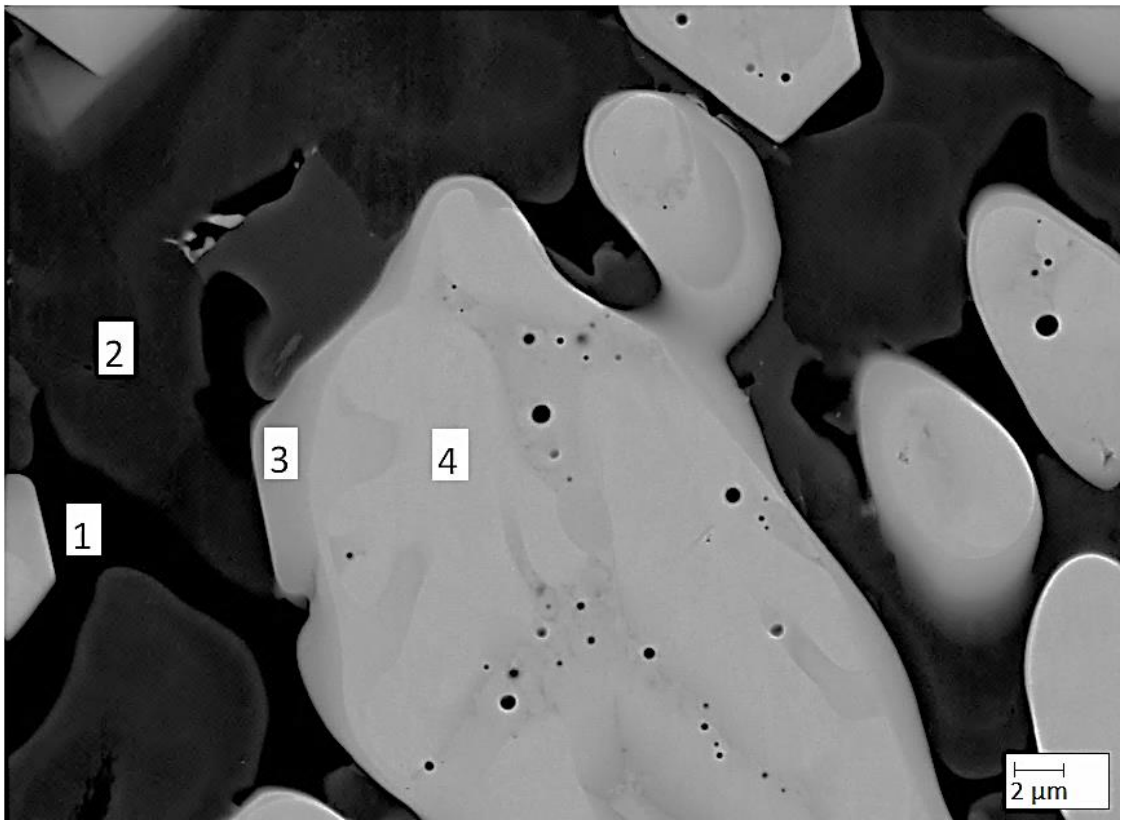

Figure 51: High magnification SEM image showing the different phases in a polished cross-section of the Si-Ti-Ta alloy.

Table 14: EDS results obtained from the positions 1-4 of the SEM image of the Si-Ti-Ta alloy shown in Figure 51.

Position on micrograph	Atomic %		
	Si	Ti	Ta
1	100.0	0	0
2	75.6	24.2	0.2
3	69.6	15.3	15.1
4	69.5	8.0	22.5

The EDS results (Table 14) suggested the following phases: free silicon on position 1 and (TaTi)Si_2 solid solution on position 3. It was not entirely achievable to conclusively deduce the identities of the phases on positions 2 and 4, but they could possibly be containing free silicon and 5-3 silicides (either Ti_5Si_3 or, or both).

The XRD pattern of the Si-Ti-Ta alloy is shown in Figure 52. The XRD analysis of the alloy revealed the presence of $TaSi_2$, $TiSi_2$, Ti_5Si_3, Ta_5Si_3 and free silicon.

The $TaSi_2$ from the present investigation, which is typified by hexagonal lattice of $CrSi_2$ (C40), had the lattice parameters of $a = b = 4.778$Å and $c = 6.565$Å. There was a slight shift of the *a* and *b* parameters from the typical $a = b = 4.783$Å (Goldschmidt, 2013: 336), as also shown in the XRD pattern by a shift of the $TaSi_2$ peaks to the left by about 0.5°. This signifies a lattice strain by expansion owing to the insertion of $TiSi_2$ into the crystal structure by $TiSi_2$.

The presence of Ti_5Si_3 was positively identified in addition to that of the disilicide ($TiSi_2$). The lattice parameters of the tetragonal crystals of Ti_5Si_3 were $a = b = 7.448$Å and $c = 5.114$Å. Similarly, Ta_5Si_3 was positively identified and had the following lattice parameters: $a = b = 9.880$Å and $c = 5.060$Å. Thus the Ta_5Si_3 has larger unit cells than Ti_5Si_3.

Free Si islands (black phase in Figure 51) were seen to occur with attachments to the bright phase grain boundaries. This phase of Si islands, which was confirmed by EDS, had peaks closely associated with the $TaSi_2$ peaks.

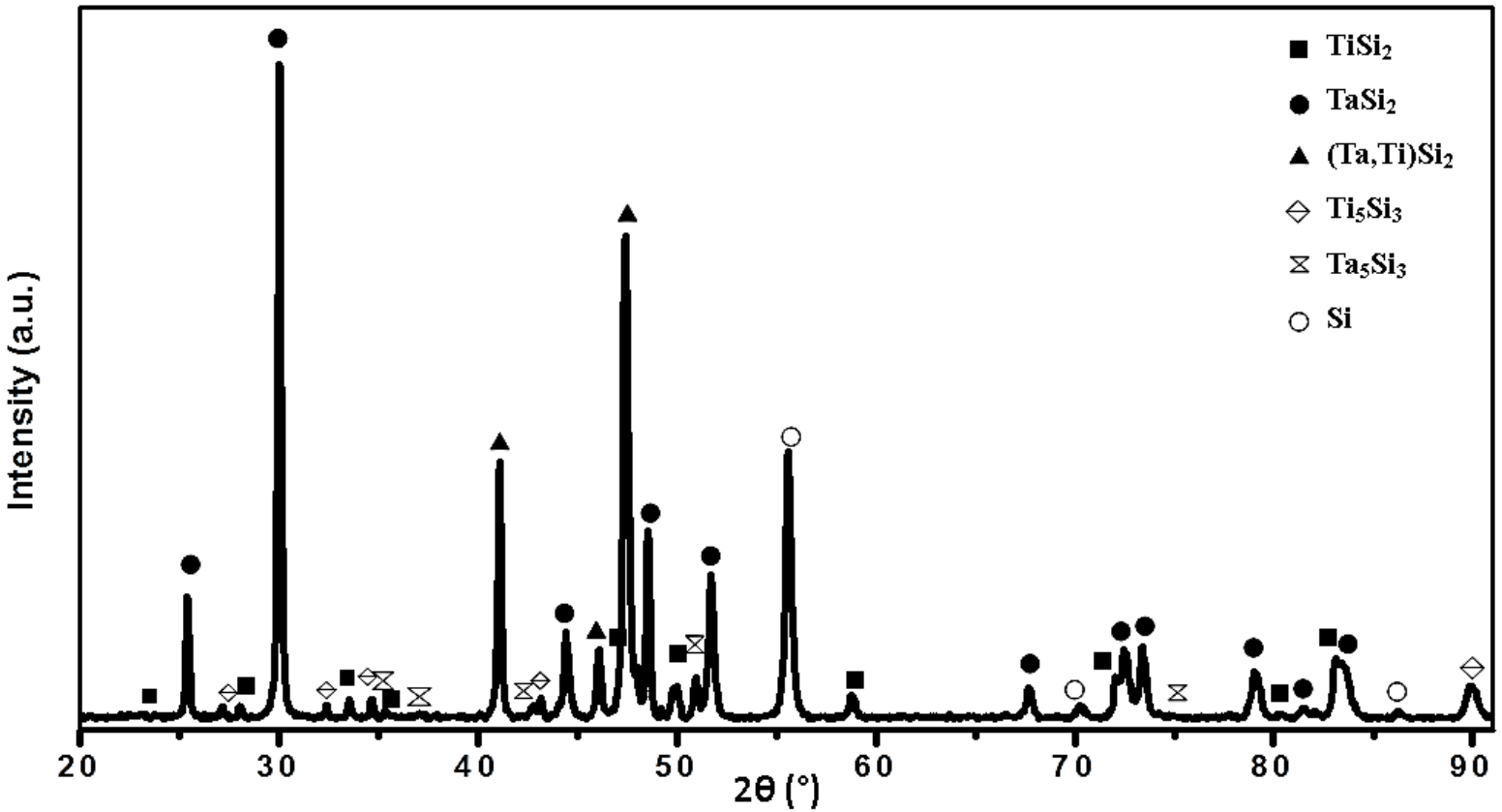

Figure 52: Diffractogram for alloyed $TaSi_2$-$TiSi_2$ powders.

4.4 C/Si-Ti-Ta REACTION COUPLES

From the C/Si-Ti-Ta reaction couples tested at different temperatures (1500°C, 1600°C, 1700°C and 1800°C) for 30 minutes, the resulting interface regions are shown in Figure 53.

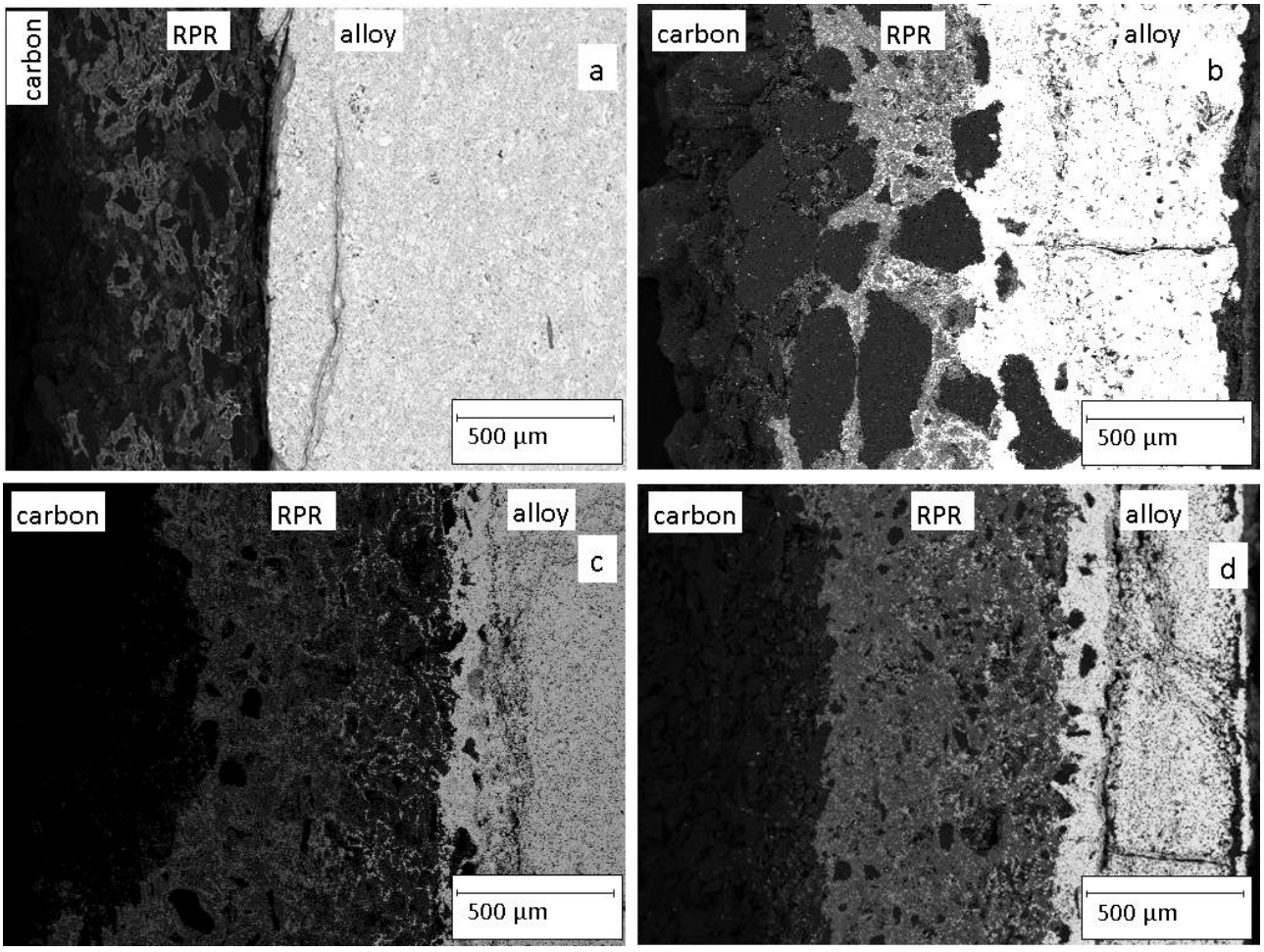

Figure 53: BSED-SEM micrographs of cross-sections of the C/Si-Ti-Ta diffusion-reaction couples prepared by contacting carbon powder and Si-Ti-Ta alloy by spark plasma sintering in vacuum at 1500°C (a), 1600°C(b), 1700°C(c) and 1800°C(d) for 30 minutes.

4.4.1 Couple Heat Treated at 1500°C

It can be seen in the 1500°C couple (Figure 54) that limited melting occurred, whereby a silicon-rich phase melted and infiltrated across the C/alloy interface to fill the interstices between the carbon particles and reacted to form SiC. It is known that the melting in the alloy was very limited, considering the evident solid integrity of the block of alloy (Figure 53). The physical disparity between the reaction zone and the alloy is evidence that there was very limited melting in the system.

The SEM-EDS maps in Figure 54 give the idea that at 1500°C, Ti and Si species transport the most in the melt, probably in the form of $TiSi_2$, before the $(Ta,Ti)Si_2$ melt. Ta exists in minute quantities in the reaction products region (RPR). Even the backscattered micrograph in Figure 54 shows a light grey phase (predominantly Ti) versus a white phase (predominantly Ta) in the RPR evident in the other micrographs of the couples heat treated at 1600°C, 1700°C and 1800°C. The very minute quantity of Ta in the products region confirms this.

Furthermore, the carbon particles are significantly intact, giving the idea that carbon did not react significantly, and the formation of carbides of silicon and the transition metals was limited. A definite band consisting predominantly of Ta, Ti, and C is formed at the reaction zone/alloy interface. In this band carbon is found in very minute quantities – also confirmed by EDS values obtained along the band – however. As such, it can be assumed that this band is made up of minute quantities of (Ta,Ti)C formed from the $(Ta,Ti)Si_2$ solid solution.

4.4.2 Couples Heat Treated at 1600°C - 1800°C

These three couples prepared heat treated at 1600°C, 1700°C and 1800°C (Figure 55 - Figure 57) all show the presence of liquid phases in the alloy.

Couple heat treated at 1600°C (Figure 55): A markedly synchronized presence of both Ti and Ta in the products zone of the couple heat treated at 1600°C was observed. The coherent pattern formed by the Ta and Ti elements suggests the infiltration of the $(Ta,Ti)Si_2$ melt at this stage. As in the other EDS maps of the couples prepared at other

temperatures, Si dominates the product regions. The overall images give the idea that (Ti,Ta)C crystallises in the SiC matrix.

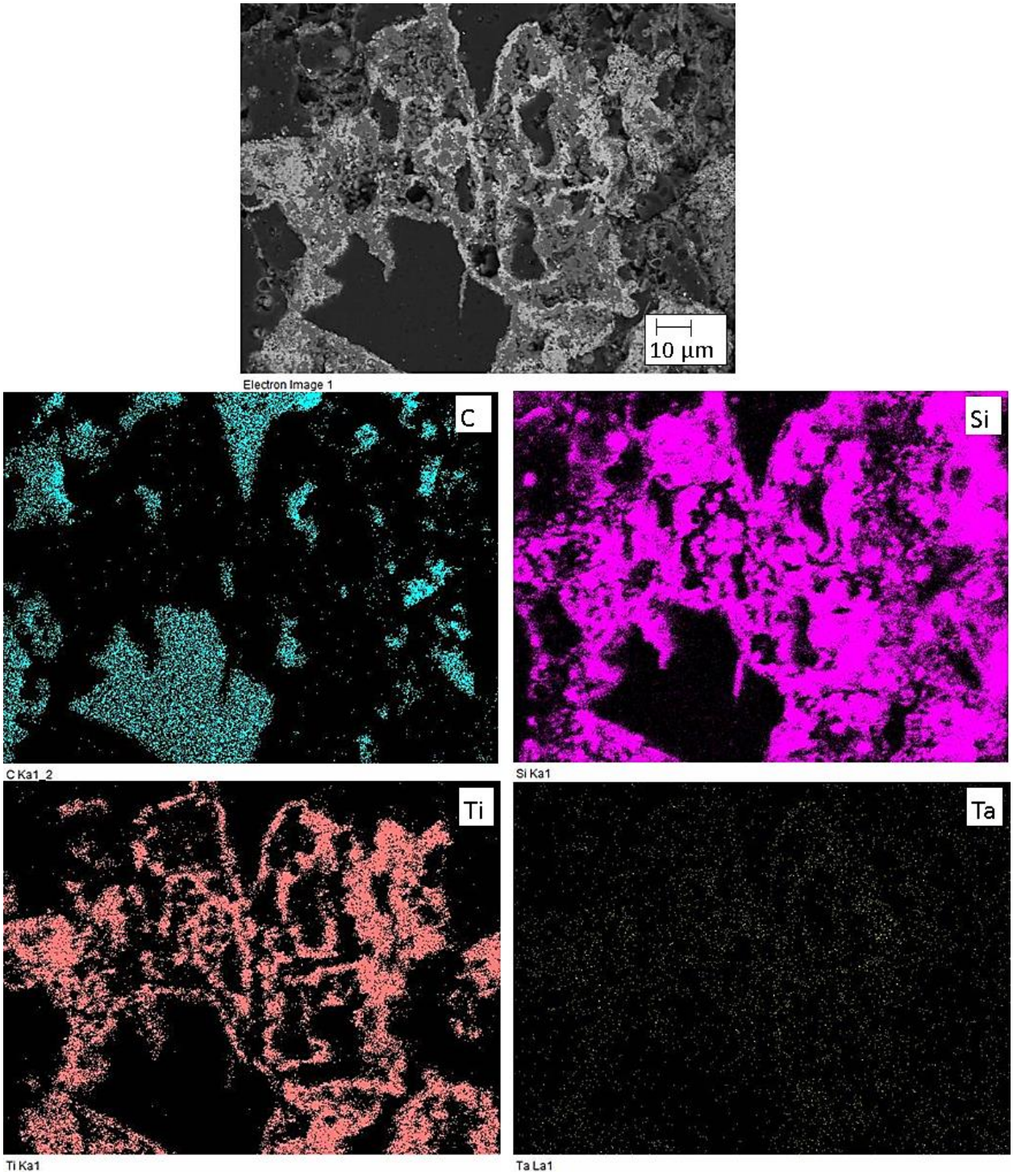

Figure 54: BSED-SEM micrograph and associated SEM-EDS maps of the cross-section of the C/Si-Ti-Ta diffusion-reaction couple prepared by spark plasma sintering at 1500°C for 30 minutes.

.

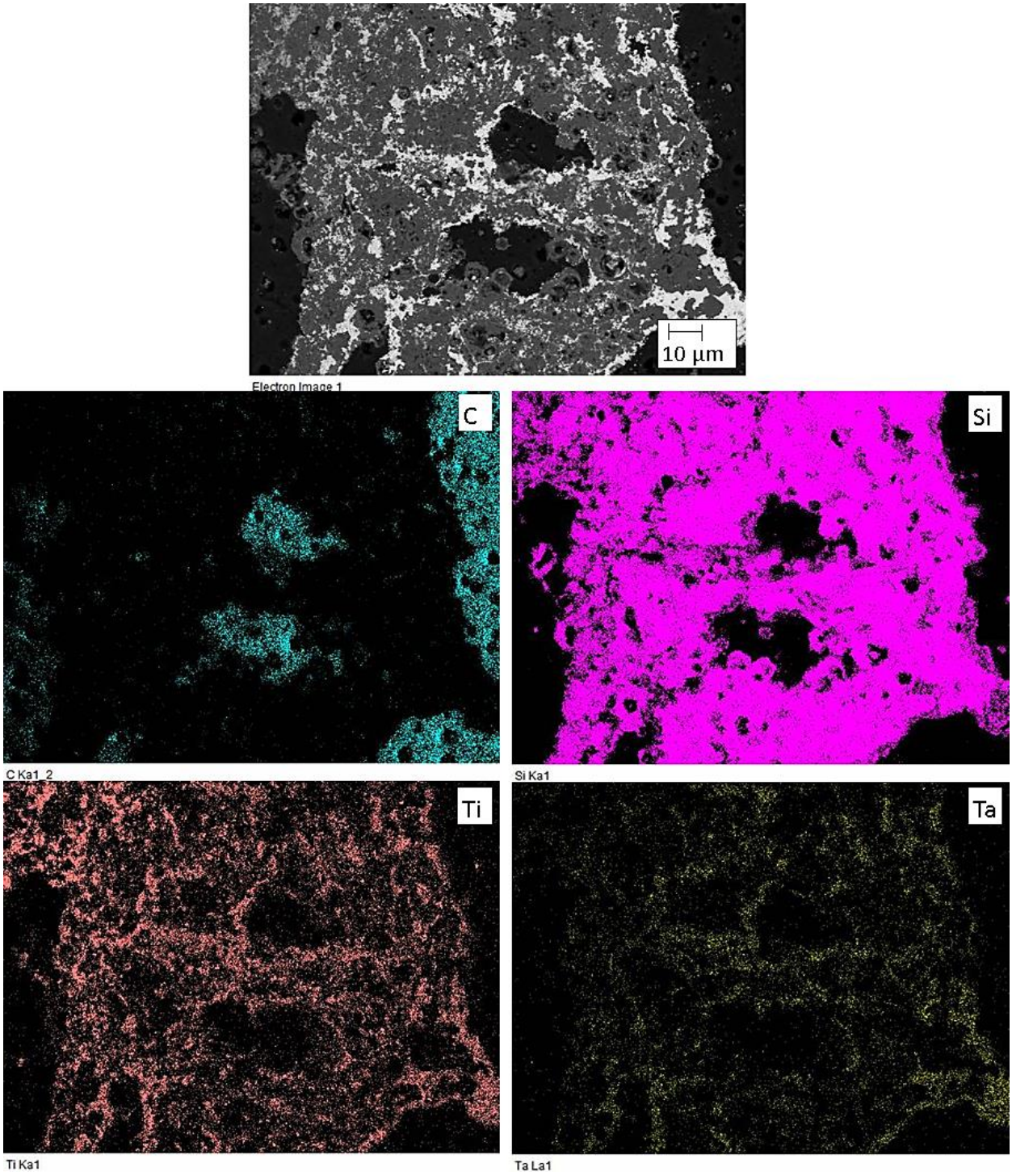

Figure 55: BSED-SEM micrograph and associated SEM-EDS maps of the cross-section of the C/Si-Ti-Ta diffusion-reaction couple prepared by spark plasma sintering at 1600°C for 30 minutes.

Couple heat treated at 1700°C (Figure 56): The couple is mainly characterized by the achievement of better homogeneity in the RPR than in the couple heat treated at 1500°C and 1600°C. The dissolution of carbon particles is very clear in the micrograph – evidence of the carbides-formation reactions.

The region at the C/RPR interface is dominated by TiC (light grey phase). The central RPR region is dominated by SiC (dark grey phase) and TaC co-occurring with TiC (white phase). This must be the (Ta,Ti)C solid solution embedded in SiC. On the other end of the RPR, at the alloy/RPR interface exist a Si-depleted region which is rich in Ta and Ti. Its existence can be considered to have been caused by Ta_5Si_3 and Ti_5Si_3 infiltrating as separate phases from the (Ta,Ti)Si_2 melt.

Couple heat treated at 1800°C (Figure 57): The elemental maps display impressive homogeneity of carbides formed both in the RPR and also in the former alloy region. Carbon shows to have diffused through the (Ta,Ti)C band, right into the alloy region (which was predominantly $TaSi_2$) to form carbides of Si, Ti, and Ta. This observation can be explained by the Arrhenius relations for the exponential increase in rates of diffusion and reaction with increase in temperature.

The homogeneity of the carbides formed [SiC, TaC, TiC and (Ta,Ti)C] increased with an increase in the RMI temperature.

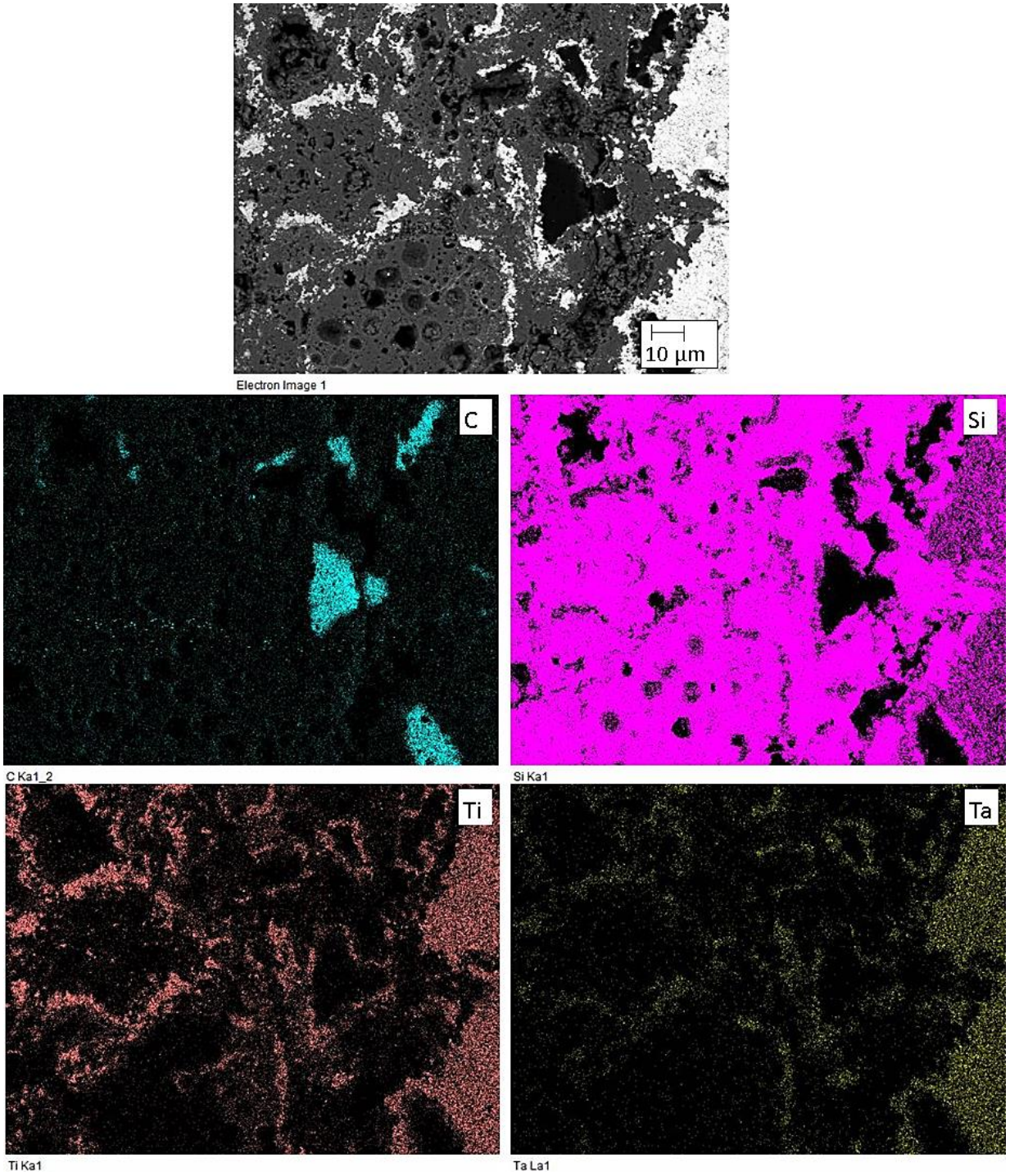

Figure 56: BSED-SEM micrograph and associated SEM-EDS maps of the cross-section of the C/Si-Ti-Ta diffusion-reaction couple prepared by spark plasma sintering at 1700°C for 30 minutes.

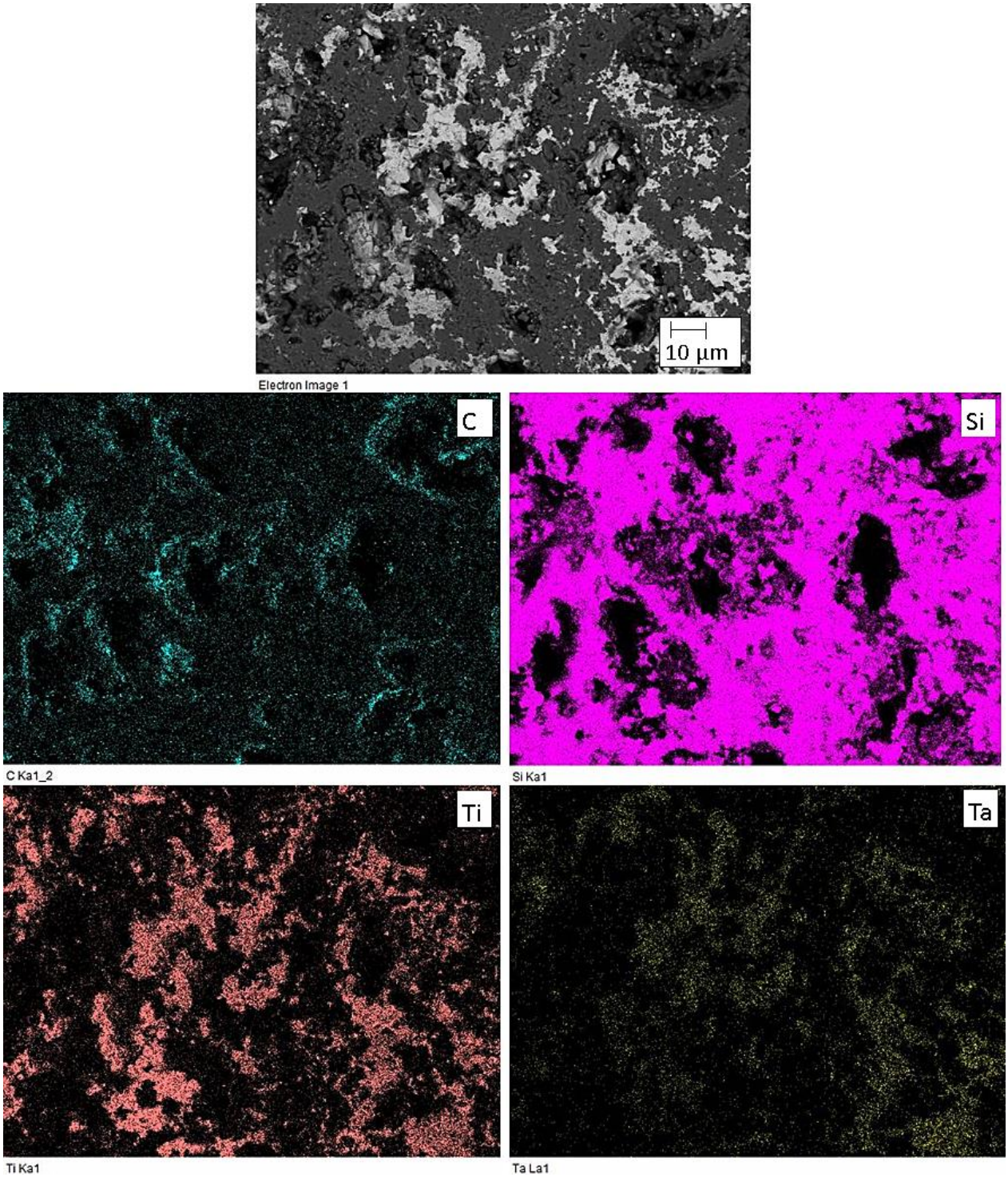

Figure 57: EDS maps of the cross-section of the C/Si-Ti-Ta diffusion-reaction couple prepared by spark plasma sintering at 1800°C for 30 minutes.

The homogeneity of the carbides formed [SiC, TaC, TiC and (Ta,Ti)C] increased with increase in the RMI temperature. This can be attributed primarily to the increase in the liquid fraction of the melt. The amount of the liquid fraction in the alloy during RMI was determined by the Lever Rule calculations using Equations 29 and 30. The phase diagram in Figure 58 was used.

$$x_L = \frac{(B_i - A_i)}{(C_i - A_i)} \tag{29}$$

$$x_S = \frac{(C_i - B_i)}{(C_i - A_i)} \tag{30}$$

Where: x_L and x_S represent the fraction of alloy in liquid phase and the fraction of alloy in solid phase, respectively.

A_i, B_i, C_i represent the at.% composition of Ti at the points A_i, B_i, C_i respectively.

Table 15 shows the results of the Lever Rule calculations on the 1600°C, 1700°C and 1800°C tie lines. Clearly, at 1600°C the amount of liquid in the alloy is slightly more than a third of the amount of solid therein. As is expected, the liquid fraction increases with an increase in temperature. As such, at 1800°C more than three-quarters of the alloy is in molten state.

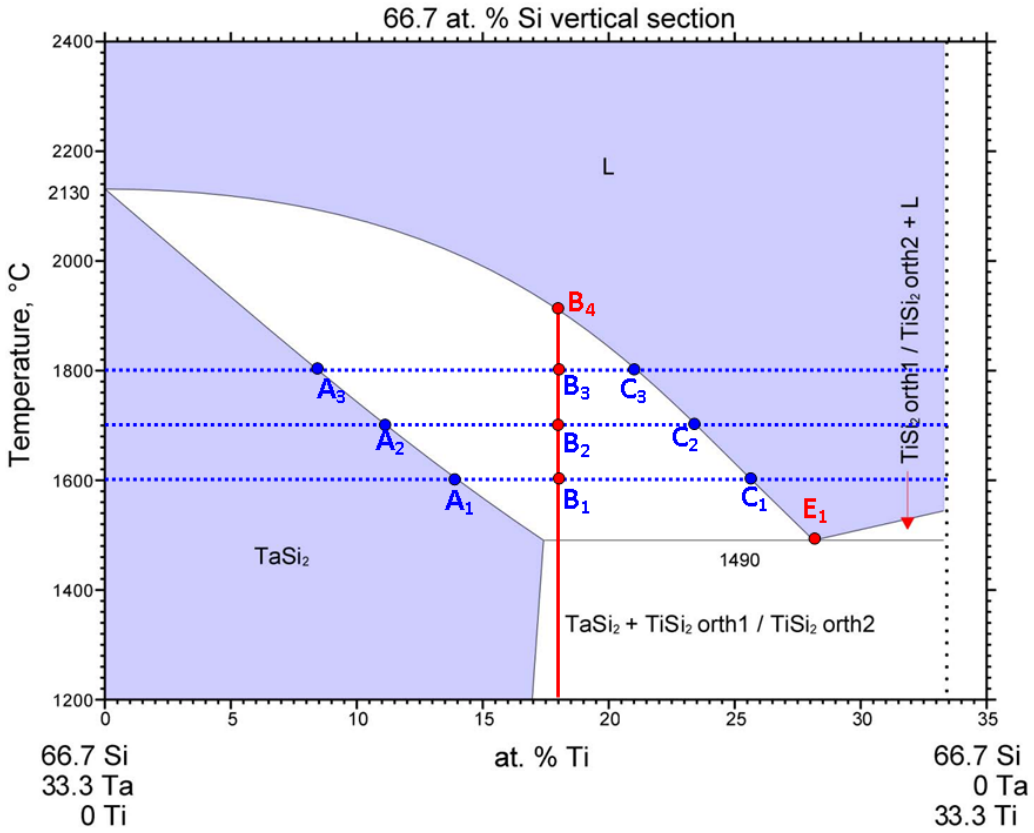

Figure 58: $TaSi_2$-$TiSi_2$ phase diagram (Kudielka, 1956) showing the tie lines at 1600°C - 1800°C.

It is known that the calculated ratios are valid only if the alloy melting occurs in equilibrium. It is practically possible at temperatures around and below 1700°C that the infiltration of a Si-Ti-rich melt will occur before equilibrium is achieved in the alloy. The consequence is that $TaSi_2$ will be left on top of the carbon preform.

Table 15: Phase weight fractions in the alloy at given RMI temperature as determined by the Lever Rule.

Temperature	at.% Ti at A*i*	at.% Ti at B*i*	at.% Ti at C*i*	wt.% Liquid Fraction	wt.% Solid Fraction
1600°C	8.5	17.9	21.0	35%	65%
1700°C	11.0	17.9	23.5	56%	44%
1800°C	14.0	17.9	25.5	76%	24%

4.5 THE C_f/C- SiC-TiC-TaC COMPOSITE

RMI of Si-Ti-Ta alloy into the C_f/C composite preforms at 1600°C, 1700°C and 1800°C gave the microstructures shown in Figure 59. From this figure, it is clear that a gradient matrix was realised at 1600°C where the formation of carbides [SiC and (Ta,Ti)C] is limited. At 1700°C carbides of tantalum and titanium which are seen as pronounced islands in the predominantly SiC matrix were formed. At 1800°C tantalum and titanium carbides have a more pronounced presence in the matrix. Here the carbon fibres in the composite seem to have fused with the matrix.

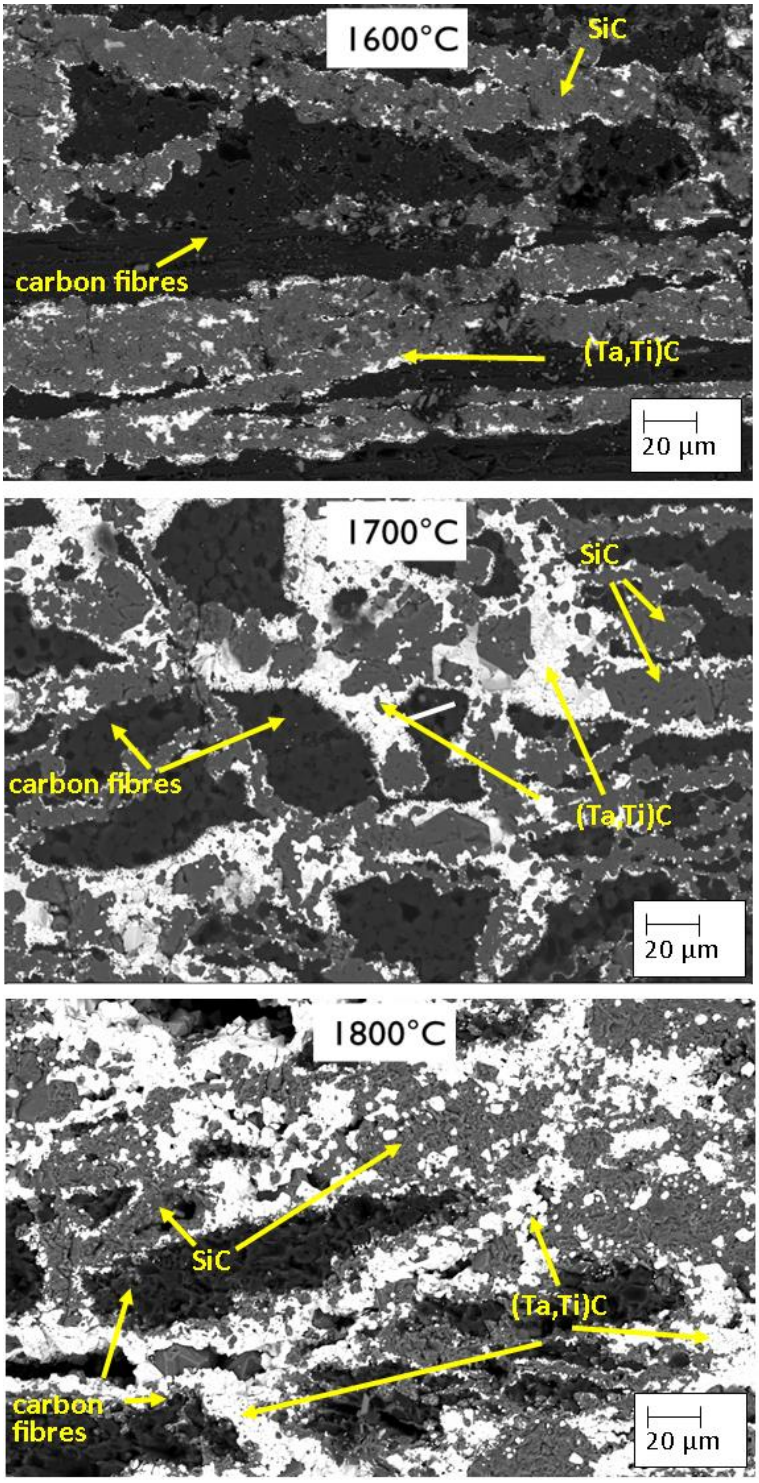

Figure 59: BSED-SEM micrographs of the cross-sections of C_f/C-SiC-TiC-TaC composites comparing the microstructures obtained by increasing the temperature for reactive-melt-infiltration by SPS for 30min. From top to bottom, the RMI temperature was 1600°C, 1700°C and 1800°C.

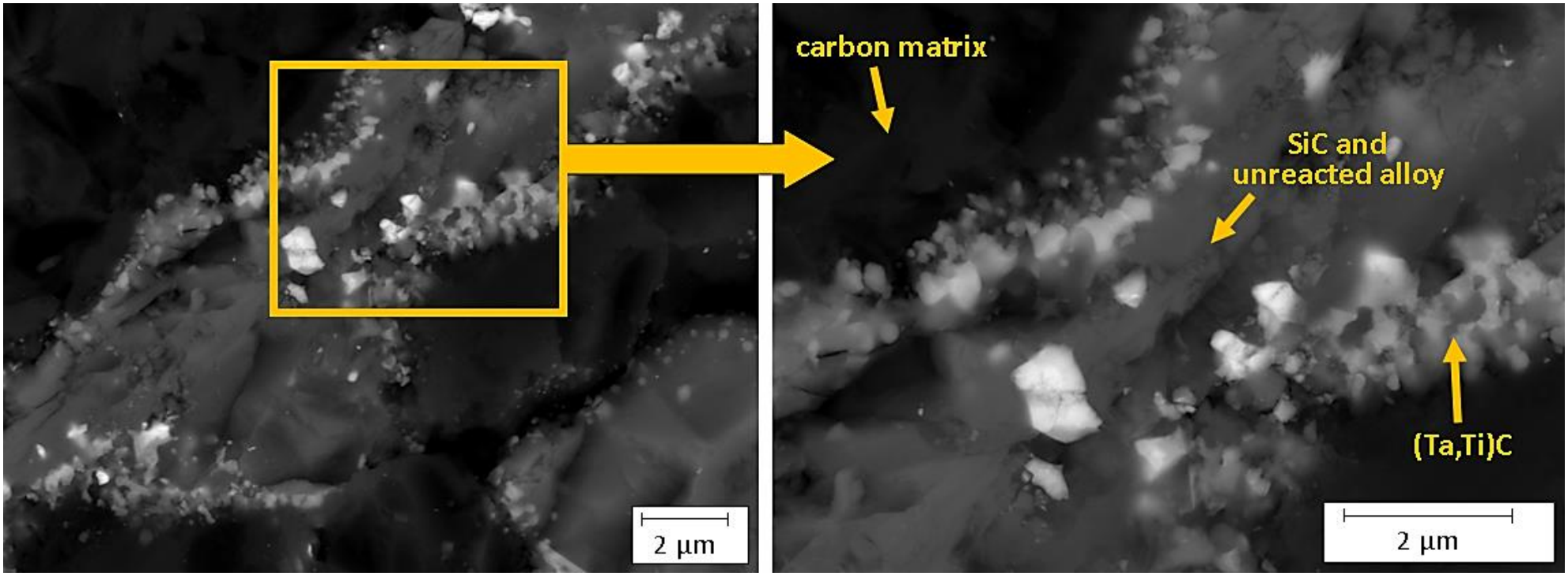

Figure 60: BSED-SEM images showing microstructures of the cross-section of the C_f/C-SiC-TiC-TaC composite prepared by RMI at 1600°C for 30 minutes using SPS.

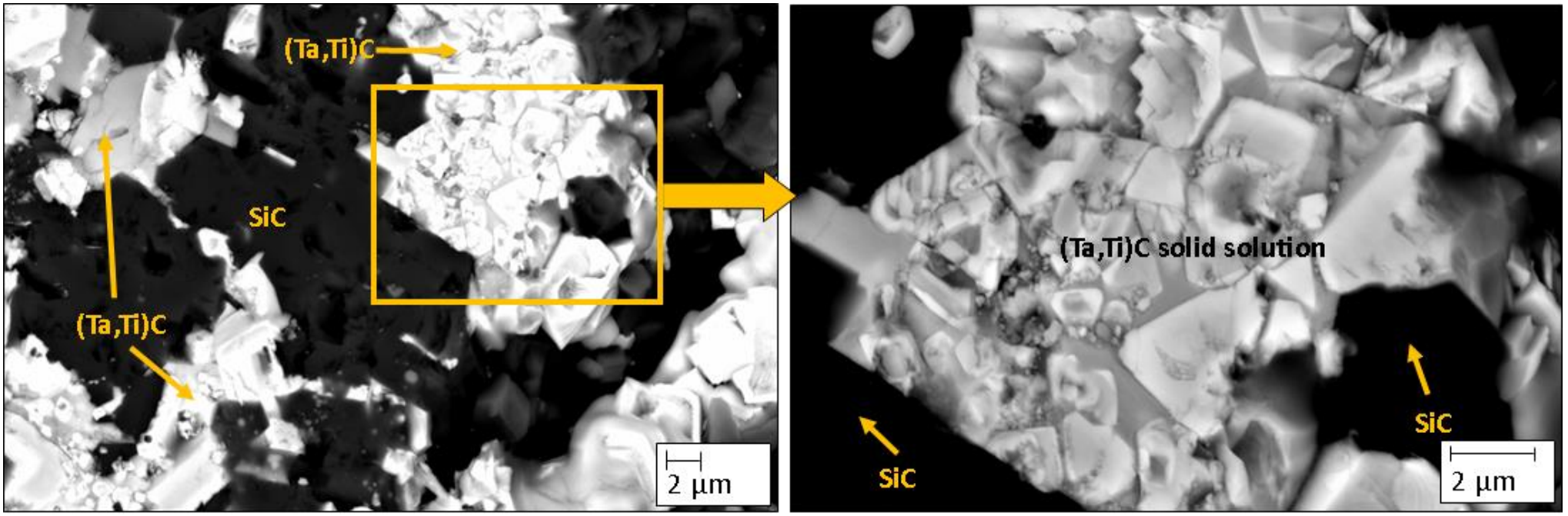

Figure 61: BSED-SEM images showing microstructures of the cross-section of the C_f/C-SiC-TiC-TaC composite prepared by RMI at 1700°C for 30 minutes using SPS.

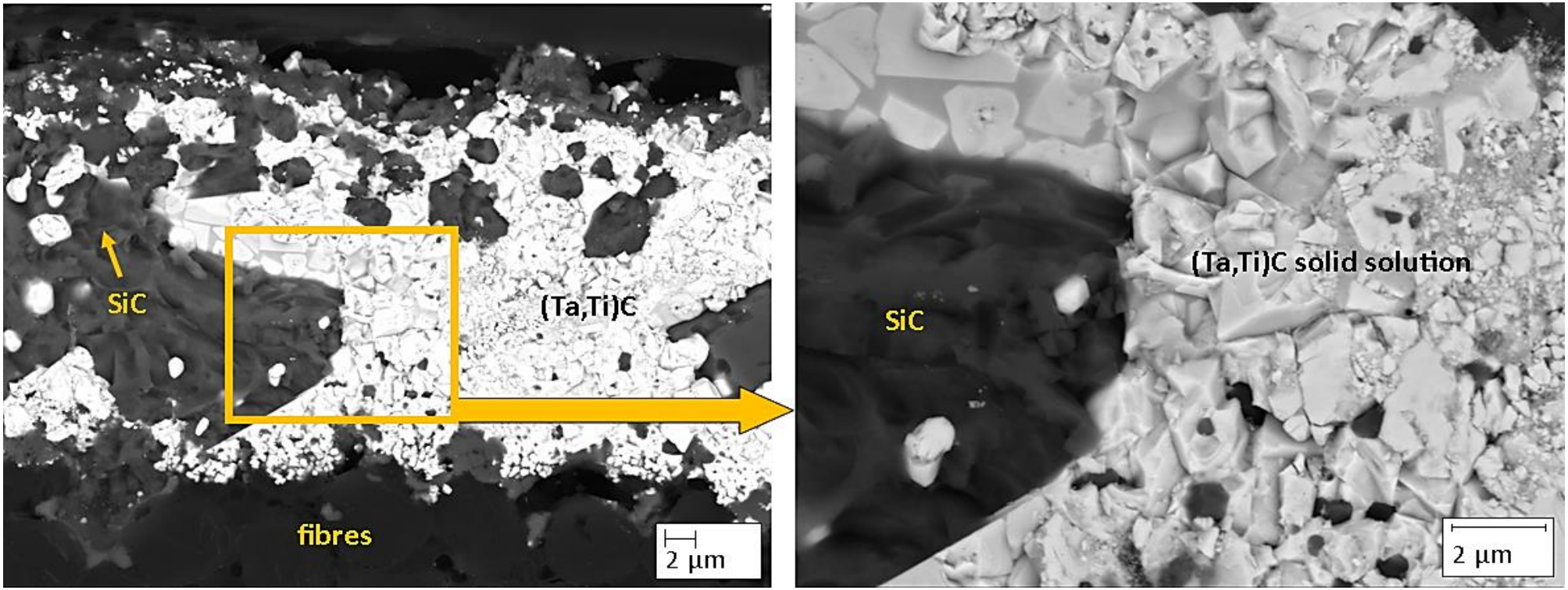

Figure 62: BSED-SEM images showing microstructures of the cross-section of the C_f/C-SiC-TiC-TaC composite prepared by RMI at 1800°C for 30 minutes using SPS.

4.5.1 Phases Present in the Composite

C_f/C-SiC-TiC-TaC produced by SPS at 1600°C

In the C_f/C-SiC-TiC-TaC produced at 1600°C (Figure 60) a white phase which precipitated close to the carbon matrix/alloy interface was observed. Here the (Ta,Ti)C phase precipitated out of the predominantly SiC (formed according to Reaction 31) containing unreacted $(Ta,Ti)_xSi_y$. Thus a gradient matrix of the solid solution of transition metal carbides [(Ta,Ti)C], SiC, and transition metal silicides $(Ta,Ti)_xSi_y$] was formed.

$$Si + C \rightarrow \beta\text{-}SiC \quad (31)$$

Figure 63 shows the existence of the silicide phases ($TaSi_2$, Ta_5Si_3, $TiSi_2$, Ti_5Si_3) and free silicon (Si) in the diffractogram in which RMI was performed at 1600°C. Si and β-SiC show to be the main phases dominating the obtained pattern. C and (Ta,Ti)C were also identified.

C_f/C-SiC-TiC-TaC produced by SPS at 1700°C

Figure 61 reveals the existence of more pronounced dissolution of phases in one another than in the phases shown in Figure 60. The bright white grains are not strictly distinct from the light grey phase contiguous to the grains. From the EDS analysis performed on Figure 61, the light grey phase is silicon-rich, with 20.9 at.% Si [the rest being C, Ta and Ti]; while the bright white phase had the least of silicon, with 4.8 at.% Si [the rest being C, Ta and Ti]; and the dull white phase at about 10.9 at.% Si [the rest being C, Ta and Ti]. It is noteworthy to point out that it was necessarily impossible to exclusively distinguish the carbide phases in the SEM micrographs mainly because of the multiple dissolutions and diffusions which evidently occurred during the formation of the carbide phases. This is confirmed also by the peak overlaps shown in the XRD patterns and the inconclusive EDS results obtained.

Thus the silicides solid solution reacted with carbon according to the reactions shown in Reactions 31-36:

$TaSi_2$ (l) + 3C (s) → TaC (s) + 2SiC (s) (31)

$TiSi_2$ (l) + 3C (s) → TiC (s) + 2SiC (s) (32)

$(Ta,Ti)Si_2$ + 3C (s) → (Ta,Ti)C (s) + 2SiC (s) (33)

Ti_5Si_3 (l) + 8C (s) → 5TiC (s) + 3SiC (s) (34)

Ta_5Si_3 (l) + 8C (s) → 5TaC (s) + 3SiC (s) (35)

Alternatively, for Reactions 34 and 35, a possibility also exists of having the 5-3 silicides reacting with the silicon phase before infiltration into the carbon preform to give disilicides (Reactions 36 – 37). The resultant disilicides then react with the carbon matrix as given in Reactions 31 – 33.

Ti_5Si_3 + 7Si (s) → $5TiSi_2$ (l) (36)

Ta_5Si_3 + 7Si (s) → $5TaSi_2$ (l) (37)

C_f/C-SiC-TiC-TaC produced by SPS at 1800°C

Figure 62 shows a rather homogeneous matrix compared to the microstructure of the C_f/C-SiC-TiC-TaC composite heat treated at 1600°C (Figure 60). The white phase is more extensively distributed in the SiC milieu (more clearly in Figure 62). A close look at the reacted alloy/carbon matrix interface shows a band of predominantly SiC. This is similar to the evidence presented in the couple studies results presented in foregoing section. This occurrence is proof that the formation of the transition metal carbides is driven by the diffusion of carbon in the alloy.

The grouped diffractograms (in Figure 63) for the C_f/C-SiC-TiC-TaC composite heat treated at 1600°C, 1700°C and 1800°C UHTCs show the following: SiC has the most pronounced peaks still, as in the other two patterns for the 1600°C and 1700°C UHTCs. Shouldering the SiC peaks are the TaC, TiC and (Ti,Ta)C phase

peaks – that is why the SiC peaks have broad bases and narrow tips. For the purpose of presentation, TaC and TiC peaks have not been labelled on the diffractogram. These have been collectively labelled as (Ti,Ta)C. These peaks are clustered in the respective order of TaC, (Ti,Ta)C, SiC and TiC. The (Ti,Ta)C peaks are consistently more inclined to the TiC peaks than the TaC peaks. This trend suggests that the (Ti,Ta)C contains TaC in higher proportions than the TiC.

It is not clear why the $TiSi_2$ and β-Si peaks at about 55° and 56° respectively became broader and closer to each other in the 1800°C pattern than in the 1700°C pattern, especially considering the observed trend of having silicides and free silicon peaks gradually diminishing with increasing temperature from 1600°C to 1800°C. Peaks of residual $TiSi_2$, $TaSi_2$ and their solid solution [$(Ta,Ti)Si_2$] were detected. The Ta_5Si_3 and Ti_5Si_3 phases are not present in the 1800°C pattern, showing that they were converted into carbides according to the Equations 33 and 34, or according to the Reactions 35 and 36 routes.

Similarly, the free Si phase showed a complete disappearance at 1800°C. At 1600°C the Si peak, evident at about $2\theta=33°$, is very pronounced; it diminished gradually from the 1700°C to the 1800°C pattern. As the free Si peaks diminished, the SiC peaks became even more pronounced as the RMI temperature was increased.

The peaks initially clustered at $47°<2\theta<50°$ in the 1600°C pattern show a gradual fusion as the RMI temperature was increased to 1700°C and 1800°C. This trend could be attributed to the occurrence of interdiffusion in the TaC, (Ti,Ta)C, SiC and TiC species identified to be constituting the peaks.

At $2\theta=30°$-31° is an evidently amorphous bump at 1600°C first, followed by a slightly sharpened peak at 1700°C, and then final disappearance at 1800°C. This suggests slight graphitic ordering in the carbon (peak at 31°) from 1600°C to 1700°C.

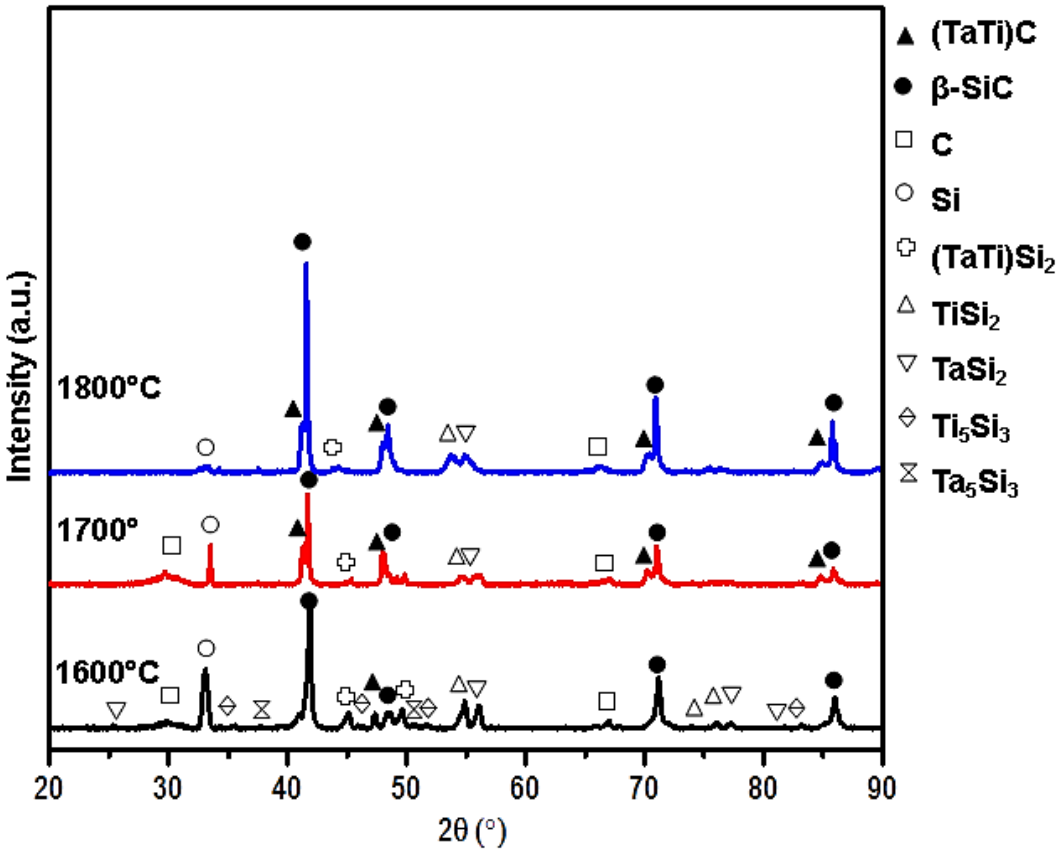

Figure 63: XRD spectra of C_f/C-SiC-TiC-TaC composites whereby reactive melt infiltration was performed by spark plasma sintering at 1600°C, 1700°C and 1800°C for 30minutes.

There was a shift of the TaC peaks to the left in both the 1700°C and 1800°C XRD patterns. The shift increased with increasing 2θ values. Furthermore, the shift of the TaC peaks to the left increases with temperature from 1700°C to 1800°C. There was also a pronounced overlapping of TiC and SiC peaks, showing they gave similar reflections in the patterns. Furthermore, the unit cells (face centred cubic) of these phases at 1700°C and 1800°C (shown in Table 16) were comparable: a = 4.358Å for TiC and a = 4.352Å for SiC at 1700°C; a = 4.354Å for TiC and a = 4.351Å for SiC at 1800°C.

Table 16: Lattice parameters of the phases present in the UHTCs prepared at 1600°C, 1700°C and 1800°C by SPS. Lattice parameters were determined by Rietveld refinement using TOPAS software.

	Lattice Parameter, *a* (Å)		
Phase	1600°C	1700°C	1800°C
TaC	Not present in pattern	4.453 ± 0.0073	4.454 ± 0.0017
TiC	Not present in pattern	4.358 ± 0.0081	4.354 ± 0.0022
(Ta,Ti)C	4.3802 ± 0.0096	4.3941 ± 0.0067	4.3972 ± 0.0015
Beta-SiC	4.3583 ± 0.0084	4.3524 ± 0.0067	4.3517 ± 0.0013

The TaC lattice parameters in Table 16 show a very slight increase from 1700°C to 1800°C. These values are lower than the widely accepted lattice values of a = 4.455 for TaC (Kosolapova, 1971), probably owing to the existence of vacant C sites. All TiC lattice parameters shown in Table 16 are larger than the reported value of 4.32861 for the stoichiometric TiC_x (x = 1) (Wei *et al.*, 2011). This might be due to the existence of TiC in the form of a continuous solid solution with TaC which has larger unit cell dimensions. Values attained in this work could also suggest the unlikely possibility of substoichiometric forms of TiC_x (x < 1).

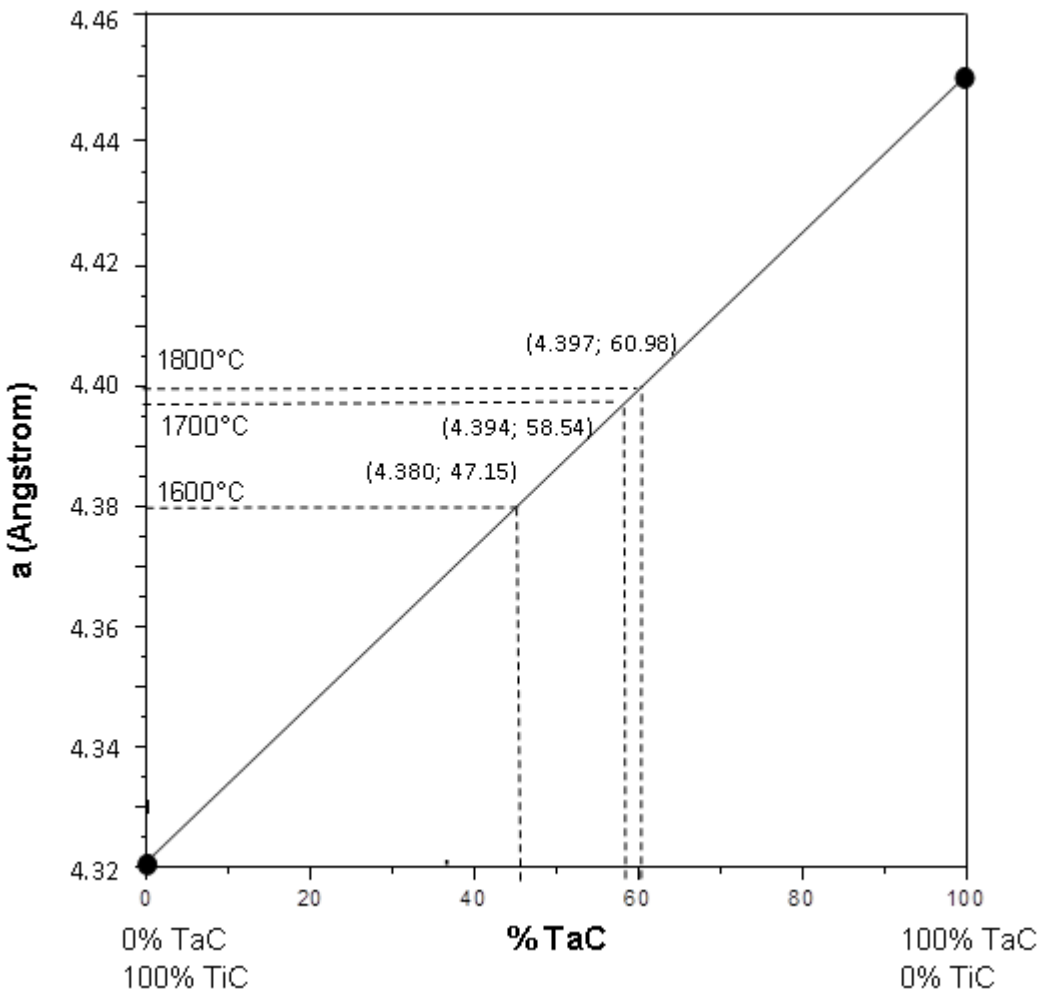

Figure 64: Graph of experimentally determined lattice parameters (after Reitvield refinement) of the (Ti,Ta)C solid solution in the UHTC prepared at 1600°C, 1700°C and 1800°C, against atomic % tantalum exchange.

The peaks of the (Ta,Ti)C solid solution increased in intensity from 1700°C to 1800°C. The extent of solid solution between TaC and TiC was determined by interpolating the lattice parameters of the (Ta,Ti)C at a given temperature (1700°C and 1800°C) on the straight line graph linking the lattice parameters of the TaC to that of TiC, as shown in Figure 64.The linear relationship between the lattice parameter and the atomic percent of tantalum in the solid solution was established by McMullin and Norton (1953). The estimated compositions of TaC in solid solutions are given in Figure 64. At 1600°C the (Ta,Ti)C solid solution consisted of about 47.15 at.% of TaC (52.85 at.% TiC), 1700°C the (Ta,Ti)C solid solution

consisted of about 58.54 at.% of TaC (41.46 at.% TiC), and at 1800°C the solid solution consisted of about 60.98 at.% of TaC (39.02 at.% TiC). The TiC:TaC ratios at 1600°C are very similar to the starting Ti:Ta atomic ratios in the alloy.

4.5.2 Fracture Surface

The surface at which the composites were fractured revealed the progression of the cracks propagated during fracture, and the way in which the composites absorbed the energy from the load applied.

Figure 65 shows the fracture surfaces of the composites prepared by RMI at 1600°C, 1700°C and 1800°C. The 1600°C composite shows blocks of fibres bound by matrix sticking out. The fibres did deflect the fracture cracks in bundle form. It was observed that the clusters of matrix bound to the pulled out fibre bundles or tows suggest that the viscosity of the alloy infiltrated at this temperature was very high; hence its spreading in the C_f/C composite was limited.

The 1700°C composite shows some fibres which stick out of the rest of the fracture surface, having fractured at different lengths too. This suggests that the fibres successfully impeded crack extension across the composite. The fibres deflected the crack along the fibre-matrix interface. The crack consequently followed a discursive path across the composite.

On the contrary, the 1800°C does not have any pulled out fibres at the fracture surface. It shows a continuous surface fracture surface wherein the sites occupied by fibres are not distinguishable. The micrograph suggests that the alloy infiltrated the composite to saturation and must have reacted with both the carbon matrix and the carbon fibres. This indicates matrix and fibre phases somewhat fused together. This showed that while RMI at high temperatures expedites the mass transport and reaction kinetics for the formation of a new matrix, it carries the penalty of fibre damage. Ultimately the purpose of having fibres in the composite is defeated.

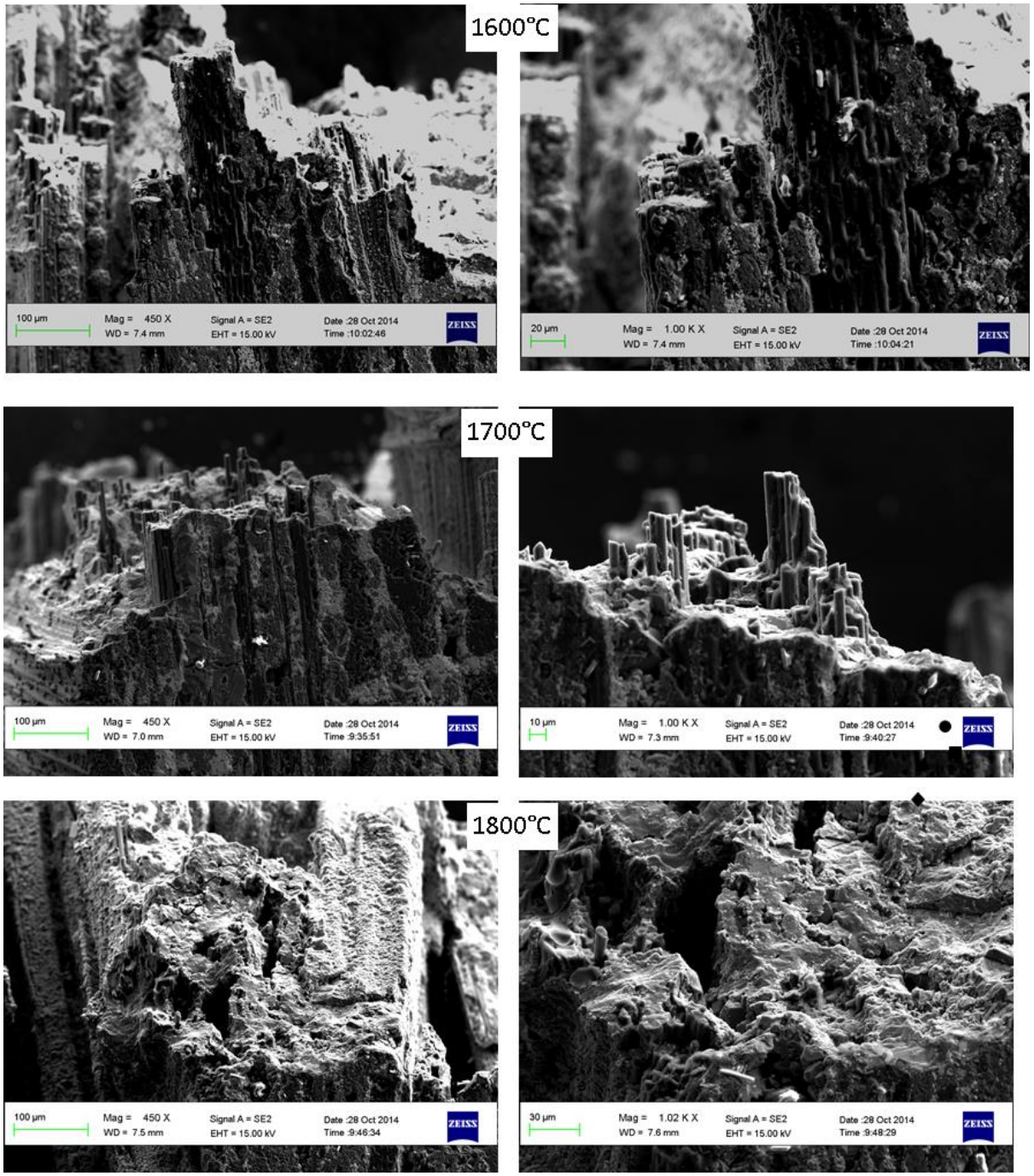

Figure 65: Secondary detector SEM micrographs showing the fracture surfaces of C_f/C-SiC-TiC-TaC composites prepared by SPS at 1600°C, 1700°C and 1800°C for 30min.

From the couple and fracture surface studies results presented in the foregoing subsections, the most favourable temperature for performing the RMI for the

present system was deemed to be 1700°C. The obtained microstructures of the 1700°C UHTC are discussed hereforth.

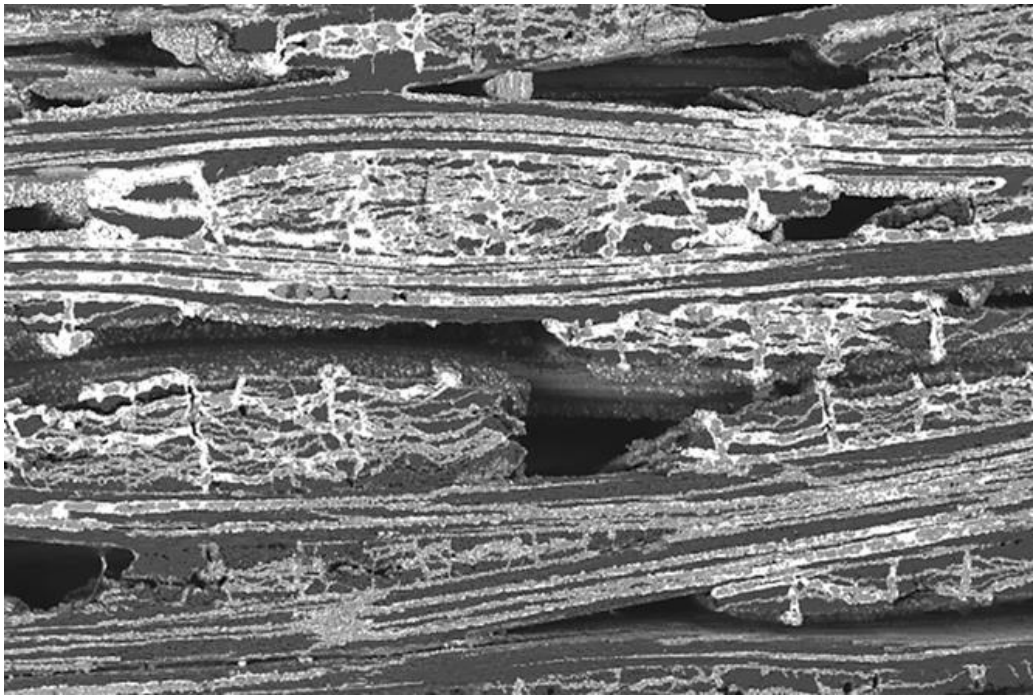

Figure 66: BSED-SEM micrograph of a cross-section of the C_f/C-SiC-TiC-TaC composite prepared by SPS at 1700°C for 30min.

A heterogeneous macrostructure was obtained after the reactive melt infiltration step. A phase-gradient is noticeable across the thickness of the composite. The upper region was the end at which alloy was infiltrated from. From Figure 66, the upper half laminates show an abundance of the white phases, predominantly (Ta,Ti)C, while the lower half laminates show an abundance of the grey phases, predominantly SiC.

The microstructure at higher magnifications is shown in Figure 67 and Figure 68. Figure 67 is a longitudinal elaboration of how the alloy lodged along the fibre tows. Figure 68 is a transverse elaboration of how the alloy infiltrated through the tows and clearly into the spaces between the individual fibres of the composite.

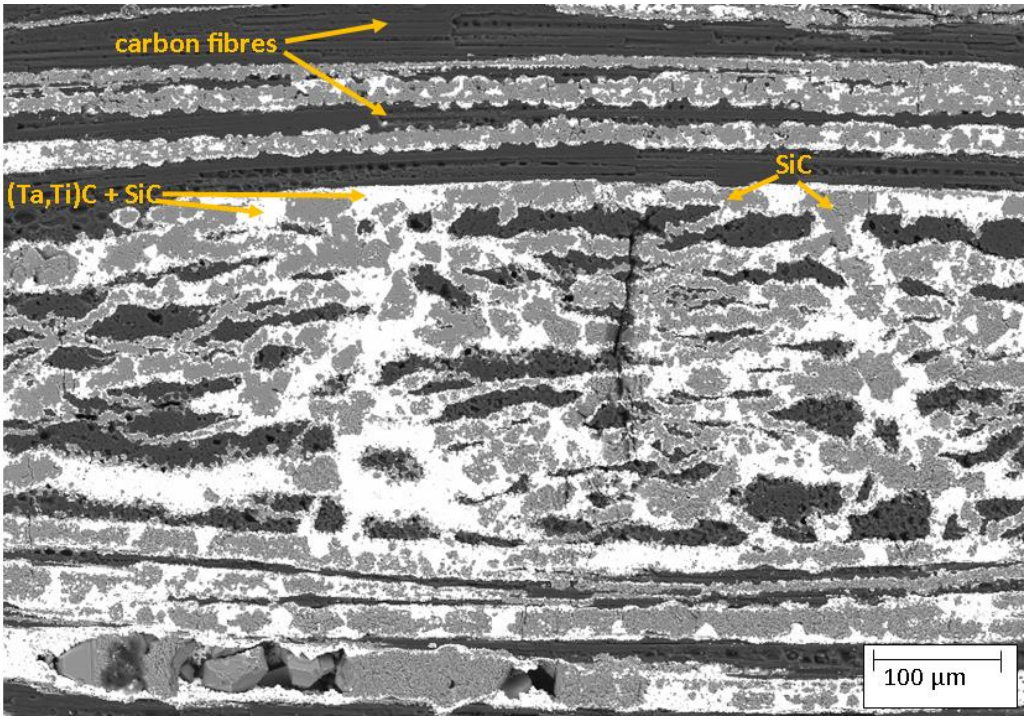

Figure 67: BSED-SEM micrograph showing the microstructure of the longitudinal cross-section of the C_f/C-SiC-TiC-TaC composite prepared by SPS at 1700°C for 30min.

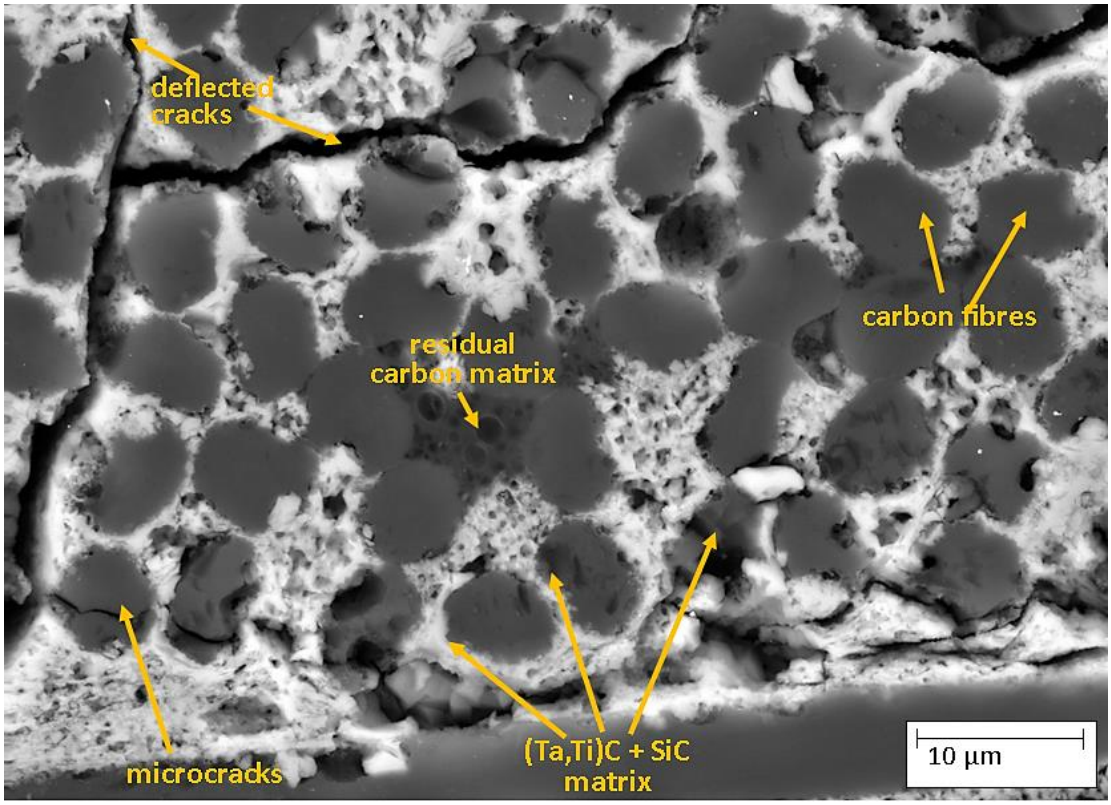

Figure 68: BSED-SEM micrograph showing the microstructure of a transverse cross-section of the C_f/C-SiC-TiC-TaC composite prepared by SPS at 1700°C for 30min.

The elemental maps in Figure 69 give confirmatory evidence of the spatial distribution of the phases identified from the XRD analysis results.

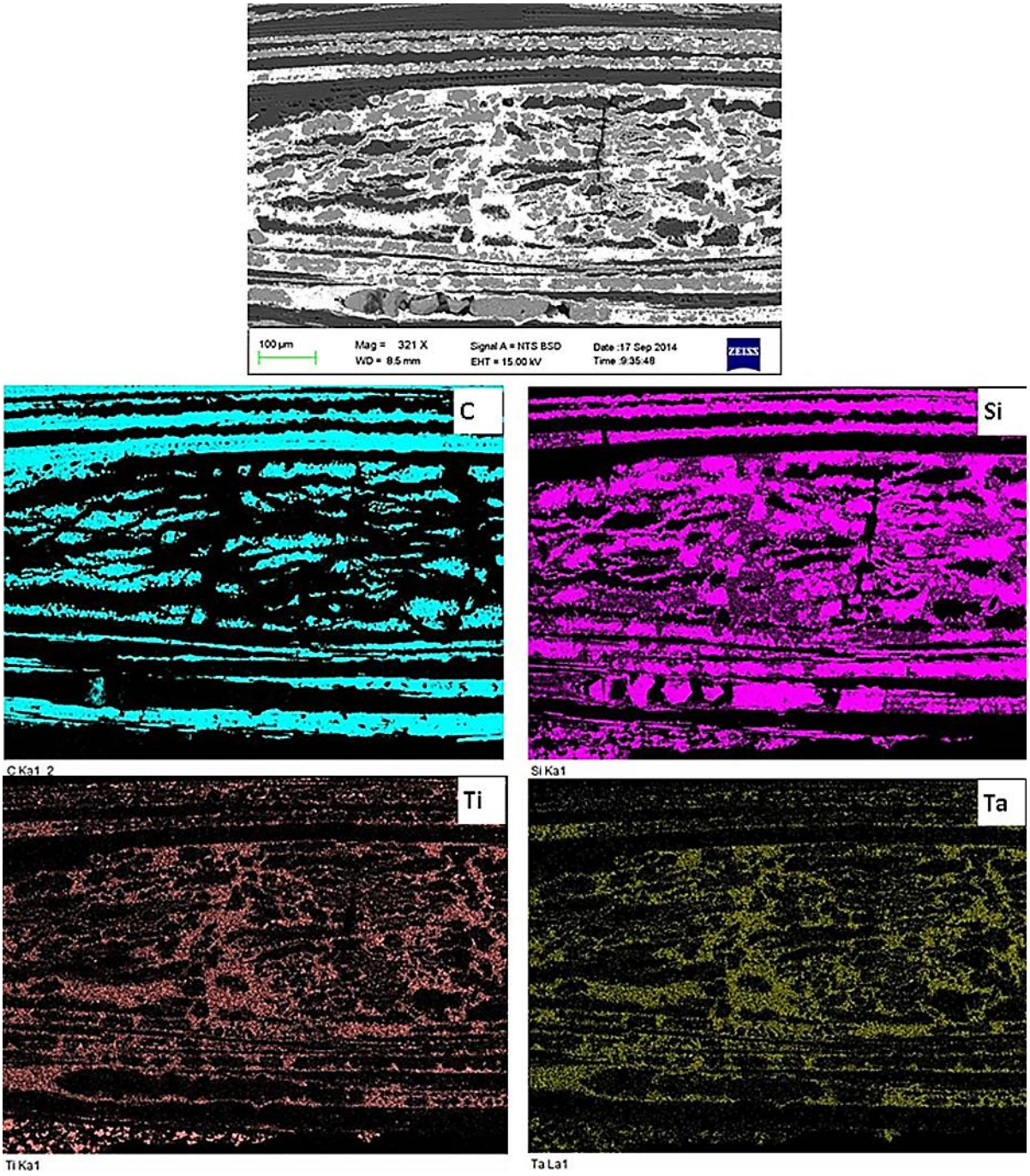

Figure 69: BSED-SEM micrograph and SEM-EDS elemental maps obtained from the cross-section of the C_f/C-SiC-TiC-TaC composite whereby reactive melt infiltration was performed by spark plasma sintering at 1700°C for 30minutes.

Matrix Cracking

The composite (Figure 70) also reveals some voids in the structure of more than 500µm length and more than 100 µm width. These voids have a marked presence at

the matrix concentrated regions. The following observations were made concerning the voids in the UHTC composite:

- They were formed by the cracking in the matrix and the consequential loosening of the matrix blocks. The probable result was matrix fall-off thus creating gaps in the structure.
- At metallographic preparation of the samples considerable debris was encountered and this is further evidence that the matrix blocks spalled off.

The cracking in the matrix can be attributed to the mismatch of the coefficients of thermal expansion in the carbides formed (Table 17). The cooling rate of 200°C/min could have induced thermal shock as well. It must be borne in mind that this high cooling rate was applied in order to constrain the disproportionation of the carbide phases formed. Figure 68 show that the cracks which occurred in the matrix deflected the fibres in their formation. This is a reflection of a favourable fibre/matrix interface.

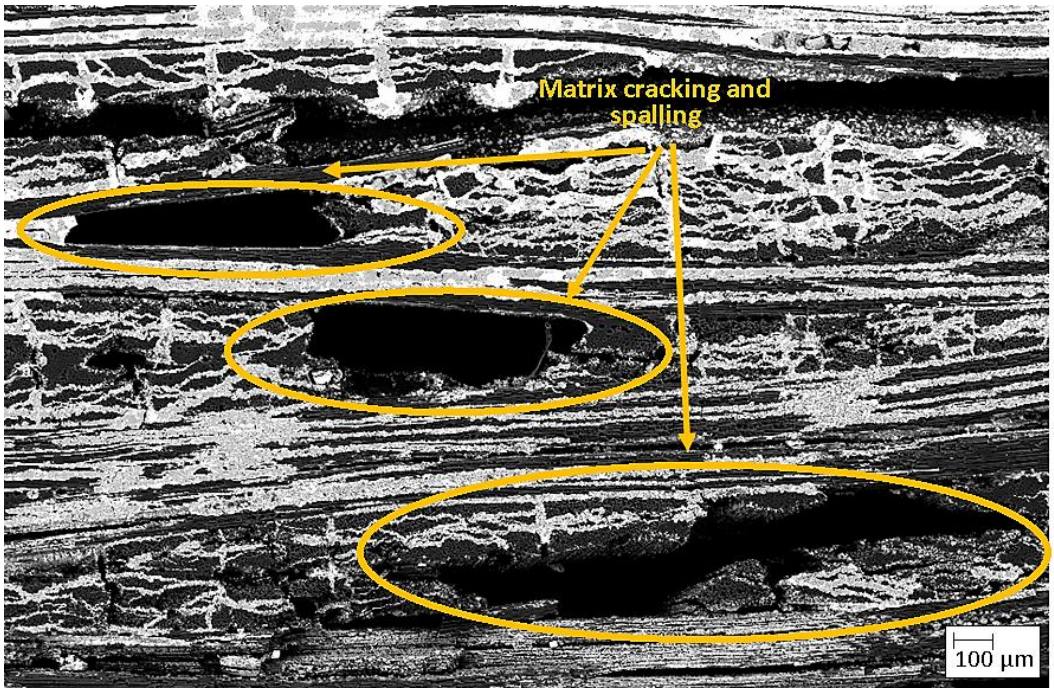

Figure 70: BSED-SEM micrograph of a cross-section of the C_f/C-SiC-TiC-TaC composite prepared by SPS at 1700°C for 30min. The figure shows how the matrix cracked, with some matrix blocks even spalling off during ceramographic preparation.

Table 17: Linear coefficients of thermal expansion for C, SiC, TaC and TiC at specified temperature ranges.

	Linear coefficient of thermal expansion ($x10^{-6}$/K)	Range of Temperature (K)	References
C	1.6 – 2.1[a]	300 - 2500	Pradere & Sauder (2008).
SiC	4.5	293 – 1673	Wali & Yang (2012)
TiC	9.5 ± 0.3	293 – 2973	Wali & Yang (2012)
TaC	6.4 ± 0.3	293 – 2273	Wali & Yang (2012)
[a] Range of values for transversely determined CTE on fibres derived from rayon, PAN and pitch.			

4.6 ABLATED C_f/C COMPOSITE

Figure 71 shows photographs of the virgin (before ablation) C_f/C composites and the discs that were exposed to the oxyacetylene flame for different durations: 2.5s, 5.0s, and 7.5s.

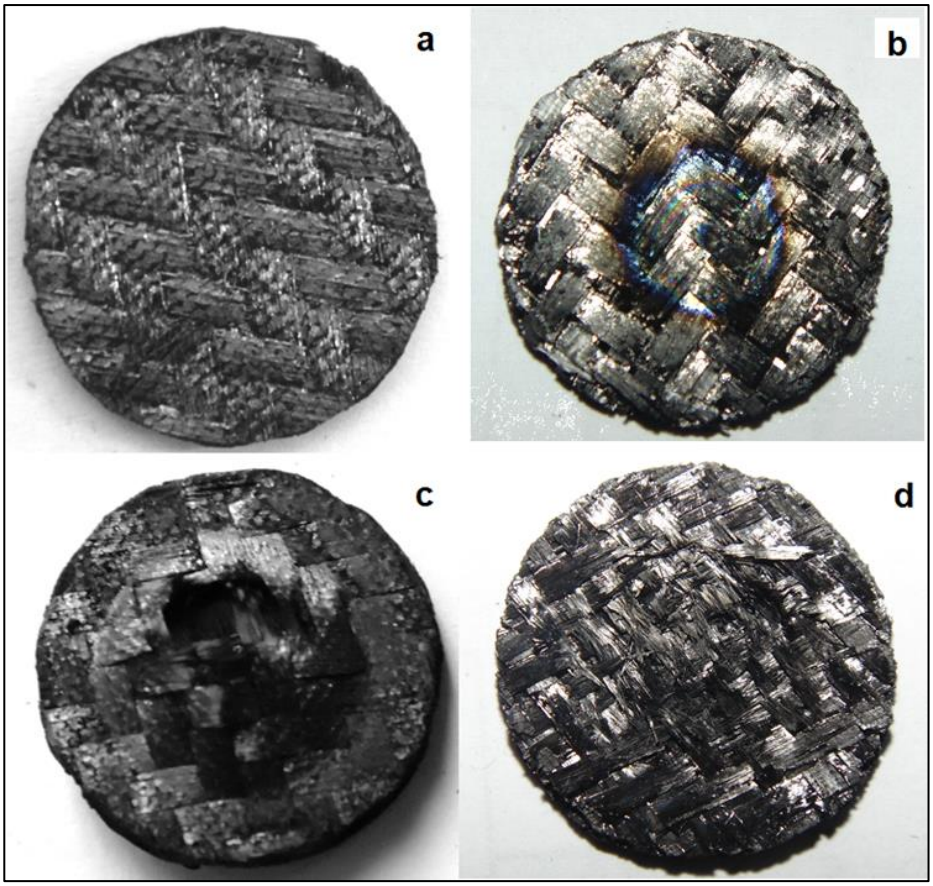

Figure 71: Photographs of C_f/C composite discs of 20mm diameter: (a) Unexposed to flame (b) 2.5s flame exposure time (c) 5.0s flame exposure time (d) 7.5s flame exposure time.

The disc photographs in Figure 71 show that the C_f/C composite exposed to the flame for 2.5s (b) has no immediately obvious damage on a macro-scale. On the other hand, the disc exposed for 5.0s shows to have burst open and delaminated on the central region directly exposed to the flame. The disc exposed for 7.5s shows pitted damage which was radially extensive on the surface of the disc.

The following mass and linear ablation rates (Table 18) were calculated from the ratio of change in mass and thickness, respectively, to time. The mass ablation rate gradually increased with increasing exposure time to the flame. While the linear ablation rate increased with increasing exposure time, the rate more than doubled between 5.0s and 7.5s of exposure. This shows the worsened deepening of the

crater formed at the surface exposed directly to the flame – suggesting worsening mechanical damage of the C_f/C composite with time.

Table 18: Mass and linear ablation rates of the C_f/C discs exposed to the oxyacetylene flame for 2.5 seconds, 5.0 seconds, and 7.5 seconds.

Time of exposure to oxyacetylene flame	Mass Ablation rate	Linear Ablation rate
2.5s	0.0129 g/s	0.0870 mm/s
5.0s	0.0218 g/s	0.1176 mm/s
7.5s	0.0402 g/s	0.3773 mm/s

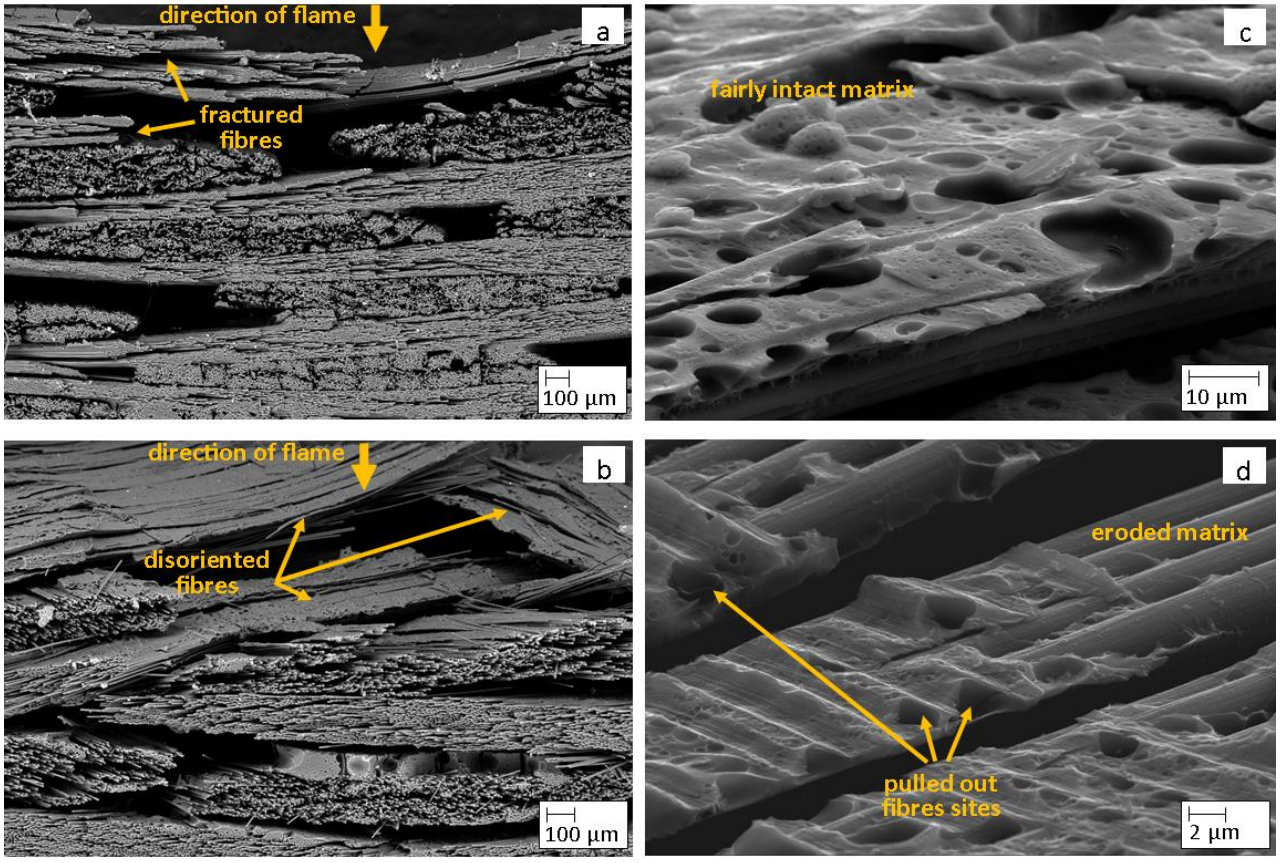

Figure 72: SE-SEM micrographs of the cross-section of the C_f/C composite exposed to the oxyacetylene flame for 2.5seconds.

The microstructures of the ablated C_f/C composites are shown in Figure 72 . The disc exposed for 2.5s shows upper layer laminates to have been damaged (Figure 72a). Fibres in these layers were fractured by the impact of the oxyacetylene flame gases on the composite surface. Thereafter delamination of the fractured fibre tows occurred, and the blowing away of the debris followed. This left the matrix of the underlying layer of fibres exposed to the flame (Figure 72c). Consequential erosion of the matrix occurred (Figure 72d) at 5.0s of exposure to the flame, thus exacerbated fibre fracturing and fibre tows disorientation occurred. Some matrix in-between fibre tows remained intact such that the fibres fractured and left the composite in bundle form.

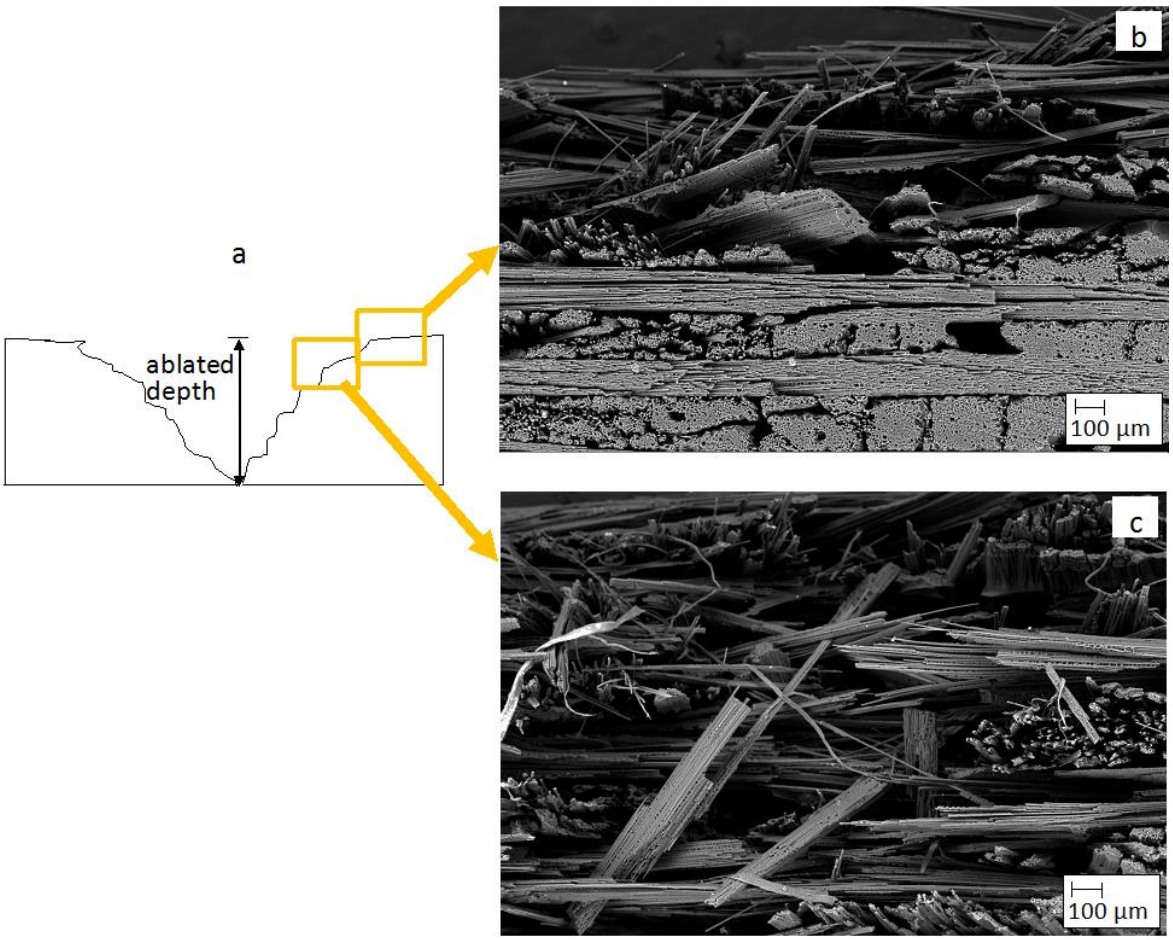

Figure 73: (a) Schematic of the crater formed by thermomechanical damage; (b) SE-SEM micrographs of the cross-section of the C_f/C composite exposed to the oxyacetylene flame.

The schematic in Figure 73a shows how an ablation crater formed in the C_f/C composite due to the thermomechanical damage imposed by the oxyacetylene flame. The crater narrows down from the upper laminates to the lower laminates of the C_f/C composite. The micrographs in Figure 73b and Figure 73c show how the residual matrix holding the fractured tows was eroded away too. The fibre disorientation has worsened at this stage.

The carbon in the ablated C_f/C composite was amorphous and the XRD results (Figure 74) showed structures of the carbon identical to those of the virgin C_f/C composite reported in Section 4.2.7 (Figure 42).

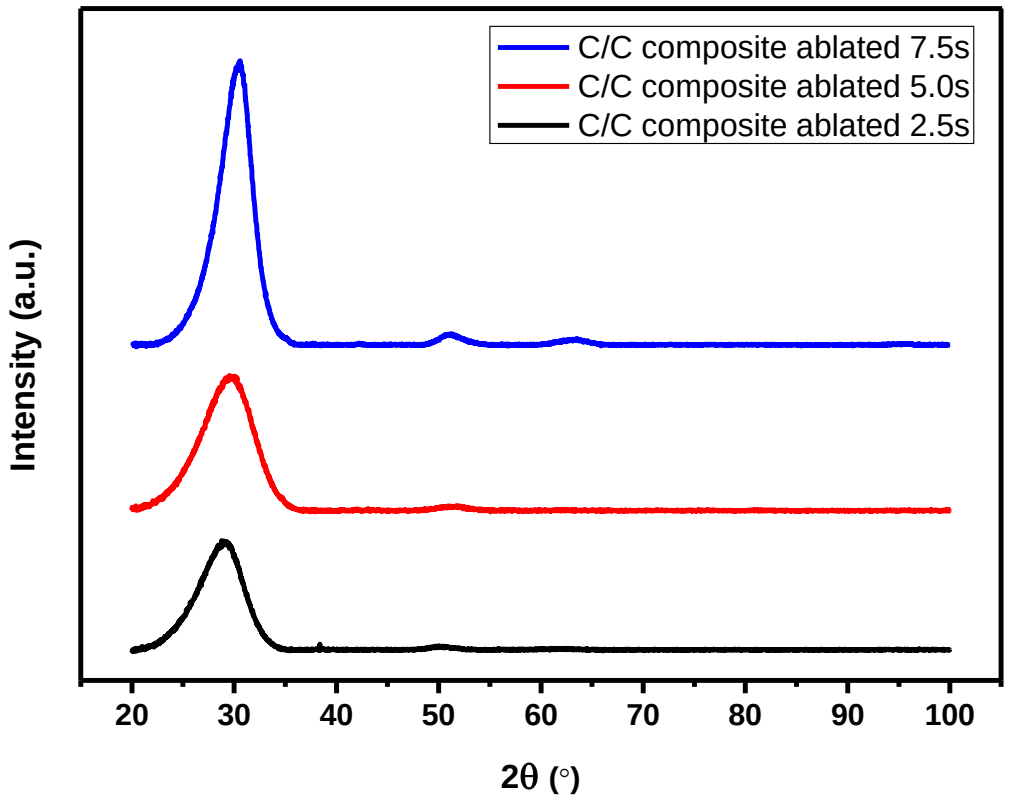

Figure 74: XRD diffractogram of the C_f/C composite surface exposed to the oxyacetylene flame for 2.5s, 5.0s and 7.5s

4.7 ABLATED C_f/C-SiC-TiC-TaC COMPOSITE

Figure 75 shows photographs of the virgin C_f/C-SiC-TiC-TaC (before ablation) and the discs that were exposed to the oxyacetylene flame for different durations: 2.5s; 5.0s, and 7.5s.

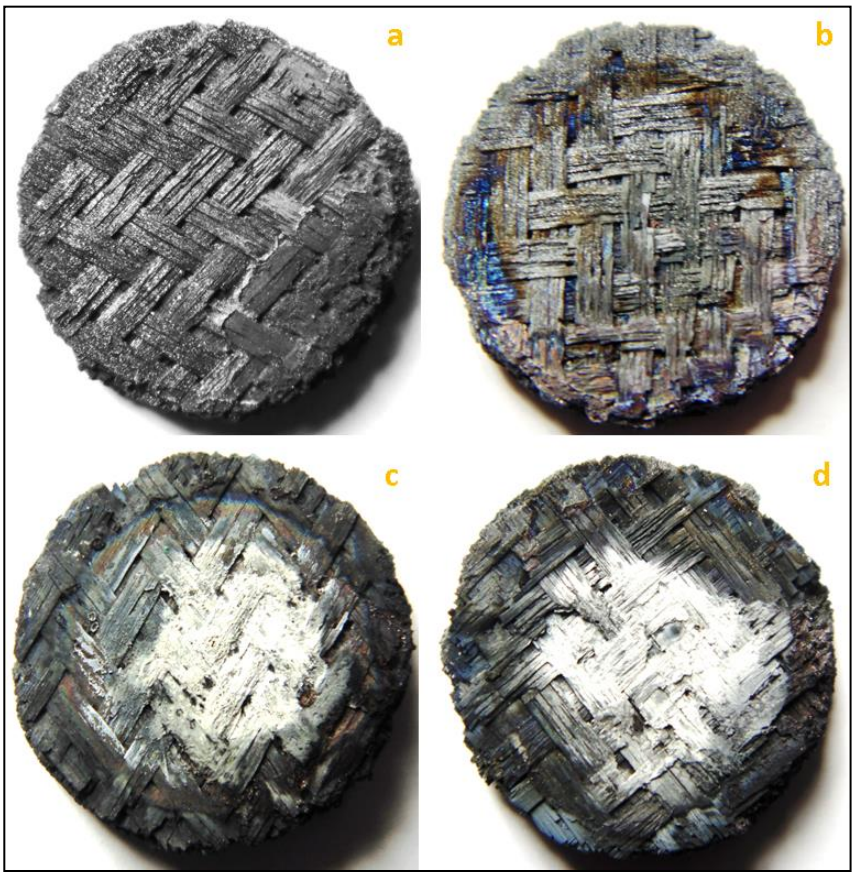

Figure 75: UHTC discs of 20mm diameter: (a) Unexposed to flame (b) 2.5s flame exposure time (c) 5.0s flame exposure time (d) 7.5s flame exposure time.

The following mass and linear ablation rates (Table 19) were calculated from the ratio of change in mass and thickness, respectively, to time.

Table 19: Mass and linear ablation rates of the UHTC discs exposed to the oxyacetylene flame for 2.5 seconds, 5.0 seconds, and 7.5 seconds.

Time of exposure to oxyacetylene flame	Mass Ablation rate	Linear Ablation rate
2.5s	0.00327 g/s	0.00224 mm/s
5.0s	0.00342 g/s	0.00208 mm/s
7.5s	0.00388 g/s	0.00216 mm/s

4.6.1 Microstructure of Ablated UHTCs

Different exposure times to the oxyacetylene flame produced different microstructures especially on the surface that was directly exposed as shown in Figure 78.

2.5s Exposure time: the composite [in Figure 75b] does not show any scale formation after exposure to the flame. The composite, however, shows aggravated cracking and physical degradation on the upper most layer (80-100μm) thickness) in Figure 76. This layer shows that pitting erosion and ablation to have occurred. The ablated sample also shows some char rings on the peripheries of the discs, similar to those appearing on the sample holder. This ring was defined by the flame boundaries on the C_f/C-SiC-TiC-TaC sample.

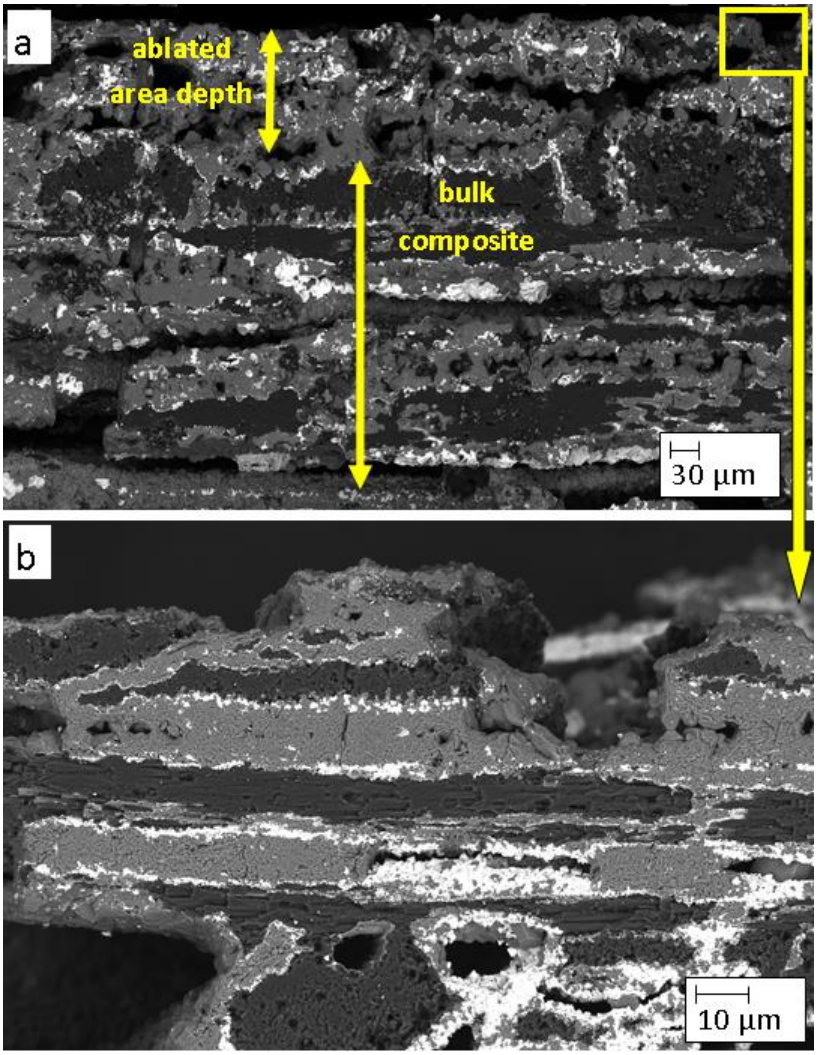

Figure 76: BSED-SEM micrographs of the cross-section of the UHTC exposed to the oxyacetylene flame for 2.5seconds.

5.0s Exposure time: The ablated disc [in Figure 75c] shows some white scale on the central area which was exposed to the oxyacetylene flame. The scale formed showed two rather distinct microstructured layers. Layer 1 has crumpled popcorn-like scale morphology. There exist some huge pores along the interface line between layer 1 and 2 which allow the ingress of oxygen other than the paths located at the top of the composite. The morphologies shown in Figure 77 resemble that of popped kernels of corn. In Figure 77b, layer 2 showed suppressed or limited 'popping' versus layer 1 in which significant 'popping' of the composite material occurred.

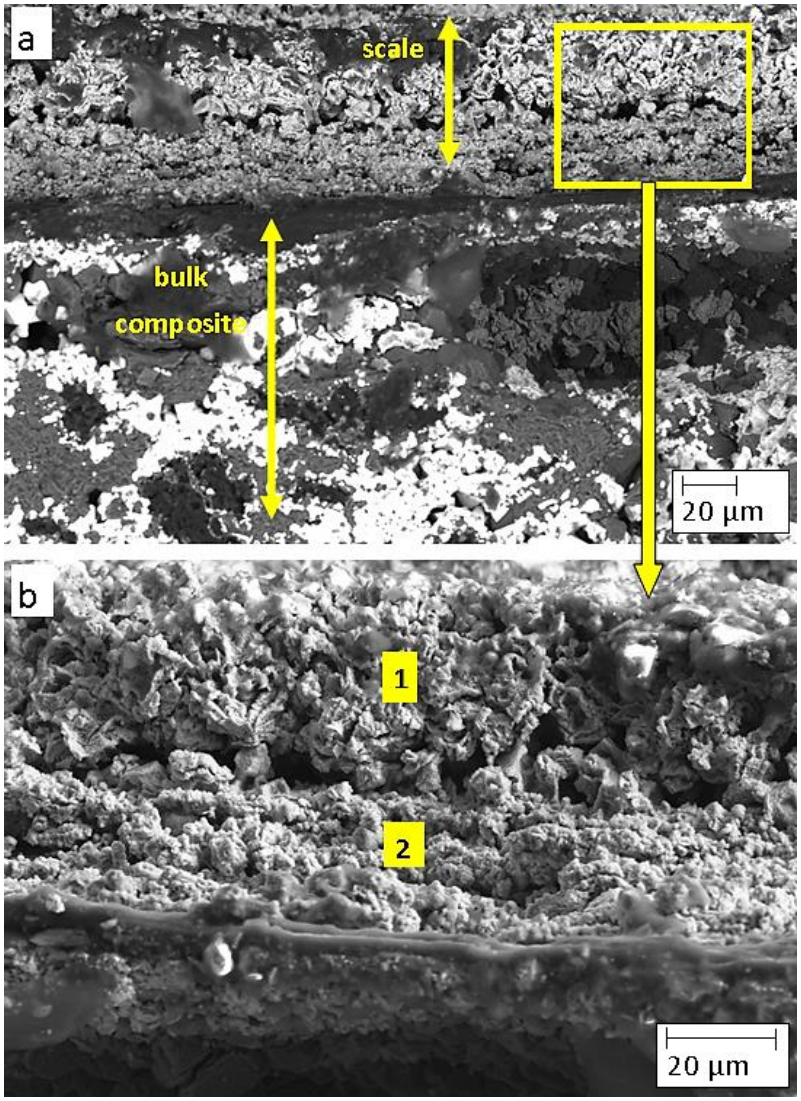

Figure 77: BSED-SEM micrographs of the cross-section of the UHTC exposed to the oxyacetylene flame for 5.0 seconds

7.5s Exposure time: the SEM micrograph in Figure 78 shows a layer of the ablation products of thickness about 120µm. This layer showed four distinctly stratified bands, with distinct morphologies and chemical composition profiles. Layer 1 is the top band which has crumple morphology, similar to layer 1 in Figure 78b. The ablation products show a loose texture, also comprising of sparse black blotches in the layer.

Layers 4, 2 and 1 in Figure 78 show limited, moderate, and significant 'popping' respectively. Layer 3 clearly shows a dense layer with a distinct lustre and texture.

This layer (3) presents the evidence of the self-healing concept. As seen in Figure 79, there exist macro cracks and micro cracks. In the microcracks, there is seen a molten liquid which intruded into the formed micro-cracks and closed up the openings. The inception of macro-cracking also prompted the sealing of the fissures by way of a stitched-up fashion. The microstructure could be envisaged to be the result of the release of oxidation product gases which overcome the sealing effect of the glass formed in the matrix and the composite progresses to the morphology shown in Layer 2.

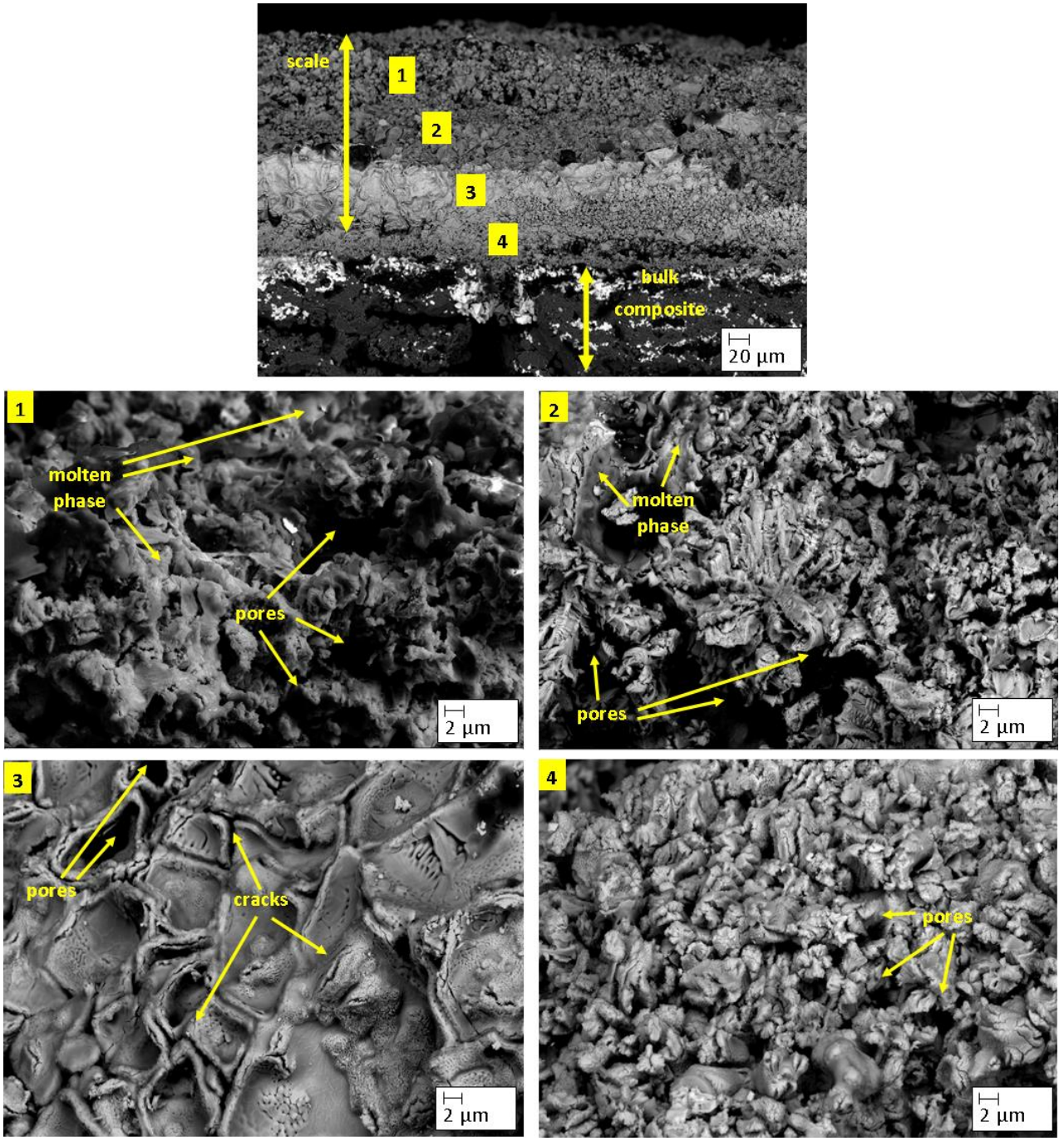

Figure 78: BSED-SEM micrographs of the cross-section of the UHTC exposed to the oxyacetylene flame for 7.5 seconds. 1-4 are micrographs of the individual layers of the scale which formed on the UHTC.

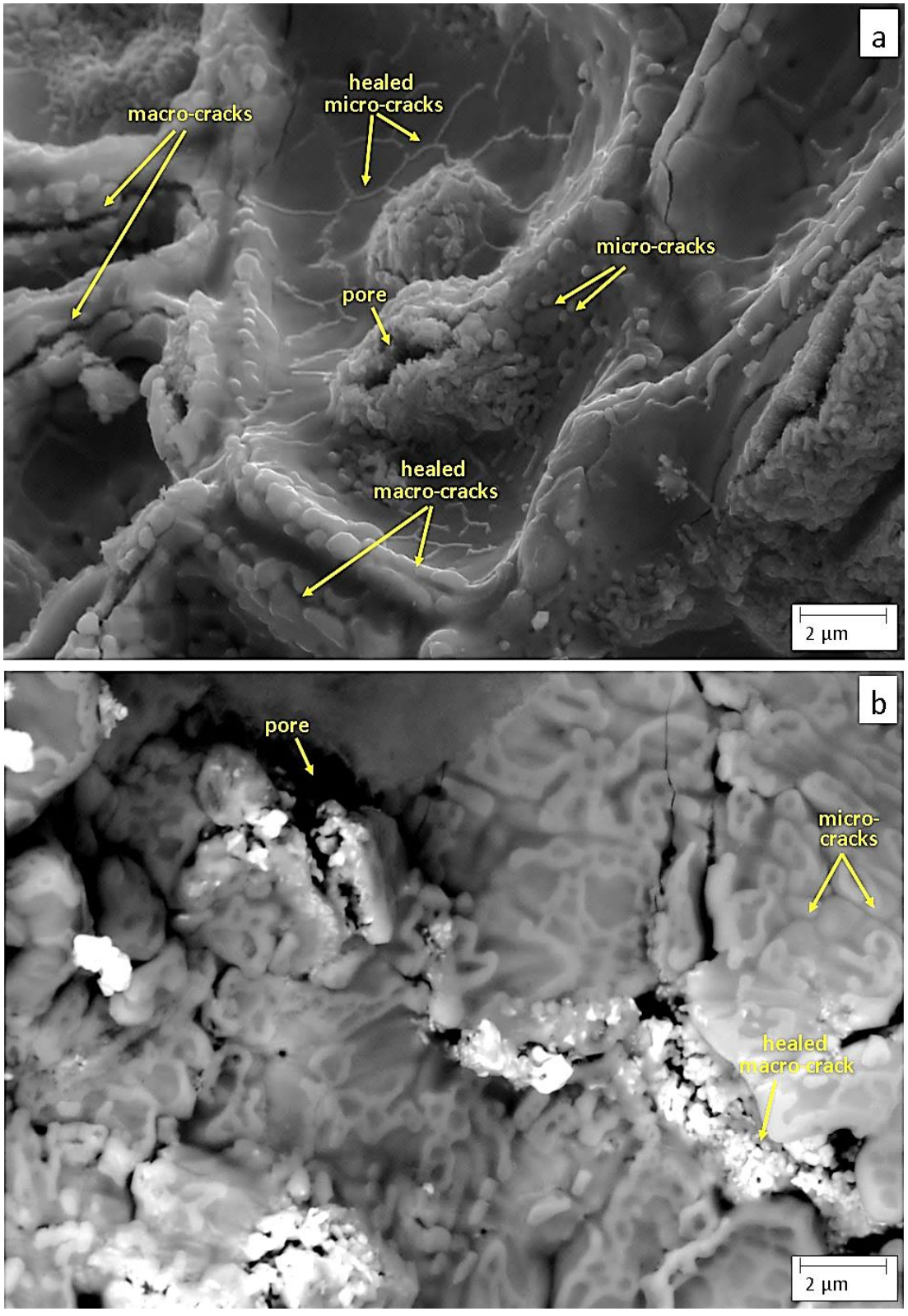

Figure 79: BSED-SEM micrographs of (a) the cross-section (Region 3 in Figure 78), and (b) the upper surface of the UHTC exposed to the oxyacetylene flame for 7.5 seconds

The ash profile microstructures suggest that the oxidation of the composite occurs in gradient profile which advances into the bulk of the composite. The development of the said microstructures can be explained as follows: the volatile gases formed expand within the composite structure and when beyond the critical vapour pressure of equilibrium the gases break out rupturing the composite and leaving behind some pores. As the release of gases intensifies, so does the rupturing in the composite. Spongy flakes burst outwards from the inside in a popping fashion – hence the parallel to the manner in which popcorn pops and the resultant morphology.

The bursting apart of the composite exposes the inside of the composite to oxygen, hence exacerbating the oxidation reactions in the composite. This also advances the sites of oxidation and this is how the scale profile extends into the bulk of the composite.

4.6.2 Phases Present in the Ablated UHTC

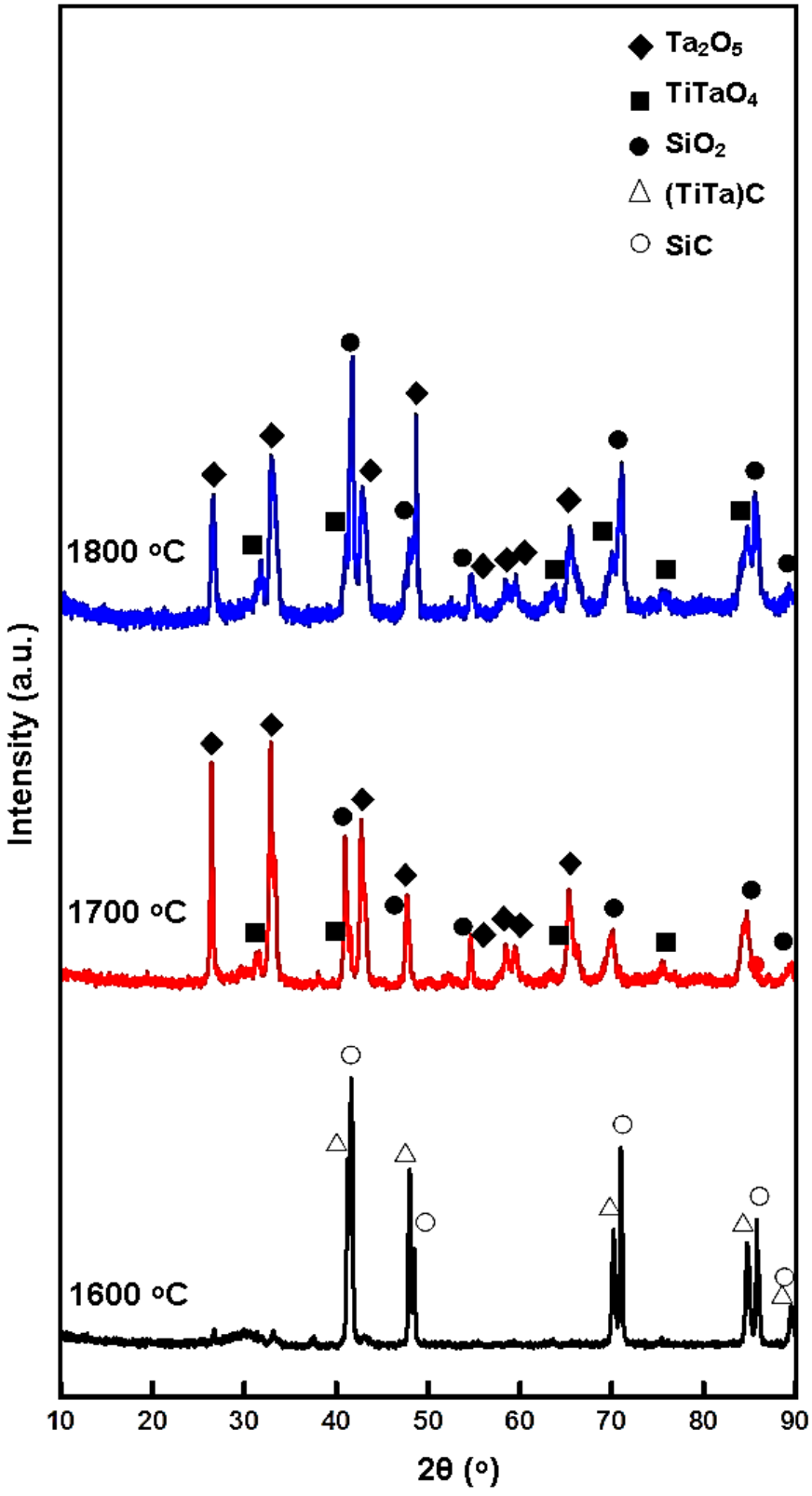

Figure 80: XRD diffractograms of the surface of the UHTC exposed to the oxyacetylene flame for 2.5s, 5.0s and 7.5s.

The XRD pattern in Figure 80 shows a pattern similar to that of the 1700°C UHTC whereby the major peak occurring at 2θ=42° is that of SiC and is overlapped by the peaks of the (Ti,Ta)C, TiC and TaC phases. While the UHTC generally resisted oxidation over 2.5 seconds, a closer look at the XRD pattern in Figure 80 shows that there are some very small peaks occurring at 2θ = 27°, 32.5°, 33.5°, and 43° which represent Ta_2O_5. The quantities of these oxides could be very minute but they give an indication that oxidation was beginning in the composite.

At 5.0 seconds, the transition metal carbides oxidised to form Ta_2O_5 and $TiTaO_4$. The peaks overlapped at several positions as shown in Figure 80. However, the original carbides also persisted in the ceramic mixture suggesting that not all the carbide phases were converted to oxides, a phenomenon attributed to short time exposure. After 7.5 seconds (pattern in Figure 80, the whole range of carbides in the UHTC formed oxides, including SiO_2 – all the SiC phase was oxidised to SiO_2.

The physical integrity of the composite is compromised by the exposure of the UHTC to excessively high temperatures before thermochemical decomposition occurs.

Thermochemical decomposition occurs predominantly by oxidation. Carbon oxidises to form gaseous CO and CO_2 as the temperatures at which the inner core of the flame will be at around 3000°C-3300°C. The release of these gases from the UHTC introduces porosity as seen in the upper layer of the scale in the UHTC exposed for 7.5s.

$$SiC + 2O_2\,(g) \rightarrow SiO_2 + CO_2\,(g) \quad (38)$$

$$C\,(s) + O_2\,(g) \rightarrow 2CO\,(g) \quad (39)$$

$$CO\,(g) + O_2\,(g) \rightarrow 2CO_2\,(g) \quad (40)$$

Ablation for 5.0s: The reactions must have occurred according to the Reactions 41 and 42:

$$4TaC\,(s) + 7O_2\,(g) \rightarrow 2Ta_2O_5\,(s) + 4CO\,(g) \quad (41)$$

$$2TiC\,(s) + 3O_2\,(g) \rightarrow 2TiO_2\,(s) + 2CO\,(g) \quad (42)$$

Ablation for 7.5s: The XRD pattern suggests that reactions must have occurred according to the Reactions 41 and 42:

$$(TaTi)C_2\ (s) + 3O_2\ (g) \rightarrow TaTiO_4\ (s) + CO\ (g) \qquad (43)$$

The XRD results show that the TaC was oxidised the most compared to the TiC and SiC in the composite. Both TaO and Ta_2O_5 were positively identified in the XRD analysis. As shown in the EPMA-BSE image in Figure 81, the major cracks in the region of interest appear at positions 6, 9 and 13. Two less intense cracks appear at positions 17 and 20.

From the graphs shown in Figure 81, the Ta graph showed a gradual decline in counts from position 1 to position 20. At crack positions, the Ta graph from LLIF spectrometer readings show some slightly elevated counts at positions 6, 9, 15 and 17. With Si, elevations are noticeable at positions 5, 7, 10, 15 and 20. The Ti graph shows a gradual decline in counts from position 1 to 20, a trend similar to the Ta graph, although the Ti graph shows some dips in counts at crack positions (6, 9, 13 and17). On the other hand, C has clear depressions at positions 6-10, 14 and 16-20.

The Ta element showed the highest counts on the surface of the scale (>6000 on TAP) than the rest of the elements. Ta shows an increased presence especially at the cracks, unlike Ti which shows a decrease in counts at the crack positions. These results suggest that Ta_2O_5-SiO_2 is more active in crack healing than the TiO_2-SiO_2 eutectic or possibly the $TaTiO_4$-SiO_2 eutectic.

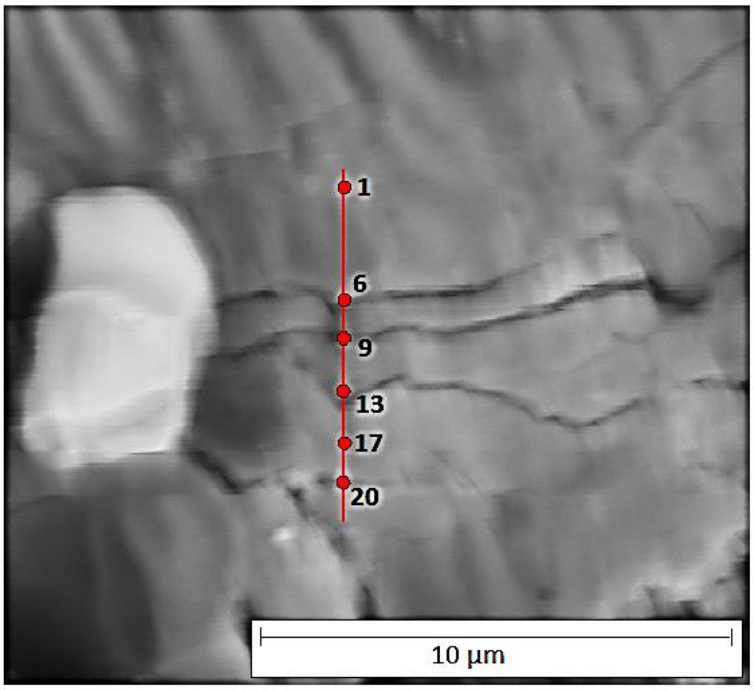

Figure 81: EPMA-BSE image of the surface of the ablated UHTC exposed to the oxyacetylene flame.

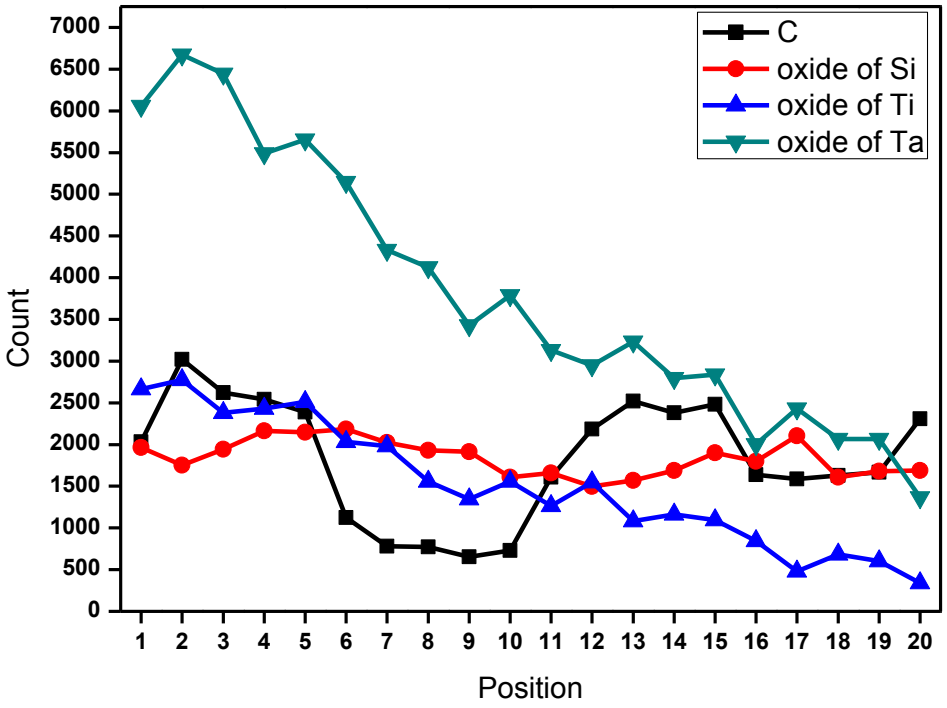

Figure 82: EPMA elemental X-ray count graphs for Ta, Ti, Si and C taken over the 20 points shown in the BSE image (Figure 81).

4.8 SUMMARY

A C_f/C composite preform of density 1.54g/cm^3 and open porosity 21% was prepared by 3 cycles of PIP using phenolic resin. An amorphous carbon matrix resulted. The Si-Ti-Ta alloy prepared by arc melting from $TaSi_2$ and $TiSi_2$ powders formed tantalum titanium silicides solid solutions [$(Ta,Ti)Si_2$ and $(Ta,Ti)_5Si_3$]. When the alloy was infiltrated into the C_f/C composite preform at 1700°C by SPS for 30 minutes carbides of Ta, Ti and Si and the (Ta,Ti)C solid solution were obtained. At an infiltration temperature of 1600°C the phase composition of the resulting composite was dominated by unreacted silicides. SiC is the only carbide which was convincingly formed, although (Ta,Ti)C was observed to have incipiently precipitated at the C/alloy interface. At an infiltration temperature of 1800°C the carbide formation reactions extended to the reinforcing fibres, thus compromising the fibres' reliability.

Upon exposure to an oxyacetylene flame at about 3000°C, the C-TaC-TiC-SiC composite showed thermomechanical degradation first, and thermochemical degradation thereafter. After 7.5s of exposure to the oxyacetylene flame, the UHTC showed a low mass ablation rate of 0.00388 g/s and no linear ablation rate owing to the scale of the oxides formed adhering to the surface of the composite. The scale showed that the composite constituents had the ability to form glassy self-healing compounds based on SiO_2.

CHAPTER 5 – DISCUSSION

5.1 OVERVIEW

This chapter interprets the results presented in Chapter 4 in the context of previous findings in literature. The microstructural aspects of the resultant C_f/C composite skeleton obtained is discussed. Interestingly, the Si-Ti-Ta alloy revealed more phases than are usually documented in literature on the $TaSi_2$-$TaSi_2$ system – the similarities and differences are deliberated on accordingly. Findings from the reaction couple and actual composite studies are used to propose a mechanism by which the C_f/C-SiC-TiC-TaC UHTC formed. Changes in the lattice parameters especially for the interstitial solid solution of (Ta,Ti)C are also deliberated on. The performance of the fabricated C_f/C-SiC-TiC-TaC UHTC under oxyacetylene flame is compared to that of similar contending UHTCs based on TaC and TiC. The mechanism by which the oxides form during exposure to an oxidising environment is discussed too.

5.2 THE C_f/C COMPOSITE PREFORM

The carbon-fibre-reinforced carbon matrix was obtained after the carbonization of the previously phenolic resin matrix by heat treatment.

In the present study were obtained XRD results similar to Tzeng (2002) on the C_f/C composite from using a constant carbonization temperature of 1000°C during the reiterated PIP cycles. The contrary aspect though, was that Tzeng (2002) used higher carbonization temperatures and also performed the graphitisation step. This similarity suggested that the duration of exposure of phenolic resin and the subsequent carbon to a certain critical carbonization temperature changes the intensity of the XRD peaks which indicated a shift in the ordering of the carbon crystallites in the matrix.

From the Raman spectroscopy prototype peak patterns presented by Chu and Li (2006), the pattern obtained herein matched that of activated charcoal at the same

wavelength (514.5nm). It is widely recognised that glass-like carbons have similar structures, regardless of the polymer source, and a similarity in the Raman scatterings too was expected. However, the Raman pattern in this work was similar to that presented by Ko *et al.* (2000). The semi-quantitative analysis of the Raman shifts and the XRD crystallite sizes indicated a highly disordered non-graphitised structure. Ko *et al.* (2000) found an increase in crystallite size during the carbonization of phenolic resin. From their work (Ko *et al.*, 2000), the carbon structure was observed to emerge at temperatures above 400°C inclusive, and the phenolic resin structures vanished completely at 600°C to give glass-like carbon. It is generally accepted that the D and G peaks give information about the sp^2 and sp^3 bonding in the carbon material analysed. The G peak is associated with the graphitic nature of the carbon. The D peak is associated with the disorder in the carbon – an indication of the graphitic range of the sample.

The folded and crumpled microstructure obtained in the present work meant that the carbon matrix has a high surface area to volume ratio. If this microstructure is to be explained by the fullerene-based model of Harris (1997, 2005), the matrix is made up of nanoparticles (crystallites) with non-six (pentagon and heptagon) member rings of carbon. sp^2 hybridised bonding dominates between the carbon atoms. The folding and curving in the structure accounts for the bits of sp^3 bonding present, although this is still to be proven. For now, the formation of closed 'pockets' or 'cages' at high temperatures is attributed to fullerene isomerisation as explained in the work of Stone and Wales (1986). This is the limitation with the fullerene related model – it does not encompass the peculiarities and reasons for the microporosity in the non-graphitizing carbon matrices.

It is known that non-graphitizing carbon is microporous. It is suiting to refer to the work of Gupta and Harrison (1994) to explain the formation of a wide range of pore sizes in the matrix. The formation of macropores occurs at temperatures below 200°C (during curing) hence a lot of heterogeneities exist in the matrix at this stage. By deduction, the large voids emanate from trapped air from the mixing of the resin with catalyst which has to be performed vigorously for about 1 minute. The other pores which may exist obviously emanate from the release of water vapour from the resin, as well as free phenolic resin. Between 450°C and 800°C the breaking

down of the crosslinks in the resin occurs hence even larger pores result in the matrix. This is because smaller pores in neighbouring vicinities to each other coalesce into fewer and larger pores. At this stage the matrix network comprises of low density areas of aromatic units and through these pyrolysis gases can permeate. Open porosity formation is dominant at this stage.

The complexity of the pore network pertaining accessibility to liquid infiltrants (indicated by the tortuosity) increased dramatically after the first densification cycle. Thereafter, it levelled off, suggesting the attainment of maximum of tortuosity in the system.

Differences in the thermal expansion of the matrix and the fibres in the C_f/C composite thus lead to anisotropic shrinkage. With surface-treated fibres, interfacial covalent bonding occurs between the functional groups of the surfactant and the resin's hydroxyl groups (Fitzer, 1998). This bonding is meant to reduce the pulling away of the matrix from the fibres. It is essential also for debonding to occur at this interface in the case of a fracturing load being applied to the composite. The formation of the longitudinal cracks along the matrix-fibre interface is serious drawback for the reactive melt infiltration process. The infiltrated alloy will have direct access to the fibres and is likely to react with the fibres, thus deteriorating their mechanical capabilities.

5.3 THE Si-Ti-Ta ALLOY

From the phase diagram (Figure 58), quenching the alloy showed to arrive at the $TaSi_2$+$TiSi_2$ phase which represents a solid solution of $TaSi_2$ and $TiSi_2$. It is known that when two transition metal silicides exist in a system, there is either a resultant solid solution, or a ternary compound. Because $TaSi_2$ and $TiSi_2$ have similar interatomic spacing (M-Si ≈ 2.65Å), the dissolution of $TiSi_2$ into $TaSi_2$ [≈52% at 1490°C (Shabalin, 2014:346)] does not change the lattice parameters (Goldschmidt, 2013). Gladyshevskii *et al.* (1964) reported that the solubility of $TaSi_2$ in $TiSi_2$ is considered insignificant.

The crystal structure of the orthorhombic $TiSi_2$ [Fmmm space group (69)] obtained in this study was previously recorded by Smith *et al.* (1997) as an intermediate phase of the C49 to C54 structures transformation. The lattice parameters herein obtained (a = 4.428Å; b = 4.779Å; c = 9.078Å) are in exact agreement with those obtained by Smith *et al.* (1997) by modelling.

The $TaSi_2$ from the present investigation, which is typified by hexagonal lattice of $CrSi_2$ (C40), had the lattice parameters of $a = b = 4.778$Å and $c = 6.565$Å. There was a slight shift of the *a* and *b* parameters from the typical $a = b = 4.783$Å (Goldschmidt, 2013: 336), as also shown in the XRD pattern by a shift of the $TaSi_2$ peaks to the left by about 0.5°. This signifies a lattice strain by expansion owing to the invasion of the crystal structure by $TiSi_2$. The lattice parameters of $TaSi_2$ in literature are scattered, however, as shown in the compilation of Schlesinger (1994)'s work on the Ta-Si system.

The existence of irregular phases in the alloy (Ta_5Si_3, Ti_5Si_3 and Si) is attributable to very high quenching rates during arc melting, which froze these otherwise metastable phases in the $TiSi_2$-$TaSi_2$ system. Concerning the pentametal-trisilicide (Ta_5Si_3 and Ti_5Si_3) phases, Kocherzhinskij *et al.* (1981) reported the existence of a eutectic between Ta_5Si_3 and $TaSi_2$ phases at 1960°C at approximately 62 at.% of Si composition. Two forms of Ta_5Si_3 are possible in the 14/mcm (140) space group – the Cr_5B_3 typified form and the W_5Si_3 typified form. When compared with the lattice parameters ($a = b = 9.86$Å and $c = 5.05$Å) reported by Nowtony *et al.* (1961), the lattice parameters ($a = b = 9.880$Å and $c = 5.060$Å) in the present work, which are in strong agreement, suggested the existence of the Cr_5B_3 form. A discrepancy thus exists between the α-Ta_5Si_3 reported by Kocherzhinskij *et al.* (1981) for the $L \leftrightarrow TaSi_2 + Ta_5Si_3$ relation and the β-Ta_5Si_3 form conditions related to the present work.

The lattice parameters for Ti_5Si_3 ($a = b = 7.448$Å and $c = 5.141$Å) closely coincide with the values ($a = b = 7.444$Å and $c = 5.143$Å) reported by Quakernaat and Visser (1974) which were for the pure form of the intermetallic. Tantalum is soluble in Ti_5Si_3 and is capable of expanding the silicide lattice structure

(Goldschmidt, 2013), but this occurrence of enlarged lattice parameters was not observed.

5.4 THE C_f/C-SiC-TiC-TaC UHTC COMPOSITE

Here it is important to discuss the mechanism by which the C_f/C-SiC-TiC-TaC UHTC composite was formed through reactive melt infiltration.

5.4.2 Alloy Infiltration

The infiltration and consequential formation of carbides in the C_f/C composite skeleton can possibly occur in two different routes:

1. At the $TiSi_2$-$TaSi_2$-Si eutectic
2. At the $TiSi_2$-$TaSi_2$ eutectic

The $TiSi_2$-$TaSi_2$-Si eutectic: The infiltration happens by virtue of a eutectic between the (Ti,Ta)Si_2-Si phases. Here the influence of the penta-trisilicides (Ta_5Si_3, Ti_5Si_3) is noteworthy, on the condition that the reaction between the M_5Si_3 and Si is slow. Infiltration occurs before equilibirum in the system reaches the eutectic reaction at about 28 at.% Ti (E_1 in Figure 58). As such, the $TiSi_2$-$TaSi_2$-Si eutectic dominates the system and infiltration takes place herein. It is important to point out that no literature was found on the $TiSi_2$-$TaSi_2$-Si eutectic.

The $TiSi_2$-$TaSi_2$ eutectic: Here the noteworthy reaction of the penta-trisilicides (Ta_5Si_3 and Ti_5Si_3) with Si occurs to give disilicides ($TiSi_2$ and $TaSi_2$) faster than the infiltration of melt into the C_f/C preform occurs. Thus equilibrium is shifted along the liquidus line to the eutectic point (E_1 in Figure 58).

5.4.3 Carbides-Formation Mechanism

From the results obtained in the present study, the matrix carbides can be envisaged to have formed by the following mechanism:

- Upon infiltration of melt into the carbon preform, the dissolution of carbon in the alloy melt occurs and precipitation reactions ensue to form initially SiC and TiC, and then (Ti,Ta)C. This reaction occurs rapidly. This is contrary to the mechanism presented by Mukasyan and White (2009) in which the rate of infiltration by Si was faster than the rate at which SiC was formed.

- Here the formation of the said carbides limits the further dissolution of carbon and the further carbide-forming reactions are controlled by the diffusion of carbon at the grain boundaries through the products layer. Here further reactions proceed slower than in the former process. As explained earlier, there exists a competition between carbide formation reaction kinetics and carbon diffusion kinetics. As such, the explanation which ascribes the formation of carbides to the diffusion of C into the melt and the consequential crystallization of the carbide (Pampuch *et al.*, 1986; Margiotta, 2009) is subscribed to.

- It is herein emphasized that the diffusion of carbon is greater than that of silicon, by virtue of the atomic radius of carbon being less than that of silicon. This assumption agrees well with the work of Wang *et al*. (2012) who fabricated a C_f/C-SiC-ZrC and attributed the mechanism to the formation of SiC first and the subsequent diffusion of carbon from the matrix through the SiC layer to reach the Zr-Si alloy and react to form a gradient SiC-ZrC matrix.

- It is known that the rate of diffusion of carbon in titanium and tantalum is two orders of magnitude greater than the rate of diffusion of the metals in carbon (Upadhyaya, 1996). Furthermore, tantalum and titanium transport fast in silicide melt. It is supposed herein that the exothermicity of the carbides forming reactions contributes to the increase in the diffusion constant of carbon across the alloy. From the data compilation by Upadhyaya (1996) on the heats of formation of carbides, TaC and TiC formation generates at least three times the heat generated by SiC formation.

Titanium and tantalum carbides precipitate together into a solid solution (Ti,Ta)C, wherein the phase diagram by English (1961) in Figure 83 depicts it as a substoichiometric (Ti,Ta)$C_{0.95}$ phase. This phase is contrary to that of Rudy (1967)

who showed a fully stoichiometric phase of (TaC,TiC). Titanium and tantalum are known to form interstitial carbides of the NaCl lattice structure (cubic-face-centred) with non-stoichiometric compositions. Here the carbon atoms squeeze and fit into the transition metal lattice. The homogeneity of the carbides is not perfect – the interstitial places in the octahedral metal structure are filled with carbon atoms but not always completely (Upadhyaya, 1996).

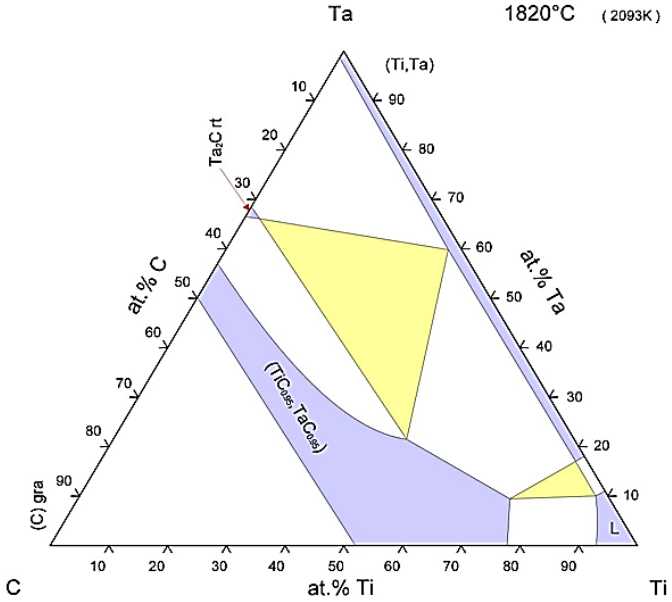

Figure 83: Isothermal ternary phase diagram for the Ta-Ti-C system at 1820°C (English, 1961).

5.5 PERFORMANCE OF THE C_f/C COMPOSITE

Observations on the thermomechanical degradation of the C_f/C composite preform when exposed to an oxyacetylene flame agree well with the findings of Zaman *et al.* (2012). Zaman *et al.* (2012) also found that matrix ablation was greater than fibre ablation. Ablation of the outer fibre layers proceeded faster than the inner core layers. As such, fibres acquired a needle-like shape initially, and then degraded to blunt shaped edges. In the present work only the former shape was observed versus the latter, most likely because of the shorter exposure times used herein. The degradation of the fibre outer shell has also been reported by Farhan *et al.* (2013).

Table 20: Comparison of the mass and linear ablation rates of the C_f/C composite fabricated in the present work to similar C_f/C composites in literature.

Composite	Mass Ablation Rate (g/s)	Linear Ablation Rate (mm/s)	References	Comment
C_f/C	0.0402	0.0377	Present Work	2D composite prepared by PIP from phenolic resin and PAN fibres Exposed to oxyacetylene flame at 4.2MW/m^2 for 7.5s.
C_f/C	0.0127	0.0333	Paul *et al.* (2013)	Prepared by phenolic resin slurry impregnation and pyrolysis route Exposed to flame for 30s.
C_f/C	0.00231[a] 0.00332[b]	0.00318[a] 0.00630[b]	Zaman *et al.* (2012)	Four directional composite made from 2 coal tar pitches and PAN fibres. Exposed to oxyacetylene flame for 30s.
C_f/C	≈3.5	≈0.001	Farhan *et al.* (2013)	Four directional composite made from from 2 coal tar pitches. Testing by arc jet at Mach number 1.13–1.19 and heat flux 4 MW/m^2 for 30s.
[a] value for z-direction fibres – fibres transverse to the surface of the composite [b] value for xy-fibres - fibres parallel to the surface of the composite				

From Table 20, the work of Zaman *et al.* (2012) is peculiar from the rest in that the ablation rates decreased with increase in exposure time. The linear ablation rate in the present study compares well to that of Paul *et al.* (2013), although the mass ablation rate in the former is more than three times in the latter study. On the other hand, Farhan *et al.* (2013)'s mass ablation rate on the 4-D C_f/C composite they prepared is two orders higher than obtained in this work, and three orders greater than the rates obtained by Zaman *et al.* (2012). The difference between Farhan *et*

al. (2013) and Zaman *et al.* (2012) is very unusual considering the similarity in the materials they synthesized.

5.6 PERFORMANCE OF THE C_f/C-SiC-TiC-TaC UHTC COMPOSITE

Ablation Rates

Comparison of the C_f/C-SiC-TiC-TaC UHTC composite in the present study with closely related UHTCs recorded in literature shows that the mass and linear ablation rates in the present work are one order lower than the rest as shown in Table 21.

Table 21: Comparison of the mass and linear ablation rates of the C_f/C-SiC-TiC-TaC fabricated in the present work to similar UHTCs in literature.

Composite	Mass Ablation Rate (g/s)	Linear Ablation Rate (mm/s)	References	Comment
C_f/C-SiC-TiC-TaC	0.0038	0.00216	Present Work	Prepared by PIP-RMI Ablation for 7.5s, flame 19mm away
C_f/C-TaC-SiC	0.021	-	Pienti *et al.* (2015)	32 vol.% of TaC
C_f/TaC-SiC	0.0116 0.017	0.026 0.013	Zhang *et al.* (2008) Hu *et al.* (2013)	60 vol.% TaC. Prepared by SI-LSI Ablation for 60s, flame 10 mm away. Back T ≈ 2100°C. Prepared by SI-PIP
C_f/Si	0.0103 0.0166	0.042 0.062	Fan *et al.* (2012) Zhang *et al.* (2008)	Prepared by SI-LSI Ablation for 60s, flame 10 mm away. Back T ≈ 2100°C. Prepared by SI-PIP
C_f/SiC/Ti_3SiC_2	0.0063	0.024	Fan *et al.* (2012)	A ceramic/MAX phase composite made by SPS

It is important to immediately point out that it is very difficult to compare mass and linear ablation rates in literature considering the diversity of ablation test procedures and parameters used by different scholars. Although the two most

common standards are the National Standard Committee of China's GJB323A-96 and the American Society for Testing and Materials' E285-08, numerous studies still differ on the distance of the UHTC sample from the flame; the oxygen and acetylene flow rates; and the duration of exposure of the sample to the flame. As such the subsequent discussion will dwell on the products of ablation rather.

Ablation products

XRD studies on the oxidation of the C_f/C-SiC-TiC-TaC UHTC composite revealed the existence of $TiTaO_4$ of the space group P42/mnm (136) and of a tetragonal structure with lattice parameters $a = b = 4.61100$Å, and $c = 2.98200$Å. Studies on the $TiTaO_4$ compound conducted by Petersen et al (1992) showed that this is a ternary compound where the oxidation states of the transition metals are Ti^{3+} and Ta^{5+}. Here the $TiTaO_4$ compound is typified by the rutile structure (TiO_2). There is limited literature on the formation of this ternary compound.

Previous studies by Pienti *et al.* (2015) have shown that a Ta_2O_5-SiO_2 eutectic melt is formed at 1560°C and the glassy Ta-Si-O phase is capable of sealing the cracks in the UHTC thus protecting it from excessive oxygen ingress. The Ta_2O_5 was said to precipitate from the melt later. Ta-Si-O and Si-C-O glassy phases were both formed in the system studied by Pienti *et al.* (2015).

At the interface SiO is in vapour form while SiO_2 is in molten form. The increase in the vapour pressure of SiO exacerbates the degradation of the SiO_2 glassy protection. The reaction of the diffusing SiO with oxygen at the interface results in the much desired SiO_2 which heals the composite. When the vapour pressure of SiO is greater than the atmospheric pressure, the SiO ruptures the SiO_2 scale formed (Opeka *et al.*, 2004; Li *et al.*, 2008).

At lower temperatures (<1600°C), SiC is oxidised passively as in Equations 45 – 46. The SiO_2 scale formed grows and blocks oxygen from reaching the virgin composite due to SiO_2's low permeability to oxygen. Active oxidation then kicks in with increasing temperature and lower oxygen pressure, whereby the previously formed SiO_2 and the virgin SiC reacts with oxygen (in plasma gas form) as in Equations 47 - 49. Thus the SiO_2 is lost subject to the low oxygen pressure (Opeka

et al., 2004; Li *et al*., 2008). The diffusion coefficient of oxygen through the formed oxide species also determines the amount of protection the oxide is capable of providing to the UHTC.

$$SiC\ (s) + O_2\ (g) \rightarrow SiO_2\ (s) + CO_2\ (g) \quad (45)$$

$$2SiC\ (s) + 3O_2\ (g) \rightarrow 2SiO_2\ (l) + 2CO\ (g) \quad (46)$$

$$SiO_2\ (s) + O\ (g) \rightarrow SiO(s) + O_2\ (g) \quad (47)$$

$$SiC\ (s) + O_2\ (g) \rightarrow SiO\ (g) + CO\ (g) \quad (48)$$

$$SiC\ (s) + 2SiO_2\ (g) \rightarrow 3SiO\ (g) + CO\ (g) \quad (49)$$

Numerous studies identified a layer of SiO_2 at the surface of exposure of the UHTC. Results obtained herein seem to be contradictory to the explanation of Yi *et al.* (2010) that the SiO_2 formed is sublimated and cannot be identified in the resultant ablated UHTC. This notion was also supported by the findings of Chen et al (2013) who identified SiO_2 in the UHTCs that were oxidised under stagnant air at 1200°C, but did not detect the same for the UHTCs that were ablated under an oxyacetylene flame at about 3000°C.

The gradient ash profile advances into the bulk of the composite. The volatile gases formed expand within the composite structure and when beyond the critical vapour pressure of equilibrium the gases break out rupturing the composite and leaving behind some pores. As the release of gases intensifies, as does the rupturing in the composite, spongy flakes burst outwards from the inside in a popping fashion – hence the parallel to the manner in which popcorn pops and the resultant morphology.

The bursting apart of the composite exposes the inside of the composite to oxygen, hence exacerbating the oxidation reactions in the composite. This also advances the sites of oxidation and this is how the scale profile extends into the bulk of the composite.

CHAPTER 6 – CONCLUSIONS

6.1 OVERVIEW

A novel C_f/C-SiC-TiC-TaC composite was successfully fabricated by combining two successive liquid infiltration methods - phenolic resin infiltration and pyrolysis, followed by reactive melt infiltration of Si-Ti-Ta alloy. A predominantly carbide matrix of SiC, TaC, TiC, and solid solution of (Ta,Ti)C was obtained. Characterisation of the composite under oxyacetylene flame at around 3000°C showed impressive linear ablation resistance and good mass ablation resistance. Oxidation reactions produced scale which was not easily eroded away, and combinations of glassy phases with seal-healing abilities on the cracks that formed in the composite were characteristic of the C_f/C-SiC-TiC-TaC composite. As such, the C_f/C-SiC-TiC-TaC composite promises to be a good candidate for extreme environments encountered in hypersonic flight aerospace and aircraft vehicles.

6.2 CONCLUSIONS

From the results and findings presented in Chapter 4, the following conclusions were arrived at:

- An amorphous and pseudo-glassy carbon-fibre-reinforced carbon matrix was obtained by curing a resole phenolic resin at 100°C for 8 hours and carbonising at 1000°C for 1 hour, in three iterative steps of densification. The C_f/C composite had a density of 1.54g/cm^3 and open porosity of 21%. The pore size distribution was largely macroporous with a wide range of 3.2 – 31.6µm pore diameters.

- During pyrolysis a violent reaction occurs between 250°C and 350°C. This causes the conchoidal fracturing of the matrix and the consequential delamination of the carbon-carbon composite layers. A considerable number of initial C_f/C composites fail at this stage during processing.

- The 66.7Si-17.9Ti-15.4Ta alloy prepared by arc melting from $TaSi_2$ and $TiSi_2$ powders formed an interstitial solid solution of (Ta,Ti)Si_2. Ta_5Si_3 and Ti_5Si_3 were also identified as metastable phases, associated with free silicon.

- Reactive melt infiltration was a successful technique for melting and infiltrating the Si-Ti-Ta alloy into the initial C_f/C composite, and the consequential reaction with the carbon matrix. A temperature of 1700°C was reckoned acceptable for the formation of the C_f/C-SiC-TiC-TaC composite by pressureless spark plasma sintering for a processing duration of 30 minutes.

- Infiltration of the 66.7Si-17.9Ti-15.4Ta (at.%) alloy occurs at the $TiSi_2$-$TaSi_2$-Si eutectic point (influenced by the the penta-trisilicides, Ta_5Si_3 and Ti_5Si_3) or at the $TiSi_2$-$TaSi_2$ eutectic point (whereby the penta-trisilicides initially react with Si and have no influence on the infiltration). Non-eutectic composition infiltration can occur with mixed liquid-solid alloy phases, giving rise to a gradient of phases across the height of the preform.

- Monocarbides of the alloy constituent elements (TaC, TiC, and SiC) and the solid solution of (Ta,Ti)C were formed by a mechanism in which carbon in the C_f/C matrix dissolved in the alloy upon contact. Thereafter reactions proceed by carbon diffusion through the carbides layer. The resultant was a matrix consisting of precipitated (Ta,Ti)C solid solution embedded in bulk SiC.

- The homogeneity of the carbides formed [SiC, TaC, TiC and (Ta,Ti)C] increased with an increase in the RMI temperature. A functionally-graded carbides matrix profile was not necessarily obtained in this work as was initially anticipated. Such a structure was only obtained at low RMI temperatures (1600°C) wherein both molten alloy infiltration and transition metal carbides formation was limited. At higher temperatures (1700°C and 1800°C), a fairly homogeneous microstructure of the said carbides [SiC, TaC, TiC and (Ta,Ti)C] is obtained because of the formation of solid solutions. At 1600°C the (Ta,Ti)C solid solution consisted of about 47.2 at.% of TaC (52.8 at.% TiC), at 1700°C the (Ta,Ti)C solid solution consisted of about 58.5 at.%

of TaC (41.5 at.% TiC), and at 1800°C the solid solution consisted of about 61.0 at.% of TaC (39.0 at.% TiC).

- A temperature trade-off is required in performing reactive melt infiltration – a high temperature ensures sufficient alloy transport and satisfactory extent of carbide-forming reactions consequential reaction, at the cost of fibre damage however. Fibre damage compromises the fracture toughness of the overall composite. In the present work such a high temperature was 1800°C. A low temperature limits the extent and rate of carbide formation reactions, and such a temperature in the present work was 1600°C.

- Upon exposure to an oxyacetylene flame according to the ASTM E285-80(2002) Standard Test Method for Oxyacetylene Ablation Testing of Thermal Insulation Materials, for 7.5s, the C_f/C-SiC-TiC-TaC UHTC shows an impressive mass ablation rate of 0.00388 g/s and a linear ablation rate of 0.00216 mm/s. The ablation rates are an order lower than those obtained for plain the C_f/C composite (mass ablation rate of 0.0402g/s and a linear ablation rate of 0.377 mm/s).

- Thermomechanical ablation precedes thermochemical ablation when the C_f/C-SiC-TiC-TaC UHTC is exposed to an oxyacetylene flame. The ash profile revealed that the oxidation of the composite occurs in gradient profile which advances into the bulk of the composite. The volatile gases formed expand within the composite structure and when beyond the critical vapour pressure of equilibrium the gases break out rupturing the composite and leaving behind some pores. As the release of gases intensifies, so does the rupturing in the composite. Spongy flakes burst outwards from the inside in a popping fashion – similar to the manner in which popcorn bursts and the resultant morphology. The bursting apart of the composite exposes the inside of the composite to oxygen, hence exacerbating the oxidation reactions in the composite. This also advances the sites of oxidation and this is how the scale profile extends into the bulk of the composite.

- The C-SiC-TiC-TaC matrix, when in service, cracks due to thermal expansion mismatches of the carbides contained therein. Glassy phases of SiO_2, and possibly $TaTiO_4$-SiO_2 and Ta_2O_5-SiO_2 are formed during oxidation reactions; they intrude and fill-up the cracks, and hence heal-up the matrix.

6.3 RECOMMENDATIONS

- The present study has explored the possibility of performing RMI at a non-eutectic composition of the $TaSi_2$-$TiSi_2$ and the shortcoming of obtaining a macro-gradient of phases across the depth of the UHTC discs has been recorded.

  Studies on performing RMI at eutectic composition are therefore recommended for future work.

- Further studies could be done focussing on the optimisation of the amount of alloy that would fully impregnate the composite and leaving no residual layer on the surface of the composite.

- Mechanical characterisation of the C_f/C-SiC-TiC-TaC UHTC composite is important for determining its structural capabilities in service. Here mechanical tests could be conducted on both the virgin composite and the ablated composite for comparison purposes. Fracture toughness, hardness, flexural strength etc. are some key properties to test.

- More oxidation and ablation tests could be done to confirm the results presented in this study. These can be in the form of arc jet testing, wind tunnel testing, laser heating, air furnace heating etc.

REFERENCES

Ahmad, S., Azad, A., & Loughlin, K. (2005). A study of permeability and tortuosity of concrete. In *30th conference on our world in concrete and structures* (pp. 23-24).

Aligizaki, K. K. (2005). *Pore structure of cement-based materials: testing, interpretation and requirements*. CRC Press.

Astrov, D.N., Kryukova, N.A., Zorin, R.B., Makarov, V.A., Ozerov, R.P.; Rozhdestvenskii, F.A., Smirnov, V.P., Turchaninov, A.M. (1972) in ICDS Database. Available from: <https://icsd.fiz-karlsruhe.de/search/basic.xhtml;jsessionid=488DA42252298404A51EBA9F669A2E9B>. [23 March 2015].

Atta-Obeng, E. (2011). *Characterization of phenol formaldehyde adhesive and adhesive-wood particle composites reinforced with microcrystalline cellulose*(Doctoral dissertation, Auburn University).

Ban, L. L., Crawford, D., & Marsh, H. (1975). Lattice-resolution electron microscopy in structural studies of non-graphitizing carbons from polyvinylidene chloride (PVDC). *Journal of Applied Crystallography*, *8*(4), 415-420.

Barbante, P. F., & Magin, T. E. (2004). Fundamentals of hypersonic flight–Properties of high temperature gases. *RTO AVT Lecture Series on "Critical Technologies for Hypersonic Vehicle Development"(von Karman Institute, Rhode-Saint-Genese, Belgium, 2004), RTO-EN-AVT-116*, 5-1.

Bellosi, A., Monteverde, F., & Sciti, D. (2006). Fast Densification of Ultra-High-Temperature Ceramics by Spark Plasma Sintering. *International journal of applied ceramic technology*, *3*(1), 32-40.

Bergin, C. (2013). Falcon 9 boost as Merlin 1D engine achieves major milestone, March 20, 2013. Available from: <http://www.nasaspaceflight.com/2013/03/falcon-9-boost-merlin-1d-engine-achieves-milestone/>. [19 October 2013].

Bruker (2013). Total Pattern Analysis Solution (TOPAS), TOPAS_Flyer_DOC-H88-EXS013_V2, Bruker

Carney, C. M., Parthasarathy, T. A., & Cinibulk, M. K. (2011). Oxidation resistance of hafnium diboride ceramics with additions of silicon carbide and tungsten boride or tungsten carbide. *Journal of the American Ceramic Society*, *94*(8), 2600-2607.

Castaing, J., & Costa, P. (1977). Properties and uses of diborides. In *Boron and Refractory Borides* (pp. 390-412). Springer Berlin Heidelberg.

Chen, S., Hu, H., Zhang, Y., Zhang, C., & Wang, Q. (2013). Effects of TaC amount on the properties of 2D C/SiC–TaC composites prepared via precursor infiltration and pyrolysis. *Materials & Design*, *51*, 19-24.

Chen, Y., Chen, Z., Xiao, S., & Liu, H. (2008). A novel thermal degradation mechanism of phenol–formaldehyde type resins. *Thermochimica Acta*, *476*(1), 39-43.

Chen, Z. K., Xiong, X., Li, G. D., & Wang, Y. L. (2009). Ablation behaviors of carbon/carbon composites with C-SiC-TaC multi-interlayers. *Applied Surface Science*, *255*(22), 9217-9223.

Chu, P. K., & Li, L. (2006). Characterization of amorphous and nanocrystalline carbon films. Materials Chemistry and Physics, *96*(2), 253-277.

Clougherty, E., Pober, R., & Kaufman, L. (1968). Synthesis of Oxidation Resistant Metal Diboride Composites. *Transactions of the Metallurgical Society of the AIME*, *242*(6), 1077–1082.

Composites Technology (2013a). *GKN invests in microwave oven for composites curing*. Available from: <http://www.compositesworld.com/news/gkn-invests-in-microwave-oven-for-composites-curing>. [27 October 2013].

Composites Technology (2013b). *Large industrial microwave system*. Available from: <http://www.compositesworld.com/products/large-industrial-microwave-system>. [27 October 2013].

Conley, R. T., & Bieron, J. F. (1963a). A kinetic study of the oxidative degradation of phenol-formaldehyde polycondensates using infrared spectroscopy. *Journal of Applied Polymer Science*, *7*(1), 171-180.

Conley, R. T., & Bieron, J. F. (1963b). A study of the oxidative degradation of phenol-formaldehyde polycondensates using infrared spectroscopy. *Journal of Applied Polymer Science*, *7*(1), 103-117.

Cornell, V. P. (2009). Resins for the Hot Zone, Part I: Polyimides. *High-Performance Composites. Composites World*, July 2009. Available from: <http://www.compositesworld.com/articles/resins-for-the-hot-zone-part-i-polyimides>. [28 August 2013].

Creighton, J. R., & Ho, P. (2001). Introduction to CVD in J.H. Park & T.S. Sudarshan (eds), *Chemical Vapour Deposition*, Ohio: ASM International.

Darcy H. (1856). *Les fontaines publiques de la ville de Dijon: exposition et application des principes à suivre et des formules à employer dans les questions de distribution d'eau*. Victor Dalmont.

Devi, G. R., & Rao, K. R. (2013). Carbon Carbon Composites: An Overview. *Defence Science Journal*, *43*(4), 369-383.

Dezellus, O., & Eustathopoulos, N. (1999). The role of van der Waals interactions on wetting and adhesion in metal/carbon systems. *Scripta Materialia*, *40*(11), 1283-1288.

Dezellus, O., Hodaj, F., & Eustathopoulos, N. (2003). Progress in modelling of chemical-reaction limited wetting. *Journal of the European Ceramic Society*, *23*(15), 2797-2803.

Dezellus, O., Hodaj, F., Mortensen, A., & Eustathopoulos, N. (2001). Diffusion-limited reactive wetting: spreading of Cu-Sn-Ti alloys on vitreous carbon. *Scripta materialia*, *44*(11), 2543-2549.

Dhami, T. L., & Bahl, O. P. (2005). *Challenges in Carbon/Carbon Composites Technologies.*

English, J.J. (1961). C-Ta-Ti Phase Diagram. ASM Alloy Phase Diagrams Center http://www1.asminternational.org/asmenterprise/APD/PrintViewAPD.aspx>. [28 August 2013].

Fahrenholtz, W. G., Hilmas, G. E., Talmy, I. G., & Zaykoski, J. A. (2007). Refractory diborides of zirconium and hafnium. *Journal of the American Ceramic Society*, *90*(5), 1347-1364.

Fan, X., Yin, X., He, S., Zhang, L., & Cheng, L. (2012). Friction and wear behaviors of C/C-SiC composites containing Ti< sub> 3</sub> SiC< sub> 2</sub>. *Wear*, *274*, 188-195.

Fan, X., Yin, X., Wang, L., Cheng, L., & Zhang, L. (2013). Processing, microstructure and ablation behavior of C/SiC–Ti< sub> 3</sub> SiC< sub> 2</sub> composites fabricated by liquid silicon infiltration. *Corrosion Science*, *74*, 98-105.

Farhan, S., Ul-Haq, N., & Kuo, W. S. (2013). Degradation behavior of 4D carbon/carbon composites under supersonic oxidative air plasma. *Ceramics International*, *39*(6), 7135-7142.

Fitzer, E. (1998). *Carbon reinforcements and carbon/carbon composites*. Springer.

Foust, J. (2014) SpaceX launches Thaicom 6, *NewSpace Journal*.

Franck, A. (2004). *Understanding Rheology of Thermosets*. TA Instruments AAN015.

Franklin, R. E. (1951). Crystallite growth in graphitizing and non-graphitizing carbons. Proceedings of the Royal Society of London. Series A. Mathematical and Physical Sciences, *209*(1097), 196-218.

Gern, F. H., & Kochendörfer, R. (1997). Liquid silicon infiltration: description of infiltration dynamics and silicon carbide formation, *Composites Part A: Applied Science and Manufacturing*, *28*(4), 355-364

Gladyshevskii, E. I., Lakh, V. I., Skolozdra, R. V., & Stadnik, B. I. (1964). The mutual solubility of disilicides of the transition metals from groups IV, V, and VI. *Powder Metallurgy and Metal Ceramics*, *3*(4), 278-282.

Goldschmidt, H. J. (2013). *Interstitial alloys*. Elsevier.

Goodman, D.L., & Palmese, G.R. (2002). Curing and Bonding of Composites using Electron Beam Processing in *Handbook of Polymer Blends and Composites*, A. Kulshreshtha and C. Vasile, (eds.) Vol 1 (pp 459-498). Rapra Technology Ltd.

Griffiths, S. K., & Nilson, R. H. (2000). Chemical Vapor Infiltration: Optimization of Processing Conditions. *Surface Engineering Series Volume 2: Chemical Vapor Deposition, 2*, 183.

Guo, W., Xiao, H., Yasuda, E., & Cheng, Y. (2006). Oxidation kinetics and mechanisms of a 2D-C/C composite. *Carbon*, *44*(15), 3269-3276.

Gupta, A., & Harrison, I. R. (1994). Small-angle X-ray scattering (SAXS) in carbonized phenolic resins. *Carbon*, *32*(5), 953-960.

Han, J. C., He, X. D., & Du, S. Y. (1995). Oxidation and ablation of 3D carbon-carbon composite at up to 3000 C. *Carbon*, *33*(4), 473-478.

Harris, P. J. F. (1997). Structure of non-graphitising carbons. *International Materials Reviews*, *42*(5), 206-218.

Harris, P. J. F. (2005). New perspectives on the structure of graphitic carbons. *Critical Reviews in Solid State and Materials Sciences*, *30*(4), 235-253.

Harris, P. J. F., & Tsang, S. C. (1997). High-resolution electron microscopy studies of non-graphitizing carbons, *Philosophical Magazine A* **76**(3), 667-677.

Heppenheimer, T. A. (2009). *Facing the Heat Barrier: A History of Hypersonics*. NASA History Series. Government Printing Office, USA.

Holder, D.W. & Monaghan, R. J. (1960). Wind Tunnels and Shock Tunnels for Hypersonic Research, *The New Scientist*, 20 October 1960.

Hu, H., Wang, Q., Chen, Z., Zhang, C., Zhang, Y., & Wang, J. (2010). Preparation and characterization of C/SiC–ZrB 2 composites by precursor infiltration and pyrolysis process. Ceramics International, *36*(3), 1011-1016.

Hu, H., Zhang, Y., Zhang, C., & Wang, Q. (2013). Effects of TaC amount on the properties of 2D C/SiC–TaC composites prepared via precursor infiltration and pyrolysis. *Materials & Design*, *51*, 19-24.

Inagaki, M. (2013). Advanced Carbon Materials in *Handbook of Advanced Ceramics: Materials, Applications, Processing, and Properties*, Ed. S. Somiya, Academic Press, 2nd Edition, 25-60

Inagaki, M., & Kang, F. (2006). *Carbon materials science and engineering: from fundamentals to applications*. 清华大学出版社有限公司.

Inagaki, M., & Kang, F. (2014). *Materials Science and Engineering of Carbon: Fundamentals*, Butterworth-Heinemann

Jackson, W. M., & Conley, R. T. (1964). High temperature oxidative degradation of phenol–formaldehyde polycondensates. *Journal of Applied Polymer Science*, *8*(5), 2163-2193.

Jacobson, N. S., & Curry, D. M. (2006). Oxidation microstructure studies of reinforced carbon/carbon. *Carbon*, *44*(7), 1142-1150.

Jiang, D. E., Van Duin, A. C., Goddard III, W. A., & Dai, S. (2009). Simulating the initial stage of phenolic resin carbonization via the ReaxFF reactive force field. *The Journal of Physical Chemistry A*, *113*(25), 6891-6894.

Jiang, H., Wang, J., Wu, S., Wang, B., & Wang, Z. (2010). Pyrolysis kinetics of phenol–formaldehyde resin by non-isothermal thermogravimetry. *Carbon*, *48*(2), 352-358.

Jiang, H., Wang, J., Wu, S., Yuan, Z., Hu, Z., Wu, R., & Liu, Q. (2012). The pyrolysis mechanism of phenol formaldehyde resin. *Polymer Degradation and Stability*, *97*(8), 1527-1533.

Johnson, S. (2011). Ultra High Temperature Ceramics: Application, Issues and Prospects. 2nd Ceramic Leadership Summit, Baltimore, MD.

Katzman, H. A. (1990). *Polyacrylacetylene Resin Composites.* California: Defense Technical Information Center.

Kerrebrock, J. L. (1989). *Hypersonic Technology for Military Application***,** Washington, DC: National Academies Press.

Klučáková, M. (2004). Rheological properties of phenolic resin as a liquid matrix precursor for impregnation of carbon–carbon composites with respect to conditions of the densification process. *Composites science and technology*,*64*(7), 1041-1047.

Ko, T. H., Kuo, W. S., & Chang, Y. H. (2001). Microstructural changes of phenolic resin during pyrolysis. *Journal of applied polymer science*, *81*(5), 1084-1089.

Ko, T. H., Kuo, W. S., & Lu, Y. R. (2000). The influence of post-cure on properties of carbon/phenolic resin cured composites and their final carbon/carbon composites. *Polymer composites*, *21*(1), 96-103.

Kocherzhinskij, Yu. A., Kulik, O.G., & Shishkin, E.A. (1981). Phase diagram of the tantalum - silicon system. *Doklady Akademii Nauk SSSR, 261*(1), 106-108.

Komolafe, B., & Medraj, M. (2014). Progress in Wettability Study of Reactive Systems. *Journal of Metallurgy*, 2014.

Kosolapova, T. Y. (1971). Carbides: Properties, Production, and Applications.

Krenkel, W., (2009). Cost effective processing of CMC composites by melt infiltration (LSI-process). In *Ceramic Engineering and Science Proceedings*, 443-454.

Kudielka, H. and Nowotny, H. (1956). *Si-Ta-Ti Phase Diagram*. ASM Alloy Phase Diagrams Centre. Available from: <http://www.asminternational.org/asmenterprise/APD>. [19 March 2013].

Kumar, A., Lobo, R. F., & Wagner, N. J. (2005). Porous amorphous carbon models from periodic Gaussian chains of amorphous polymers. *Carbon*, *43*(15), 3099-3111

Labruquere, S., Bourrat, X., Pailler, R., & Naslain, R. (2001). Structure and oxidation of C/C composites: role of the interface. *Carbon*, *39*(7), 971-984.

Lamouroux, F., Bertrand, S., Pailler, R., Naslain, R., & Cataldi, M. (1999). Oxidation-resistant carbon-fiber-reinforced ceramic-matrix composites. *Composites Science and Technology*, *59*(7), 1073-1085.

Landry, K., Kalogeropoulou, S., & Eustathopoulos, N., (1998) Wettability of carbon by aluminum and aluminum alloys, *Materials Science and Engineering A254*, 99–111

Levine, S. R., Opila, E. J., Halbig, M. C., Kiser, J. D., Singh, M., & Salem, J. A. (2002). Evaluation of ultra-high temperature ceramics for aeropropulsion use. *Journal of the European Ceramic Society*, *22*(14), 2757-2767.

Li, J., Lenosky, T. J., Först, C. J., & Yip, S. (2008). Thermochemical and mechanical stabilities of the oxide scale of ZrB2+ SiC and oxygen transport mechanisms. *Journal of the American Ceramic Society*, *91*(5), 1475-1480.

Li, K. Z., Shen, X. T., Li, H. J., Zhang, S. Y., Feng, T., & Zhang, L. L. (2011). Ablation of the carbon/carbon composite nozzle-throats in a small solid rocket motor. *Carbon*, *49*(4), 1208-1215.

Lopata, J. V., & Sidwell, D. R. (2003). *Electron Beam Processing for Composite Manufacturing and Repair*, Radtech Report September/October 2003, 32-34.

Ma, W., Wang, S., Cui, J. P., Zhang, S. T., Fan, B. C., & He, Y. Z. (2008). Thermal decomposition kinetic model of phenolic resin. *Acta Physico-Chimica Sinica*, *24*(6), 1090-1094.

Manocha, L. M. (2003). *High performance carbon-carbon composites.* Sadhana, 28(1-2), 349-358.

Margiotta, J. C. (2009). *Study of Silicon Carbide Formation by Liquid Silicon Infiltration of Porous Carbon Structures*. ProQuest.

McKee, D. W. (1987). Oxidation behavior and protection of carbon/carbon composites. *Carbon*, *25*(4), 551-557.

McMullin, J. G., Norton, J. T., Cadoff, I., & Nielsen, J. P. (1953). The Ternary System Ti-Ta-C. *J. Metals*, *5*(9), 1205-1208.

Meetham, G. W., Van de Voorde, M. H., & Voorde, M. H. (2000). *Materials for high temperature engineering applications*. Springer.

Monteverde, F., Bellosi, A., & Scatteia, L. (2008). Processing and properties of ultra-high temperature ceramics for space applications. *Materials Science and Engineering: A*, *485*(1), 415-421.

Mukasyan, A. S., & White, J. D. (2009). Electrically induced liquid infiltration for the synthesis of carbon/carbon–silicon carbide composite. *Ceramics International*, *35*(8), 3291-3299.

Naslain, R. (2004). Design, preparation and properties of non-oxide CMCs for application in engines and nuclear reactors: an overview. *Composites Science and Technology*, *64*(2), 155-170.

Naslain, R. (2006). Ceramic Matrix Composites: Matrices and Processing, *Concise encyclopedia of composite materials* (Ed. A. Mortensen). Elsevier, 140-146.

National Research Council (1995). *Reusable Launch Vehicle: Technology Development and Test Program.* Washington, DC: National Academies Press.

Nelson, E. S., & Collela, P. (2000). *Parametric study of reactive melt infiltration*. NASA/TM-2000-209802.

Nowotny, H. and Laube, E. (1961). The Thermal Expansion of High Melting-Point Phases, *Planseeber. Pulvermetall., 9*, 54-59.

Opeka, M. M., Talmy, I. G., & Zaykoski, J. A. (2004). Oxidation-based materials selection for 2000 C+ hypersonic aerosurfaces: theoretical considerations and historical experience. *Journal of materials science*, *39*(19), 5887-5904.

Ouchi, K. (1966). Infra-red study of structural changes during the pyrolysis of a phenol-formaldehyde resin. *Carbon*, *4*(1), 59-66.

Ouchi, K., & Honda, H. (1959). Pyrolysis of coal. 1. Thermal cracking of phenolformaldehyde resins taken as coal models. *Fuel*, *38*(4), 429-443.

Palmisiano, M. N., Jakubenas K. J., & Baranwal, R. (2004). *Reaction-Forming Method for Producing Near Net-Shape Refractory Metal Carbides*. Patent No. US 6,764,620 B1, United States of America.

Pampuch, R., Walasek, E., & Bialoskorski, J. (1986). Reaction mechanism in carbon-liquid silicon systems at elevated temperatures. *Ceramics International*,*12*(2), 99-106.

Parker, J. A. (1967). *The effects of molecular structure on the thermochemical properties of phenolics and related polymers*. National Aeronautics and Space Administration.

Parthasarathy, T. A., Kerans, R. J., & Opeka, M. (2007b). *A Model for the Oxidation of Refractory Diborides (Preprint)*. UES INC DAYTON OH.

Parthasarathy, T. A., Rapp, R. A., Opeka, M., & Kerans, R. J. (2007a). A model for the oxidation of ZrB< sub> 2</sub>, HfB< sub> 2</sub> and TiB< sub> 2</sub>. *Acta Materialia*, *55*(17), 5999-6010.

Parthasarathy, T. A., Rapp, R. A., Opeka, M., & Kerans, R. J. (2009). Effects of phase change and oxygen permeability in oxide scales on oxidation kinetics of ZrB2 and HfB2. *Journal of the American Ceramic Society*, *92*(5), 1079-1086.

Paul, A., Venugopal, S., Binner, J. G. P., Vaidhyanathan, B., Heaton, A. C. J., & Brown, P. M. (2013). UHTC–carbon fibre composites: Preparation, oxyacetylene torch testing and characterisation. *Journal of the European Ceramic Society*, *33*(2), 423-432.

Paul, D. B., Clay, C. L., Harber, B., Croop, H., Glass, D., & Scotti, S. (2000). Extreme environment structures. *Progress in Astronautics and Aeronautics*, *188*, 145-200.

Peters, M., Hemptenmacher, J., Kumpfert, J., & Leyens, C. (2003). Structure and properties of titanium and titanium alloys. *Titanium and Titanium Alloys: Fundamentals and Applications*, 1-36.

Petersen, A., Mueller Buschbaum, H. (1950) in ICDS Database. Available from: <https://icsd.fiz-karlsruhe.de/search/basic.xhtml;jsessionid=488DA42252298404A51EBA9F669A2E9B>. [19 March 2015].

Pienti, L., Sciti, D., Silvestroni, L., Cecere, A., & Savino, R. (2015). Ablation tests on HfC-and TaC-based ceramics for aeropropulsive applications. *Journal of the European Ceramic Society*, *35*(5), 1401-1411.

Pierson, H. O. (1996). *Handbook of Refractory Carbides & Nitrides: Properties, Characteristics, Processing and Apps*. William Andrew.

Qian, Y., Zhang, W., Ge, M., & Wei, X. (2013). Frictional response of a novel C/C-ZrB2-ZrC-SiC composite under simulated braking. *Journal of Advanced Ceramics*, *2*(2), 157-161.

Quakemaat, J. and J.W. Visser. *High Temperatures - High Pressures* 6: 515-517. 1974.

Racault, C., Langlais, F., & Naslain, R. (1994). Solid-state synthesis and characterization of the ternary phase Ti3SiC2. *Journal of materials Science*, *29*(13), 3384-3392.

Rosso, M. (2006). Ceramic and metal matrix composites: Routes and properties. *Journal of Materials Processing Technology*, *175*(1-3), 364-375.

Rudy E., Progulski J. (1967). A Pirani furnace for the precision determination of the melting temperatures of refractory metallic substances. *Planseeber Pulvermetall*, 15(1): 13–45.

Rudy, E. & Progulski, J. (1967). A Pirani furnace for the precision determination of the melting temperatures of refractory metallic substances. *Planseeber Pulvermetall*, 15(1): 13–45.

Rudy, E., & Progulski, J. (1967). A Pirani furnace for the precision determination of the melting temperatures of refractory metallic substances.*Planseeber Pulvermet*, *15*(1), 13-45.

Sanjeev, D. J. (2013). *Ceramic Composites: A Case Study of Ballistic Impact*. BSc Thesis submitted to the University of Pune.

Savage G. (1993). *Carbon–Carbon Composites*. Chapman & Hall.

Schlesinger, M. E. (1994). The Si-Ta (silicon-tantalum) system. *Journal of phase equilibria*, *15*(1), 90-95.

Shabalin, I. L. (2014). *Ultra-High Temperature Materials I: Carbon (Graphene/Graphite) and Refractory Metals*. Springer.

Shi, L., Guo, B. L., Liu, Y. M., & Li, J. T. (2012). Characteristic of Plasma Sheath Channel and its Effect on Communication. *Progress in Electromagnetics Research*, *123*, 321–336.

Singh, A. (2001). Radiation processing of carbon fibre-reinforced advanced composites. *Nuclear Instruments and Methods in Physics Research*, *185*(1–4), 50–54

Singh, A., Saunders, C. B., Barnard, J. W., Lopata, J. V., Kremers, W., Mcdougall, T.E., Chung, M., & Tateishi, M. (1996). Electron Processing of Fibre Reinforced Advanced Composites. *Radiation Physics and Chemistry*, *48*(2), 153-170.

Singh, M., & Behrendt, D. R. (1992). *Studies on the reactive melt infiltration of silicon and silicon-molybdenum alloys in porous carbon* (No. N-93-12398; NASA-TM--105860; E--7320; NAS--1.15: 105860; CONF-920448--). National Aeronautics and Space Administration, Cleveland, OH (United States). Lewis Research Center.

Smeacetto, F., Salvo, M., & Ferraris, M. (2002). Oxidation protective multilayer coatings for carbon–carbon composites. *Carbon*, *40*(4), 583-587.

Smith, P. L., Ortega, R., & Brennan, B. (1997). Pseudo-C11b phase formation of titanium disilicide during the C49 to C54 transition. *MRS Proceedings*, 481, 605.

Stone, A. J., & Wales, D. J. (1986). Theoretical studies of icosahedral C 60 and some related species. *Chemical Physics Letters*, *128*(5), 501-503.

Storms, E. K. (1967). *The refractory carbides* (Vol. 2). New York: Academic Press.
Strong, A. B. (2008). *Fundamentals of Composites Manufacturing: Materials, Methods, and Applications*, 2nd Edition. Michigan: Society of Manufacturing Engineers.

Suryanarayana, C. (2001). Mechanical alloying and milling. Progress in materials science, 46(1), 1-184.

Tang, S., Deng, J., Wang, S., Liu, W., & Yang, K. (2007). Ablation behaviors of ultra-high temperature ceramic composites. *Materials Science and Engineering: A*, *465*(1), 1-7.

Trick, K. A., & Saliba, T. E. (1995). Mechanisms of the pyrolysis of phenolic resin in a carbon/phenolic composite. *Carbon*, *33*(11), 1509-1515.

Trick, K. A., Saliba, T. E., & Sandhu, S. S. (1997). A kinetic model of the pyrolysis of phenolic resin in a carbon/phenolic composite. *Carbon*, *35*(3), 393-401.

Tuinstra, F., & Koenig, J. L. (1970). Raman spectrum of graphite. *The Journal of Chemical Physics*, *53*(3), 1126-1130.

Tzeng, S. S., & Chr, Y. G. (2002). Evolution of microstructure and properties of phenolic resin-based carbon/carbon composites during pyrolysis. *Materials Chemistry and Physics*, *73*(2), 162-169.

Ultramet Advanced Materials Solutions (2013). Available from: <http://www.ultramet.com>. [02 April 2013].

Upadhyaya, G. S. (1996). *Nature and properties of refractory carbides*. Nova Science Pub Inc.

Ushakov, B. F., Zagryazkin, V. N., & Panov, A. S. (1972). Interaction of graphite with titanium and zirconium, Izv. AN USSR, Neorganicheskie Materialy, 8, 1921.

Voitovitch, R., Mortensen, A., Hodaj, F., & Eustathopoulos, N. (1999). Diffusion-limited reactive wetting: study of spreading kinetics of Cu-Cr alloys on carbon substrates," *Acta Materialia*, vol. 47(4):1117–1128.

Wali, N., & Yang, J. (2012). Reactive Melt-Infiltration Processing of Fiber-Reinforced Ceramic Matrix Composites. *Ceramics and Composites Processing Methods*, 351.

Wang, C. J. (1996). The effects of resin thermal degradation on thermostructural response of carbon-phenolic composites and the manufacturing process of carbon-carbon composites. *Journal of reinforced plastics and composites*, *15*(10), 1011-1026.

Wang, J., Jiang, H., & Jiang, N. (2009). Study on the pyrolysis of phenol-formaldehyde (PF) resin and modified PF resin. *Thermochimica Acta*, *496*(1), 136-142.

Wang, M. C., & Zhao, T. (2007). Polyarylacetylene blends with improved processability and high thermal stability. *Journal of Applied Polymer Science* *105*(5), 2939 - 2946.

Wang, Y., Zhu, X., Zhang, L., & Cheng, L. (2011). Reaction kinetics and ablation properties of C/C–ZrC composites fabricated by reactive melt infiltration. *Ceramics International*, *37*(4), 1277-1283.

Wang, Y., Zhu, X., Zhang, L., & Cheng, L. (2012). C/C-SiC-ZrC Composites Fabricated by Reactive Melt Infiltration with $Si_{0.87}Zr_{0.13}$ alloy. *Ceramics International* **38**, 4337–4343.

Wei, S., Xu, B. Q., Bin, Y., Sun, H. Y., Song, J. X., Wan, H. L., & Dai, Y. N. (2011). Preparation of TiC powders by carbothermal reduction method in vacuum. *Transactions of Nonferrous Metals Society of China*, *21*(1), 185-190.

Weisshaus, H., Kenig, S., Kastner, E., & Siegmann, A. (1990). Morphology development during processing of carbon-carbon composites. *Carbon*, *28*(1), 125-135

Windhorst, T., & Blount, G. (1997). Carbon-carbon composites: a summary of recent developments and applications. Materials & Design, *18*(1), 11-15.

Wuchina, E., Opila, E., Opeka, M., Fahrenholtz, W., & Talmy, I. (2007). UHTCs: ultra-high temperature ceramic materials for extreme environment applications. *The Electrochemical Society Interface*, *16*(4), 30-36.

Yi, W., Yongdong, X., Yiguang, W., Laifei, C., & Litong, Z. (2010). Effects of TaC addition on the ablation resistance of C/SiC. *Materials Letters*, *64*(19), 2068-2071.

Yin, Q., Zhu, B., & Zeng, H. (2010). Microstructure, Property and Processing of Functional Ceramics. Springer.

Zaldivar, R.J., & Rellick, G.S. (1991). Some observations on stress graphitization in carbon-carbon composites, *Carbon* **29**(8), 1155-1163.

Zaman, W., Li, K. Z., Ikram, S., Li, W., Zhang, D. S., & Guo, L. J. (2012). Morphology, thermal response and anti-ablation performance of 3D-four directional pitch-based carbon/carbon composites. *Corrosion Science*, *61*, 134-142.

Zhang, D.Y., Zhang, C.R., Hu, H.F., & Zhou, Y.L. (2008). Preparation and Properties of 2D C/SiC-TaC Composites. *Key Engineering Materials*, *1771*, 368-372.

Zhao, D., Zhang, C., Hu, H., & Zhang, Y. (2011). Ablation behavior and mechanism of 3D C/ZrC composite in oxyacetylene torch environment. *Composites Science and Technology*, *71*(11), 1392-1396.

Zou, L., Wali, N., Yang, J. M., Bansal, N. P., & Yan, D. (2011). Microstructural characterization of a Cf/ZrC composite manufactured by reactive melt infiltration. *International Journal of Applied Ceramic Technology*, *8*(2), 329-341.